



Microstructure and sensing properties of LaMO₃ (M=Co, Fe) thin films

Mateusz Jedrusik

► To cite this version:

Mateusz Jedrusik. Microstructure and sensing properties of LaMO₃ (M=Co, Fe) thin films. Chemical Physics [physics.chem-ph]. Université de Toulon; AGH University of Science and Technology (Cracovie, Pologne), 2019. English. NNT : 2019TOUL0013 . tel-02498329

HAL Id: tel-02498329

<https://theses.hal.science/tel-02498329>

Submitted on 4 Mar 2020

HAL is a multi-disciplinary open access archive for the deposit and dissemination of scientific research documents, whether they are published or not. The documents may come from teaching and research institutions in France or abroad, or from public or private research centers.

L'archive ouverte pluridisciplinaire **HAL**, est destinée au dépôt et à la diffusion de documents scientifiques de niveau recherche, publiés ou non, émanant des établissements d'enseignement et de recherche français ou étrangers, des laboratoires publics ou privés.

ÉCOLE DOCTORALE ED 548
IM2NP UMR CNRS 7334

THÈSE présentée par :

Mateusz JEDRUSIK

soutenue le : **09 décembre 2019**

pour obtenir le grade de Docteur en Physique

Spécialité : Sciences des Matériaux

Microstructure and sensing properties of LaMO₃ (M=Co, Fe) thin films

THÈSE dirigée par :

Mme LEROUX Christine
Mme KOPIA Agnieszka

Professeure, Université de Toulon
Professeure, Université de Cracovie

JURY :

Mme.TWARDOWSKA Agnieszka

Rapporteuse, professeure, Université Pédagogique de Cracovie

Mme. HEBERT Sylvie

Rapporteuse, DR CNRS, CRISMAT Caen

M. MAZIARZ Wojciech

Examineur, Professeur, Académie des Sciences Polonaise PAS, Cracovie

M.KONSTANTY Janusz

Examineur, Professeur, AGH Cracovie

M. BERGER Franck

Examineur, MCF HDR, Université de Bourgogne Franche Comté

M. ARAB Madjid

Examineur, MCF HDR, Université de Toulon

Mme LEROUX Christine

Directrice de thèse, Professeure, Université de Toulon

Mme KOPIA Agnieszka

Directrice de thèse Professeure, AGH Cracovie

M. TURQUAT Christian

Invité, MCF, Université de Toulon

M. CIENIEK Lukasz

Invité, MCF, AGH Cracovie

AKADEMIA GÓRNICZO-HUTNICZA

IM. STANISŁAWA STASZICA W KRAKOWIE

Wydział Inżynierii Metali i Informatyki Przemysłowej

ROZPRAWA DOKTORSKA

pt.

„Microstructure and sensing properties of LaMO_3 (M=Co, Fe) thin films”

Akademia Górniczo-Hutnicza im. Stanisława Staszica

Wydział: Inżynierii Metali i Informatyki Przemysłowej

Katedra: Inżynierii Powierzchni i Analiz Materiałów

Imię i nazwisko autora rozprawy

mgr inż. Mateusz Jan Jędrusik

Stopień/tytuł naukowy, imię i nazwisko promotora rozprawy

dr hab. inż. Agnieszka Kopia

Stopień/tytuł naukowy, imię i nazwisko promotora pomocniczego rozprawy

dr inż. Łukasz Cieniek

Podpis dyplomanta: Podpis promotora:

Kraków 2019

„Uprzedzony o odpowiedzialności karnej na podstawie art. 115 ust. 1 i 2 ustawy z dnia 4 lutego 1994 r. o prawie autorskim i prawach pokrewnych (t.j. Dz.U. z 2006 r. Nr 90, poz. 631 z późn. zm.): „Kto przywłaszcza sobie autorstwo albo wprowadza w błąd co do autorstwa całości lub części cudzego utworu albo artystycznego wykonania, podlega grzywnie, karze ograniczenia wolności albo pozbawienia wolności do lat 3. Tej samej karze podlega, kto rozpowszechnia bez podania nazwiska lub pseudonimu twórcy cudzy utwór w wersji oryginalnej albo w postaci opracowania, artystyczne wykonanie albo publicznie zniekształca taki utwór, artystyczne wykonanie, fonogram, wideogram lub nadanie.”, a także uprzedzony o odpowiedzialności dyscyplinarnej na podstawie art. 211 ust. 1 ustawy z dnia 27 lipca 2005 r. Prawo o szkolnictwie wyższym (t.j. Dz. U. z 2012 r. poz. 572, z późn. zm.) „Za naruszenie przepisów obowiązujących w uczelni oraz za czyny uchybiające godności studenta student ponosi odpowiedzialność dyscyplinarną przed komisją dyscyplinarną albo przed sądem koleżeńskim samorządu studenckiego, zwanym dalej "sądem koleżeńskim"”, oświadczam, że niniejszą pracę dyplomową wykonałem(-am) osobiście i samodzielnie i że nie korzystałem(-am) ze źródeł innych niż wymienione w pracy.”

Kraków, dnia
Podpis dyplomanta:

Acknowledgments

It is my pleasure to acknowledge the roles of several people who were big support in complementation of my Ph.D thesis.

First of all, I would like to express my gratitude to my supervisors, dr hab. inż. Agnieszka Kopia and Prof. Christine Leroux, as well as my co-supervisors, Ph.D Christian Turquat and Ph.D Łukasz Cieniek, for scientific care and motivation to work. I truly enjoyed working with them.

I would also like to thank DSc. Paweł Pasierb and Prof. Madjid Arab for providing help during gas tests.

Mateusz Jędrusik acknowledges the financial support of the French Government and the French Embassy in Poland.

List of abbreviations, symbols and markings

Abbreviation	Explanation
AFM	Atomic Force Microscopy
CVD	Chemical Vapor Deposition
EDS	Energy Dispersion X Ray Spectroscopy
PLD	Pulsed Laser Deposition
SEM	Scanning Electron Microscopy
TEM	Transmission Electron Microscopy
XPS	X Ray Photoelectron Spectroscopy
XRD	X Ray Diffraction
SE	Sensing electrode
RE	Reference electrode
S	Sensor sensitivity
T	Temperature (°C)
e	Electric charge (C)
λ	Wavelength of absorbed laser radiation (nm)
E	Impulse energy (J)
ε	Energy density (J/cm ²)
p	Gas pressure (Pa)
R_t	Relative texture factor
L_D	Effective length of Debye
EGS	Electrochemical gas sensor
AGS	Amperometric gas sensor
TBS	Tree phase boundaries
C-YSZ	Cubic Yttrium Stabilized Zirconia
PSZ	Partially stabilized zirconia
TZP	Tetragonal zirconia polycrystal

Table of contents

1	INTRODUCTION.....	7
2	BACKGROUND	10
2.1	GAS SENSING TECHNOLOGIES.....	10
2.1.1	Overview of electrochemical gas sensors.....	11
2.1.2	Overview of resistance gas sensors.....	20
2.2	CHARACTERISTICS OF MATERIALS FOR GAS SENSORS	28
2.2.1	Perovskites as sensing electrodes.....	28
2.2.2	Cristal structure of LaFeO_3	29
2.2.3	Cristal structure of LaCoO_3	30
2.2.4	Cristal structure of YSZ materials.....	34
2.3	PLD METHOD FOR THIN FILMS DEPOSITION.....	36
2.4	OBJECTIVE AND THESIS OF WORK.....	44
3	METHODOLOGY AND RESEARCH TECHNIQUES.....	46
3.1	THIN FILM DEPOSITION	46
3.1.1	Target preparation.....	46
3.1.2	Thin films preparation.....	46
3.2	RESEARCH TECHNIQUES.....	48
3.2.1	X-Ray Diffraction.....	48
3.2.2	Scanning Electron Microscopy.....	48
3.2.3	Atomic Force Microscopy.....	48
3.2.4	Transmission Electron Microscopy.....	48
3.2.5	X-ray photoelectron spectroscopy.....	51
3.2.6	Resistance measurements.....	52
3.2.7	Electrochemical measurements.....	54
4	STRUCTURAL CHARACTERIZATION	56
4.1	STRUCTURAL CHARACTERIZATION OF LaCoO_3 THIN FILMS.	56
4.1.1	LaCoO_3 thin films on Si (100) substrate.....	56
4.1.2	LaCoO_3 thin films on C-YSZ (100) substrate.....	64
4.1.3	LaCoO_3 thin films on T-YSZ substrate.....	72
4.2	STRUCTURE CHARACTERIZATION OF LaFeO_3 THIN FILMS.	76
4.2.1	LaFeO_3 thin films on Si (100) substrate.....	76
4.2.2	LaFeO_3 thin films on C-YSZ (100) substrate.....	85
4.2.3	LaFeO_3 thin films on T-YSZ substrate.....	98
5	GAS MEASUREMENTS	104
5.1	RESISTANCE MEASUREMENTS	104
5.1.1	LaCoO_3	104
5.1.2	LaFeO_3	113
5.2	ELECTROCHEMICAL MEASUREMENTS	122
6	EXTENDED SUMMARY AND PERSPECTIVES	131
7	FIGURE INDEX.....	136
8	TABLE INDEX.....	140
9	REFERENCES.....	142

1 INTRODUCTION

Because of the industry evolution and the increasing human impact on nature, air pollution is one of the main challenges of today's world. Hence due to larger people's awareness, air pollution control has become an important topic in public debates resulting in the large availability of information on air quality to the citizens. Gas detection devices are now common in all branches of industry such as the automotive (lambda probe, SCR system), aviation, energy, medicine (diagnosis of diseases). Current gas sensors can detect, among others, the amount of CO , CO_2 , NO , NO_2 , NH_4 , SO_2 (see Table 1); these gases being well-known to have a negative impact on human health.

Table 1. Examples of gas sensor application in various industries according to [1].

Market / application	Examples of detected chemical compounds and classes
Automotive	$O_2, H_2, CO, NO_x, HC_s,$
IAQ	$CO, CH_4, \text{humidity}, CO_2, VOCs,$
Food	Bacteria, chemicals, toxins, pH, $CO,$
Agriculture	$NH_3, \text{Amines}, \text{humidity}, CO_2, \text{pesticides},$
Water treatment	pH, $Cl_2, NO_x, HC, NH_3, H_2S,$
Environmental	pH, heavy metal ions, $SO_x, CO_2, NO_x, NH_3, H_2S$
Industrial safety	Indoor air quality, toxic gases,
Utilities [gas, electric]	$O_2, CO, HC_6, SO_x, CO_2,$
Petrochemical	$HC_x,$ conventional pollutants,
Steel	$O_2, H_2, CO,$ conventional pollutants
Aerospace	$H_2, O_2, CO_2,$ humidity

To respond to public concerns and using a precautionary approach, European Union lawmakers introduced restrictions on the maximum amount of harmful gases emitted from the combustion process of car engines. These new European standards have forced car manufacturers to develop more efficient, less polluting engines. For instance, in diesel engines, this has been achieved by introducing a Selective Catalytic Reduction (SCR) system (see Figure 1) in which a NO_x sensor, directly mounted in the exhaust gas system of the car, is a key component. This sensor detects the content of harmful NO_2 in the exhaust gas; the information is then transmitted to the controlling system and depending on the NO_2 content, a certain amount of urea solution is

injected into the exhaust gases. Urea causes the decomposition of NO_x into N_2 and H_2O . The system must quickly, reliably and accurately determine the exhaust gas composition, so that the right amount of urea is injected.

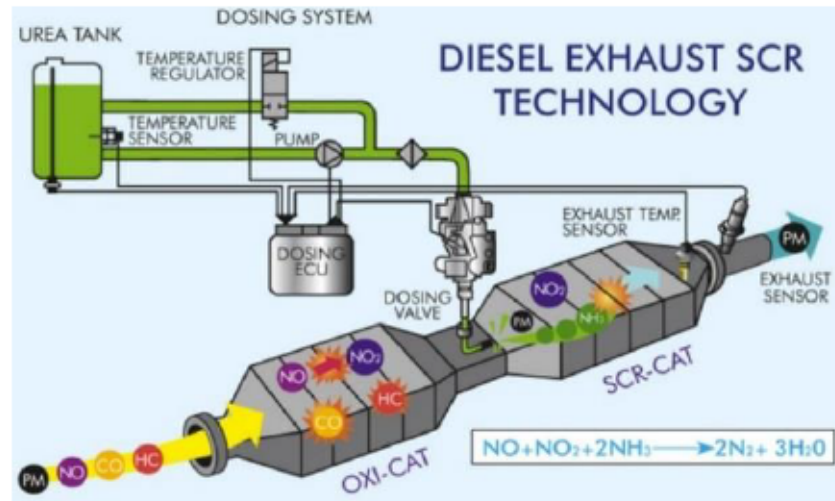


Figure 1. SCR system in diesel engines developed to reduce NO_x emissions [2].

Another example for gasoline engine is the lambda probe (see Figure 2), which is responsible for dispensing air in the fuel-air mixture. In order to obtain optimal combustion parameters, the lambda probes test the oxygen content before and after the catalyst and, based on the measured composition, the fuel-air mixture is set. The more accurate and the quicker the measurement, the better is the reduction of pollution emissions into the atmosphere.

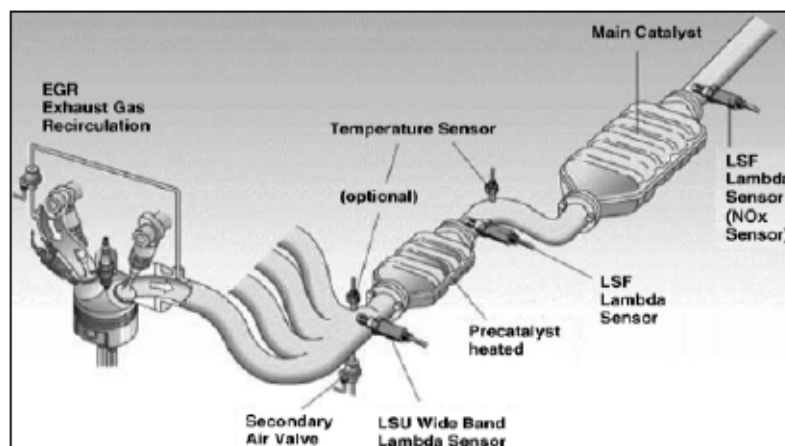


Figure 2. Gas sensor in the modern car exhaust system [3].

The energy industry is another important user of gas sensor. In order to reduce emissions, power plant efficiency must be increased. To achieve this, it is necessary to increase the temperature and pressure of the steam supplied to the turbines. Therefore, sensors must be resilient to extreme conditions of use. For automotive applications, the ideal gas sensor should be able to work at high temperatures, in an environment of many gases, and still be accurate, sensitive and

fast responding over time. Currently, thick-film sensors dominate the market and are mainly manufactured in Germany, Switzerland, Japan and United Kingdom. Increasing requirements regarding sensitivity and reaction time have forced manufacturers and scientists to look for alternatives to systems currently available. In recent years, thin-film gas sensor technology, with nanometric grain size, has become extremely popular and promising with a significant increase in sensitivity, reduced response time and gas detection threshold as compared to thick film sensors. However, thin-film sensors, based on materials used for thick-film technology, have shown a weak stability, prompting scientists to look for alternative materials. A promising class of materials is perovskites, which are well-known for their good electrical properties and high thermal stability, up to 1000 K.

2 BACKGROUND

2.1 GAS SENSING TECHNOLOGIES

Gas sensor is a device that detects and quantify the presence, sometimes the concentration, of gases in a specific volume. In gas sensor technologies, the information about gases is converted into a useful signal (electric, thermic, etc.). Gas sensors are mainly used to detect harmful gas such CO [4], NO_x [5, 6], H₂ [7], NH₃ [8] and SO₂ [9].

Different technologies are available on the market and the physical phenomenon originating in the gas detection determines the type of the sensor. Essentially, Sensors can be divided into five types:

- electrochemical gas sensor (EGS),
- resistance sensor (RS),
- optical sensor,
- surface acoustic wave sensor,
- calorimetric sensor.

The gas sensors have the same criteria regardless of the mechanism of operation, the basic ones being a high sensitivity and selectivity regarding the gas of interest, a short response time and regeneration time, the ability to work in a wide range of temperatures and a good stability over time [10]. EGS and RS gas sensor usually contain the following elements:

- a gas sensing electrode (SE),
- a support like Si, YSZ, Al₂O₃,
- a heating system,
- an electrode.

The sensing layer or sensing electrode (SE) is one of the key elements in gas sensing devices since it is the active element that interact with the gas.; this interaction leads to the production of an electrical signal, which is modified and amplified to get a useful signal. Hence, the selection of the material for sensing layer is crucial. Materials for sensing layer can be divided into three categories:

- materials with ionic conductivity in the form of inorganic oxides: SnO₂ [11, 12], TiO₂ [13], ZnO [14], WO₃ [15], ZrO₂ [16],
- materials with mixed conductivity: SrTiO₃ [17], LaMnO₃ [18], LaCoO₃ [4], LaFeO₃ [19],

- conductive polymers, nanostructures and nanocomposites.

This distribution is generic because the materials for sensing layer change of conduction mechanism depending on temperature, gas pressure or the presence of dopants.

One interesting class of materials, because it shows a mixed conductivity, is perovskites whose general chemical formula is ABX_3 , where A and B are cations (A larger in size than B) and X is the anion usually oxides or halogens. In the case of ABO_3 type compounds, it is usual to observe a deviation from stoichiometry in oxygen mainly due to an unusual or a mixture of degree of oxidation of the cation B. This non-stoichiometry results in the occurrence of oxygen vacancies that play a critical role in the electrical conductivity of the material especially at high temperature. It is important keep in mind that in the case of perovskite compounds both electrons and holes contribute to the general conductivity although one mechanism of conduction is usually favored depending on chemical composition of perovskites. Besides, perovskite compounds are recognized for their excellent thermal and chemical resistance, making them very good candidates as sensing material in hostile environments. Because of all these characteristics, perovskite compounds were chosen as sensing layer for this research work.

Finally, because of their properties, perovskites have a good potential as sensing layer for electrochemical and resistance gas sensors; the principle of these two types of sensors will then be presented hereafter.

2.1.1 Overview of electrochemical gas sensors

Fundamentally, electrochemical sensors are constituted of a sensing electrode, SE, exposed to the gas and that is an electron conductor and a reference electrode, RE, usually made of platinum (Pt) separated by a thin electrolyte (solid or liquid) acting as an ion conductor. An example of an electrochemical gas sensor is given in Figure 3.

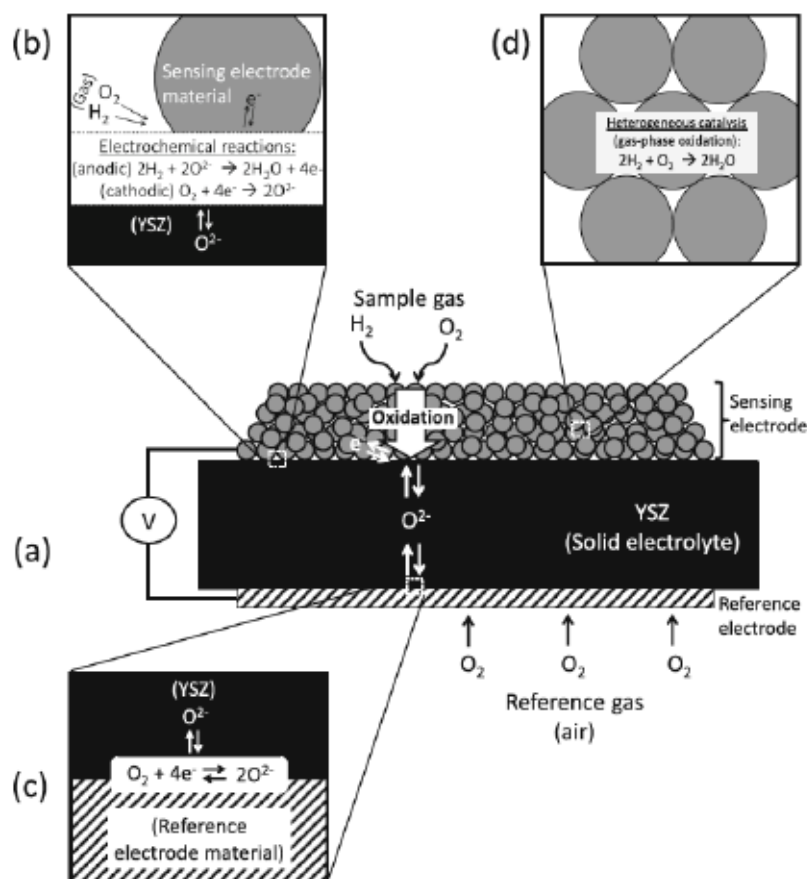


Figure 3. Illustration of a) the typical construction of a mixed-potential type YSZ-based sensor, including b) the electrochemical reactions that occur at the SE/YSZ interface and c) the equilibrium RE reaction of O₂ at the interface of RE/YSZ, as well as d) the SE layer [20].

The selection of the reference electrode (RE) material is very important. These electrodes are used to transfer the measuring signal by means of electrical wires to the controller. The electrode material must have high chemical stability, not react with SE as well as with substrate. Usually, RE is made from noble metals such as Au [21], Pt [21, 22] or Pd [23]. However, several studies comparing various RE materials such as Au, Pt, and Pd [21] – [24] have shown that the RE has a limited influence of on sensor sensitivity. These studies also revealed that Au electrodes have a lower stability than Pt electrodes.

The electrolyte material is responsible for ion transfer between SE and RE. One of the great advantages of electrochemical gas sensors is the possibility of miniaturization, because sensitivity is size independent [25]. The electromotive force (EMF) in this system is generated as a result of the charges exchange between the two electrodes. This EMF is then proportional to concentration of gas present in the environment. Electrochemical sensors are available and well-known and popular at the market.

Because of their practicality, solid electrolyte sensors replaced most of the liquid electrolyte. As solid electrolyte, one can cite ZrO_2 [25], YSZ [26][27][28] – [29], Al_2O_3 [25], SO_2 [30], Ag [31], NASICON [32].

A popular electrolyte is Yttrium Stabilized Zirconia, or YSZ, in which the ionic conduction occurs via the oxygen anions. Not only, this material is characterized by a high ionic conductivity, but also by a high chemical stability over a wide range of temperature.

Solid electrolyte allows a more practical use of the electrochemical sensors in particular since solid electrolyte-based sensor are able to work at higher temperature. This type of sensor can work as potentiometric sensor [1]. Measurements of the equilibrium potential of the solid electrolyte-electrode cells system enable oxygen detection via the Nernst's equation [33]. Sensors of this kind are called potentiometric sensors. Table 2 summarizes the ion conductivity of different solid electrolytes. YSZ has a high conductivity and is also stable in extreme environments making it one of the best choices as solid electrolyte [34]. High ion conductivity of electrolyte is highly desirable that's why author chose YSZ [27].

Table 2. Electrical conductivity values of solid electrolytes at 600 °C [8] [9][10]– [11]

Oxygen ion conducting solid electrolytes	Conductivity (S. cm^{-1})
Bi_2O_3	3.10^{-3}
Gd_2O_3 doped CeO_2	4.10^{-3}
$\text{Bi}_2\text{Cu}_{0.1}\text{V}_{0.9}\text{O}_{5.35}$	1.10^{-1}
YSZ (8 mol % Y_2O_3)	5.10^{-2}

Solid electrolyte must meet several requirements. First, the solid electrolyte must possess a high chemical stability for a stable functioning over time. Indeed, the electrolyte should be able to work at high temperature and pressure while exposed to reactive gases (NO_2 , CO_2 , NH_3 , etc.). On the other hand, the solid electrolyte must possess a high sensitivity, which implies the selected materials should reactive with high ionic conductivity in a wide range of temperatures and pressures. Finally, the solid electrolyte should have a similar thermal expansion as compared with the other sensor components. Indeed, during the temperature increase, difference in thermal expansion rates between the SE and the electrolyte may trigger cracks within the sensor components causing further operation impossible.

Currently, SnO_2 is the most popular material as sensing electrode [4, 11, 12]. However, SnO_2 -based gas sensors have two issues for industrial demands. First, these sensors present a poor Selectivity (or cross-sensitivity) towards the target gas or cross-sensitivity towards other gases making measurements inaccurate. Second problem is that these sensors do not satisfying the industrial requirement concerning sensitivity. Because of that, scientists have been looking for new materials.

The above-mentioned sensor characteristics —sensitivity and selectivity— mainly depend on the SE material and its morphology. A large number of materials has been studied as sensing electrode. For instance, one could mention Liu *et al.* [28] who used thick layer of In_2O_3 on YSZ (8% mol Y_2O_3) as SE. The layer was sintered at three temperatures $T = 800, 1000, 1200^\circ\text{C}$. This work concludes on a high sensitivity of the sensor in presence of NO_2 for a SE sintered at $T = 1000^\circ\text{C}$ and a 30-days stability at an operating temperature of 700°C . But certainly, the mostly alternative SE class of materials studied is perovskites compounds.

As mentioned earlier, perovskites are characterized by a high stability at elevated temperatures with a mixed conductivity. Using a screen-printing technic, Cvejic *et al.* [29] produced a NdCoO_3 layer doped with Sr on the YSZ. They showed high sensitivity of the generated sensor in presence of NO_x gases. The use of the $\text{Nd}_{0.9}\text{Sr}_{0.1}\text{CoO}_3$ electrode caused the decomposition of NO_2 into N_2 on its surface and the adsorption of the oxygen produced to oxygen permeation inside the perovskite.

$\text{Ba}_x\text{Sr}_{1-x}\text{FeO}_3$ ($x = 0.01, 0.5, 0.9, 1$) perovskites in the form of films on the YSZ substrate were examined by Iio *et al.* [35]. Sensitivity of the sensor for NH_3 , NO_2 , NO , C_3H_6 , CH_4 , H_2 , C_3H_8 gases was tested and a very good sensitivity was obtained in the temperature range $450\text{--}600^\circ\text{C}$. Hence, this material can be used as a lambda (λ) probe. In addition, the authors investigated the sensor stability as a function of time in the CO atmosphere. It was shown that the electrical potential difference of sensor was constant for 14 days of continuous operation. For its part, Tho *et al.* [26] was the first to use LaMO_3 ($M = \text{Mn}, \text{Co}, \text{Fe}, \text{Ni}$) perovskites on the YSZ substrate (8% of Y_2O_3) as SE for the detection of NO , NO_2 , C_3H_8 , CH_4 gases. Films were obtained by screen printing followed by a sintering at temperatures ranging from 700 to 1300°C . The films obtained by this method were of few micrometers thick. These films showed high sensitivity and selectivity to NO_2 from 450°C to 650°C . Thin films sintered at 1300°C showed high response ($\Delta V = 60 \text{ mV}$) under 60 ppm of NO_2 . Later, studies showed that high sensitivity

to NO_2 could be obtained also for LaFeO_3 and LaCoO_3 [36][37] – [38]. These films produced by screen printing have a thickness in the micrometer range.

Ueda *et al.* [39] was the first to investigate the influence of the SE thickness on sensor sensitivity. The authors showed also that high sensitivity can be obtained with a NiO sensing electrode with dimensions as small as 250 nm. Thin films obtained by magnetron sputtering with thickness of 250 nm and 500 nm were tested and the sample with smallest thickness showed almost two times higher sensitivity in NO_2 at 60 ppm. From this work, one can expect to increase sensitivity of sensors simply by switching from micrometer-size films to nanometer-size films. There is no previous study in literature referring to nanometric films based on LaCoO_3 and LaFeO_3 as sensing electrodes on substrates YSZ, which justifies the novel character of this research.

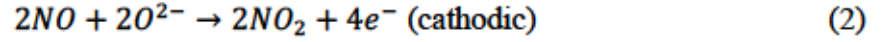
Electrochemical gas sensor (EGS) are working based on reaction occurring between surface of sensing electrode (SE) and the target gas. As a result of this reaction, electromotive force (EMF) between SE and RE is created [20]. Electromotive force is converted into a useful signal.

Because of work principle, electrochemical gas sensor can be divided in four groups:

- amperometric,
- potentiometric,
- conductometric,
- capacitive.

In potentiometric gas sensor, electrical potential is measured between the two electrodes SE and RE. In that configuration, the SE with Pt electrode is in contact with the target gas while the RE is only in contact with oxygen. The generated potential is directly proportional to the logarithm of the gas concentration as described the Nernst's law. The main advantage of this type of sensors is its ability to detect a wide range of gas concentrations, its stability over time. Moreover, all reactions affecting sensitivity are at equilibrium.

The principle of operation will be discussed based on the reaction between SE with NO_x . A reference electrode exposed to air only acts as an oxygen electrode and its potential is determined at a constant oxygen concentration. On the other hand, on SE, oxygen and NO_x can react on three phase boundary (TPB) which is contact of gaseous phase, electron conductor (Pt or SE) and ionic conductor (SE or substrate). In the gas containing NO, the following cathode and anode reactions with presence of oxide ions can be taken:



It is caused by the oxidation of NO to the NO₂ equilibrium concentration. On SE, NO₂ would tend to dissociate up to equilibrium concentration. This would lead to the following reactions on the SE:

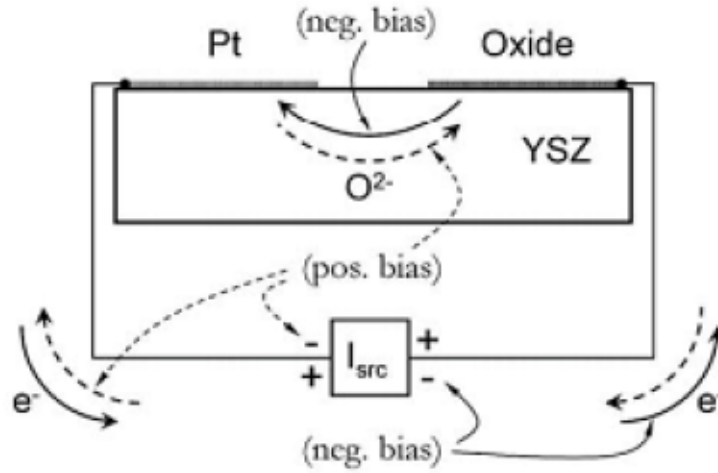
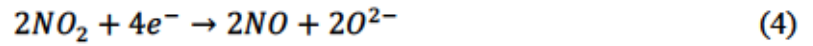


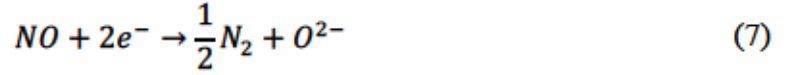
Figure 4. Schematic of current flow in a biased sensing element. O^{2-} represents an oxygen ion in the YSZ substrate [3].

Figure 4 schematically summarizes the directions of each species for both negative and forward bias. With a negative voltage, the following oxidation reactions must occur on the Pt electrode to ensure the current flow:



or

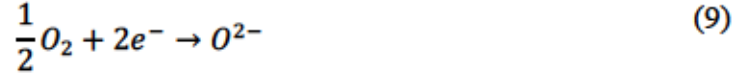




or



or



In reactions (5)–(9), all ions are in a gaseous state. O^{2-} are oxygen ions in the electrolyte (YSZ). NO_2 and NO tend to partially reduce or oxidize to form an equilibrium mixture of NO_2 and NO . Quantitative analysis can be performed by measuring the polarization curves of the sensor in {air + NO } or {air + NO_2 }. As the NO or NO_2 concentrations in the air increases, the polarization curves consequently shift up or down.

On the surface of SE with high catalytic activity, the cathodic NO_2 reaction can lead to NO_2 decomposition:



This will reduce the sensitivity of the sensor. To prevent the decomposition of NO_2 on SE at high temperature, one should use material with the highest possible porosity and large grains, when TPB is situated at the substrate-layer interface. [40]. Low catalytic activity towards the gas (reaction (10)) leads to high sensitivity for NO_2 .

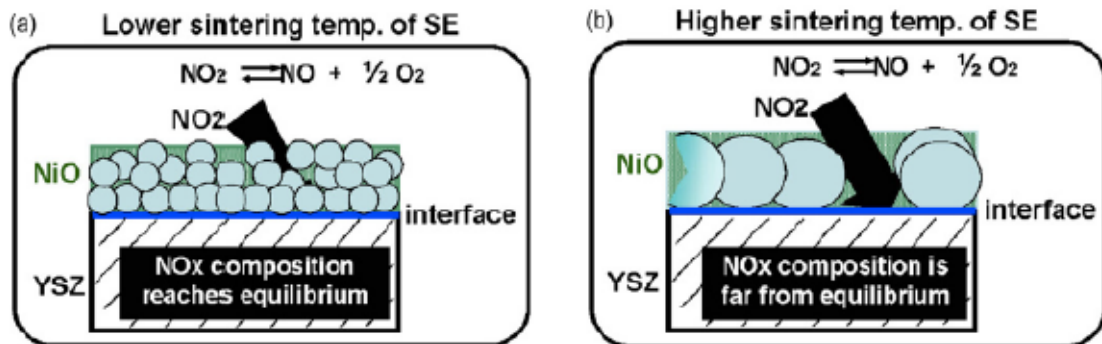


Figure 5. Influence of pore size and grain size on catalytic activity and NO_2 decomposition on the SE surface [40]

The influence of SE grain size and porosity on NO_2 decomposition reactions is shown in Figure 5. As a result of the presence of large pores, NO_2 gas diffuses through the SE towards TPB

(interface of NiO and YSZ), as a result of which there is less contact of the tested gas particles with the SE surface. Therefore, NO₂ can reach TPB without decomposing into NO. With a porous SE structure, NO_x may be far from equilibria when it reaches TPB after diffusion through the SE layer. This phenomenon is not applicable to materials with mixed conduction, in other materials porous structure can have positive influence on sensitivity but it can have negative influence on response time [25, 41].

The detection mechanism is complex, the sensor sensitivity depends on many factors, the two most important of them being the adsorption-desorption mechanism and catalytic activity leading to NO₂ decomposition.

Regarding the adsorption-desorption mechanism, NO₂ behavior on the SE surface, if NO₂ adsorption on the SE surface is strong this can lead to high catalytic activity for the cathodic reaction:



Adsorption – desorption of oxygen on the surface of SE. Strong oxygen absorption is not always associated with low catalytic activity for the anode reaction:



However, low SE activity towards O₂ is the basis for obtaining a response to NO and NO₂ [42].

As for the SE catalytic activity towards non-electrochemical gas phase decomposition reaction of NO₂



Zhuikov and Miura [43] demonstrated that the lower the catalytic activity towards NO₂ at the SE surface, the higher the sensitivity to NO₂ at high temperatures. The sensitivity and selectivity of electrochemical sensor depends on the sensing electrodes of their structure and chemical composition. Peter Martin *et al.* [44] showed that the morphology (structure and thickness) of

Cr₂O₃ sensing electrodes produced by colloidal spray on YSZ has an effect on the properties of the gas sensor and the reaction between NO_x and O₂. Table 3 gathers the sensitivity results of sensors with different thickness. As Peter Martin *et. al.* [44] proved that not only the sintering temperature affect sensitivity (see Figure 6) but also SE thickness (see Table 3). As we can observe sample sintered at 1000 °C with thickness 2.8 µm showed higher sensitivity than sample with 3.6 µm thickness.

Table 3. Electrode thickness and NO sensitivity for the sensors according to [44].

	Ia	Ib	IIa	IIb	IIIa	IIIb	Pt (air ref.)
Sintering temperature (°C)	1000	1000	1100	1100	1200	1200	1000
Thickness (µm)	2.8	3.6	2.7	3.5	2.3	3.5	1–2
500 ppm NO, 500 °C (mV)	-45	-20	-45	-49	-45	-45	-20
500 ppm NO, 550 °C (mV)	-45	-20	-45	-49	-45	-45	-20
500 ppm NO, 600 °C (mV)	-7	-2	-8	-14	-17	-19	-1

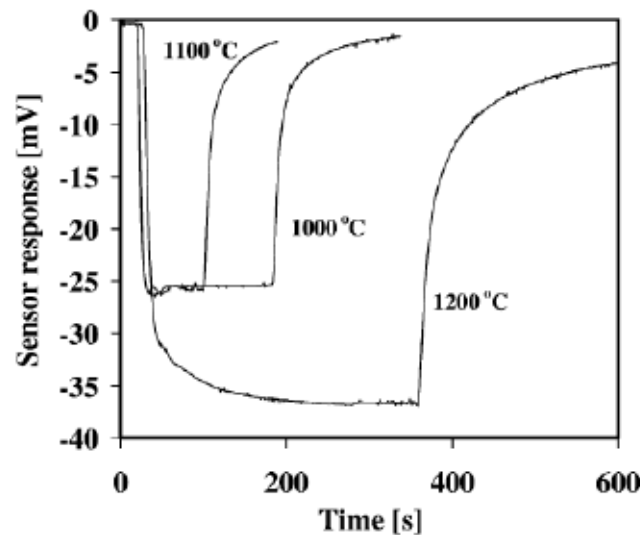


Figure 6. Response vs. time for sensors Ia, IIa, and IIIa exposed to 500 ppm NO in 10% O₂ at 550 °C. The sensing electrodes had initially the same thickness but different sintering temperatures of 1000, 1100 and 1200 °C, respectively. The initial baseline at ~0 mV represents the equilibrium response prior to introduction of the NO into the gas stream [44].

Microstructure have a significant effect on the sensor response. The results presented by Peter Martin *et. al.* (see Table 3) [44] show a dependence on electrode thickness which indicates multiple, competing mechanisms determine the NO sensor response.

2.1.2 Overview of resistance gas sensors

Currently, there are many different configurations of resistance sensors, but they have the same basic elements as described in Figure 7:

- a sensing electrode (SE) surface of the material that have contact with gas and is mainly responsible for the sensor's sensitivity [45],
- the substrate whose role is to support the SE,
- and the electrodes, usually platinum.

In many cases, the sensor also contains a heater to reach the correct operating temperature and membranes.

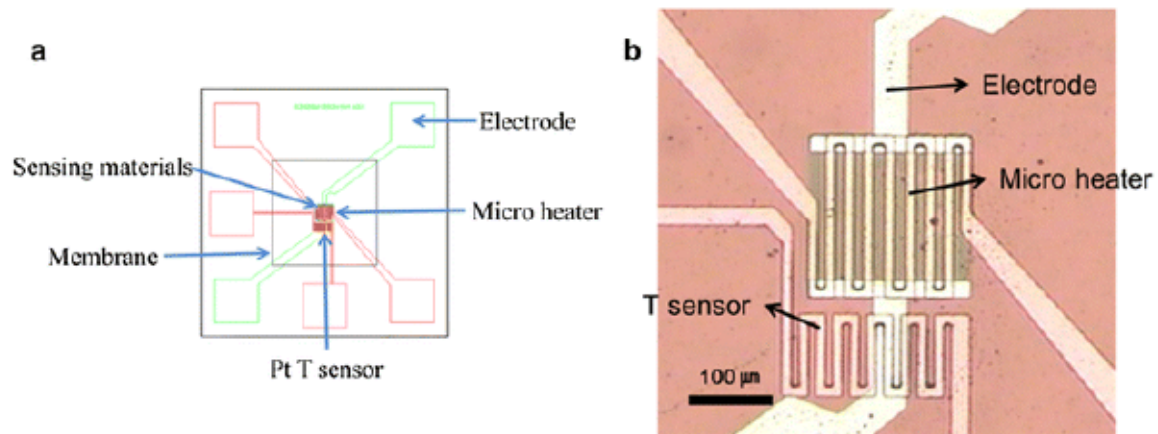


Figure 7. Resistance gas sensor equipped with membrane and heater [46].

The key element of a resistive sensor, RS, is the SE whose surface is the place of a number of key reactions including physical adsorption, chemical adsorption and surface and volume defects range c and d in Figure 9.

Physical adsorption originates in the Van der Waals interactions between oxygen atoms and the SE surface. The energy of these bonds is low and does not affect SE conductivity, because it does not modify the energy structure of the surface [46] range a in Figure 8. On the other hand, chemical adsorption occurs as a result of interaction of electrons of molecules adsorbed with the surface of SE, it leads to the formation of active surface states. Surface states take over electrons from the SE conductivity band, this process is called ionosorption and this is a key mechanism for the sensor's operation [47] range b in Figure 8. The network gaps in the SE surface and in the volume of SE are filled by oxygen atoms. The interaction of oxygen with the SE layer is dependent on temperature and oxygen partial pressure.

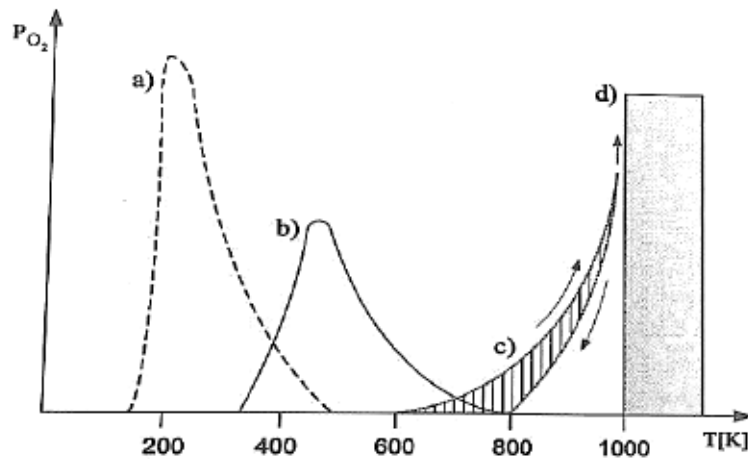


Figure 8. Oxygen partial pressure as a function of temperature illustrating the desorption of oxygen from a semiconductor (ZnO) a) physical adsorption, b) chemisorption, c) surface defects, d) volume defects [25]

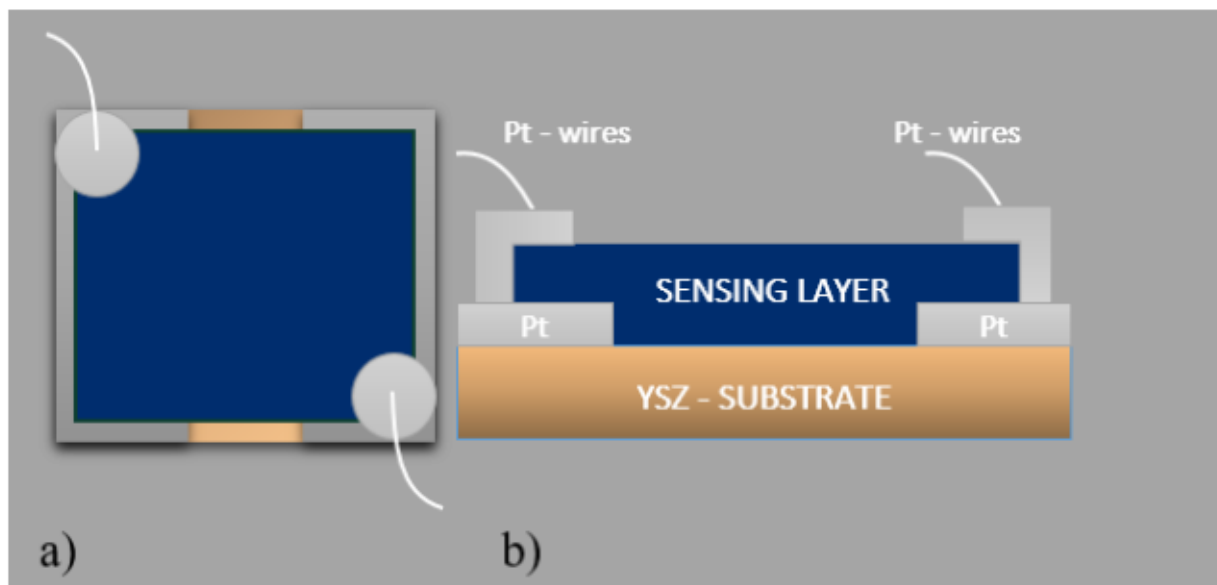


Figure 9. Configuration of a resistive gas sensor: (a) top view, (b) cross section view.

Sensing electrode can come in many forms: films, powder or crystal. Examples of materials for SE was presented in paragraph 2.1.1. Sensitivity of the sensor depends on the process of producing SE and the added dopants. Dopants, catalysts and stabilizers are introduced to modify the material properties. This modifies the surface, chemical composition and structure of the SE. Dopants may increase number of the active centers in SE and thus increase the sensitivity of the sensor.

All gas sensors components are located on the substrate. Gas sensor can be produced as planar sensors, tubes or rods. Substrate material should show a high stability in wide range of

temperatures, chemically inert and should also be a good insulator with high chemical stability. The most commonly materials are Al_2O_3 (low production costs), SiO_2 , Si, MgO , BeO .

The role of the electrodes is to collect transfer the signal by means of electrical wires to the measuring device. High chemical stability, nonreactive towards other components of gas sensor and surrounding gases are most important requirements for electrodes.

Commercial resistance gas sensors use thick-film; however, recently, thin-film sensors have attracted academic and industry interests due to the higher sensitivity thin films as compared to thick films. The influence of grains size on sensitivity have been intensely studied by Pisarkiewicz [25]. His research proved that nano-size grains materials exhibit a high sensitivity and a short response time.

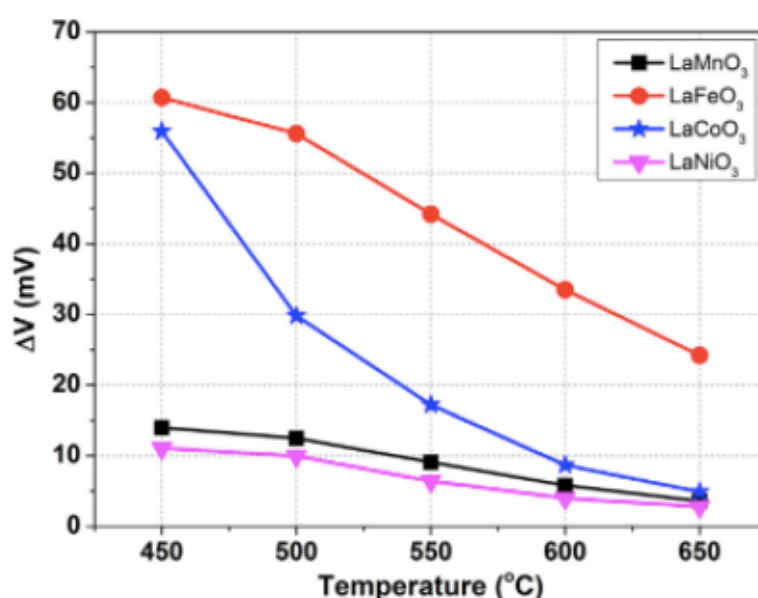


Figure 10. Sensitivity of perovskites in 60 ppm of NO_2 [26].

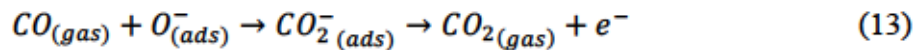
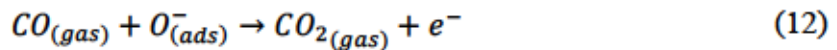
Sensitivity of different material as SE are shown in Figure 10. Under 60 ppm of NO_2 , LaFeO_3 and LaCoO_3 have the best sensitivity in comparison to LaNiO_3 and LaMnO_3 . In this work, perovskites LaCoO_3 and LaFeO_3 were used as sensing electrodes due to their very good chemical and physical properties as well as high conductivity [39], [48][49] – [50] in resistance sensors.

The resistance sensor generates an electrical signal due to the interaction of the gas with the gas-sensitive layer. In fact, the gas reacts with the sensing layer generating a change in the SE conductivity, thus in SE resistance. These variations of resistance are then measured; this is the useful signal. Interaction of gas particles with adsorbed oxygen particles is necessary to change

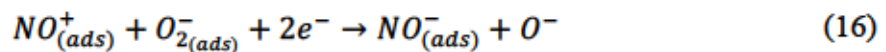
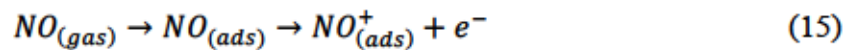
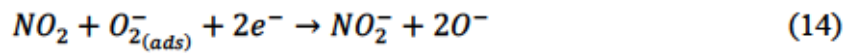
the layer resistance. Resistance gas sensor can be divided in two groups regarding physical phenomena responsible for signal creation. Bulk conduction-based sensors and surface layer-controlled gas sensors. In this work gas sensor with use of layer will be described. Working temperature of surface layer sensors is lower than bulk conduction-based gas sensors, typically 300 – 800°C. Temperature is strongly influencing sensitivity of the sensor. The temperature should be low enough to allow sufficient surface adsorption and slow down the bulk defect equilibration processes, but high enough for catalysis reactions and charge transfer between the surface layer and the bulk.

Depending on the type of gas, different chemical reactions can occur on the SE surface depending on the reducing or oxidizing nature of gas of interest.

In the case a reducing gas like CO , the reactions are as follows:



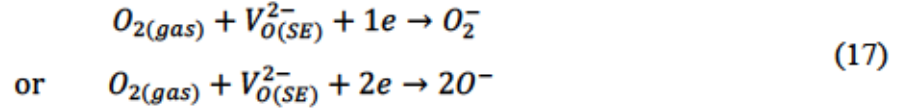
While for an oxidizing gas like NO_x , the reactions are:



In reactions (12) to (16), the oxygen from atmosphere is very much involved and play an important role in this process. Due to the electron transfer between the gas and SE, the material resistance changes. Oxygen is found not only in gas, but also in gas-sensitive material for example (NiO [51]–[52][53][54] [55], CuO [50], [56][57]– [58], ZnO [59], SnO₂ [11], WO₃ [60]) and very popular perovskites.

They have character of acceptor centers, therefore the electrons from the SE conductivity band pass to them by charging them negatively, while the SE surfaces is charged positively.

The chemisorption of oxygen on the surface of SE is presented in reactions:



As a result of this process, a double layer of charges was created, which causes an increase in the conductivity bands upwards (towards higher energies), a potential barrier V_s is created and the transfer of electrons to the acceptor centers is no longer possible. Depletion layer is created on the SE surface. The height of the created barrier depends on the concentration of chemo-absorbed oxygen. Therefore, by introducing a reducing atmosphere, SE increases its conductivity due to a decrease in the potential between the crystalline barrier (in the case of granular materials), while the contact of SE with oxidizing gas will increase the resistance of the layer.

The depletion layer thickness is characterized by Debye length L_D . As the L_D size increases, the concentration of electric charge carriers decreases, which is why this value is also information about the sensitivity and detection threshold of the sensor. L_D increases with increase of temperature (T) and decreases with increase of electron density (n_0).

Debye length is calculated from formula:

$$L_D = \sqrt{\frac{\epsilon \epsilon_0 K T}{e^2 n_0}} \tag{Equation 1}$$

Where ϵ_0 is the permittivity of free space, ϵ is the dielectric constant, K is the Boltzmann constant and e is the elementary charge.

To understand influence of morphology, layer thickness or grain size on gas sensor performance it is necessary to understand all phenomenon occurring in material during contact with gas. An electrical core-shell layer is formed on the surface due to oxygen absorption. In the n-type conductor, as a result of oxygen adsorption on the surface of the material, electronic core-shell configuration is created (see Figure 11a). Semiconducting zone and EDL (electron depletion layer) on particle coatings are formed. Oxygen adsorption on the surface of the material in the p-type conductor creates HAL (hole accumulation layer) near the surface of the material due to electrostatic interaction between oppositely charged particles (see Figure 11b), which causes the formation of core-shell configuration, resistive region in particle cores and semiconductor films HAL near the particle surface. In n-type semiconductors, the change in sensor resistance under the influence of the gas depends on the resistive shell to shell contact between SE particles

(see Figure 12a). Thus, equivalent n-gas sensor circuits can be explained as series of connections between semiconductor cores (R_{core}) and resistive intermolecular connections (R_{shell}) (see Figure 12b).

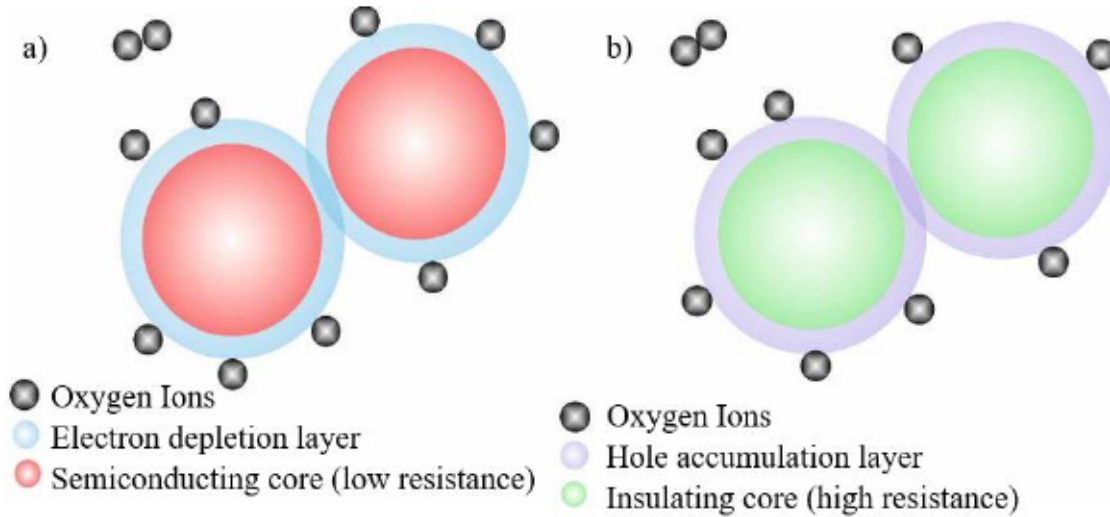


Figure 11. a) N-type and b) P-type core-shell formation [61]

In the presence of a reducing gas, e.g. CO, a semiconductor n-type uses ionized oxygen ions (O^{2-} , O^-) to oxidize the reducing gas. Remaining electrons attach to the semiconductor core. As a result of this phenomenon, the resistance of the material decreases in proportionally to the concentration of the gas. The mechanism of the conductivity of p-type semiconductors can be explained by parallel mechanisms in a wide resistive core (R_{core}) and along narrow, shells (R_{shell}).

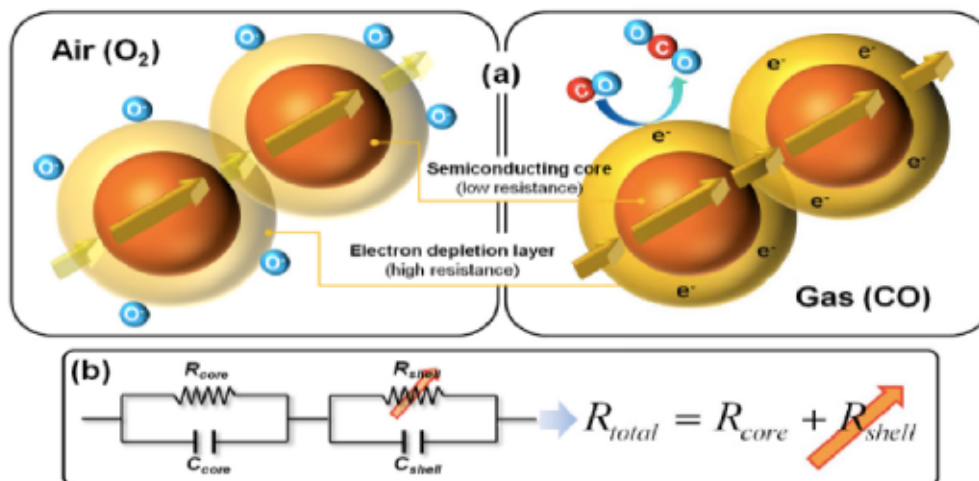


Figure 12. Gas sensing mechanism and equivalent circuit of n-type oxide semiconductors [62].

The conductivity model of p-type semiconductors has been explained by Barsan *et al.* [62]. In Figure 13a, area B represents the contact area of two grains, while regions A and C show areas

of contact of the electrode with SE. In this configuration, the electrons introduced into the material as a result of the oxidation reaction between the reducing gas and oxygen anions from the SE surface, which reduces the number of electron holes in the shell layer, resulting in increased resistance of the material (see Figure 13b-c).

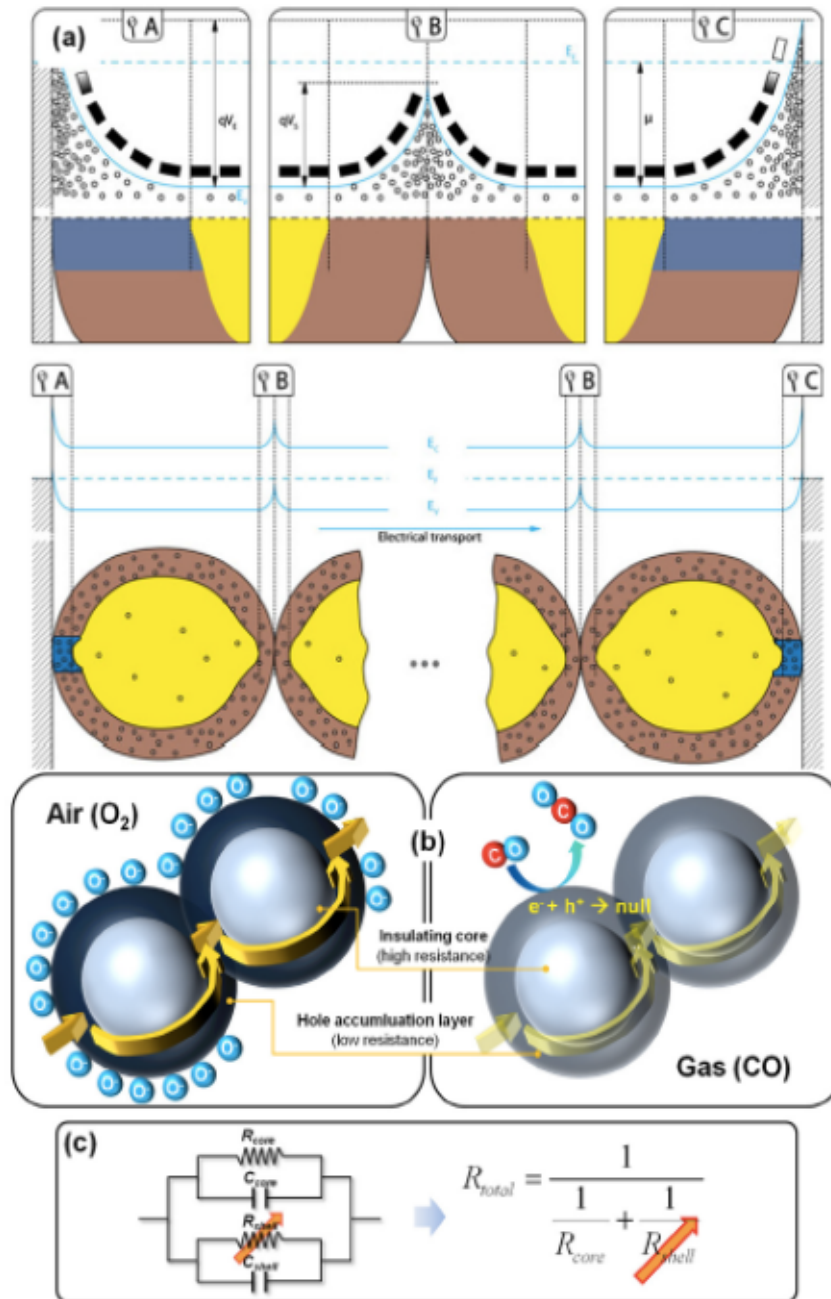


Figure 13. Sensing layer of p-type semiconductor [62].

Some materials are characterized by the possibility of changing the type of response along with a change in temperature or gas pressure. As shown by Minh and Takahashi [63], the partial oxygen pressure increases can lead to a change in conductivity type (see Figure 14).

Conductivity of such materials can be divided into 3 zones: an n-type zone, a mixed zone and a p-type zone.

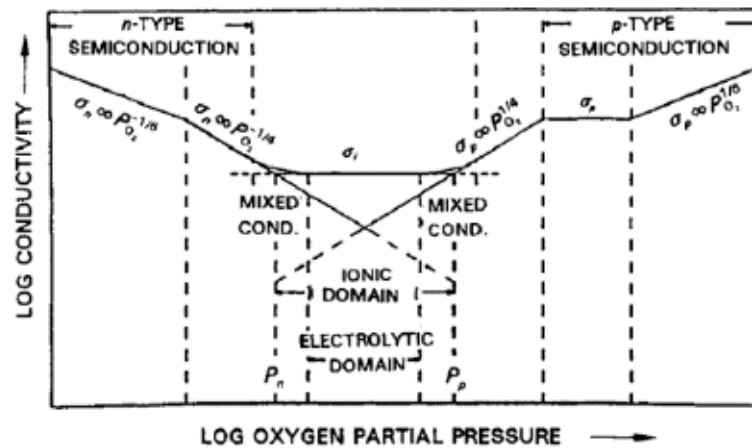


Figure 14. Changes in electrical conductivity as a function of oxygen partial pressure for $\text{Mo}_2\text{-B}_2\text{O}_3$ [63].

Mixed zones have lower electrical conductivity than n and p zones (see Figure 14). As oxygen pressure increases, the conductivity decreases, then the mixed area begins, where both types of conductivity occur at the same time. This region has the lowest electrical conductivity. This is due to overlap and competitive conductivity phenomena. A further increase in pressure causes change the type of conductivity to p-type. In this range, the conductivity increases with oxygen pressure. This indicate that resistance gas sensor has not only preferential working temperature but also gas pressure.

2.2 CHARACTERISTICS OF MATERIALS FOR GAS SENSORS

2.2.1 Perovskites as sensing electrodes

Due to the high material properties demands on SE, scientists are paying special attention to perovskites. It is a family consisting of a crystallographic structure associated with the CaTiO_3 mineral. The ideal perovskite structure is cubic structure. Perovskites have the general formula ABX_3 . The ideal cubic structure is not often found, most of the perovskites are deformed. These materials attracted the great attention of scientists for many years, the first research conducted by Goldschmidt et al. in 1920. As a result of deformation, the perovskites have reduced symmetry, which has a huge impact on their magnetic and electrical properties. Due to mixed conductivity (ionic and electronic) they are currently used in the electrical industry [64], gas sensors [29], [36], in the automotive industry [43], SOFC [65] and many other industries.

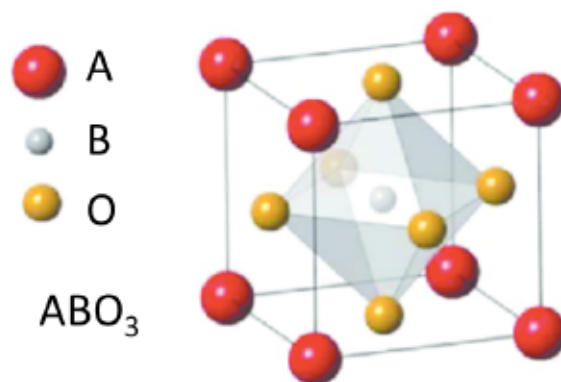


Figure 15. Example of cubic perovskite structure.

Cell of perovskite is presented in Figure 15. Cation B in the middle of cube (gray) has in its neighborhood 6 ions of oxygen (yellow) and they create a BO_6 octahedra. Larger ions (red) are in the cell corners. The structure presented in Figure 15 is ideal structure, in reality this cell is deformed due to mismatch of ion radius. It leads to ions shift from original position. Element A is mainly a metal cation from the group of lanthanides, alkaline, e.g. La, Li, Be, Ca. A atoms are characterized by a large radius and atomic number of 12. The element B is mainly substituted with cations with atomic number 6 and smaller radius such as: Ti, Nb, Ta Mn, Fe, Co. B atoms are surrounded by 6 O atoms which are non-metallic elements mainly oxygen or fluorine. Perovskites with transition metal ions (TMI) as element B have interesting electrical and magnetic properties, these properties are associated with unfilled 3d electron shells. In this work two perovskites were used as SE material: LaFeO_3 and LaCoO_3 .

2.2.2 Cristal structure of LaFeO₃

LaFeO₃ is part of the perovskite family and has very good anti-ferromagnetic (AFM), ferromagnetic (FM), ferro-elastic (FEL) and catalytic properties and high ionic conductivity O₂ [66][67][68] – [69]. The LaFeO₃ crystallographic structure is an orthorhombic deformation of the above presented cubic cell, linked to tilting of FeO₆ octahedra along the axes of the cubic cell (Fig.16). The enlarged unit orthorhombic cell parameters are then related to the cubic one by $\mathbf{a}_0=\mathbf{a}_c+\mathbf{b}_c$, $\mathbf{b}_0=-\mathbf{a}_c+\mathbf{b}_c$, $\mathbf{c}_0=2\mathbf{c}_c$, in the Pbnm (n°62) choice. The relations between Miller indices in the orthorhombic Pbnm and in the cubic settings are then:

$$\begin{cases} h_c = (h_o - k_o)/2 \\ k_c = (h_o + k_o)/2 \\ l_c = l_o/2 \end{cases}$$

Another setting Pnma will also be used in this work, with \mathbf{b}_0 being the long axis. The relations between Miller indices in the orthorhombic Pnma and in the cubic settings are then:

$$\begin{cases} h_c = (h_o - l_o)/2 \\ k_c = k_o/2 \\ l_c = (h_o + l_o)/2 \end{cases}$$

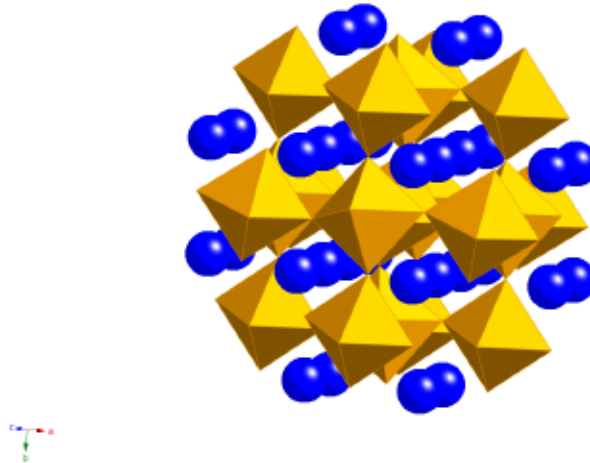


Figure 16. LaFeO₃ structure, showing the tilting of the octahedra, in the Pnma setting.

The cell parameters and main properties of LaFeO₃ are presented in Table 4.

LaFeO₃ is used in various forms: powders [66], thin films [67] for the SE in gas sensors. At work Lee [68] has been shown that Fe-O bonds are more active toward the gas as a result of faster oxygen reduction on the Fe-O surface with (010) orientation than on La-O bonds in LaFeO₃ films [69].

Table 4. Crystal structure and properties of LaFeO₃.

Structure/property	Data	Ref.
Cell parameters	a= 5.552 Å	CIF file: #1526450
	b=5.563 Å	
	c=7.843 Å	
	$\alpha=\beta=\gamma= 90^\circ$	
Cell Volume	0.2422 nm ³	[70]
Space Group	<i>Pbnm</i> [62]	
Density	6.48 g.cm ⁻³	
Neel Temperature	750 K	

LaFeO₃ is usually doped with elements on second oxidation state: Sr, Co, Ca, Ba, Cu, Li, Mn, Zn by replacing La³⁺. Use of dopant affect oxidation state of iron from Fe³⁺ to Fe⁴⁺. It leads to creation oxygen vacancies which has strong influence on electrical conductivity of semiconductor.

2.2.3 Cristal structure of LaCoO₃

In perovskites we can observe high temperature superconductivity, band ferromagnetism and other. We can observe also different physical properties in one crystal. These phenomena can be observed in perovskites with Mn, Co, Ru. LaCoO₃ is a compound with excellent electrical, catalytic and magnetic properties. Mixed conductivity is unusual, high ionic conductivity and electric conductivity allow to used LaCoO₃ as cathode material for fuel cells (SOFCs), oxygen membranes and as a CO catalyst [71]. LaCoO₃ crystallizes in a rhombohedral structure, due to rotation and compression of the BO₆ octahedra along the [111] axis of the cubic unit cell. It remains in this form up to melting point 1740 °C (Table 5). The rhombohedral distortion of LaCoO₃ decreases with increasing temperature and A site cation concentration [72]. LaCoO₃ cell is presented in Figure 17. In this figure, position B (blue atoms) is occupied by La atoms, while the CoO₆ octahedra are represented in yellow color. The relations between the rhombohedral and cubic cell parameters are $a_R = a_C + c_C$, $b_R = b_C + a_C$, $c_R = b_C + c_C$. One can notice that the rhombohedral distortion is weak, with an angle $\alpha = 60.99^\circ$ instead of 60° in the ideal cubic structure (Table 5). Another way to describe the structure is to use the hexagonal settings, where the c axe is along the [111] axis of the unit cubic cell. The relations between the axes of the hexagonal and the cubic unit cells are $a_H = a_C - b_C$, $b_H = b_C - c_C$, $c_H = 2(a_C + b_C + c_C)$

The relations between the Miller indices of the planes in the hexagonal and cubic settings are:

$$\begin{cases} h_c = \frac{2h_H}{3} + \frac{k_H}{3} + \frac{l_H}{6} \\ k_c = \frac{-h_H}{3} + \frac{k_H}{3} + \frac{l_H}{6} \\ l_c = \frac{-h_H}{3} - \frac{2k_H}{3} + \frac{l_H}{6} \end{cases}$$

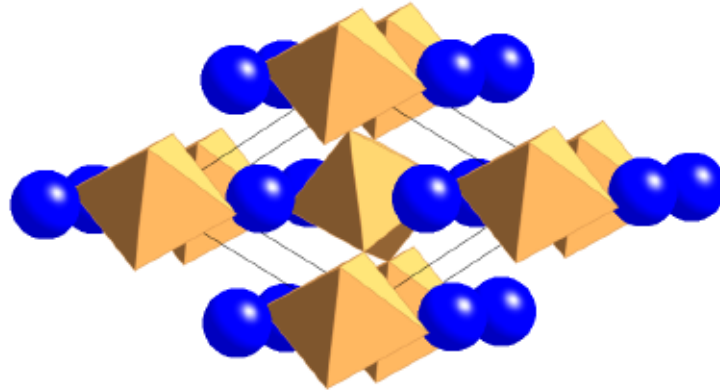


Figure 17. LaCoO₃ rhombohedral cell, showing the rotation of octahedra.

Table 5. Structure and properties of LaCoO₃

Structure/Propriety		Data	Ref.
Cell parameters	Hexagonal settings	a= 5,4350 Å	CIF file #1530874
		b= 5,4350 Å	
		c= 13,07 Å	
		$\alpha (^{\circ})= 90 \quad \beta (^{\circ})= 90 \quad \gamma (^{\circ})= 120$	
	Rhombohedral settings	a= 5,3417 Å	
		$\alpha (^{\circ})= 60.99$	
Cell volume		110,18 Å ³	
Space Group		R $\bar{3}$ c [167]	
Density		7,25 g.cm ⁻³	
Melting temperature		1740 °C	[73]

The presence of a mixed state of Co³⁺ and Co⁴⁺ affects the electrical properties. The spin state of ions is modified not only by temperature, but also by the change in gas pressure [74]. Possibility to change ion spin state of Co is unusual and it doesn't appear in other magnetic oxide materials [75].

Three spin states of cobalt ions are possible:

- low spin (LS) (0 – 100 K),
- medium spin or intermediate spin (IS) (100-500 K),
- high spin (HS) (over 500 K).

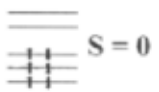
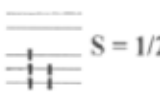
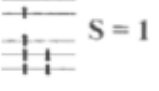
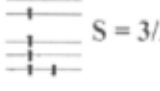
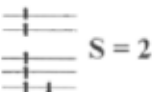
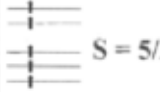
Spin State	Co ³⁺	Co ⁴⁺
LS	 S = 0	 S = 1/2
IS	 S = 1	 S = 3/2
HS	 S = 2	 S = 5/2

Figure 18. Co³⁺ and Co⁴⁺ spin states [76].

In range from 0 to 100 K ions Co³⁺ are low spin and resultant spin is equal 0. From 100 K ions of Co³⁺ are slowly changing spin state from low spin to intermediate spin this change requires energy to jump over band gap. This effect is only possible in this group of materials. Fission energy of 3d shell caused by oxygen octahedra surface and energy of spin coupling (Hund's rule) are close to thermal energy $k_B T$. That's why not only spin states can be modified by change of temperature but also by change of pressure. Pressure allows to change magnetic properties of materials by change:

- distance between atoms,
- bond length,
- angle bond.

These parameters have strong influence on ion spin state in LaCoO₃. Temperatures of existing spin state can be modified by pressure which is proved by Asai *et. al.* [77]. Normally spin change from low spin to intermediate spin occurs in 100 K, but with pressure 18.2 kbar spin-state transition temperature increased. Increase of pressure causes also extension of band gap which leads to limitation of electrical conductivity.

LaCoO₃ is a n-type conductor [4]. Electrical conductivity occurs through the charge exchange between Co - O - Co bonds which increase the ion conductivity by 3 orders of magnitude [72, 73, 78]. In range of 110 K to 350 K, excitation of electrons from a narrow valence band to

localized states at high-spin cobalt sites introduces mobile small-polaron holes and trapped electrons at stationary Co^{2+} ions [73]. Increase of temperature above 650 K leads to stabilization metallic phase which contains high spin cobalt ion Co^{3+} , medium spin Co(III) , with partially filled electron shell responsible for p-type conductivity [72], [73], [78]. Oxygen ions in LaCoO_3 diffuse due to the presence of vacancies [79]. LaCoO_3 is a promising material for detection of CO at low temperatures [80][81] – [82].

LaCoO_3 attracted the attention of scientists due to changes taking place in this material. LaCoO_3 in its basic state is a non-magnetic insulator without a long-range magnetic order. The basic spin state is associated with the Co^{3+} ion in the low spin state (LS) due to the separation of a crystal field splitting larger than Hund's - rule coupling. Perovskite consists sharing corner octahedra. Octahedra consist of oxygen ions in the corners and TM ions in the middle. La ions occupy empty spaces between octahedra. In addition to a few special cases with a cubic structure [83], [84]. Low-spin Co^{3+} configuration makes LaCoO_3 , a diamagnetic insulator at the lowest temperatures. It becomes more metallic at the highest temperature where an intermediate-spin state is stabilized at the Co^{3+} ions [85]. LaCoO_3 in range from 25 to 125 °C is semiconductor [74], [83]. Increase of temperature above 125 °C causes rapid increase of conductivity. In range 125 – 650 °C conductivity increase by magnitude of two orders. In range from 650 to 937 °C increase of conductivity less rapid and reach flat maximum. Above 937 °C conductivity decrease with increase of temperature [83].

2.2.4 Cristal structure of YSZ materials

YSZ is zirconium oxide (ZrO_2) doped by yttrium, which is a thermal insulator with high chemical stability.

This material occurs (depending on the amount of dopant) in the form:

- cubic (most common structure),
- tetragonal,
- monoclinic.

Martensitic transformation in ZrO_2 excludes this material from many applications due to the change in volume during transformation. Therefore, it is possible ways stabilize ZrO_2 . This can be achieved, by introducing the addition of yttrium, which stabilizes the ZrO_2 structure. Substituting Zr^{4+} ions by Y^{3+} , increase number of oxygen vacancies. This leads to increases of ionic conductivity of the material, which is particularly desirable in gas sensors. The ion conductivity of 8YSZ compared to other materials is shown on Fig 21. The crystal structure depends on the content of Y_2O_3 admixture, the most popular variety is the cubic structure with 9.5 mol% Y_2O_3 .

We can distinguish several crystallographic structures:

- a) C-YSZ (Cubic Yttrium Stabilized Zirconia) - solid solution ZrO_2 with an dopant of Y_2O_3 in the range of 6 - 10 mol%. Cubic material with high ionic conductivity at temperatures above 900°C [75].
- b) PSZ - ZrO_2 solid solution with Y_2O_3 dopant in the range of 4 to 5 mol%. It is a mixture of cubic and tetragonal phase, has high mechanical strength [86].
- c) TZP - is the third variant of the ZrO_2 solution with Y_2O_3 dope in the range of 1–3 mol% Y_2O_3 . It is a polycrystalline material with a tetragonal structure, thanks to which it is characterized by excellent mechanical strength and resistance to breaking, which is why it is often called ceramic steel [87][88] – [89].

In all types of YSZ, ionic conductivity is accomplished by oxygen vacancies.

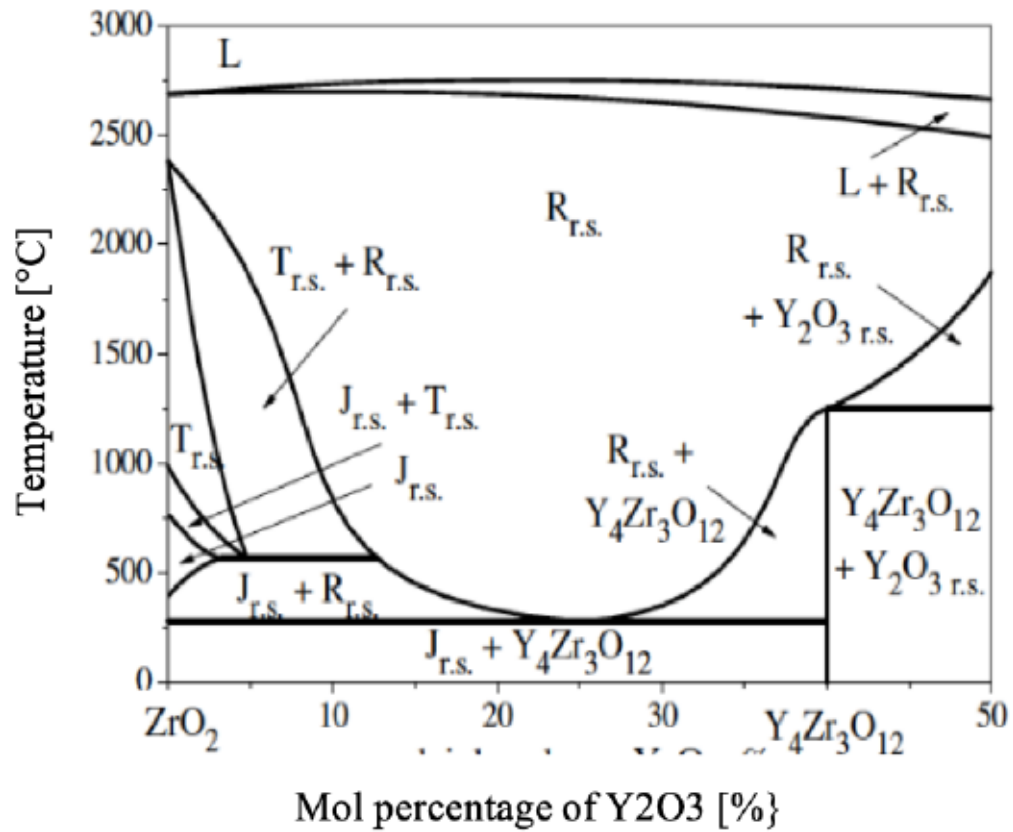


Figure 19. Phase diagram of Y_2O_3 - ZrO_2 [90].

The phase diagram (see Figure 19) shows that the tetragonal phase is not a stable phase [90]; however, this phase may be metastable at room temperature [91].

2.3 PLD METHOD FOR THIN FILMS DEPOSITION

There are many methods for producing SE for gas sensor application. The most popular methods are:

- sol gel [21],
- screen printing [39],
- CVD (Chemical Vapour Deposition) [92],
- PVD (Physical vapor deposition) [36].

In this work, the SE were produced using the PLD method, which is one of the PVD method.

The PLD method is one of the vacuum techniques. It deposits a thin film due to the ablation of the target by laser. In this method, the energy source (laser) is located outside the working chamber, thanks to which it is possible to carry out the process in a high vacuum or in a gas atmosphere [93]. The PLD method owes its popularity to the ability to transfer the stoichiometry of the target material to the substrate, high application speed (approx. 0.05 nm/ μ s) and the ability to apply any type of material (semiconductors, oxides, carbides, metals, and even polymers). During the process, the material can be deposited from several targets, which allows obtaining films of complex chemical composition. As a result of changing process parameters, the properties of the material obtained can be significantly modified, for example regarding stress, texture, reflectivity, magnetic properties, grain size, and morphology.

Parameters of PLD process can be divided into several groups:

- laser parameters (wavelength, pulse length, frequency, number of shots, energy density),
- target (target roughness, distance between the target and substrate, target rotation speed, thermal conductivity, melting point), raster,
- process parameters: temperature, gas pressure in chamber.

PLD aperture consists of the following elements (see Figure 20):

1. Laser — regardless of the type of laser, we can distinguish the basic elements as:

- an active medium is a storehouse of atoms, ions or particles that generate radiation as a result of excitation,
- a pumping system whose task is to excite the active medium,
- the optical resonator strengthens the radiation generated and forms a beam,
- cooling system,

- electrical supply system.

2. Supporting structure covering:

- process chamber,
- rotating substrate table,
- rotating table for targets,
- heater,
- quartz window.

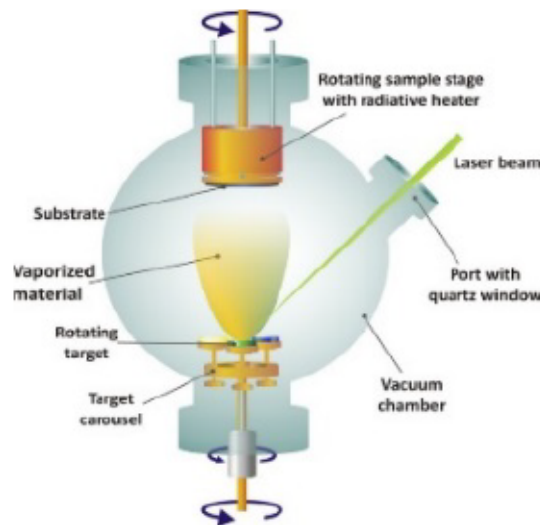


Figure 20. PLD Aperture [94].

In PLD method most common are Nd-YAG and excimer. Type of laser determine not only working principle but also efficiency and most importantly wavelength operation, different laser specification are presented in Table 6.

Table 6. Laser specification [95].

Laser	CO ₂ laser	Nd:YAG laser	Yb-fiber laser	Excimer laser
Application	SLA, SLM, SLS, LENS	SLM, SLS, LENS	SLM, SLS, LENS	SLA
Operation wavelength	9.4 & 10.6 μm	1.06 μm	1.07 μm	193, 248, 308 nm (ArF, KrF, XeCl respectively)
Efficiency	5-20 %	Lamp pump: 1-3 %, Diode pump: 10-20 %	10-30 %	1-4 %
Output power (CW)	Up to 20 kW	Up to 16 kW	Up to 10 kW	Average power 300 W
Pump source	Electrical discharge	Flashlamp or laser diode	Laser diode	Excimer recombination via electrical discharge
Operation mode	CW & Pulse	CW & Pulse	CW & Pulse	Pulse
Pulse duration	Hundreds ns-tens μs	Few ns-tens ms	Tens ns-tens ms	Tens ns
Beam quality factor (mm-mrad)	3-5	0.4-20	0.3-4	160 \times 20 (Vertical \times Horizontal)
Fiber delivery	Not possible	Possible	Possible	Specially designed fiber necessary
Maintenance periods	2000 hrs	200 hrs (Lamp life) 10,000 hrs (Diode life)	Maintenance free (25,000 hrs)	10 ⁸⁻⁹ pulses (Thyratron life)

In Nd-YAG Laser – active medium is rod shaped solid crystal $\text{Nd}^{3+}:\text{Y}_3\text{Al}_5\text{O}_{12}$. Laser have central wavelength of 1064 nm, but with use of different harmonic it can be changed in range from 266 to 1064 nm. It is one of the most popular high-power laser [95]. Light beam can be delivered by flexible optical fibers which is great advantage over CO_2 laser. Scheme of Nd-YAG laser is presented in Figure 21.

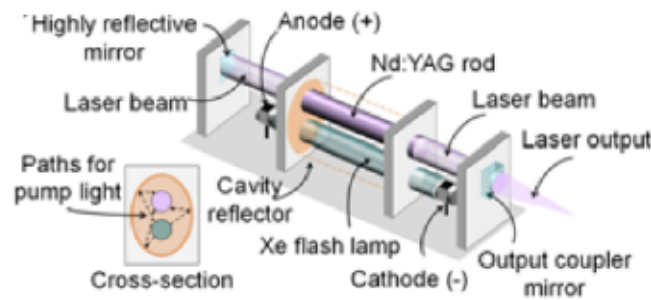


Figure 21. Scheme of a Nd:YAG laser [95].

It can work in two modes: pulse and continuous. In pulse mode equipped with q-switch duration of pulse can be several ns. In continuous mode pulse duration can reach 150 ns. Use Xenon flash lamps can lead to low beam quality. Thermal heating of optical elements causes thermal lensing and birefringence effects which have negative impact on beam quality [96] [97] – [98]. Those disadvantages are reduced by developments of diode-pumped systems [99]. Power in pulse mode can reach 20 kW and energy to 120 J. Availability made Nd-YAG very popular in many applications like: parametric study [99][100] – [101], optimizing manufacturing parameters [102], [103].

Excimer laser – belongs to ionic lasers group. The active medium of these lasers are gases e.g. XeCl , KrF . Excited dimer is gas mixture of noble gases (Ar, Kr, Xe) with halogen and buffer gas (Ne, He). Wavelength depends on used gas mixture (Table 7). ArF , KrF , and XeCl lasers are the most popular excimer lasers in industry [104].

Table 7. Excimer laser characteristic.

Laser medium	Wavelength (nm)	Output energy per pulse (J)	Average output power (W)
ArF	193	0.2 – 0.3	10
KrCl	222	0.03	1
KrF	248	0.3 – 0.4	18
XeCl	308	0.08 – 0.2	8
XeF	351	0.08 – 0.15	7

Excimer laser consists in a pump source, a gain medium and an optical resonator. The gain medium is pumped by electrical current.

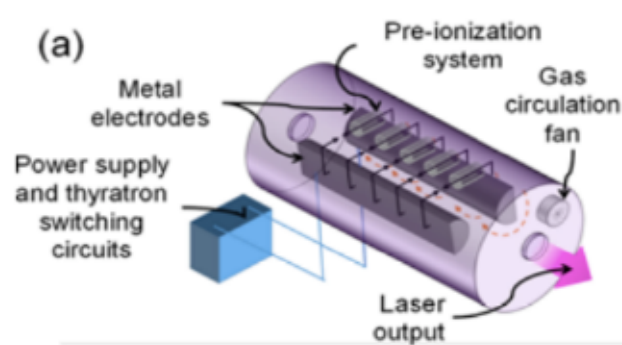


Figure 22. Scheme of excimer laser [95].

Excimer laser can work only in pulse mode, with pulsed duration of 10 – 300 ns and energy up to 2 J with a frequency of up to 1 kHz in range of UV light. One of the big advantages of this laser type is high efficiency (0.3%) and possibility of reaching high energy in UV range which is great importance because most of the materials in this have high absorptivity in this range [105]. One of drawback of this laser is one possible working frequency depended of used gas. Because in lasers used in PLD process is required high energy density (MW/cm^2), creation of high density of planting is required. Process is highly unstable and discharge last couple nanoseconds. It is realized by high voltage switch, unfortunately this is main cause of laser breakdown which makes them difficult to maintain. In excimer laser light coherence (beam quality) is lower than in Nd-YAG laser. Gases used in excimer lasers are highly corrosive, dangerous, expensive and they can work for short amount of time and they have high running cost [106].

In vacuum chamber the subsequent elements of the apparatus are located. The laser beam enters the chamber guided by a mirror system. The laser beam is focused on the surface of the target, which is most often found on a rotary table. Above the targets there is a substrate holder and a radiator in Figure 20. In the PLD process, the thin film is produced as a result of laser impact with target material which leads to material evaporation. The laser beam reaches the surfaces of the nontransparent material undergoing partial reflection and absorption depending on the physical properties of the target and its surface in Figure 23. Interaction of the laser on the target material is divided into three stages:

- a.) adsorption – as a result of which the target surface is quickly heated and then cooled, as cyclical process. As the target warms up and cools, its morphology changes, and hence its reflectivity. The state of the surface (reflectivity) significantly affects the structure and properties of the obtained films,

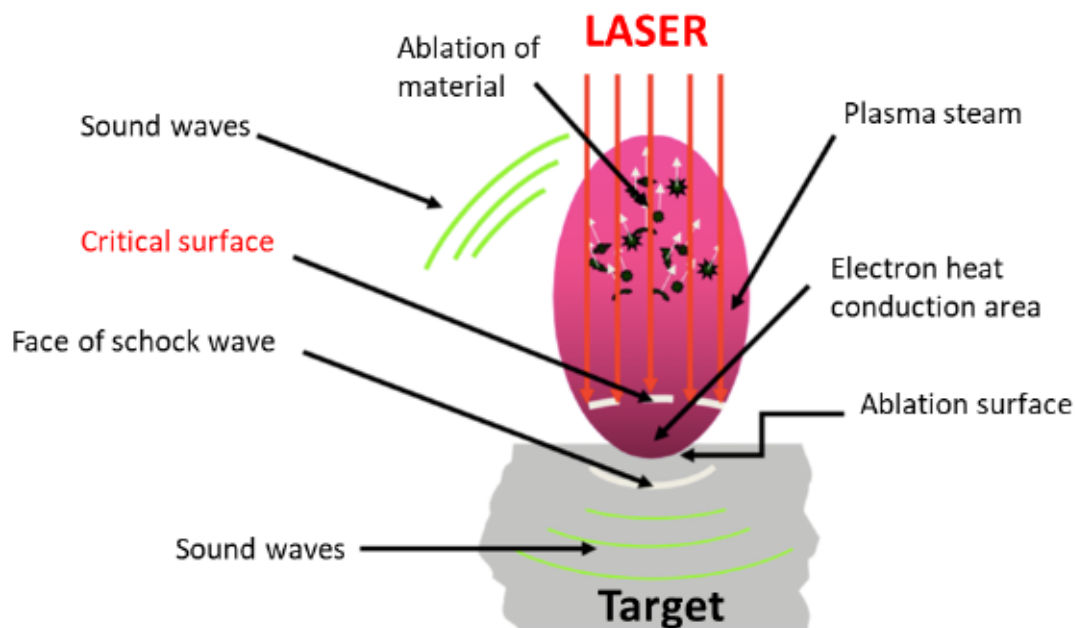


Figure 23. Interaction of the laser on target

- b.) as a result of desorption and ablation ions are detached from target. Detached particles of material are ionized and form a plasma cloud. As a result of the formation of the plasma, which shields the target surface from laser beam which leads to temperature drop on target surfaces. Local stretching and the appearance of chemical and metallurgical defects are caused by ablation phenomena created by shock wave and sound wave. This phenomenon is called relaxation,

c.) final stage is plasma shift by a velocity vector perpendicular to the surface of the target (see Figure 23).

As result of ablation process on surface, thin film is deposited which structure depends among others on target melting temperature, gas pressure and process temperature. Layer structure model deposited in vacuum with presence of plasma was described by Thornton (see Figure 24).

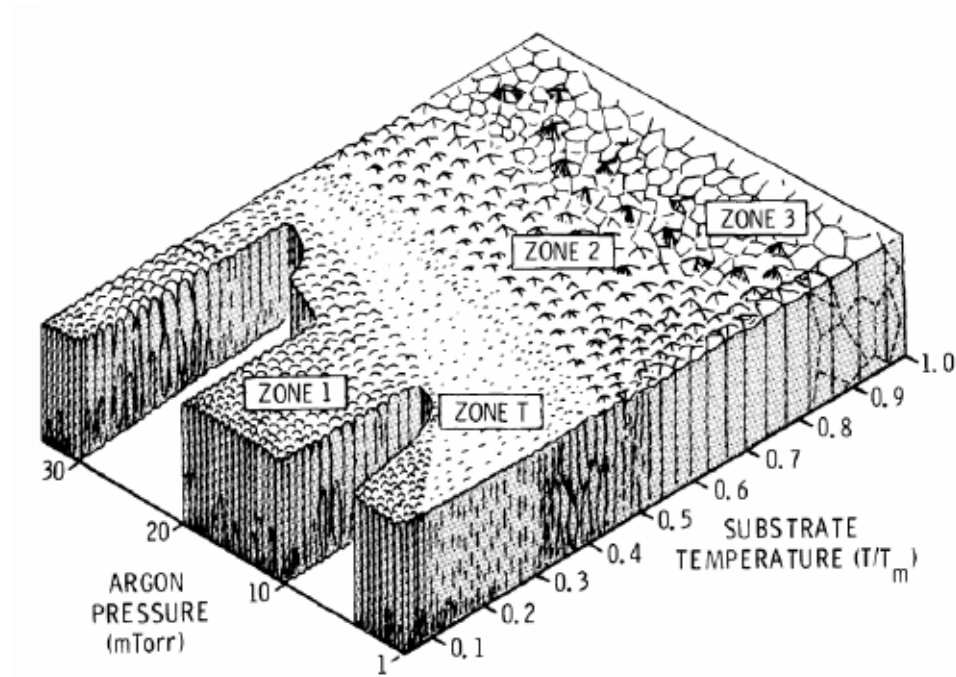


Figure 24. Structure-zone diagram for thin films by Thornton [107].

Characteristic zone for PLD method is a transition zone with a columnar structure in the range 01 to 03 T/T_m .

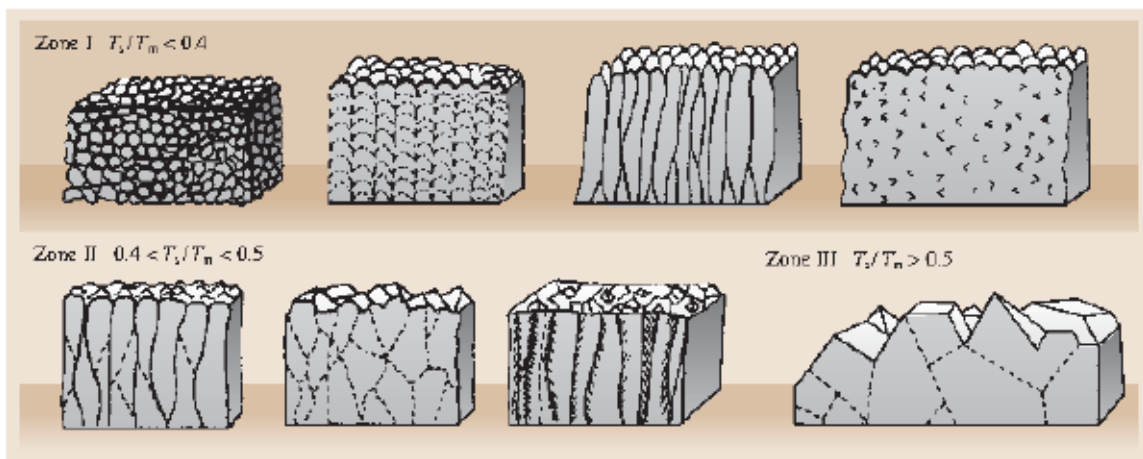


Figure 25. Schematic three-zone model for the temperature dependence of the growth thin films. T_s/T_m represents the ratio of the substrate temperature to the melting point [108].

Low process temperature can cause deposition of amorphous thin films. As Jurusik *et. al.* proved layers of Cd_2As_2 deposited at temperature $T_s/T_m < 0,4$ were amorphous (see Figure 25), consisting spherical or elongated fibrous grains or with large number of pores, cavities. Amorphous structure in I zone was also reported in semiconductor for example germanium films. Transition temperature is influenced by base pressure in vacuum chamber [109], [108].

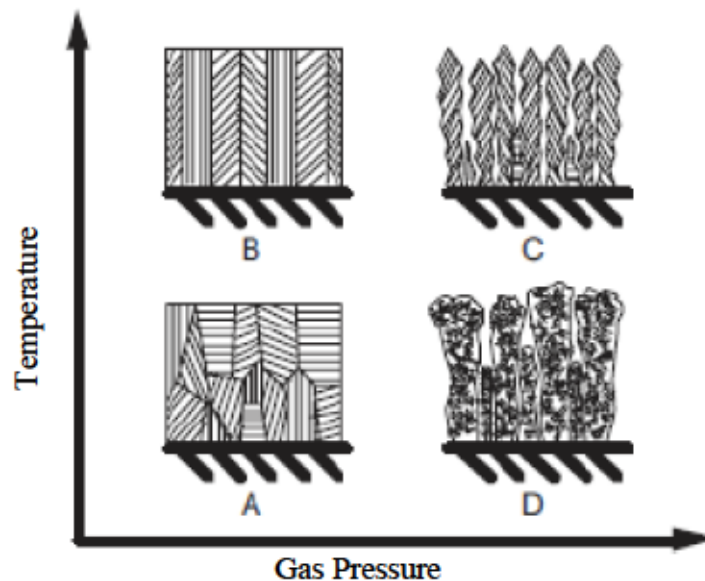


Figure 26. Impact of process parameters on thin films structure [65].

Thin films deposited in low pressure and low temperature characterize by dense polycrystal structure due to high Surface diffusion (Zone A in Figure 26). Increase of the temperature (Zone B in Figure 26) cause creation of strongly ordered columns with dense structure. Thin films deposited in high pressure and high temperature have columnar grains at the entire cross section of film. Surface diffusion is lower than in region and shadowing effect is present (Zone C in Figure 26). Region D is typical for columnar growth contain loosely packed cluster of atoms with pores. The influence of the beam energy on the kinetic energy of the deposited particles is small, however, the use of gas in the working chamber has a much stronger effect on their energy and thus on the structure of the films. During the growth of oxide films, the presence of oxygen in the chamber is necessary to create a layer with sufficient oxygen. A 0.3 mbar oxygen pressure is required to produce the perovskite structure at high temperature. Due to the presence of gas, the energy of the particles can be reduced even to 1 eV due to collisions of the disk particles (plasma cloud) with gas atoms. The probability of collision of high-energy ions is higher, which may result in the ejection of the ion from the plasma cloud, while ions with lower

energies more often reach the surface of the substrate without collision with gas atoms [93]. As a result of the increase in the working gas pressure, the plasma growth and reaction with the working gas is inhibited, which in turn reduces the energy of particles in the plasma cloud. Changes in the energy of the particles affect the structure and texture of the layer. Therefore, the laser beam energy and working gas pressure may allow controlling the structure of the obtained films. All of the above parameters affect layer growth processes.

2.4 OBJECTIVE AND THESIS OF WORK

Bearing in mind the latest reports in the literature, in this work the main purpose was to analyze the structure and properties of thin films LaCoO_3 and LaFeO_3 deposited by PLD method as sensing electrode for electrochemical and resistance sensors. LaCoO_3 and LaFeO_3 were chosen as the sensing electrode material due to their potential use in industry, chemical stability at elevated temperatures, long life, and sensitivity toward polluting gases. The thin films will be used as the sensing electrode in resistance and potentiometric sensors. In resistance sensors, surface development has strong impact on the sensing properties of gas sensor, since all adsorption and desorption phenomena occur on the surface only at a depth of 7 nm. In potentiometric sensors, not only the sensing electrode material but also the electrolyte material plays an important role. Because the gas reaction (charge exchange) occurs on TPB (three phase boundary). Si (100), YSZ95 (100) and YSZ-35 substrates were used in this work. In both case substrate and SE material has big influence on properties. The Si substrate was used as reference substrate. YSZ-95 substrate with cubic structure and orientation (100) is often used in electrochemical potentiometric sensors, while the YSZ-35 has a tetragonal type structure and very good mechanical properties, it is often called ceramic steel. The concept of the work assumed the possibility of replacing the YSZ-95 monocrystalline substrate with the polycrystalline YSZ-35 substrate, which is more resistant to damage. The main potentiometric sensors are based on thick coatings in the micrometer range, but research conducted by Ueda et al. [37] showed that also thin films (250 nm) can be used as sensing electrode. Therefore, author made attempt to produce thin nanometric layer for application as resistance and electrochemical sensors.

Taking it in to consideration in this thesis author decided to produce thin films with nanometric grains by PLD method using different substrates (Si, YSZ) and two sensing materials LaFeO_3 and LaCoO_3 . The sensors were tested to sensitive towards NO_2 .

Realization of the assumed goal required:

- selection of deposition parameters (PLD method),
- selection of substrate (solid electrolyte in electrochemical gas sensors),
- structure analysis by means of: XRD, SEM, AFM, TEM, XPS,
- measurements of sensitivity and response time in NO_2 presence,

Based on the set goals, theses were formulated:

- 1.) It is possible to produce thin films with nanometric grains by PLD method sensitive towards NO_2 .
- 2.) C-YSZ as a solid electrolyte can be replaced by TZP.

The films as electrodes will be deposited on two types of substrate, which is an additional cognitive character because they provide knowledge not only regarding the influence of the morphology of measuring electrodes but also the influence of the Y_2O_3 dopant on the properties of the sensor. The obtained results will contribute to the broadening of knowledge in the field of electrochemical sensors, which will allow to improve currently used sensors of one of the more toxic NO_x gases.

3 METHODOLOGY AND RESEARCH TECHNIQUES.

In this section, the elaboration of thin films by PLD is described, as well as the different characterization techniques used in this work.

3.1 THIN FILM DEPOSITION

3.1.1 Target preparation

LaCoO₃ targets were made by powder metallurgy, LaFeO₃ target was purchased in Kurt J. Lesker Company.

Target LaCoO₃ was made by mechanical alloying in a ball mill from powders La₂O₃ and Co₃O₄ with ratio 1:3. Process parameters are presented in Table 8.

Table 8 Parameters of mechanical alloying process.

Material	Milling time (h)	Interval (min)	Rotation speed (rpm)
LaCoO ₃	30	20	650

Preparation stages of target LaCoO₃:

- Ball milling processes,
- heating process at 700 °C for 4 hours,
- pellet obtained under pressure,
- sintering process carried out at a temperature of 1350 °C for a period of 10 hours,
- cooling in furnace.

3.1.2 Thin films preparation

In this work were used 3 types of substrates:

- Si orientation (100),
- C-YSZ 9.5 orientation (100) – Cubic structure,
- T-YSZ 3.5 – Tetragonal structure.

The dimension of substrates and preparation process before PLD deposition are summarized in Table 9.

Table 9 Sample preparation for PLD process.

Material	Dimensions	Cleaning in acetone in ultrasonic cleaner	Drying
Si	10 mm x 10 mm x 1 mm	X	X
YSZ 9,5	10 mm x 10 mm x 1 mm	X	X
YSZ 3,5	100 mm x 100 mm x 0,1 mm	X	X

Before the deposition process, the substrate was washed in acetone in an ultrasonic cleaner for 15 min, then air dried. Then substrates were installed in the PLD chamber. Due to size, YSZ 3,5 was previously cut to 10 by 10 mm pieces using a diamond saw. In Table 10, PLD parameters are shown.

Table 10. PLD parameters.

Parameter	Value
Energy	90 mJ
Target – substrate distance	70 mm
Shots in pre-ablation	10000
Shot frequency	10 Hz
Vacuum pressure	$5 \cdot 10^{-6}$ Pa
Number of shots	90000
Temperature	750 °C, 850 °C, 1000°C
Gas pressure (O ₂)	40 mTorr

As material for sensing electrodes (SE) were chosen LaCoO₃ and LaFeO₃ perovskites. In this work the following sample names were proposed: material-temperature-substrate for example LaCoO₃-750-Si as SE was used thin film of LaCoO₃ deposited at 750 °C on Si (100). Table 11 and Table 12 summarize the list of samples that will be examine in this research work.

Table 11. Sample list of LaFeO₃

Substrate	Deposition Temperature °C		
	750	850	1000
Si	X	X	X
YSZ-95	X	X	X
YSZ-35	X	X	—

Table 12. Sample list of LaCoO₃.

Substrate	Deposition Temperature °C		
	750	850	1000
Si	X	X	X
YSZ-95	X	X	X
YSZ-35	X	X	—

3.2 RESEARCH TECHNIQUES

To achieve the assumed goals several research techniques were used. To analyze phase composition and to obtain information on cell parameters, XRD in grazing incidence was performed on thin films. Surface morphology was examined by means of AFM and SEM. Information about the shape of the grains, the exposed crystallographic planes, as well as the chemical composition were collected on cross-section samples by means of XPS, TEM and HREM. The reactivity of thin films towards NO₂ was studied through resistance measurements and electrochemical tests.

3.2.1 X-Ray Diffraction

The X-ray diffractometer PAN analytical EMPYREAN DY 1061, equipped with Cu K α lamp, was used. The radiation of the copper lamp was $\lambda_{K\alpha 1} = 1.54060 \text{ \AA}$ and $\lambda_{K\alpha 2} = 1.54443 \text{ \AA}$.

X-ray analysis was carried out with the following parameters:

- fixed incidence angle $\alpha = 0.7; 1; 3^\circ$,
- angular range: $2\theta = 20 - 80^\circ$,
- measurement step: $\Delta\theta = 0.03^\circ$,
- step time: $t = 20 \text{ s}$.

Highscore software was used for phase analysis. Crystallite size and cell parameters were obtained using the MAUD refinement program.

3.2.2 Scanning Electron Microscopy

For Scanning Electron Microscopy, the Zeiss Supra 40 microscope was used. The following parameters were used for imaging: InLens detector, accelerating voltage in the range of 5 kV to 15 kV.

3.2.3 Atomic Force Microscopy

For surface analysis, the Veeco Dimension Icon TM SPM microscope was used. Results analysis was carried out using the Nanoscope V software. The tests were conducted in the scan assist mode, the size of the test surface varied from 100 nm to 2 μm with a scanning frequency 1 Hz and number of lines from 128 to 2048.

3.2.4 Transmission Electron Microscopy

Two transmission microscopes were used in this research work. The TEM Tecnai 200 kV, located at the University of Toulon, with a point to point resolution of 0.25 nm, equipped with a 4K ultra-fast One view camera allowing conventional imaging of thin films. At AGH, the

Titan Cubed 2 60-300 (FEI) in the STEM-HAADF scanning and transmission mode allowed atomic resolved chemical composition analysis of thin films.

Cross-sections for TEM were made using 3 methods: conventional, tripod and FIB

3.2.4.1 Conventional method

Sample preparation scheme using the conventional method, *i.e.* Mechanical thinning followed by dimpling and ion milling, is shown in Figure 27. The samples were cut with a diamond saw into 2 mm wide strips, then the slices were put face to face into a brass pipe filled with Gatan glue. In order to cure the glue, the pipe was heated to 100°C and hold for 1 hour. After the glue dried, the tube was cut into slices with a thickness of about 500 μm with a diamond saw. The discs obtained in this way were glued to DiscGrinder plot and polished with abrasive papers from 800 to 4000 gradations. After the initial polishing process was completed, plastic polishing discs with diamond particles grading from 3 μm to 0.1 μm were used. The sample prepared in this way was placed in the Dimpler. As a result of the wheel rotation, a cavity was formed in the sample. After reaching a material thickness of about 20 μm , the sample was placed in a Gatan PIPS, parameters are presented in Figure 27

Błąd! Nie można odnaleźć źródła odwołania..

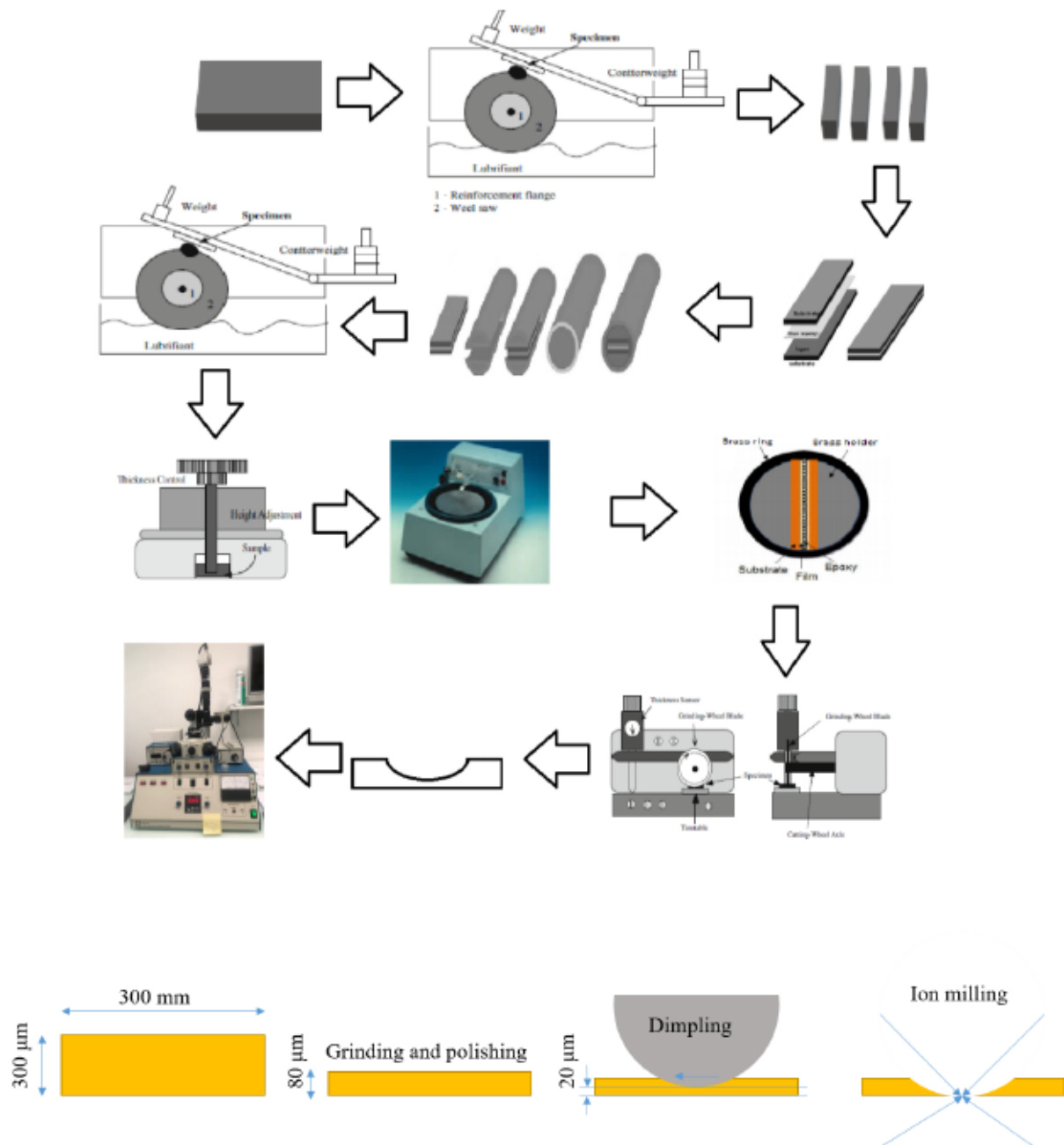


Figure 27. Scheme of conventional cross section sample preparation

Table 13. Parameters of PIPS process.

Angle (°)	Energy (kV)	Time (min)
-8/+6	5	60 – 180
-4/+6	4	30 - 180
-2/+4	4	30 - 60
-8/+8	2	30

3.2.4.2 Tripod method

Another method of cross-section preparation was the Tripod method. A description of this method is shown in Figure 28.

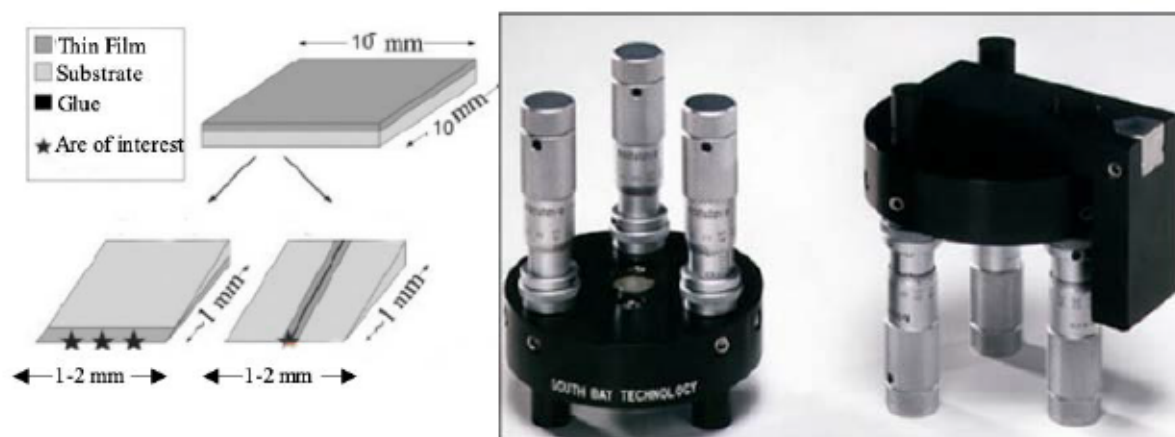


Figure 28. Tripod method [110].

In this method 3 mm sandwich was glued to Pyrex stub. Sample was polished to obtained desirable thickness. After that sample was polished with slight angle ($\alpha = 1^\circ$) to obtained thin region (60–80 nm thick) on the edge.

3.2.4.3 FIB method

Focused Ion beam, or FIB, is a method that used a focused gallium beam in order to cut a thin slice of material transparent to electrons [111]. Due to the high hardness and brittleness of YSZ 9.5, it was difficult to produce high quality cross-sections for TEM observation though the methods above mentioned. That is why we have chosen to produce TEM samples via Focused Ion beam. FIB TEM samples preparation was subcontracted to were prepared in PAN and in IC-EM at AGH.

3.2.5 X-ray photoelectron spectroscopy

X-ray photoelectron spectroscopy or XPS analysis was carried out using a PHI Versa Probe II device equipped with an Al K α 1,2 anode with energy equal to 1486.6 eV in an argon atmosphere. The first measurement was carried out on the surface of the sample, and then some of the material was removed with argon ions. Then another measurement was made, the procedure was repeated until the substrate was reached. This allowed to obtain a profile of the concentration of elements through the entire thickness of the layer. XPS analysis was subcontracted to ACPIN, a facility at AGH.

3.2.6 Resistance measurements

The study of electrical properties was carried out at the University of Toulon in the IM2NP laboratory. The electrical resistance measurements were performed using an electronic interface related to the computer. The whole experiment was controlled and monitored by a computer allowing to save data. LaFeO_3 and LaCoO_3 samples were studied under the following gases: NO_2 , CO , NH_3 . The tests were carried out in the temperature range from 25 to 450°C. A schematic of the resistance test apparatus is shown in Figure 29.

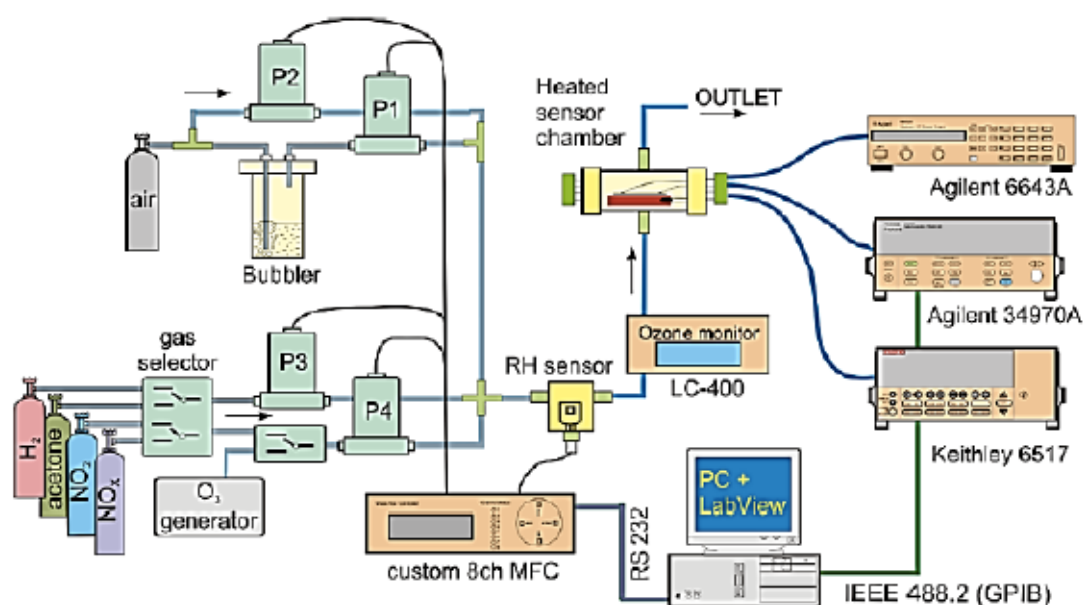


Figure 29. Schematic of the resistance gas experiment [112].

Resistance tests were carried out in a chamber with a volume of nearly 1 liter. Gas flow was 200 ml/min. A Keithley 6517 electrometer and Labview software allowed to monitor the resistance changes of the SE in presence of gases. Different gas composition was obtained by mixing NO_2 with artificial air using MKS flow controllers.

Samples before were tested in gas presence with use two different contact method:

Physical contact method — The measurements were carried out by pressing 2 needles to the sample surface. This method is characterized by high sensitivity to vibrations, which may cause the needle to move and thus change the position of the baseline. In order to eliminate these problems, the author developed other electrical contacts.

Fixed contact — Before the deposition process, 100 nm thick platinum electrodes were deposited to the substrate surfaces by the magnetron sputtering method. Figure 30 presents the sample preparation procedure used for resistance measurements.

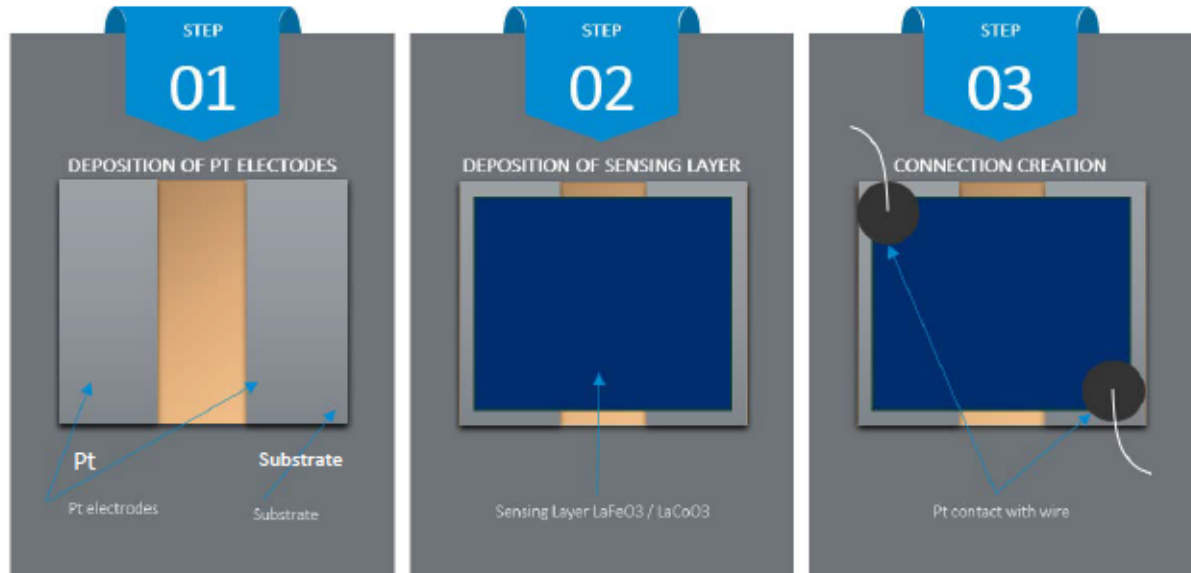


Figure 30. First stage of gas sensor preparation. Second stage of gas sensor preparation – SE deposition. Third stage of gas sensor preparation - Pt contact.

The substrate was washed in acetone in an ultrasonic cleaner and then dried in air. A 1 cm wide mask was applied to the sample and then placed in the working chamber. Platinum electrodes were deposited by magnetron sputtering, process parameters are gathered in Table 14. The next stage was to place the substrate with electrodes in the PLD chamber and SE deposition. The last stage of sample preparation was the creation of connections. To connect the sample with measuring devices, platinum paste was applied to the corner of the sample, followed by the platinum wire. To dry the platinum paste, the sample was placed in a furnace at 850°C for 30 min. Sample ready for resistance measurements is presented in Figure 31.

Table 14. Parameters of Electrodes deposition

Process Time (min)	Interval (min)	Current (μA)	Cycles number
5	3	0.1	5

To established sensitivity given formula was used:

$$Sensitivity = \frac{R_{air} - R_{gas}}{R_{air}}$$

Response time was calculated as time needed to reach 90 % of R_{gas} .

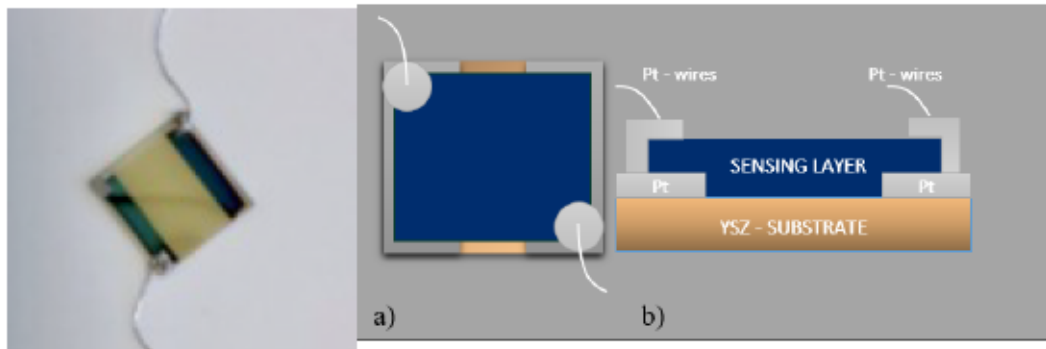


Figure 31. Prepared sample for resistance measurements a) Top view b) cross-section

3.2.7 Electrochemical measurements

The tests were carried out at AGH in the Material Science and Ceramics Department. Due to the different configuration of the electrochemical sensor from the resistance sensor, the sample preparation process was different. A platinum paste was applied to the sample in the center of SE and in the center of the substrate (see Figure 32), a platinum wire was additionally attached to the electrode on SE, enabling connection to the measuring apparatus. To fire the electrodes, the sample was placed in a furnace at 850°C. The sample prepared in this way was glued by Ceramabond 552 glue to the Al_2O_3 tube.

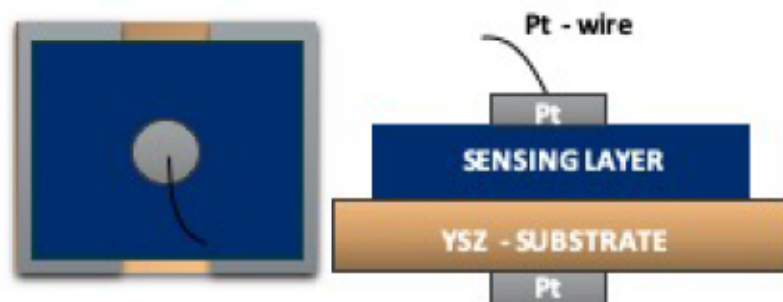


Figure 32. Fully equipped electrochemical gas sensor

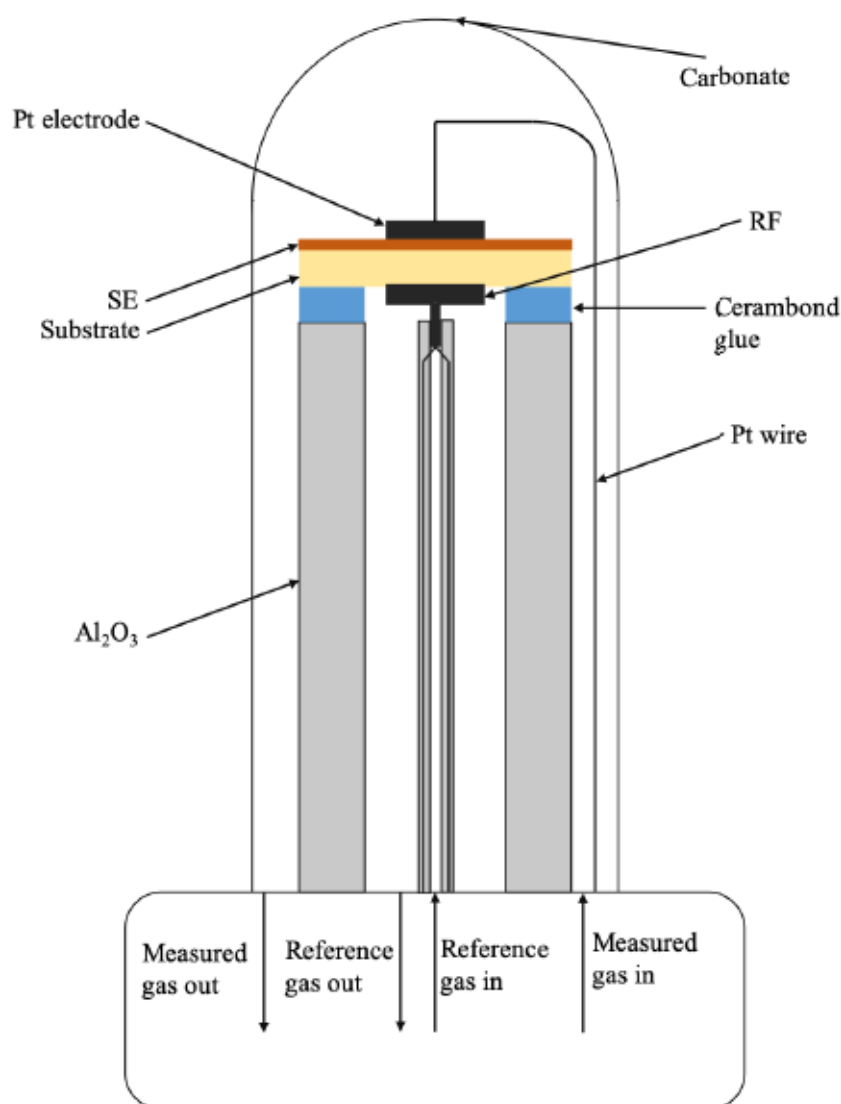


Figure 33. Schematic representation of cell.

The electromotive force (EMF) of samples was measured as function of temperature (400 – 700°C), NO_2 partial pressure and time in the cell shown in Figure 33. On the measuring part different gas composition was obtained by mixing NO_2 with artificial air using MKS flow controllers. The EMF, time, temperature was measured by using Hewlett-Packard HP 34401A multimeter, connected to the multiplexer.

4 STRUCTURAL CHARACTERIZATION

4.1 STRUCTURAL CHARACTERIZATION OF LaCoO_3 THIN FILMS.

4.1.1 LaCoO_3 thin films on Si (100) substrate

The X-Ray diffraction of LaCoO_3 -T-Si films was carried out in grazing geometry at a constant angle of incidence $\alpha = 1^\circ$. The depth of penetration calculated with the GIXA software was $z = 78$ nm. The identification of phase was based on ICPSD base card number 04-007-631 rhombohedral phase of LaCoO_3 . The X-rays diffraction patterns of LaCoO_3 thin films on Si are shown in Figure 34. All three diffractions patterns correspond to the expected rhombohedral phase. Also, there are no peaks corresponding to other phases such as La_2O_3 .

Due to measurements with a constant incident angle, we cannot examine for specific crystallographic orientation, but we can say that with increase of process temperature crystallographic orientation is changed, taking into account peaks in range from 20° to 40° . The most intense peak in LaCoO_3 -750-Si is (012), as for thin film deposited in 850°C and 1000°C the most intense peak is (110). Observation of the intensity of these two peaks allow to conclude that in the higher process temperatures (850°C and 1000°C) we have different crystallographic orientation than in the sample deposited in 750°C .

For refinements of cell parameters, we used MAUD software with the standard cif file 1530874. The results are presented in Figure 15. Due to the increase in temperature, the size of the unit cell and the angle α decrease. Computed values are larger than the reference values, which may be due to the presence of cobalt vacancies. Vacancies are influencing the ion state of Co. Change of oxidation state from Co^{3+} (0.75 \AA) to Co^{4+} (0.67 \AA) influences the cell volume by change of Co ions radius. The refinements results show that there is no significant changes in the lattice parameters for deposition temperature of 850°C and 1000°C , but thin films deposited at 750°C exhibit somewhat higher cell parameters. At angle $2\theta=56^\circ$ in LaCoO_3 -850-Si and LaCoO_3 -1000-Si samples, one can see a blur diffraction peak corresponding to (311) Si, although the substrate is (100) oriented. This is due to the grazing incidence of X rays. The angle between (311) and (100) planes in Si is 25.2° and is near of Bragg angle theta for (311) $\theta=28.28^\circ$ (λ_{Cu}), which gives in the XRD pattern a peak at an angle $2\theta=56.56^\circ$.

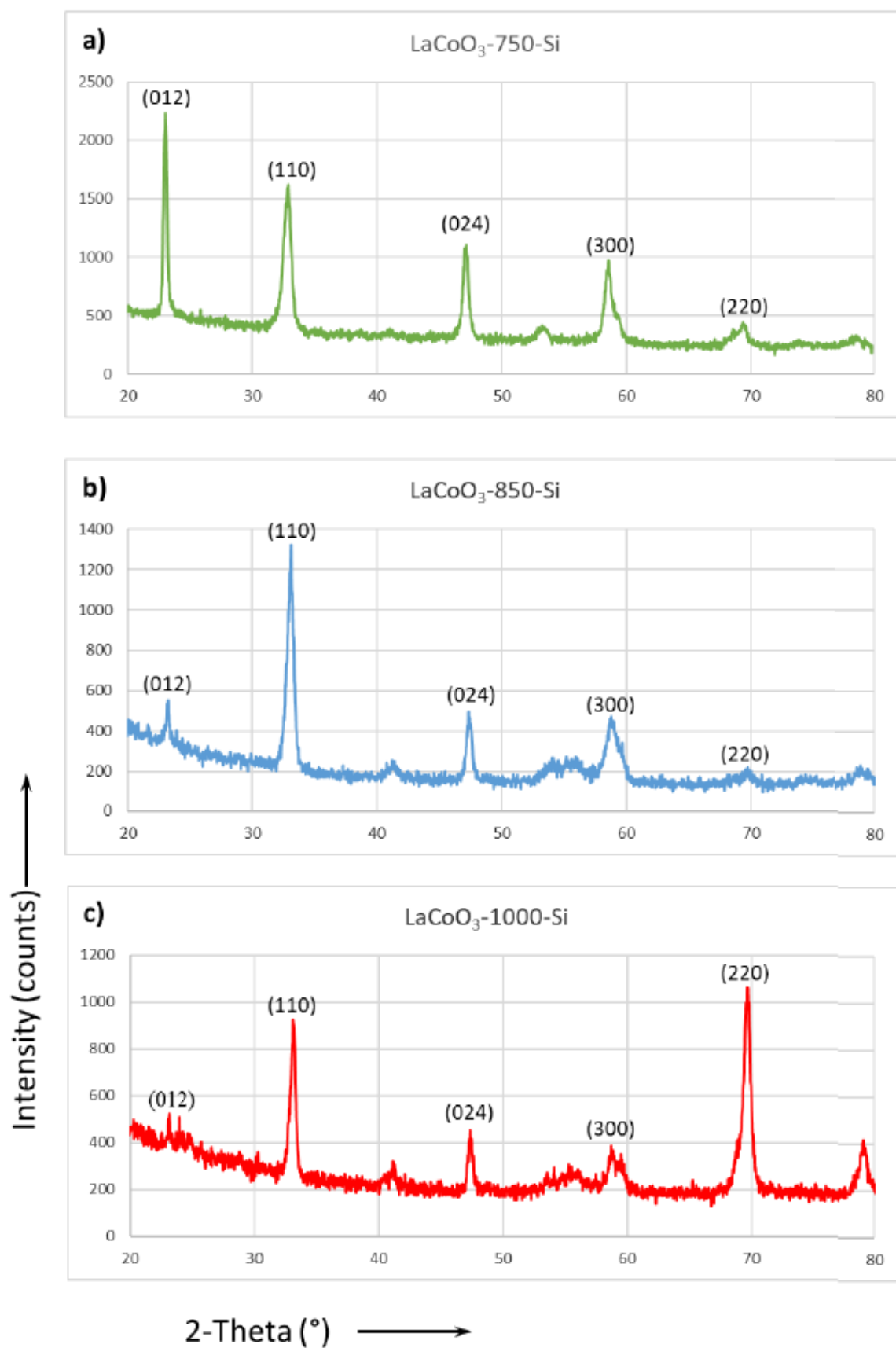


Figure 34. X-Ray Diffraction pattern of a) $\text{LaCoO}_3\text{-750-Si}$, b) $\text{LaCoO}_3\text{-850-Si}$, c) $\text{LaCoO}_3\text{-1000-Si}$. The peaks are indexed in the hexagonal settings.

Table 15. Refinement parameters obtained in MAUD software.

Sample name	a (Å)	α (°)	Vol (Å ³)	Rexp / Rwp	Crystal size
LaCoO ₃ -750-Si	5.4199	60.72	114.41	4.32/ 6.79	49 nm
LaCoO ₃ -850-Si	5.3971	60.69	112.90	6.90/10.56	51 nm
LaCoO ₃ -1000-Si	5.3980	60.67	112.90	6.25/9.16	x

The mean crystallite size was also extracted from the diffraction pattern (see Table 15). Again, due to grazing incidence, the mean size corresponds to the crystallite size parallel to the substrate. The deposition temperature does not influence the crystallite size. Due to presence of additional phases analysis of crystal size in LaCoO₃-1000-Si was not done.

Surface studies of LaCoO₃-T-Si using SEM allowed to obtain information on cracks, occurrence of droplets and microstructure of the surface.

The SE surface is one of the key factors affecting the sensitivity of the sensor due to the different activity of crystallographic planes exposed to gas. The LaCoO₃-750-Si surface is covered with a large number of nanoclusters or droplets (see Figure 35a) and cracks (see Figure 35b). Cracks are particularly undesirable in gas sensors application due to the unwanted diffusion of the gas towards the substrate. The grains of LaCoO₃ are small (20-30 nm) and do not appear faceted. As a result of the increase in deposition temperature to 850°C, the number of nanoclusters decreases (see Figure 35c). There are no literature about negative influence on gas sensing properties of nanoclusters. Nanoclusters are present but they are smaller and less frequent. There are no more cracks. Morphology and grains size are changing with deposition temperature and grains size is increasing with the increase of temperature. For LaCoO₃-850-Si, the grains are faceted with triangular section shape, with size around 100 nm. The triangular grains have flat termination. Some grains appear rectangular with a 4-facets tip termination. This triangular shape is lost for the LaCoO₃-1000-Si thin film (see Figure 35f & g). In this sample, we discovered grains with irregular shape and grain size in the range 50 – 150 nm. In order to verify the chemical composition of films and droplets, EDS analysis was performed, using the target as a standard (see Table 16). The chemical composition of the nanoclusters is consistent with the chemical composition of the layer and shows a cobalt deficiency. This result is in accordance with the cell parameters obtained by XRD refinements. Phase composition is influenced by oxygen pressure during deposition process [108]. In our case too low oxygen pressure in chamber lead to a cobalt deficiency in LaCoO₃ layer.

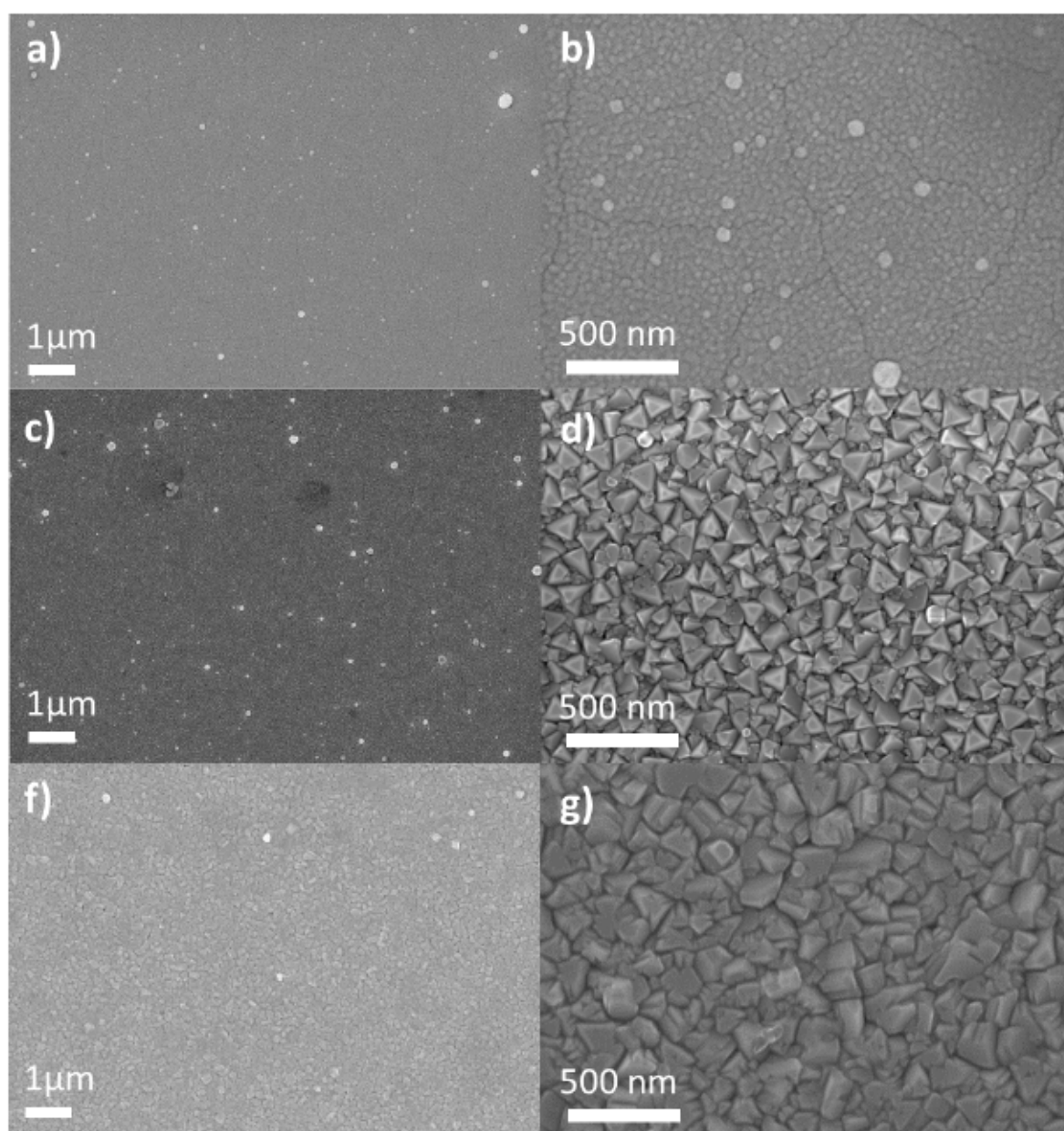


Figure 35. SEM micrographs of a) $\text{LaCoO}_3\text{-750-Si}$ - 10x b) $\text{LaCoO}_3\text{-750-Si}$ - 50x, c) $\text{LaCoO}_3\text{-850-Si}$ - 10x, d) $\text{LaCoO}_3\text{-850-Si}$ - 50x, e) $\text{LaCoO}_3\text{-1000-Si}$ - 10x f) $\text{LaCoO}_3\text{-1000-Si}$ - 50x.

The topography of thin films surface was analyzed using AFM technique. AFM analysis was carried out in area: $1\ \mu\text{m} \times 1\ \mu\text{m}$, $500\ \text{nm} \times 500\ \text{nm}$, $200\ \text{nm} \times 200\ \text{nm}$ and $100\ \text{nm} \times 100\ \text{nm}$. Selected results are presented in Figure 36a-c.

Table 16. EDS results of $\text{LaCoO}_3\text{-850-Si}$

Element	Nanocluster Region (Atomic %)	Thin film (Atomic %)
La L	56	55
Co K	44	45

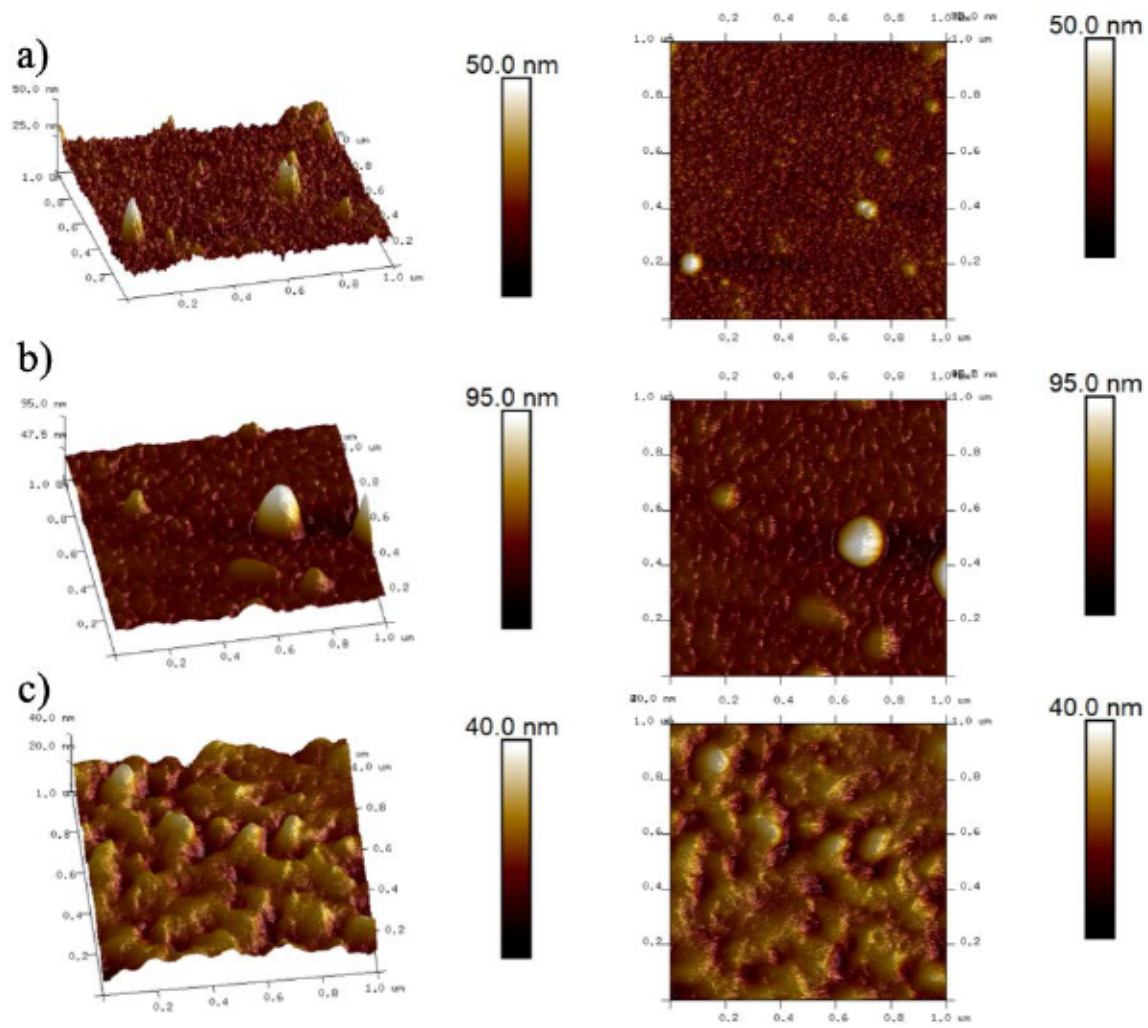


Figure 36. AFM images of LaCoO₃-Si, a) LaCoO₃-750-Si, b) LaCoO₃-850-Si c) LaCoO₃-1000-Si

The influence of deposition temperature is visible on the surface. As we observed in SEM on the LaCoO₃-750-Si surface there are a lot of small nanoclusters. The nanoclusters are smaller in thin films LaCoO₃-850-Si and less frequent, surface irregularity is bigger (see Figure 36b). No nanoclusters are observed in LaCoO₃-1000-Si (see Figure 36c). We calculate the roughness parameters R_{max} , R_a and R_q . R_q also called RMS is root mean square average of height deviation taken from the mean image data plane. R_a is average deviation from mean line. R_{max} is maximum peak to valley height.

The analysis was made in region free from the nanoclusters. All results are presented in Table 17.

Table 17 Roughness parameters of LaCoO₃-T-Si

Sample	R _a (nm)	R _{max} (nm)	R _q (nm)
LaCoO ₃ -750-Si	1.27	16.5	1.67
LaCoO ₃ -850-Si	1.54	11.9	1.92
LaCoO ₃ -1000-Si	2.51	20.0	3.13

Thin films obtained in higher temperatures are characterized by higher roughness parameters, witch change from R_a= 1.27 nm for LaCoO₃-750-Si to R_a= 2,51 nm for LaCoO₃-1000-Si. The increase of R_a parameters is consequence of the change in morphology and increase of grain size. Cross section of thin films was used for structure analysis in TEM, results are presented in Figure 37 and in Figure 39. Native SiO₂ layer (5 nm) is visible between substrate and LaCoO₃ T-Si thin film. Grains of LaCoO₃-750-Si have sharp tips (see Figure 37b), and flat ones (Figure 37a). Width of columnar grains are in range from 20 to 35 nm. The grains with flat termination have (012)_H planes exposed to gas, with a distance of 0.39 nm. FFT results are presented in Table 18. One should remember that a distance of 0.39 nm corresponds to (100)_C planes of the archetype cubic perovskite cell. The moiré observed is due to two overlapping grains with (012) type planes.

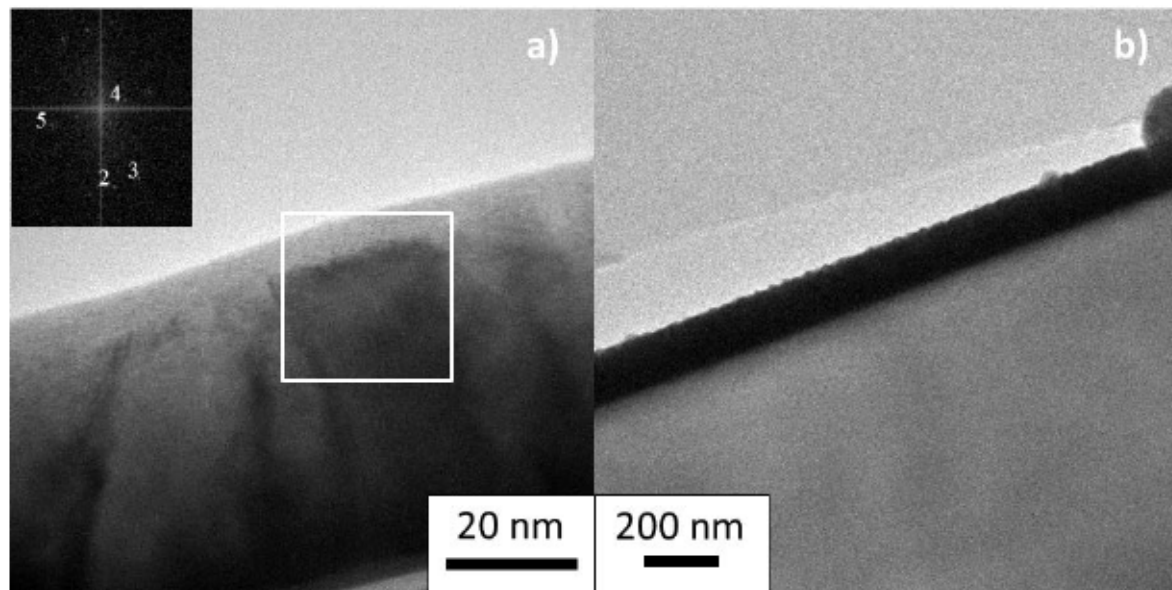


Figure 37. TEM images of LaCoO₃_750-Si a) columnar structure of the layer , and FFT of one grain b) low mag image of the layer, showing the shape of the grains termination, and the occurrence of nanocluster

Table 18. FFT results of LaCoO_3 -750-Si from Figure 37.

Number	Distance (nm)	Plane (hexagonal settings)
2	0.38	(012)
3	0.38	(012)
4	1.2	Due to Moire
5	0.6	Due to Moire

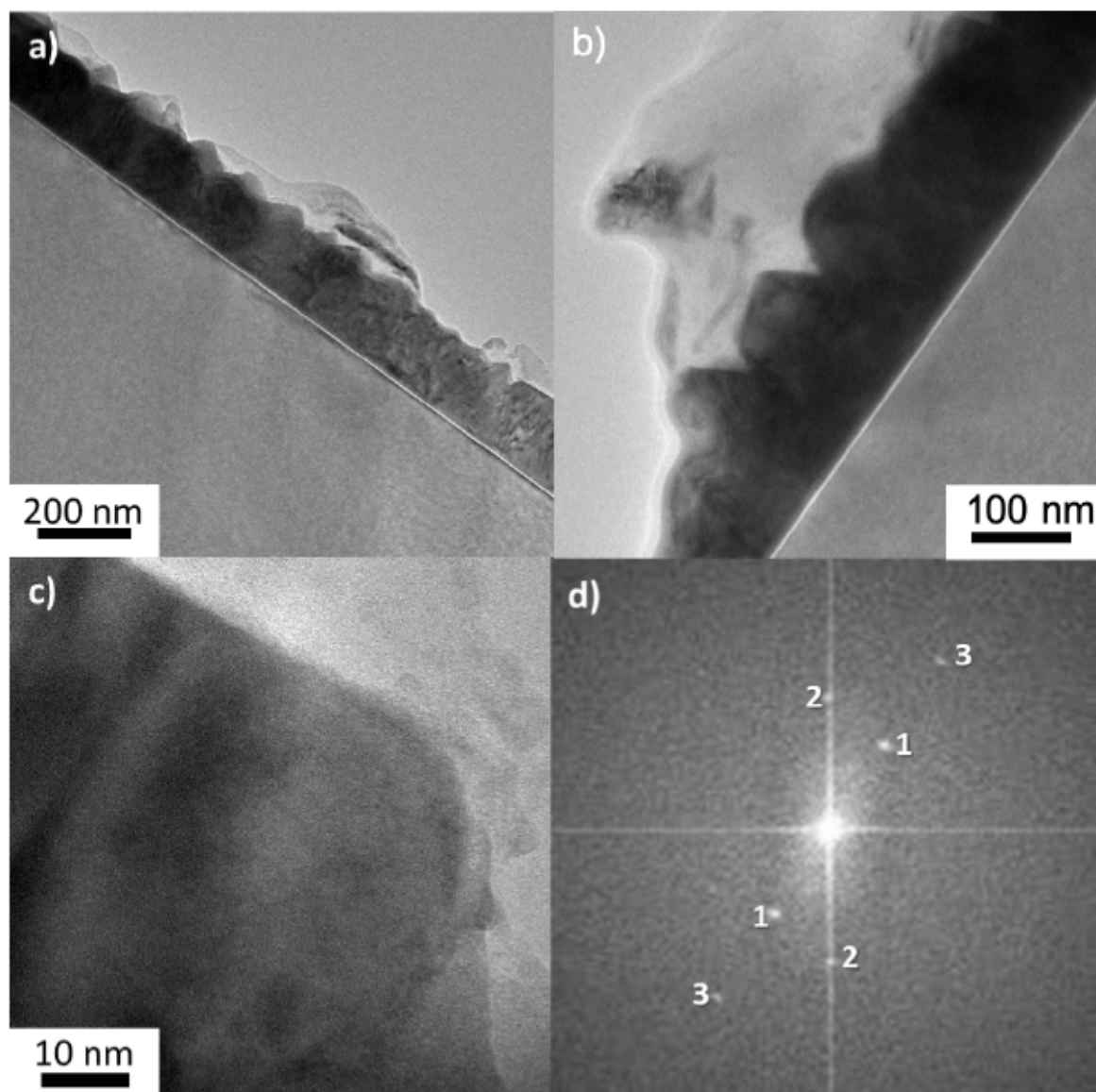


Figure 38. TEM images of LaCoO_3 -850-Si, along with one FFT from HREM image.

Table 19. FFT LaCoO_3 -850-Si from Figure 38d.

Number	Distance (nm)	Plane
1	0.38	(012)
2	0.28	(110)
3	0.19	(024)

Again, the termination of the grains is tip like or flat, and the $(012)_H = (100)_C$ planes are those exposed to gas for grain with flat terminations.

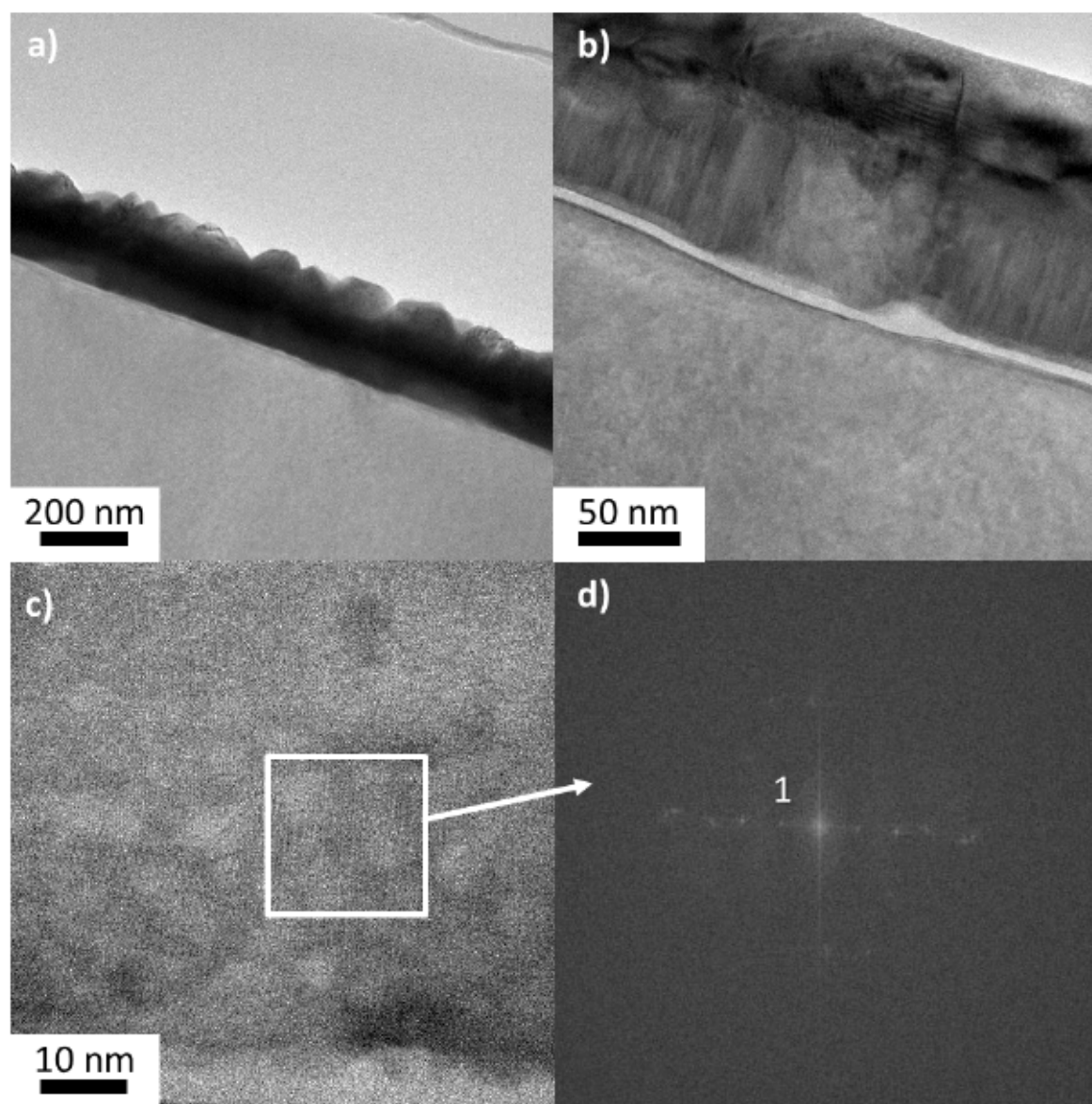


Figure 39. TEM images of LaCoO₃ 1000C-Si a) grain termination, b) thin films division c) high magnification d) FFT

Table 20. FFT LaCoO₃-1000-Si from Figure 39d.

Number	Distance (nm)	Plane
1	1.2	(002) La ₂ SiO ₇

For LaCoO₃-750-Si and LaCoO₃-850-Si, a columnar grain growth is observed. The layers have an average thickness of 170 nm (see Figure 37 & Figure 38). The roughness of the LaCoO₃-750-Si thin film seems rather low on TEM images, and a higher roughness is observed for LaCoO₃-850-Si (see Figure 38), which is in accordance with the AFM results. In LaCoO₃-850-Si we can observe column with regular triangular tips and a small flat termination. The lateral grain size varies from

75 nm to 100 nm. On the contrary, LaCoO₃-1000-Si exhibits a completely difference morphology on cross-section observation (see Figure 39). The layer consists of two distinct phases. One identified as La₂SiO₇ by high resolution electron microscopy with distance $d_{hkl}=12 \text{ \AA}$ (see Table 20), near the substrate (see Figure 39c), and second layer of LaCoO₃ on top. The presence of a La₂SiO₇ layer, with thickness of 75-85 nm, indicates that at 1000°C, Si can diffuse through the native SiO₂ barrier and built a lanthanum silicate. Silicates were already observed in thin films deposited by PLD with deposition temperature of 1100°C [113]. La₂SiO₇ phase was not observed in XRD results because of not sufficient penetration depth (78 nm).

4.1.2 LaCoO₃ thin films on C-YSZ (100) substrate

The X-rays diffraction patterns of LaCoO₃ thin films deposited on YSZ 9.5, are shown in Figure 40. The three diffractions patterns correspond to the expected rhombohedral phase (cif file 1530874), but in sample LaCoO₃-1000-YSZ95 we observe additional peak corresponding to La₂O₃ phase.

In range $2\theta = 20-40^\circ$ the most intense peaks of LaCoO₃-1000-YSZ95 phase is (110). Analysis of peak intensity allow to conclude that temperature has influence on crystallographic orientation of deposited layers. Presence of additional phase of La₂O₃ is indication that process temperature was too high. According to LaCoO₃ phase diagram Kleveland *et al* [114]. when ratio $N_{Co}/N_{Co} + N_{La}$ is equal to 0,5 only LaCoO₃ is present, but in case of cobalt deficiency, for ratio range from 0 to 0.5, up to 1500 K, a second phase (La₂O₃) is present This phase is mostly present in materials produced in temperature higher than 973 K. The results of XRD pattern refinements are presented in Table 21. Thin films deposited on Si and on C-YSZ at a given temperature have nearly the same cell volume. One observes the same call parameters for T=850°C and 1000°C. But for one given temperature, crystallite size was significantly smaller on C-YSZ substrate than one Si one.

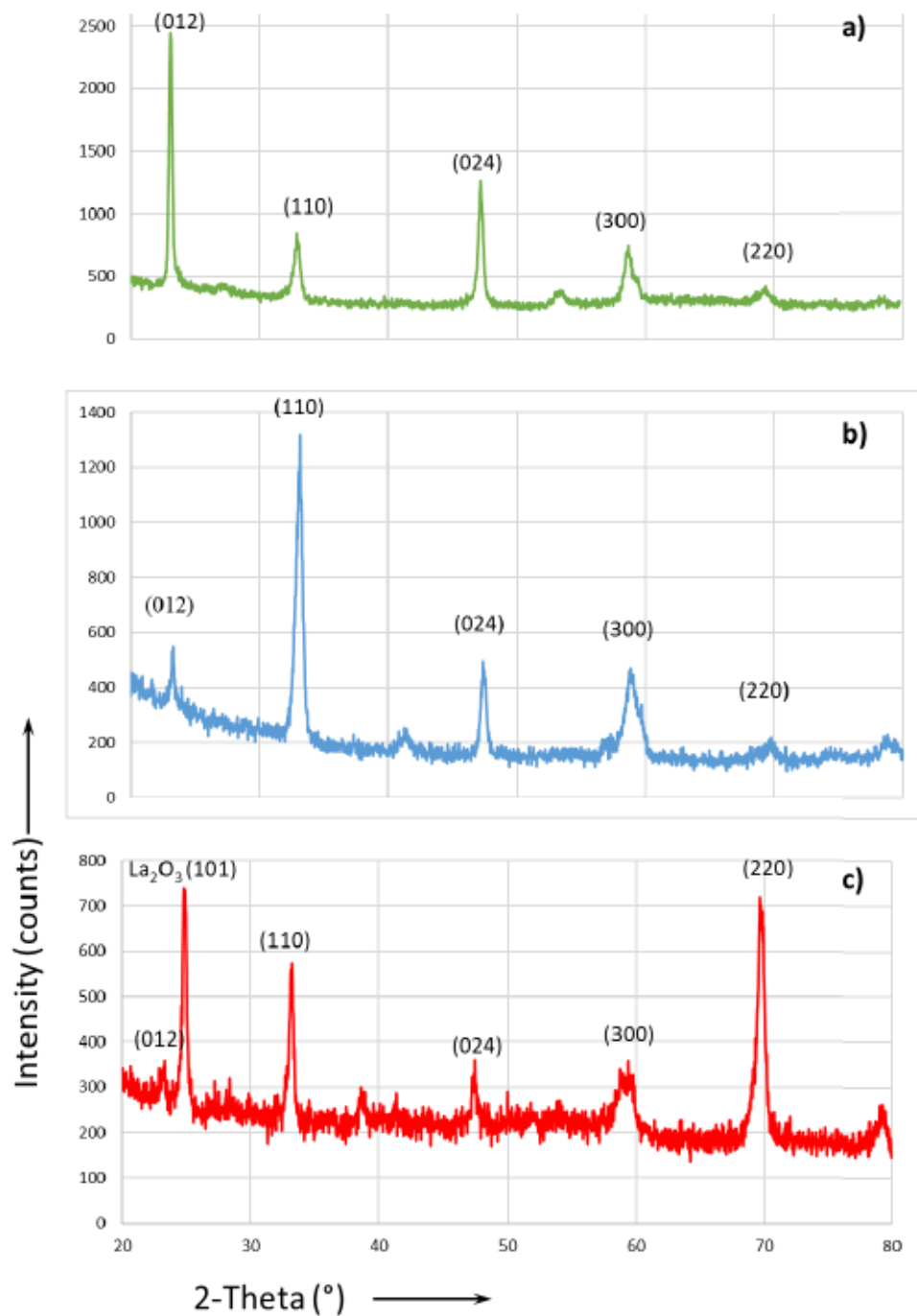


Figure 40. X-Ray Diffraction patterns of a) LaCoO₃-750-YSZ95, b) LaCoO₃-850-YSZ95, c) LaCoO₃-1000-YSZ95. Indexation in the hexagonal settings.

Table 21. MAUD refinement results for LaCoO₃-YSZ95

Sample name	<i>a</i> (Å)	α (°)	Vol (Å ³)	<i>R</i> _{exp} / <i>R</i> _{wp}	Crystal size (nm)
LaCoO ₃ -750-YSZ95	5.4208	60.6537	114.3	5.34 / 7.14	25
LaCoO ₃ -850-YSZ95	5.3918	60.71	112.613	8.04 / 10.56	36
LaCoO ₃ -1000-YSZ95	5.3912	60.7272	112.616	6.47 / 8.16	x

Due to high deposition temperature of 1000°C, undesirable La_2O_3 phase was created (see Figure 40c). This phase represents 12 % weight of the layer.

Surface analysis was conducted by SEM with mag. from 10 kx to 50 kx, chosen results are presented in Figure 41.

LaCoO_3 surface on YSZ95 at 750 °C looks like the layers obtained on Si at the same temperature, they have a large number of nanoclusters on the surface, but the cracks are not visible. Surface morphology LaCoO_3 -750-YSZ95 is similar to those of LaCoO_3 -750-Si, the grains have a –non faceted shape. As the deposition temperature increases to 850 °C, there is a slight change in the shape of the grains, but clearly the morphology of grains of LaCoO_3 -850-YSZ95 is different from the one of In LaCoO_3 -850-Si. This is due to the low thermal conductivity of YSZ, leading to lower temperature than the nominal during the deposition process. The cracks are not visible, the grain size is not affected by process temperature and we don't observe grains expansion (see Figure 41b-d). The number of nanoclusters decreased. In thin films deposited at 750 °C nanoclusters were small but densely spaced. In LaCoO_3 -850-YSZ95 nanoclusters are less densely space but they are bigger. The surface of the LaCoO_3 -1000-YSZ95 thin film presents a completely different morphology from previous samples. Small single nanoclusters are visible, the grains have the shape of long wrapped worms. The layer appears melted. Based on the obtained micrographs, it can be assumed that the process temperature of 1000°C was too high. We can conclude that thin films LaCoO_3 -1000-YSZ95 have the structure inadequate to be used as SE in gas sensor. Because in samples LaCoO_3 -750-YSZ95 and LaCoO_3 -850-YSZ95 we don't observed cracks, they are considered as promising thin films for further gas measurements.

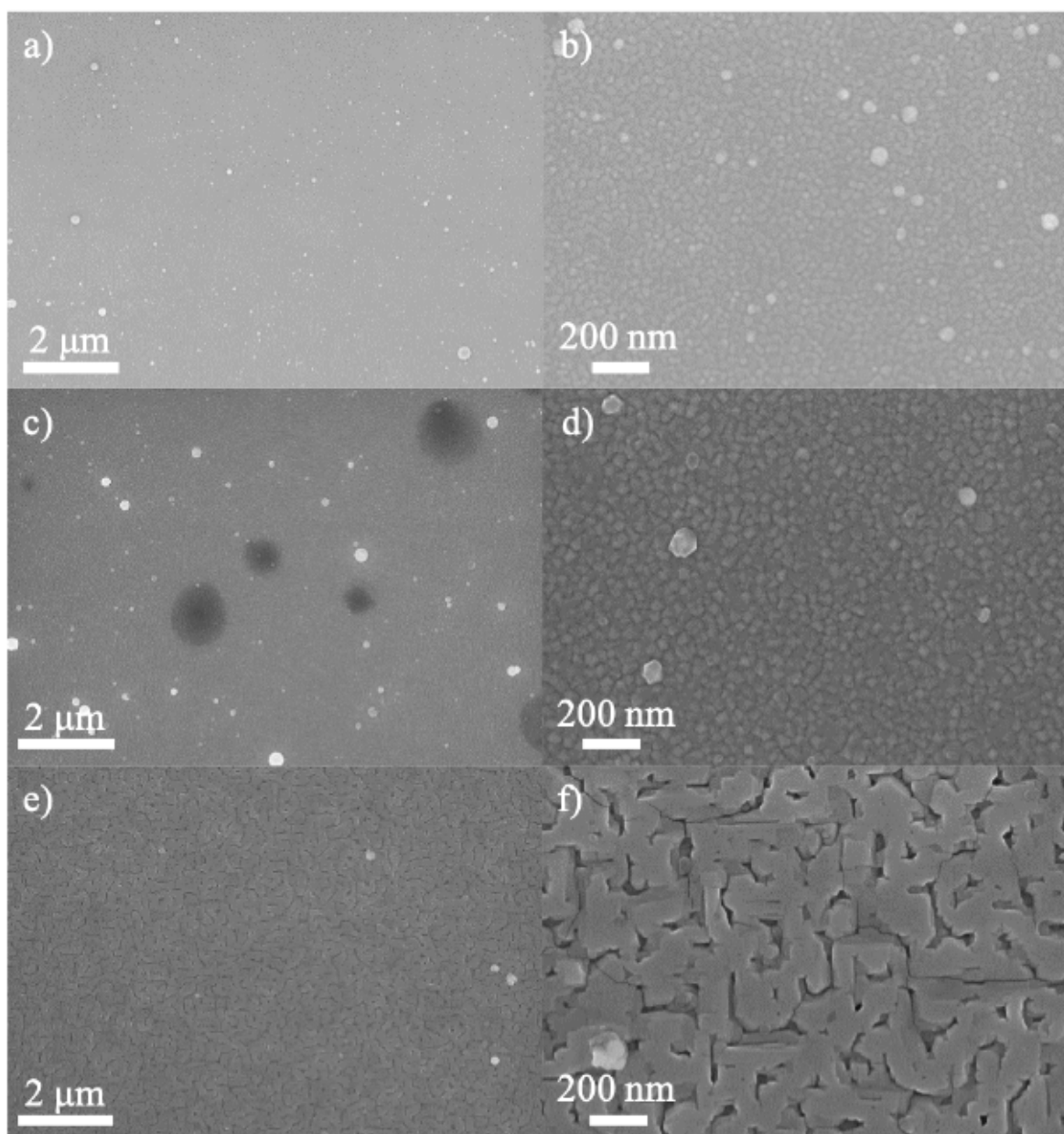


Figure 41. SEM micrographs of LaCoO₃-YSZ95 a,b) LaCoO₃-750-YSZ95 c,d) LaCoO₃-850-YSZ95 e,f) LaCoO₃-1000-YSZ95.

The topography of thin films was analyzed using AFM technique. AFM analysis was carried out in area: 1 μm x 1 μm , 500 nm x 500 nm, 200 nm x 200 nm and 100 nm x 100 nm. Selected results are presented in Figure 42 a-c.

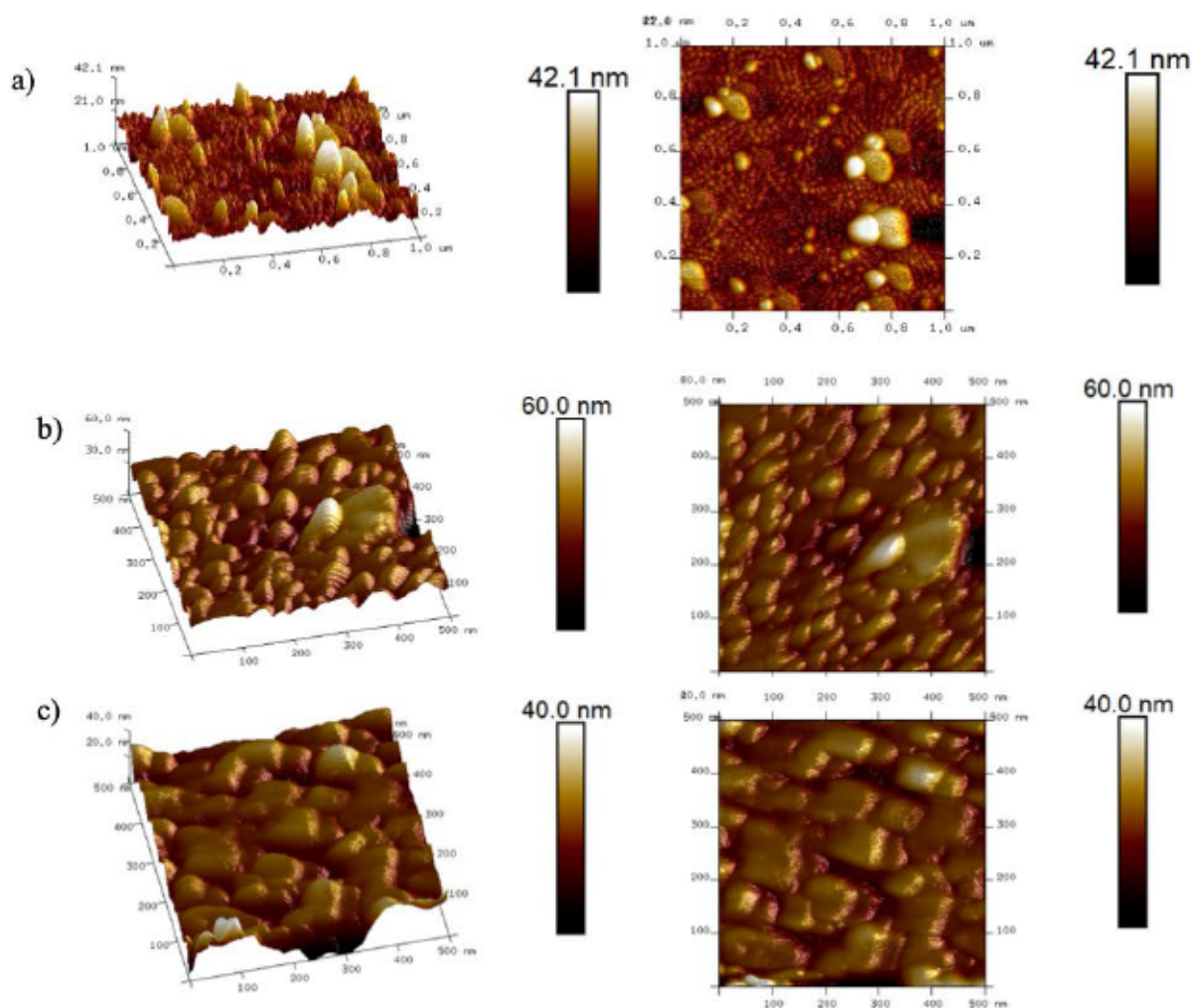


Figure 42. Surface morphology of a) LaCoO₃-750-YSZ95 b) LaCoO₃-850-YSZ95 c) LaCoO₃-1000-YSZ95.

Sample LaCoO₃-850-YSZ95 presenting highly developed surface with nanocluster (see Figure 42b). Increase of process temperature leads to increase of grain size and decrease of roughness (see Figure 42c). Base on this result we calculate the roughness parameters R_{max} , R_a and R_q . The analysis was made in the region free from the nanoclusters. All results are presented in Table 22.

Table 22. AFM results of LaCoO₃-YSZ95

Sample	R_a (nm)	R_{max} (nm)	R_q (nm)
LaCoO ₃ -750-YSZ95	2.69	21	3.37
LaCoO ₃ -850-YSZ95	2.65	20.5	3.35
LaCoO ₃ -1000-YSZ95	2.42	19.0	3.08

Thin films deposited in 1000° C are characterized by lower roughness parameters. The decrease of R_a parameters is a consequence of the change in morphology. Grains in sample LaCoO₃-1000-YSZ95 are lower and flat which leads to low R_a and R_{max} parameter than in LaCoO₃-850-

YSZ95. R_{\max} is similar to all samples it can be explained by similar absolute height of grains regardless deposition temperature.

Cross section of thin films was used for structure analysis in TEM, LaCoO_3 -T-YSZ95 results are presented in Figure 43–Figure 45.

As we can observe (see Figure 43), thin films LaCoO_3 -750-YSZ95 are very thin, around 65-70 nm structure and built with grains larger than high.

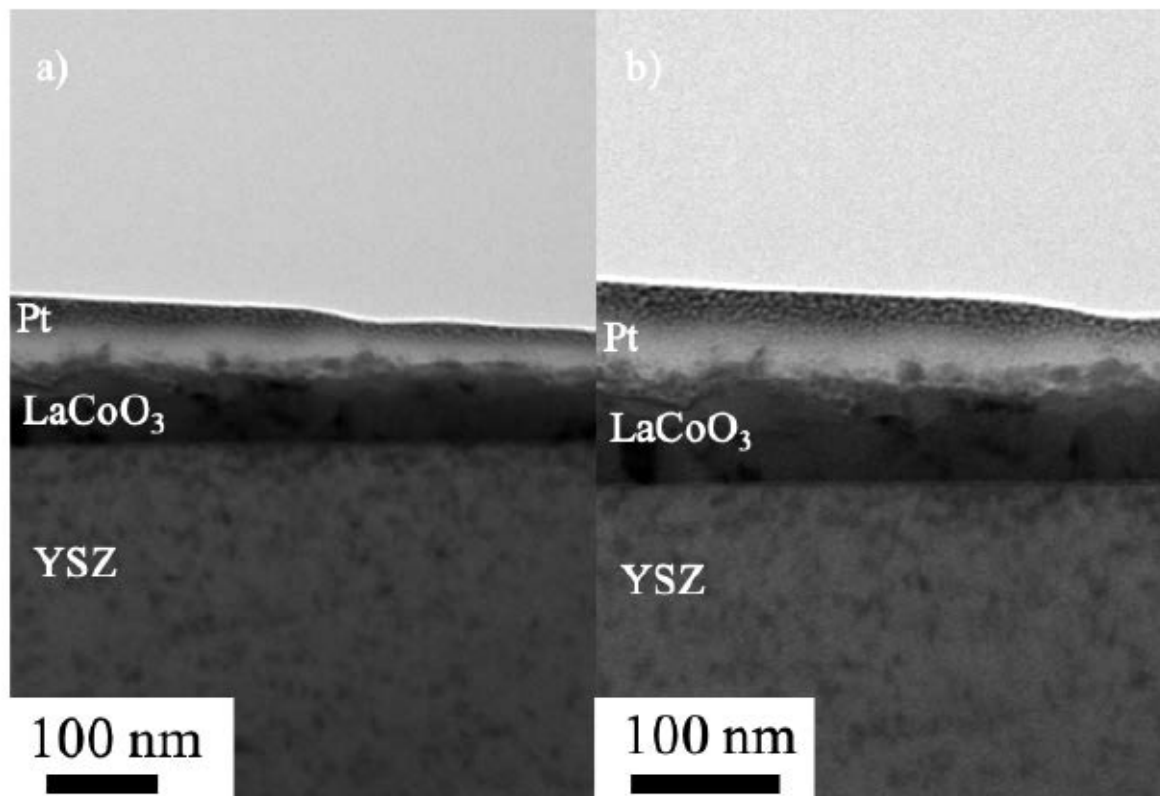


Figure 43. TEM Cross-section of LaCoO_3 -750-YSZ95 a) low magnification b) details of the LaCoO_3 grains

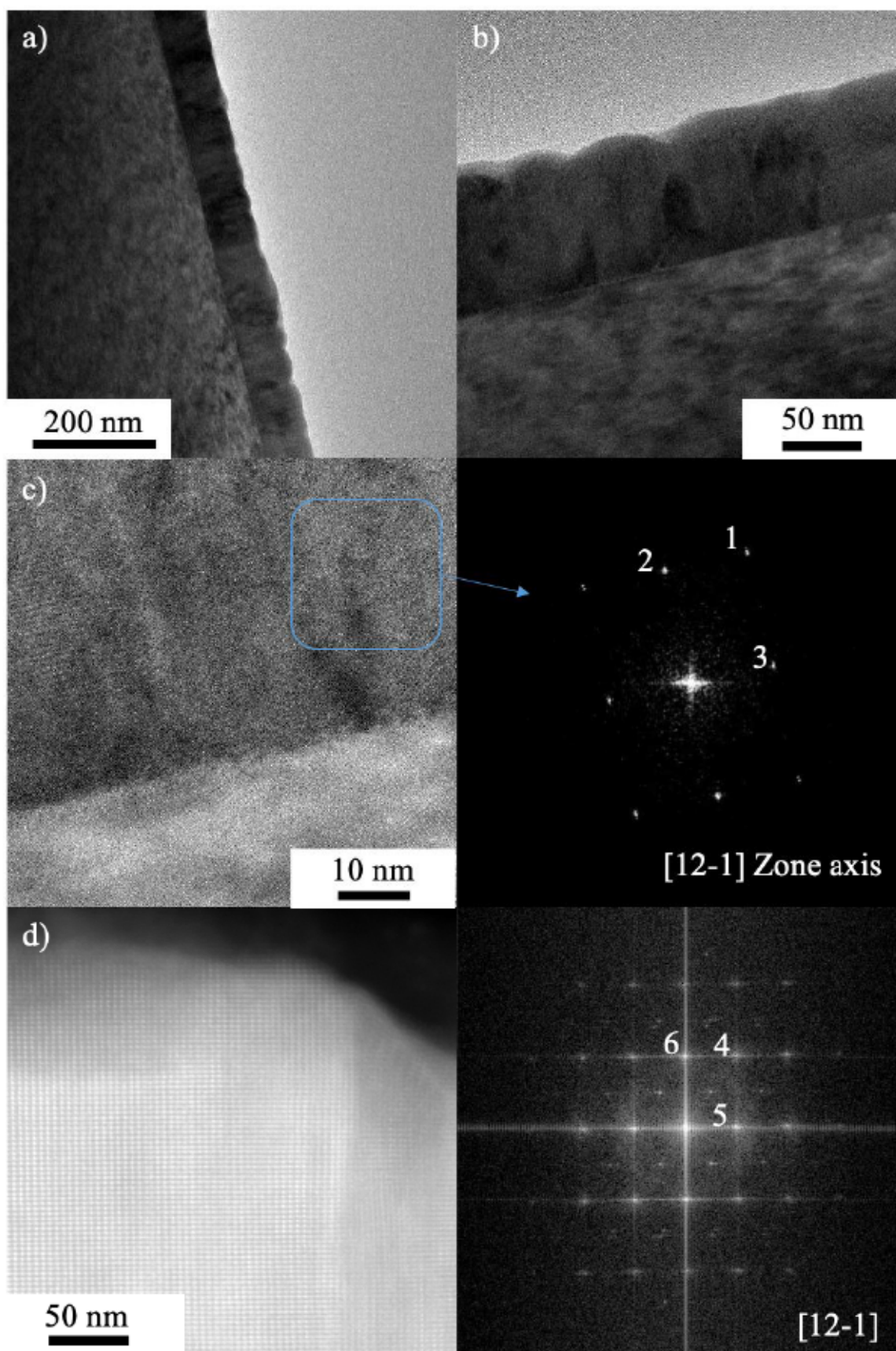


Figure 44. TEM Cross-section of LaCoO₃-850-YSZ95 a) low magnification image of the thin film b) evidence of columnar structure c) HREM image near the substrate along with FFT d) STEM-HAADF image of the top of one grain, along with FFT

Table 23. FFT results of LaCoO₃-850-YSZ95

Number	Distance (nm)	Plane	Figure
1	0.22	(202)	Figure 44f
2	0.28	(2-10)	
3	0.38	(012)	
4	0.23	(202)	Figure 44g
5	0.38	(012)	
6	0.28	(2-10)	

Sample LaCoO₃-850-YSZ95 has 90 nm thickness, which is much lower than sample produced with the same PLD parameters but on Si substrate. This can be explained by the fact that C-YSZ has a weak thermal conductivity (2 W/m.K) [115] compared to Si (130 W/m.K) [116, 117]. So, for a given nominal temperature, the top of the substrate C-YSZ is at a lower temperature than the top of the Si substrate, leading to less growth of the grains through atomic diffusion, and to lower layer thickness. Thin films contain columns growing directly from substrate to the top. Termination of columns have smother tips than for LaCoO₃-850-Si. Thin films are uniform no cracks and pores are visible. Based on FFT analysis we identified only LaCoO₃ phase. Near the substrate, or near the tip of the grains, (012)_H planes with distance 0.38 nm perpendicular to the substrate, showing a change or grain growth direction between layers on Si or on C-YSZ. Planes exposed to gas are mainly (2-10)_H=(110)_C and growth direction is [110]_H, perpendicular to the (2-10)_H planes.

Sample LaCoO₃-1000-YSZ95 (see Figure 45), as we saw on SEM micrographs, have different morphology than previous samples. With a thickness of 180 nm the layer is twice as thick than film obtained at 850°C. Grain are finished with terraces; no pointed/sharp tips are present. Cracks or pores are not visible.

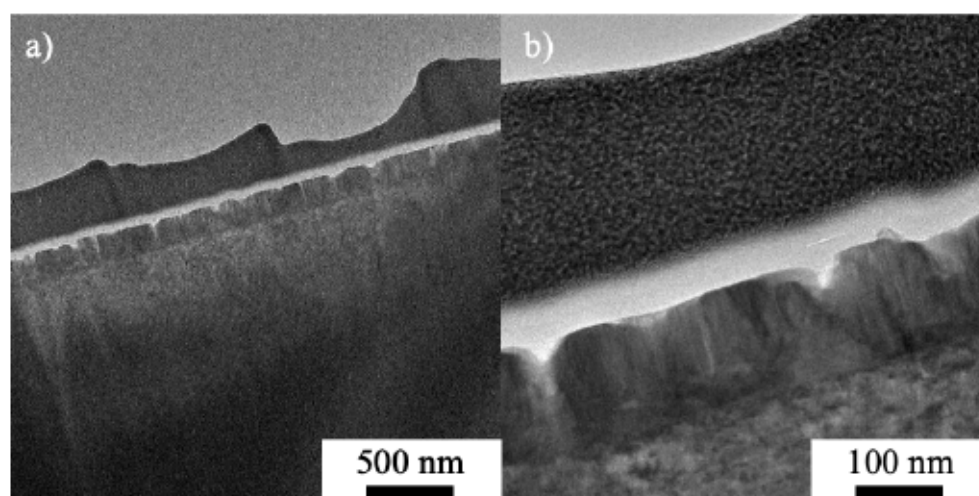


Figure 45. TEM Cross-section of a) LaCoO₃-1000-YSZ95 b) columnar structure

4.1.3 LaCoO₃ thin films on T-YSZ substrate

The X-rays diffraction patterns of LaCoO₃-T-YSZ35 thin films are shown in Figure 46. Analysis were done in Grazing geometry at a constant angle of incident $\alpha = 0.7^\circ$. The depth of penetration calculated in GIXA software was $z = 50.6$ nm.

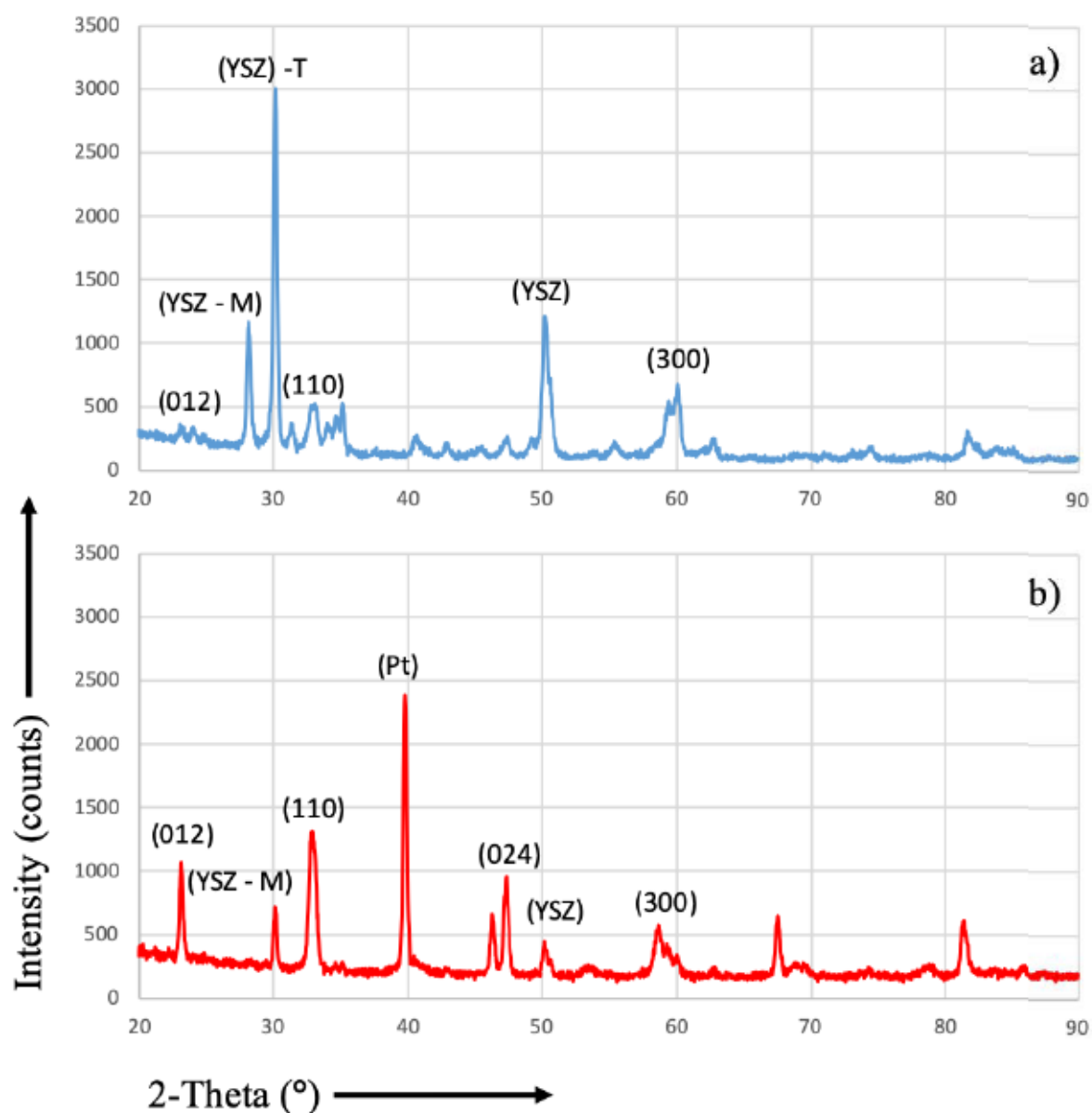


Figure 46. XRD results of LaCoO₃-YSZ35 a) 750 °C b) 850 °C

As we can observe in Figure 46 other than expected phases are present. At low deposition (750°C) temperature we can only observe (012), (110) and (300) peaks from LaCoO₃ other

peaks are linked to the YSZ35 substrate. One can notice that the substrate, is not single phased. The substrate should have tetragonal structure, but also the monoclinic phase is present.

In LaCoO_3 -850-YSZ35, Pt electrodes were deposited on the sides of the sample. That is why we can observe peaks from Pt. Peak intensity corresponding to LaCoO_3 are higher in LaCoO_3 -850-YSZ35 than in LaCoO_3 -750-YSZ35. It is due to the thin film thickness. Due to presence of YSZ35 phase and Pt the XRD patterns were not refined

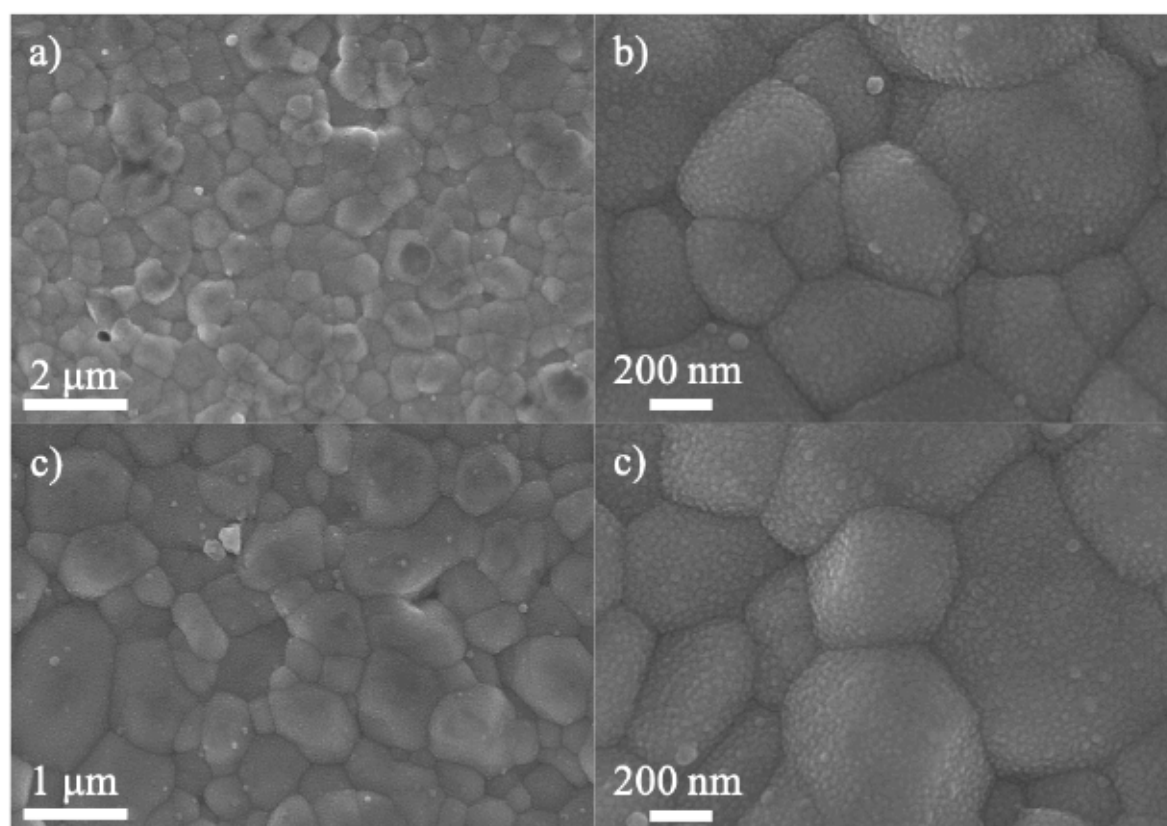


Figure 47. SEM images of LaCoO_3 -YSZ35 a) LaCoO_3 -750-YSZ35 low mag. b) LaCoO_3 -750-YSZ35 thin film grains c) LaCoO_3 -850-YSZ35 low magnification d) LaCoO_3 -850-YSZ35 thin films grains.

Topography of Thin films deposited on tetragonal substrate are much different from thin films deposited on Si and cubic YSZ. Big grains are visible (see Figure 47b), which are covered by or are built with small grains, 25–40 nm in size. Tetragonal substrate is a polycrystal with a topography of hills (see TEM image of cross section Figure 49). Big grains belong to 3,5 YSZ substrate. With bigger magnification it is clear that larger YSZ grains are covered with small LaCoO_3 grains. Cracks are not visible, grain boundaries between T-YSZ grains are strongly visible. Small nanoclusters are present (see Figure 47a) but less frequent than on LaCoO_3 -Si and on LaCoO_3 -YSZ95. Grains have spherical shape like those obtained in LaCoO_3 -750-YSZ95. Surface morphology is not affected by temperature (see Figure 47b-d).

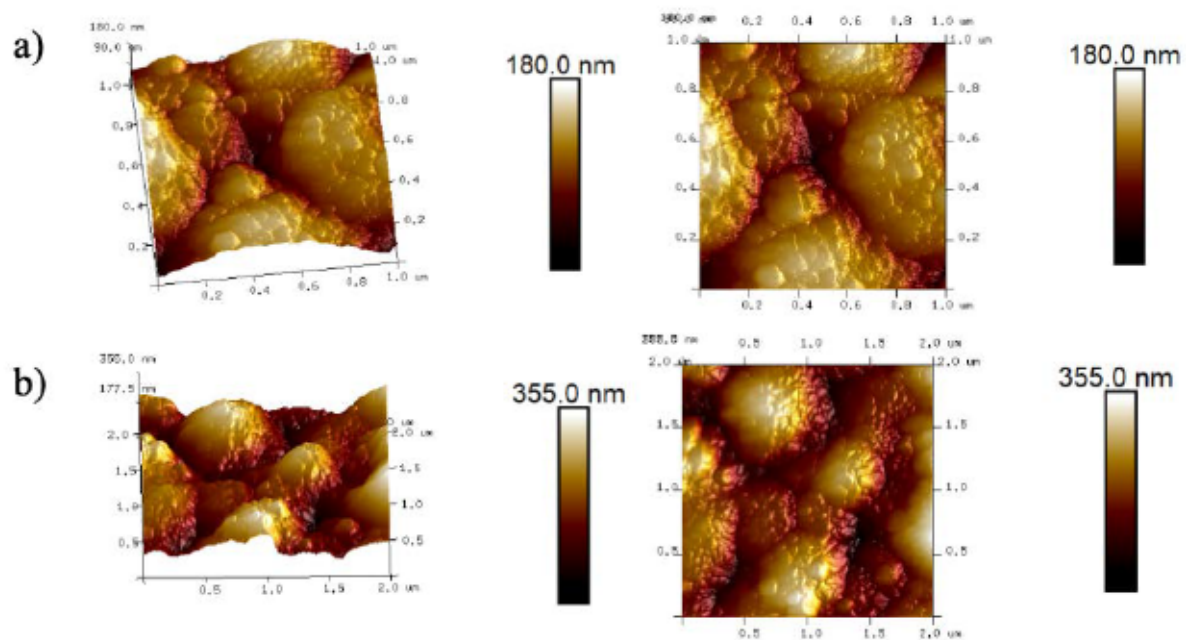


Figure 48. AFM of LaCoO₃-YSZ35 a) LaCoO₃-750-YSZ35 b) LaCoO₃-850-YSZ35

The topography of thin films was analyzed using AFM technique. Selected results are presented in Figure 48a-b. As we observed in SEM analysis on the LaCoO₃-750-Si surface small nanoclusters are presented. Grain like hills from YSZ35 substrate are covered with nanograins of LaCoO₃. We calculate the roughness parameters R_{max} , R_a and R_q . The analysis was made in the region free from the nanoclusters. All results are presented in Table 24.

Table 24. Roughness parameters of LaCoO₃-YSZ35

Sample	R_a (nm)	R_{max} (nm)	R_q (nm)
LaCoO ₃ -750-YSZ35	34.8	340	45.6
LaCoO ₃ -850-YSZ35	43.5	318	53.5

Sample LaCoO₃-750-YSZ35 is characterized by R_a parameters of 34.8 nm. It is difficult to compare roughness of LaCoO₃-750-YSZ35 with LaCoO₃-T-YSZ95 and LaCoO₃-T-Si due to different roughness of substrate. Substrate nature strongly influence on R_a and R_{max} parameters that is why LaCoO₃-T-YSZ35 thin films are only comparable towards temperature influence and material of sensing electrode (LaCoO₃ / LaFeO₃). As we can observe, R_a decrease, with increase of deposition temperature (see Table 24).

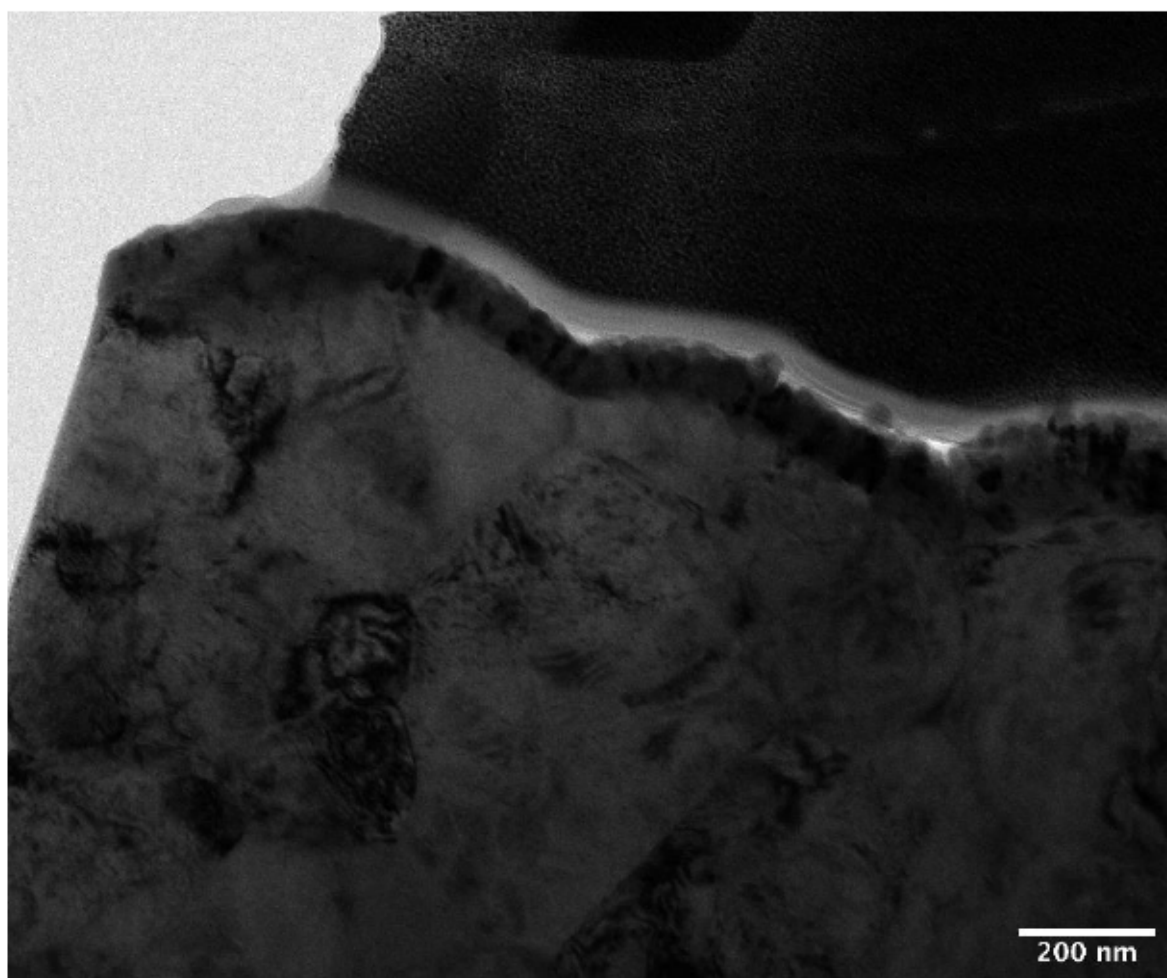


Figure 49. TEM image of LaCoO_3 -850-YSZ35

Thin film thickness is 80 nm. Topography of substrate is totally different from those observed in Si and YSZ95. The latter are monocrystals and flat. Tetragonal YSZ is polycrystal, and bumpy. Grains of YSZ are creating wide hills (up to 700 nm width). Hills are completely covered with compact thin films of LaCoO_3 , as it is shown in Figure 49.

4.2 STRUCTURE CHARACTERIZATION OF LaFeO_3 THIN FILMS.

4.2.1 LaFeO_3 thin films on Si (100) substrate

The X-rays diffraction patterns of LaFeO_3 thin films deposited on Si, are shown in Figure 54. Analysis was made in grazing incidence angle of $\alpha = 1^\circ$ and the step time of 20 s and angle step of 0.03° . The XRD patterns correspond to the expected orthorhombic LaFeO_3 phase (JCPDS 01-074-220). The peaks were indexed in the Pnma space group, where **b** is the long axis. The effective penetration depth of X-rays is $z = 89.5$ nm. The thin films have a crystalline structure.

In thin films obtained on Si undesirable phases like La_2O_3 , or iron oxides, were not noticeable in the XRD patterns. For LaFeO_3 -750-Si, the most intense peak is located at $2\theta=32^\circ$, which corresponds to the (121) Bragg reflection of LaFeO_3 (see Figure 50a). Tin film deposited at 850°C shows the same most intense peak. Thin film deposited at 1000°C has different peak intensity from the other samples. Additional peaks of LaFeO_3 are visible such as the reflections (210), (112), (212), (141) and (113). This result shows that the obtained material has a high degree of crystallinity. With increase of deposition temperature, the intensity of (121) peak decrease and intensity of (101) peak increases. This result is showing change in texture with increase of deposition temperature. Texture analysis is not possible due to changes in the reflection vector q in grazing geometry compared to Bragg Brentano Geometry, but we can analyze intensity of two peaks (101) and (121). XRD patterns were analyzed in MAUD software. The cell parameters for all three samples were refined and are given in Table 25. Volume of unit cell decrease with increase of temperature. This can be explained by the presence of Fe^{4+} ions. When the oxidation state of iron increased, Fe ion radius changes — in our case going from 0.645 \AA for Fe^{3+} to 0.585 \AA for Fe^{4+} . The decrease of cell parameters with temperature increase suggests a change of Fe oxidation state or oxidation capability [118].

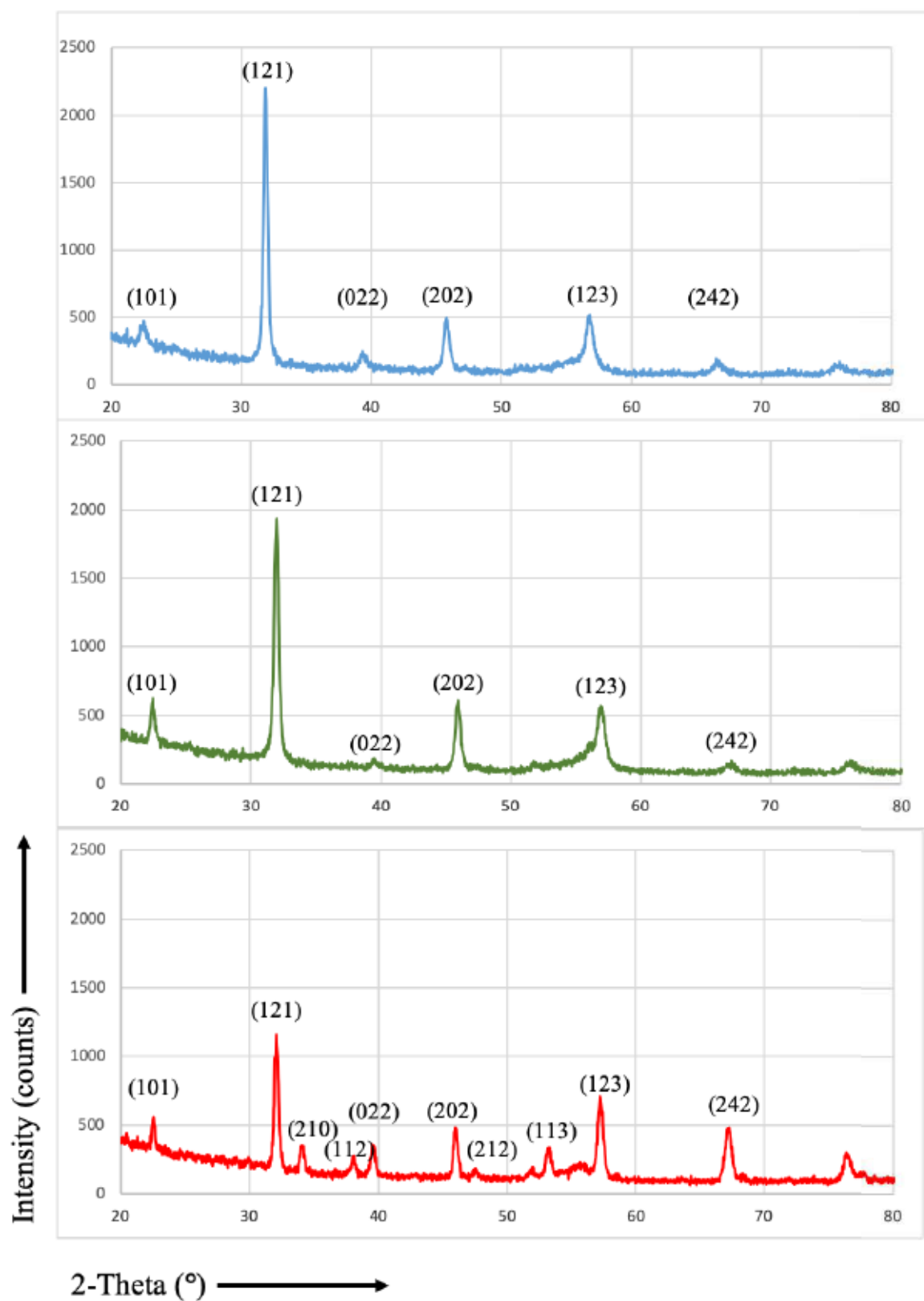


Figure 50. X-Ray Diffraction pattern of LaFeO₃-Si thin films indexed in the Pnma setting a) LaFeO₃-750-Si, b) LaFeO₃-850-Si, c) LaFeO₃-1000-Si.

Table 25. MAUD results of $\text{LaFeO}_3\text{-Si}$, in the Pbnm space group.

Sample name	a (Å)	b (Å)	c (Å)	Vol (Å ³)	Rexp / Rwp	Crystal size
$\text{LaFeO}_3\text{-750-Si}$	5.6097	5.6075	7.9092	248.7949	6.56/10.5	28 nm
$\text{LaFeO}_3\text{-850-Si}$	5.5406	5.6380	7.9110	247.1250	8.15/11.21	46 nm
$\text{LaFeO}_3\text{-1000-Si}$	5.5562	5.5755	7.8941	2445491	7.89/10.07	x

Surface observation was carried out thanks to SEM. Micrographs were taken with magnifications of 10 kx, 30 kx, 40 kx, 50 kx and 100 kx, Selected images are presented in Figure 51 and in Figure 52.

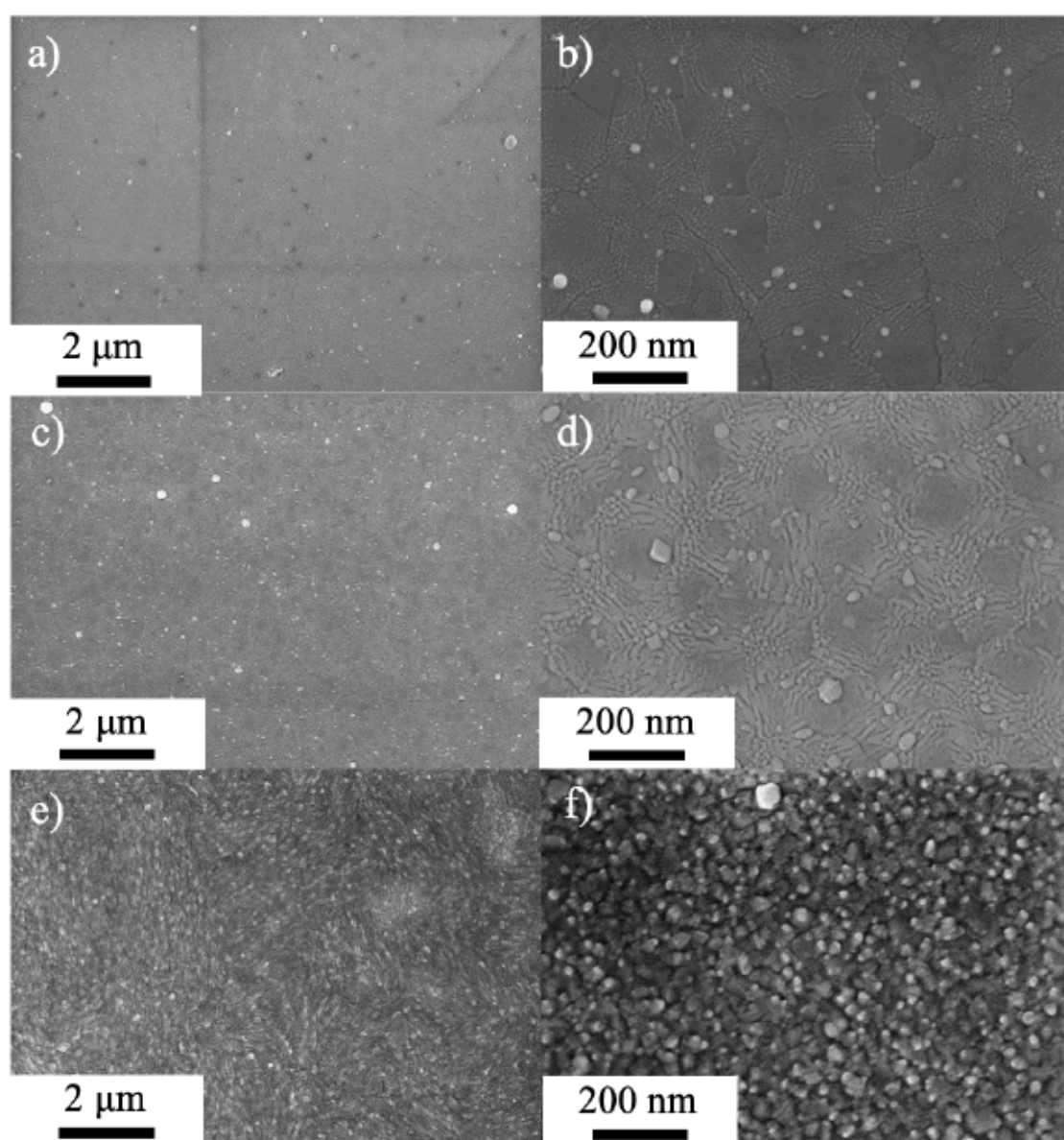


Figure 51. SEM micrographs of a) Surface of $\text{LaFeO}_3\text{-750-Si}$ with low mag. b) Morphology of $\text{LaFeO}_3\text{-750-Si}$ c) Surface of $\text{LaFeO}_3\text{-850-Si}$ with low mag. d) Morphology of $\text{LaFeO}_3\text{-850-Si}$ e) Surface of $\text{LaFeO}_3\text{-1000-Si}$ with low mag. f) Morphology of $\text{LaFeO}_3\text{-1000-Si}$.

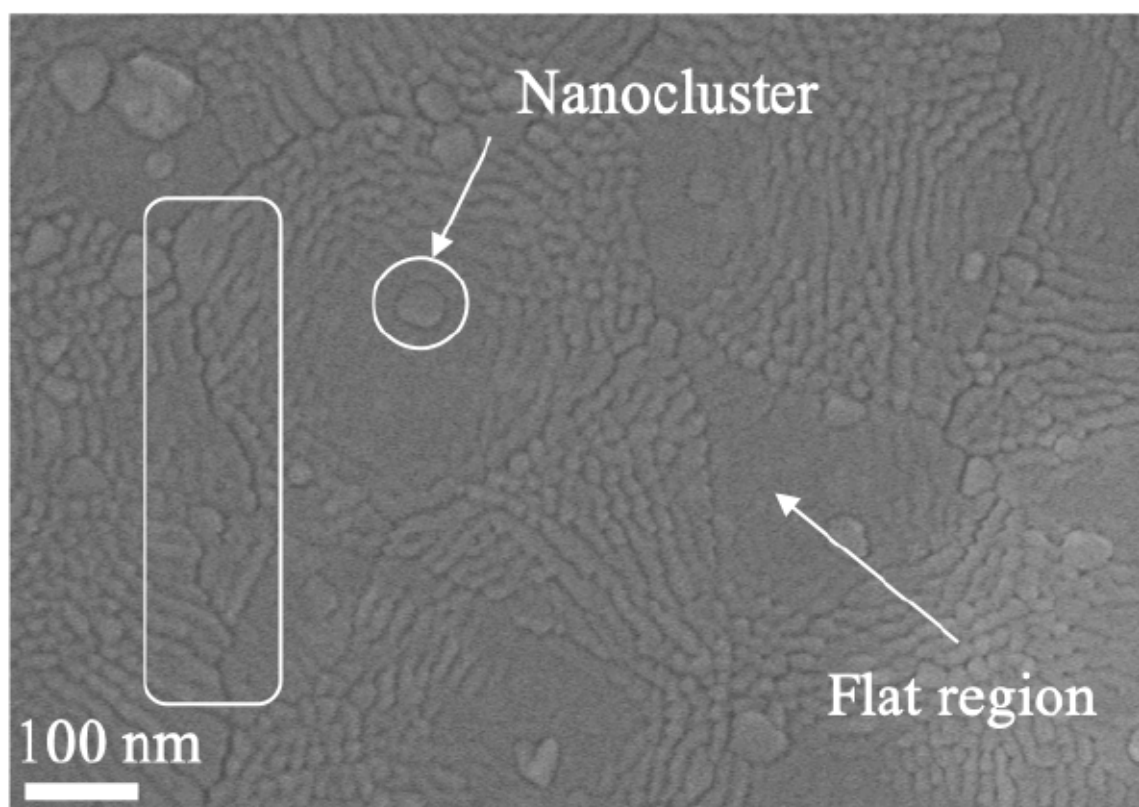


Figure 52. SEM micrographs of LaFeO₃-750-Si revealing surface microstructure in “flat” region.

On the surface of LaFeO₃-750-Si (see Figure 52), nanoclusters are visible. The surface can be divided into two areas, one with grains with sharp end and the other with a flat end. The grains have nanometric size, with a sharp tip (needles) stretched in one direction. Crack between grains is marked with a rectangle (see Figure 52). As the temperature increases to 850°C, we can observe an increase in grain size (see Figure 51c-d). The density of nanoclusters did not changed compared with LaFeO₃-750-Si (see Figure 51a-b), but their size increased. The LaFeO₃-850-Si thin films have no cracks, presents few nanoclusters and flat areas decreases. Gains in “flat” regions are more visible. The morphology of the LaFeO₃-750-Si and LaFeO₃-850-Si films is similar. However, the morphology of thin films deposited at 1000°C is significantly different. Nanoclusters and cracks are not visible at low magnification. Cracks or lines between grains are not visible. The shape of the grains changed radically. The surface consists of irregularly arranged grains in the form of tiles. We can assume that the process temperature was too high, as it was in the case for LaCoO₃-1000-Si.

Next surface examination was carried out by AFM in area: 1 $\mu\text{m} \times 1 \mu\text{m}$, 500 nm \times 500 nm, 200 nm \times 200 nm and 100 nm \times 100 nm. Selected results are presented in Figure 53a-c.

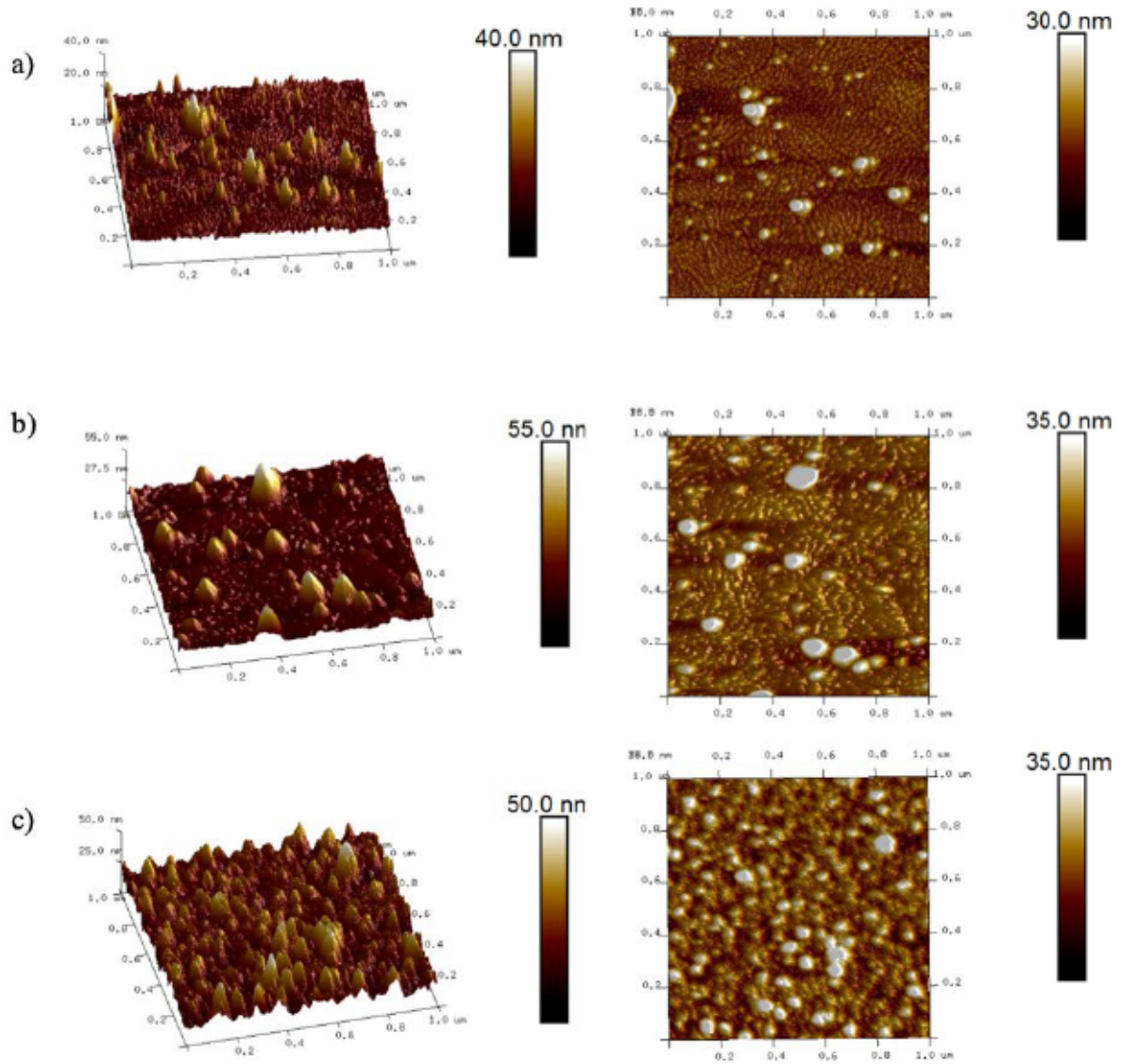


Figure 53. Surface morphology of a) $\text{LaFeO}_3\text{-750-Si}$ b) $\text{LaFeO}_3\text{-850-Si}$ c) $\text{LaFeO}_3\text{-1000-Si}$

The influence of deposition temperature is visible on the surface. As in SEM, the $\text{LaFeO}_3\text{-750-Si}$ surface exhibits nanoclusters. Single nanocluster contains multiple grains (see Figure 53b). The nanoclusters are larger in films deposited at 850°C as compared to those deposited at 750°C , however, less frequent. Different surface morphology is observed in sample deposited at $T_p = 1000^\circ\text{C}$. These results are coherent with SEM observations. Base on AFM observations, we can calculate the roughness parameters R_{max} , R_a and R_q . The measurements were undertaken in regions free of nanoclusters. All results are presented in Table 26.

Table 26. Roughness parameters of LaFeO₃-Si thin films

Sample	R _a (nm)	R _{max} (nm)	R _q (nm)
LaFeO ₃ -750-Si	1.1	9	1.36
LaFeO ₃ -850-Si	1.13	9.1	1.45
LaFeO ₃ -1000-Si	3.79	42.2	5.00

We did not observe any change of roughness parameters for the samples deposited at T = 750°C and 850°C. Thin film deposited at 1000°C has almost two times larger roughness (R_a=3.79 nm) than sample LaFeO₃-850-Si (R_a=1.13) (see Table 26). In higher temperature, grains have different form leading to an increase of R_{max} parameter from 9 nm in 750°C to 42.2 nm in 1000°C. The increase of R_a parameters is the consequence of the change in morphology and grain size increase.

Precise structure analyzes were done by TEM. Obtained thin films have columnar structure with nanometric width. In reference to Thornton model thin films obtained at 750°C and 850°C are typical for zone T with long fibrous elongated columns. TEM results on LaFeO₃-T-Si are summarized in Figure 56 , Figure 57 and Figure 58.

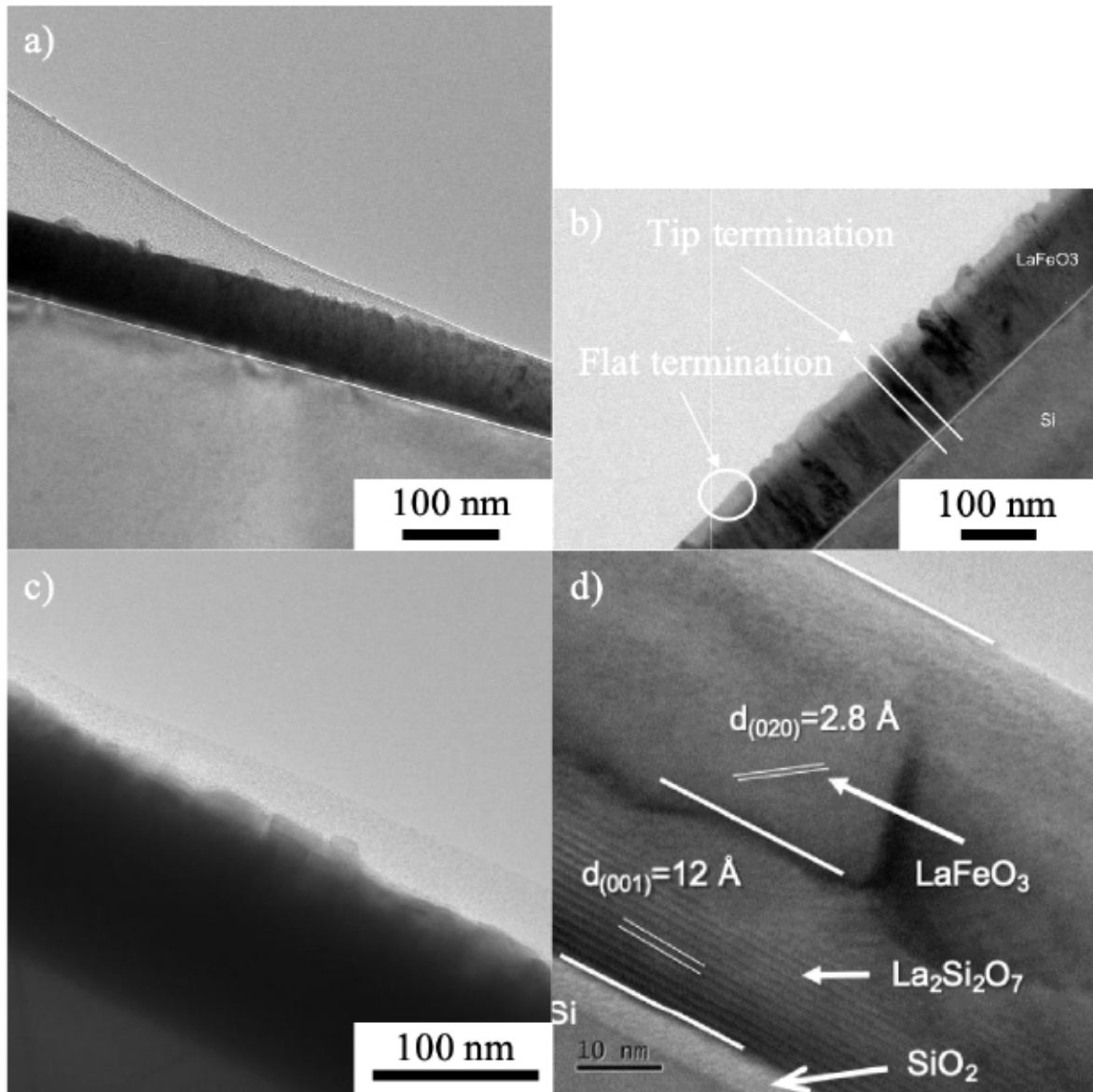


Figure 54. TEM Cross-section of a) LaFeO_3 -750-Si b) LaFeO_3 -850-Si c) LaFeO_3 -1000-Si d) LaFeO_3 -1000-Si

Grain termination is similar in 750°C and in 850°C. In lower temperatures, we can distinguish two morphologies, flat and sharp ended grains. Surface of both samples are covered with nanoclusters. Native SiO_2 layer is visible (5 nm) on Si substrate (see Figure 54d). Thickness of thin films is affected by deposition temperature. LaFeO_3 -750-Si have average thickness 85 nm (see Figure 54a) in areas free of nanocluster and around 105 nm in areas with nanocluster. Width of column with termination of “tip” is from 15 nm to 20 nm. As deposition temperature rise to 850°C thin film thickness is from 140 to 155 nm. The region with flat termination (see Figure 54a) has lower thickness around 140 nm and areas with sharp ended grains (see Figure 54b) up to 155 nm. Width of tips is in range from 20 nm to 45 nm.

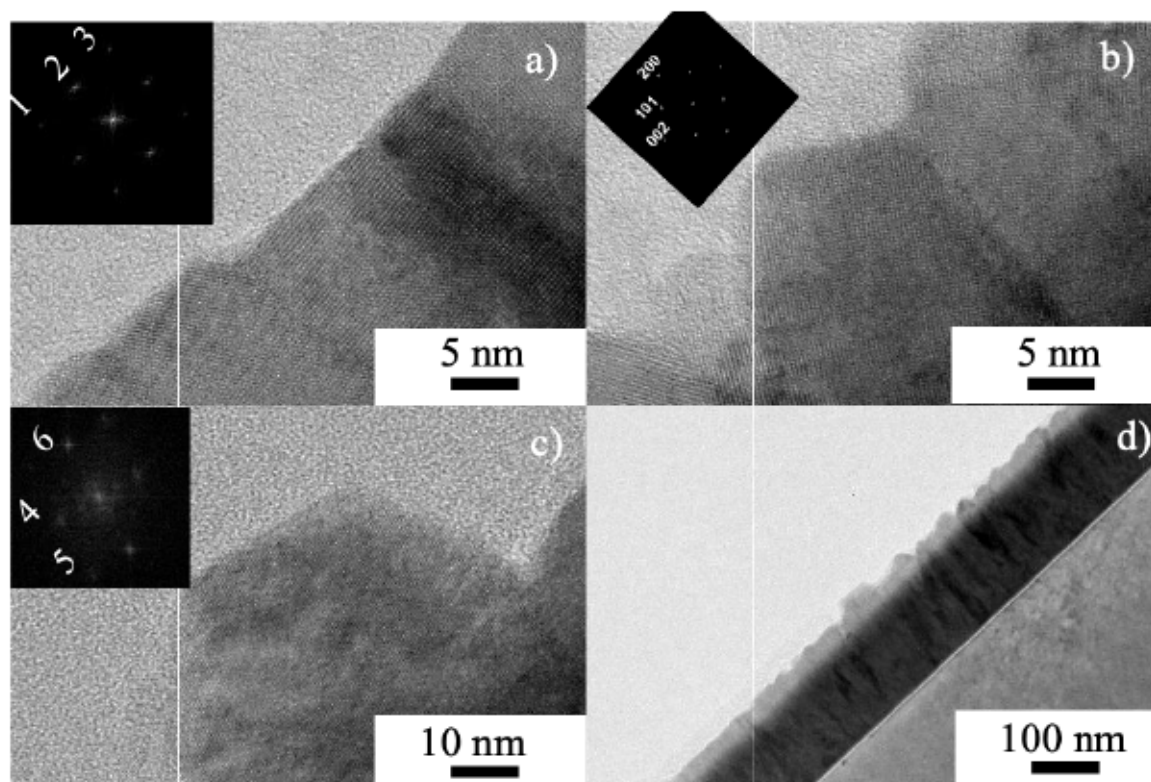


Figure 55. Cross-section of LaFeO₃-850-Si with FFT indexed in the Pnma setting a) flat termination, b) tip region, c) nanocluster d) surface morphology

Flat termination part of the grains consists in (101) planes, which are also parallel to the substrate (see Figure 55a). This means that grains with a [101] growth direction have flat termination with $\{101\}_o = \{001\}_c$ planes that will be exposed to gas. Grains with tip like termination have a [200] growth direction but $\{101\}$ planes build the tip (see Figure 55b). Again, mainly $\{101\}_o = \{001\}_c$ planes (101) will be exposed to gas. Both shapes of grains are built with the same crystallographic facets. HRTEM image along with EDS confirmed that nanocluster have the same chemical composition as thin films.

Table 27. FFT from LaFeO₃-850-YSZ95

Distance	Number	Plane	Figure
0.27	1	(002)	Figure 55a
0.39	2	(101)	
0.27	3	(200)	
0.39	4	(101)	Figure 55c
0.22	5	(022)	
0.29	6	(002)	

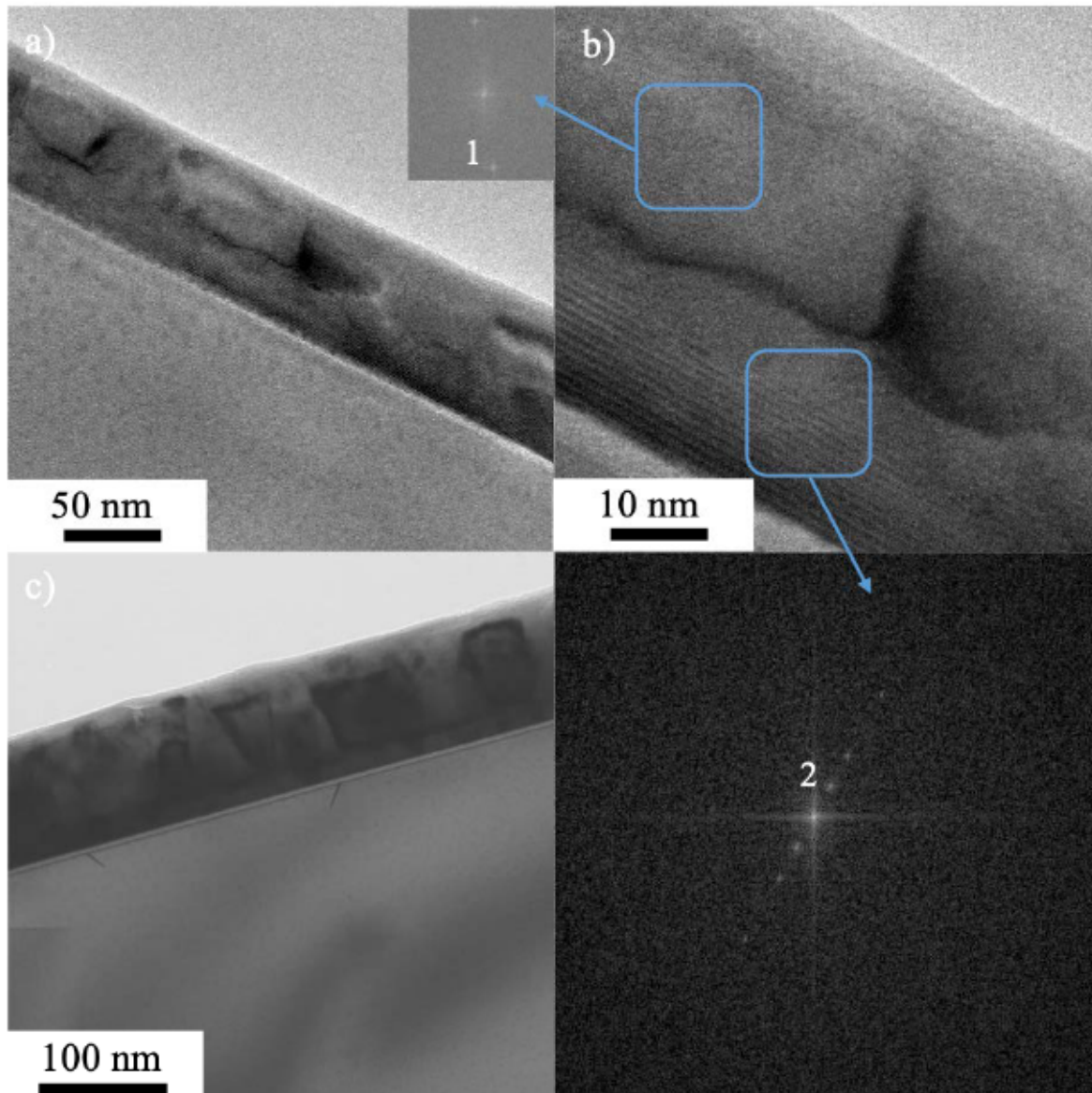


Figure 56. TEM Cross-section of LaFeO₃-1000-Si a) cross-section b) evidence of two phases in the thin film c) columns

The thin films deposited at 1000°C differs significantly from the samples deposited at lower temperatures. With temperature increase, the expected structure with the Thornton model belongs to zone 2, where $T/T_m = 0.54$. We did not observe column, the layer is divided into two zones: the first closer to the substrate, contains La₂SiO₇ (12 Å plane (001) in La₂SiO₇) (see Figure 56). The second part of the layer contains crystallographic planes in agreement with (200) or (002) reflection ($d_{hkl} = 2.8$ Å) in a LaFeO₃ structure. A significant increase in grain size is also visible (see Figure 56b). La₂SiO₇ was found only in layer close to the substrate with thickness of 25 nm. La₂SiO₇ (001) plane is parallel to the substrate. As for LaCoO₃, it appears that 1000°C is not a suitable PLD temperature when the substrate is Si, because of the formation of lanthanum silicate.

Table 28. FFT of LaFeO₃-1000-Si

Distance (nm)	Plane	Number	Figure
0.28	LaFeO ₃	1	Figure 56b
0.12	La ₂ SiO ₇	2	Figure 56a

4.2.2 LaFeO₃ thin films on C-YSZ (100) substrate

The X-rays diffraction patterns of LaFeO₃ thin films deposited on YSZ95, are shown in Figure 57. Recording was made with a grazing incidence angle of $\alpha = 0.7^\circ$, 1° and 3° . To identify phase composition, database JCPDS was used with card number LaFeO₃ (01-074-220). The effective penetration depth is $z = 89.5$ nm for $\alpha = 1^\circ$.

The comparison of obtained XRD patterns shows that the XDR pattern of thin films deposited at 1000°C is different from the two others. In LaFeO₃-750-YSZ95 and the LaFeO₃-850-YSZ95 the most intense peak at $2\theta = 32^\circ$ is consistent with a (121) peak in the LaFeO₃ structure (see Figure 57a-b). For a deposition temperature of 1000°C, the intensity of (101) peak increases greatly in comparison to intensity of (121) peak, indicating a possible modification of texture. In thin film deposited at 1000 °C additional La₂O₃ peaks are present, thus this film is clearly not a single phase. The LaFeO₃-YSZ95 XRD patterns were analyzed with MAUD software. Cell volumes were calculated thank to MAUD and are given in Table 30. Cell volume decreases slightly from to 248.32 Å³ to 242.5926 Å³ for samples deposited at 850°C and 1000°C. For sample LaFeO₃-750-YSZ95 the cell volume is somewhat smaller than for LaFeO₃-850-YSZ95. The high computation error for LaFeO₃-750-YSZ95 can be caused by low incident angle $\alpha = 0.7^\circ$ and lower penetration depth. The cell parameters and cell volume for LaFeO₃-850-YSZ95 and LaFeO₃-750-YSZ95 are significantly higher than those given in literature for stoichiometric LaFeO₃; this could be due to iron vacancies.

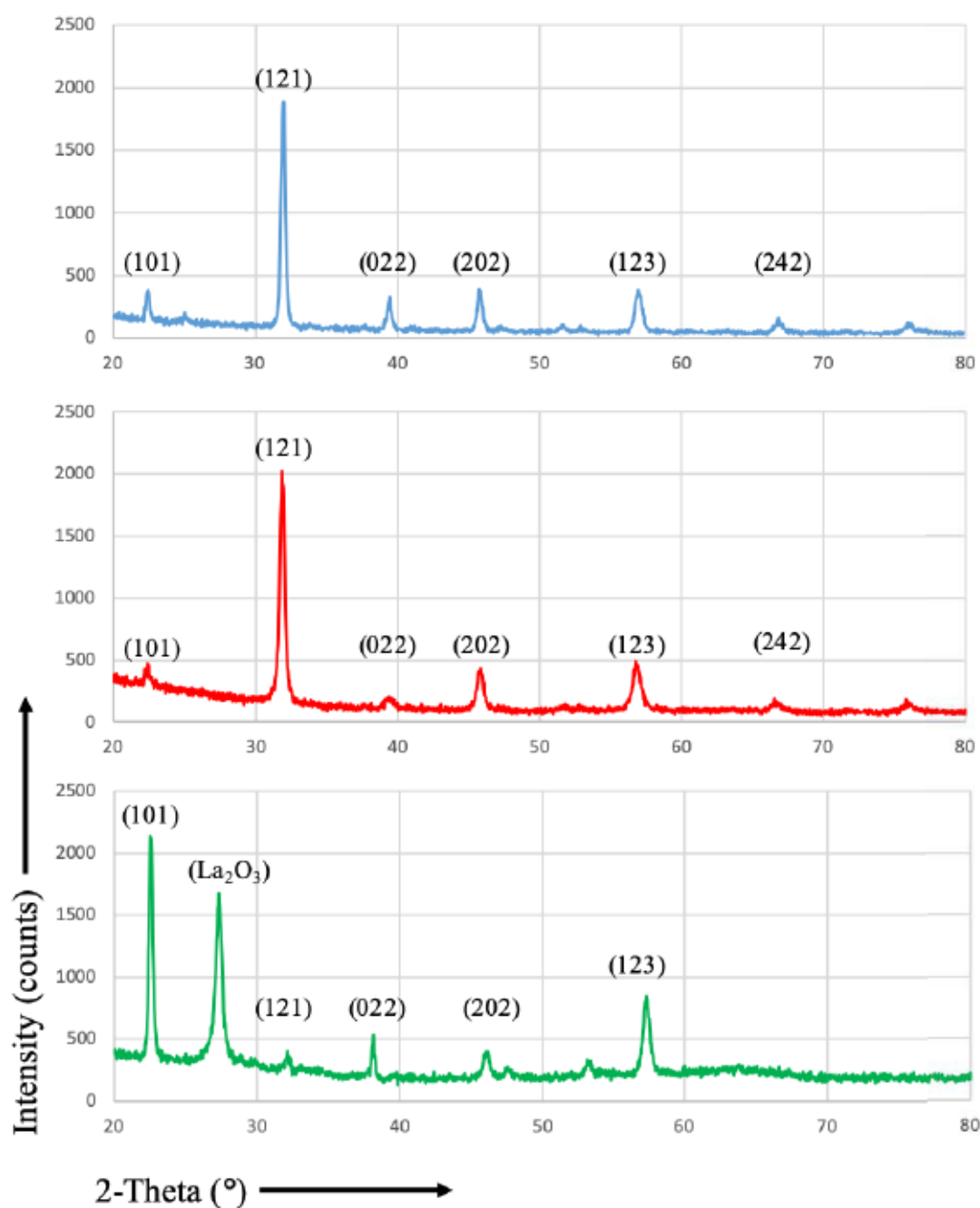


Figure 57. X-Ray Diffraction patterns indexed in the Pnma setting of a) LaFeO_3 -750-YSZ95 b) LaFeO_3 -850-YSZ95 c) LaFeO_3 -1000-YSZ95

Table 29. MAUD refinement results of LaFeO_3 -YSZ95

Sample name	a (Å)	b (Å)	c (Å)	Vol (Å ³)	R _{exp} / R _{wp}	Crystal size (nm)
LaFeO_3 -750-YSZ95	5,5936	5,5881	7,9219	247,6216	10,40/12,37	32
LaFeO_3 -850-YSZ95	5,6227	5,5826	7,9111	248,3216	8,18/9,89	40
LaFeO_3 -1000-YSZ95	5,5132	5,5772	7,8897	242,5926	5,68/10,54	x

The surface morphology of LaFeO_3 -750-YSZ95 and LaFeO_3 -850-YSZ95 are similar to those observed on LaFeO_3 deposited on Si at the same temperatures (see Figure 58). We observed many nanoclusters and grains with a sharp and flat end.

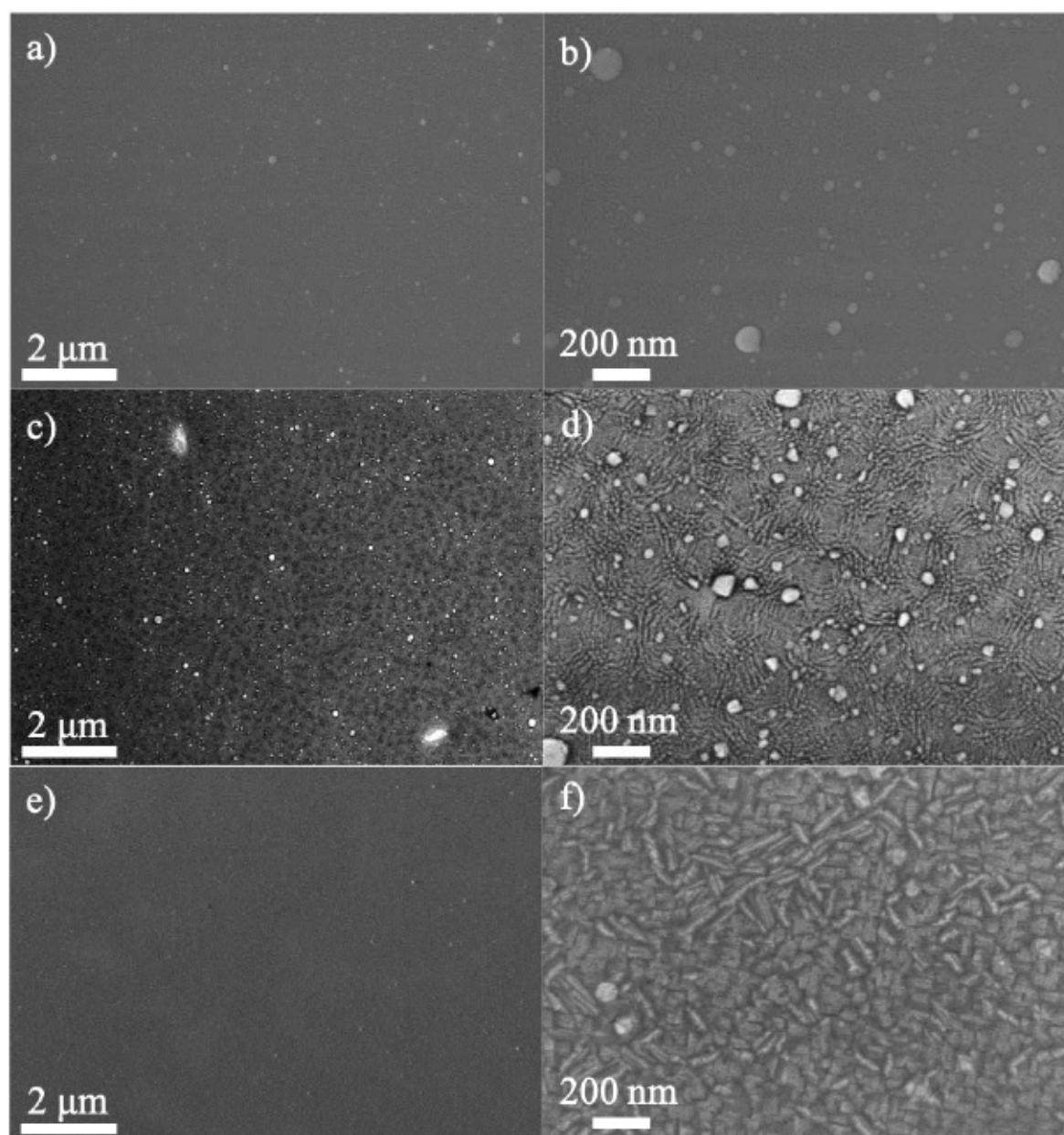


Figure 58. SEM micrographs of a) LaFeO_3 -750-YSZ95 b) LaFeO_3 -750-YSZ95 c) LaFeO_3 -850-YSZ95 d) LaFeO_3 -850-YSZ95 e) LaFeO_3 -1000-YSZ95 f) LaFeO_3 -1000-YSZ95

On YSZ substrate, nanoclusters are much more frequent than in thin films deposited on Si. This can be related to the fact that YSZ being a poor thermal conductor, the effective temperature of the YSZ is lower than the effective temperature of Si, favoring the formation of nanoclusters at the end of the deposition process. On surface of LaFeO_3 -1000-YSZ95, we also can observe some rare nanoclusters of small size (~ 50 nm). We can conclude that substrate have strong

influence on morphology of thin films deposited at 1000°C. On C-YSZ substrate, LaFeO_3 grains are in form of needles with square shape grains (see Figure 58e-f), as for the Si substrate, grains have a rounded shape (see Figure 51f)

Topography of thin films are presented in Figure 59, there are no significative difference in morphology between thin films deposited at 750°C and 850°C.

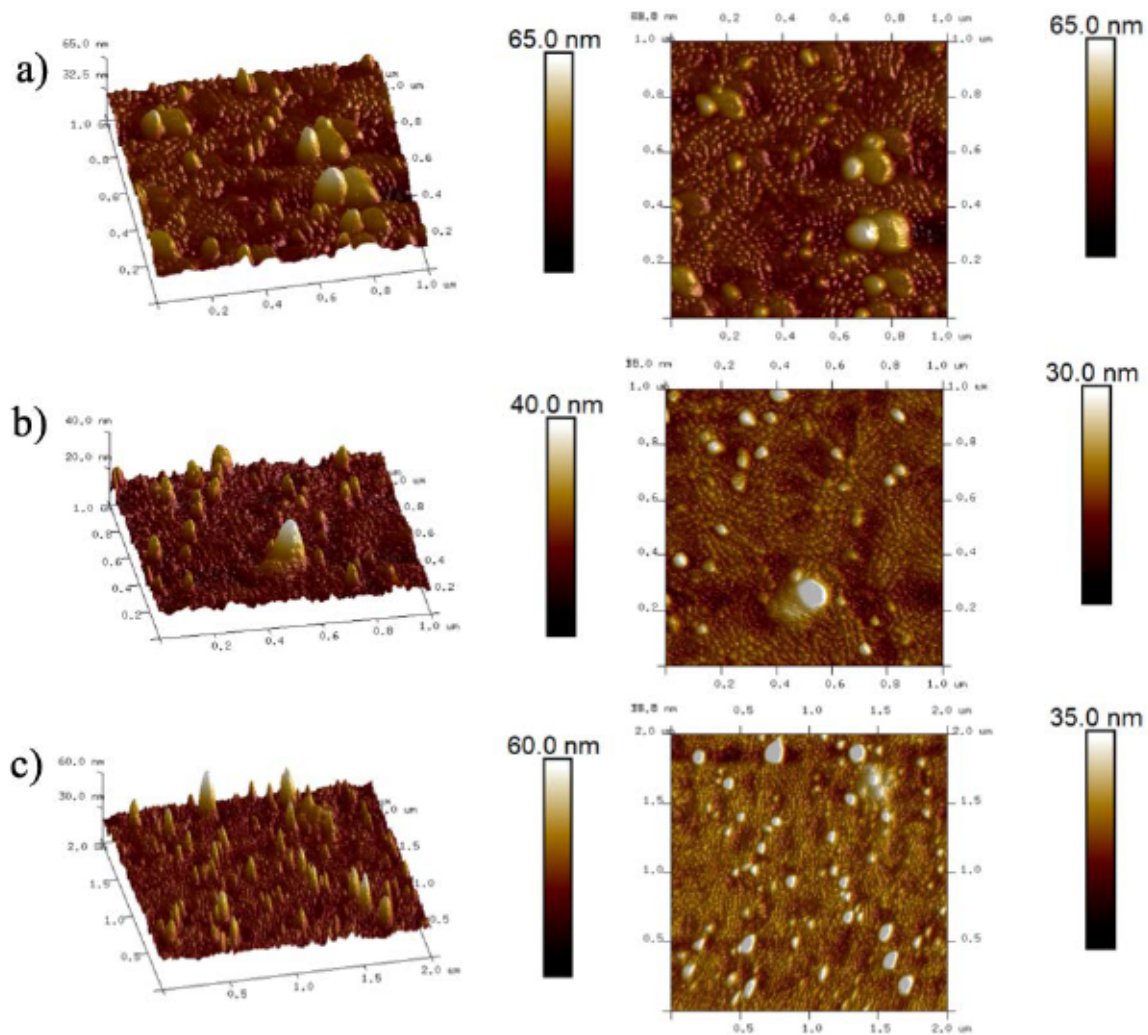


Figure 59. AFM of a) LaFeO_3 -750-YSZ95 b) LaFeO_3 -850-YSZ95 c) LaFeO_3 -1000-YSZ95.

Base on this results roughness parameters were calculated (see Table 30). All parameters were calculated in regions free of nanoclusters to allow a better comparison of the results. Thin film obtained at 850°C have R_a parameter of 1.34 nm that is higher for thin films deposited at 750°C ($R_a = 1.19$ nm). Increase in roughness is caused by increase of height tip and flat regions reduction.

Table 30. Roughness parameters of LaFeO₃-YSZ95

Sample	R _a (nm)	R _{max} (nm)	R _q (nm)
LaFeO ₃ -750-YSZ95	1.19	16.7	1.74
LaFeO ₃ -850-YSZ95	1.34	10.2	1.67
LaFeO ₃ -1000-YSZ95	1.08	9.79	1.38

In order to determine the oxidation state of La, Fe, and O X-ray Photoelectron Spectroscopy (XPS) was used. First analysis was carried out directly on the thin film surface. After this first analysis, samples were sputtered using the Ar ions; XPS analysis was then immediately carried out. This process was repeated until the substrate was reached. Each cycle of sputtering was carried out with the same parameters: an Ar energy of 2.5 keV, an ion current of 1.14 mA and a sputtered area 1×1 mm². Atomic concentration as function of depth is presented in Figure 60. The speed of material removal is constant whatever the sample. Hence, we can gain information about thin films thickness and thin film composition with depth. LaFeO₃-750-YSZ95 is the thinnest from all 3 samples (see Figure 60). After passing 5 minutes of sputtering we can observe signal from substrate. For sample deposited at 850°C, substrate was reached after 10 minutes of sputtering. The thickest film was LaFeO₃-1000-YSZ95 (15 minutes to reach the substrate by sputtering). Content of La and Fe in the thin film are homogeneous under the surface. On the surface, we often detect pollution (carbon). Atomic concentration of La and Fe in ideal LaFeO₃ should be equal to (50/50). XPS results showed that deposited thin films are non-stoichiometric with lower Fe content.

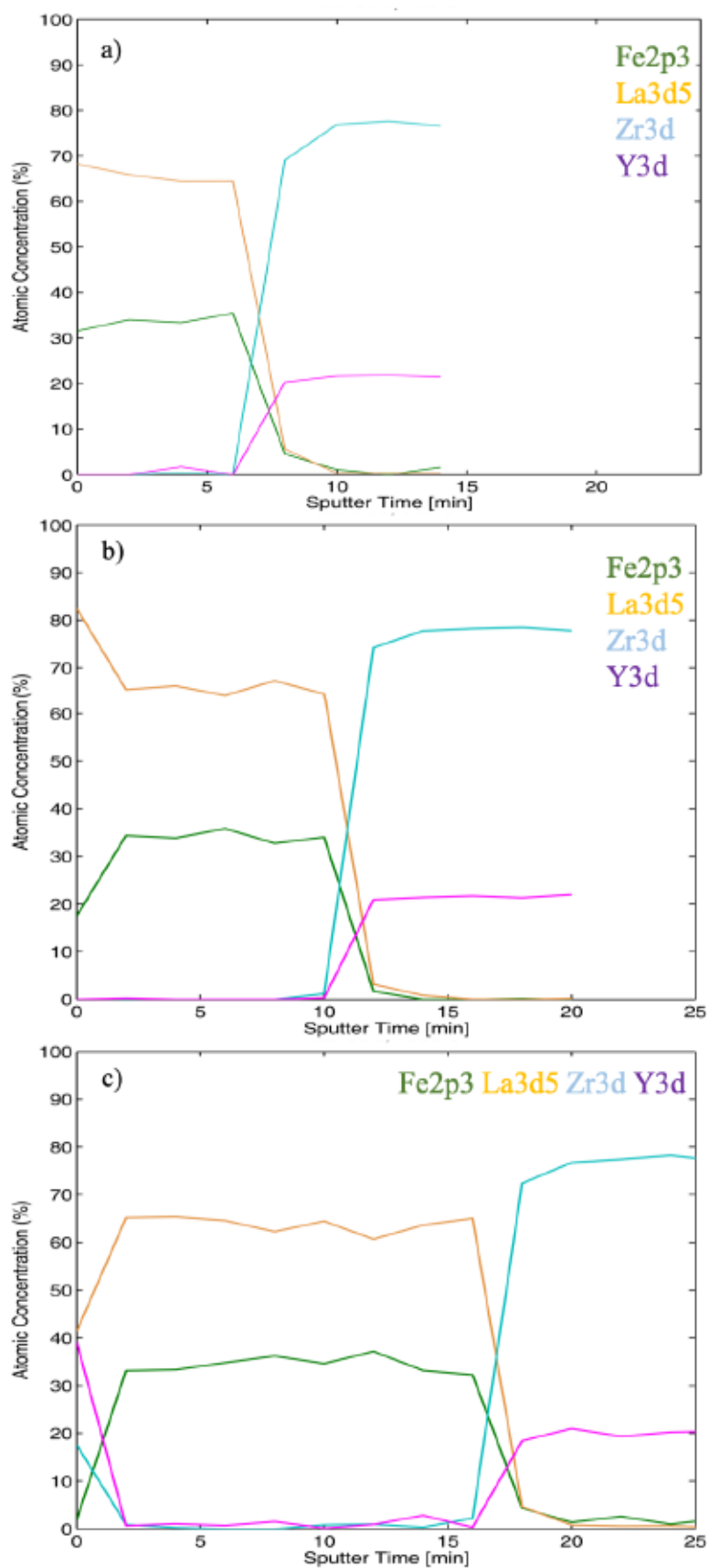


Figure 60. XPS Spectra – a) Atomic concentration in LaFeO3-750-YSZ95 profile b) Atomic concentration in LaFeO3-850-YSZ95 c) Atomic concentration in - LaFeO3-1000-YSZ95

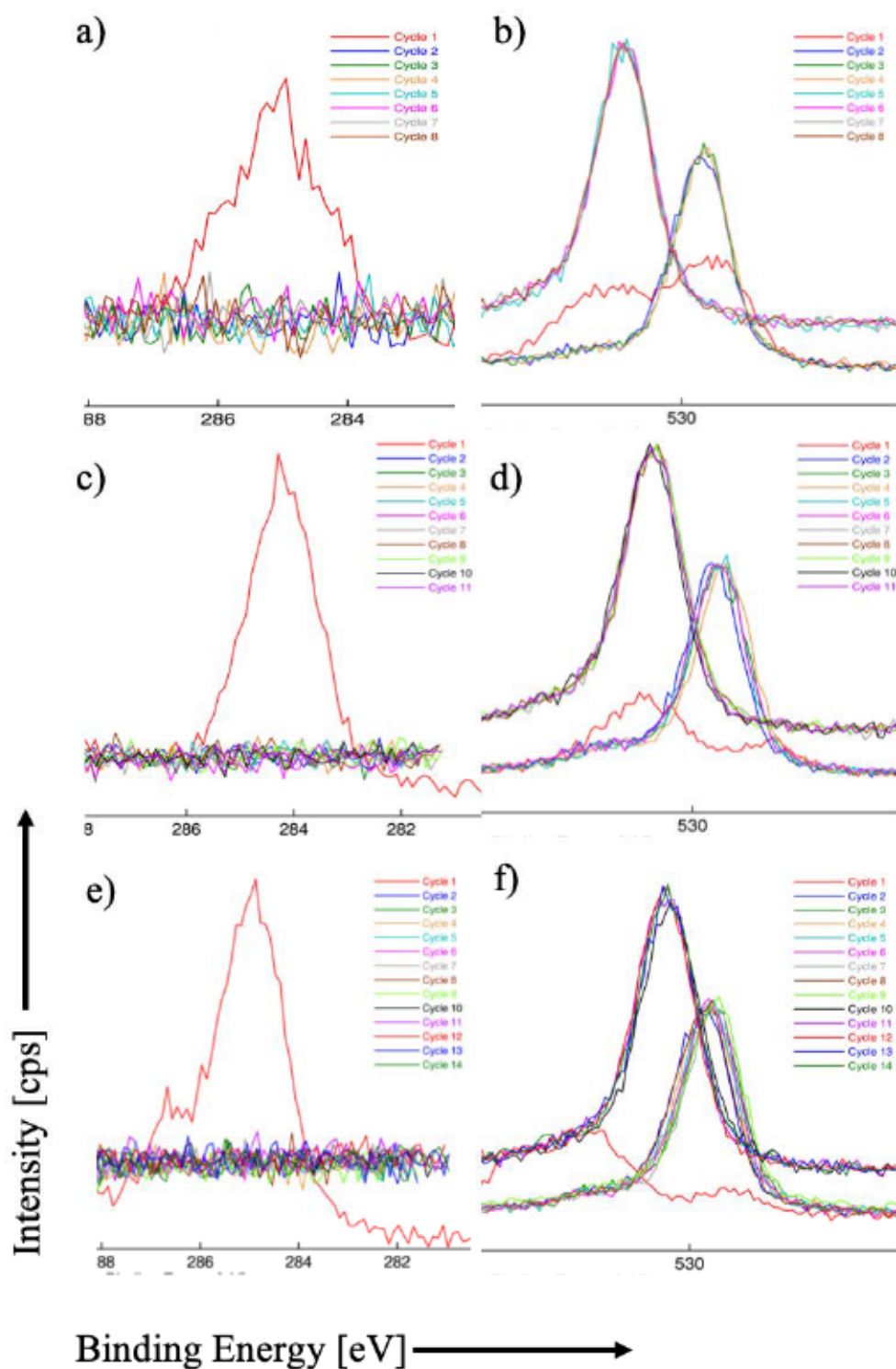


Figure 61. XPS Analysis of a) C 1s LaFeO₃-750-YSZ95 b) O 1s LaFeO₃-750-YSZ95 c) LaFeO₃-850-YSZ95 C 1s d) LaFeO₃-850-YSZ95 O 1s e) LaFeO₃-1000-YSZ95 C 1s e) LaFeO₃-1000-YSZ95 O 1s

In all samples, spectra of C 1s is observed only on the surface after 1st cycle of sputtering C 1s spectra disappears (see Figure 61). Lines of O 1s were registered on the surface (cycle 1), in the

thin film (cycles 2-9) and on the substrate (cycles 10-14). Spectra from the first cycle has band energy of BE = 531 – 533 eV. This energy is typical for oxygen in organic bond C=O [119]. The bonding energy in the layer is BE = 529.6 eV and is typical for oxygen in metal oxides in this case in LaFeO₃. After 10 cycles, BE for O 1s changed to the value BE = 530.9 eV. This bonding energy is near to the value of oxygen in ZrO₂. XPS spectra of La present two main peaks corresponding to La 3d_{3/2} and 3d_{5/2}.

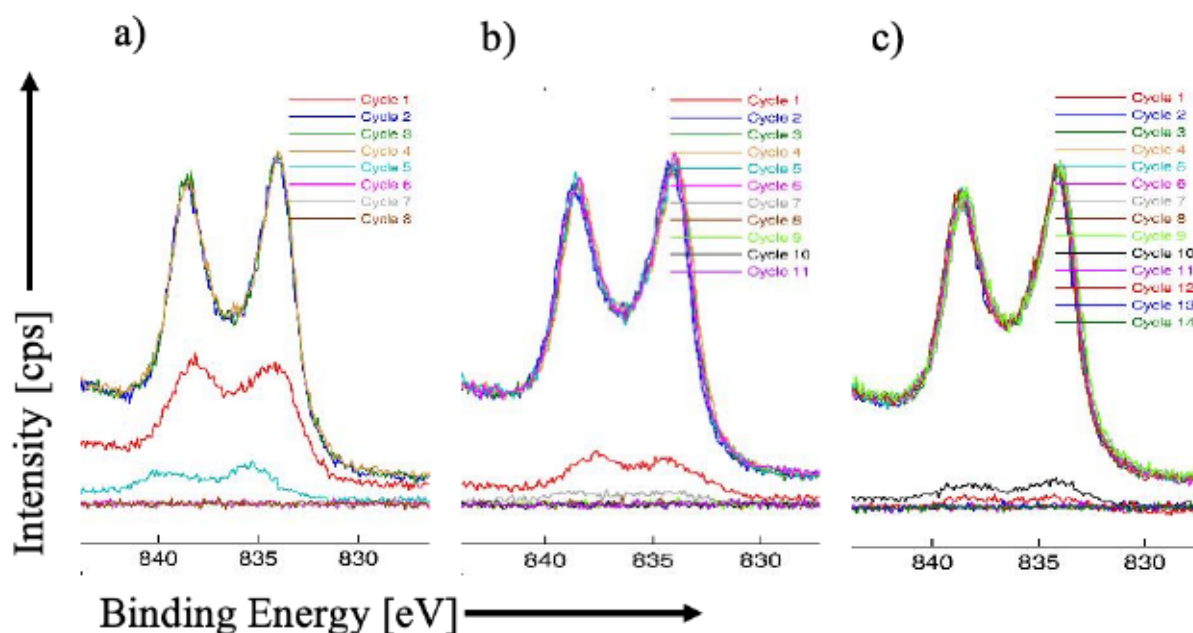


Figure 62. XPS Analysis of La 3d of thin films LaFeO₃-750-YSZ95 a) 750 °C b) 850 °C c) 1000 °C

The position and shape of the La 3d_{5/2} spectra are constant across the thin film (see Figure 62). the difference in shape and intensity of the spectra during surface analysis can be explained by presence of surface contamination. Peak broadening can be correlated with thin film stoichiometric; peak width increases with the number of structure defects. The La 3d_{5/2} spectrum consists of the main line at 834.3 eV and the satellite line at 838.2 eV. These values are typical for rare earth oxygen bonding energies [120]. Lanthanum in La₂O₃ phase is in the same oxidation state as in LaFeO₃; this means that XPS analysis is not the proper tool to detect the presence of La₂O₃ phase. When La is on 3rd oxidation state, peak at 834 eV is higher than peak at 838.2 eV and ΔE is close to 4.6 eV. This correlation and value of ΔE is observed in our XPS spectra of La.

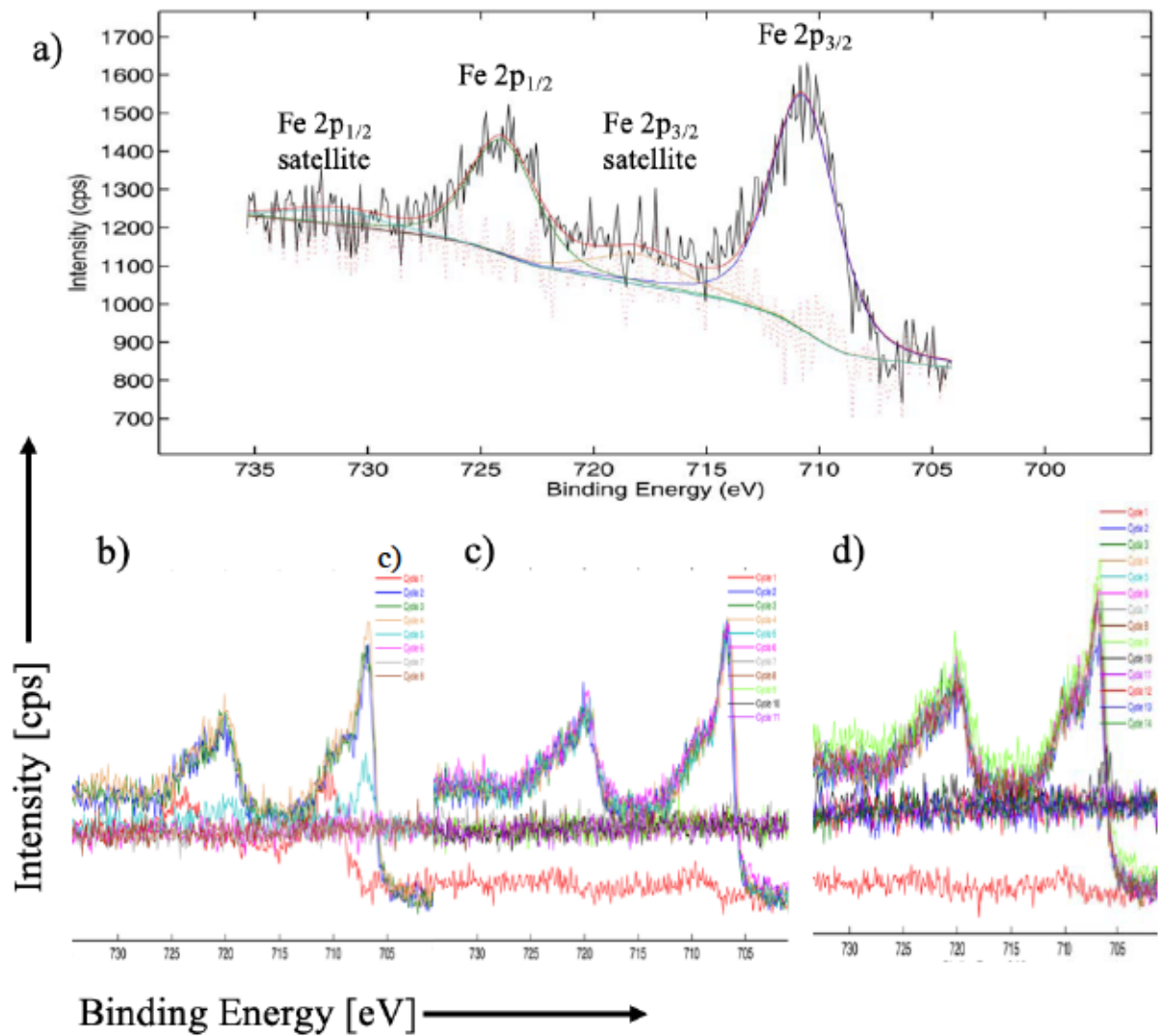


Figure 63. XPS results a) The Fe 2p spectrum obtained from the as received surface (before sputtering). b) LaFeO₃_750_YSZ95 c) LaFeO₃_850_YSZ95 d) LaFeO₃_1000_YSZ95

In the Figure 63, a XPS spectrum of non-sputtered LaFeO₃-750-YSZ is presented (see Figure 63) as well as sputtered LaFeO₃-T-YSZ (see Figure 63b-d). The effective oxidation state of iron can be found only from their initial spectra not from ion sputtered samples. Ion sputtering causes the so called "sputter induced" partial reduction of the oxidation states the Fe [121]. Two main peaks are present of Fe 2p_{3/2} at ~710,7 eV and Fe 2p_{1/2} peak at ~718.0 eV which indicates the oxidation state of Fe³⁺ [26]– [28]. Satellite peaks are also present at 717.5 eV for Fe 2p_{3/2} and 732.5 eV for Fe 2p_{1/2}. The occurrence of these satellites indicates the presence of Fe⁴⁺ in our sample; however, the small surface under the peaks also indicates a low concentration of this ions, Fe⁴⁺.

According to [27], all the Fe cations in the Fe depth profile of the oxidized sample are initially present in the trivalent state. Appearance of Fe as metallic in the depth of the thin films is due

to the preferential sputtering of oxygen and a corresponding change in oxidation state of the Fe cations during ion bombardment. After sputtering we can observe peaks shift towards lower binding energies and appearance of peak at 706 eV (see Figure 63b-d). From 2nd cycle, we can observe spectra typical for metallic iron at BE=706,7 eV. Beyond from this peak, the peak at 710.7 eV is still visible. Figure 63b-d show the photoelectron spectra for Fe 2p_{3/2} and Fe 2p_{1/2} obtained after different times of sputtering.

The next step of experiments involved TEM observations. A summary of TEM images is presented in Figure 64 for LaFeO₃-750-YSZ95, in Figure 65 for LaFeO₃-850-YSZ95 and in Figure 66 for LaFeO₃-1000-YSZ95. Cross section samples were prepared by FIB, hence the platinum coating that can be seen in TEM images. All LaFeO₃ thin films deposited on YSZ95 have columnar structure (see Figure 64–Figure 66). Homogenous columns are growing directly from substrate up to the surface. For all temperatures, thin film is free from cracks and pores. Nanoclusters are visible on surface (see Figure 66a) of LaFeO₃-750-YSZ95 and LaFeO₃-850-YSZ95 (see Figure 65–Figure 66).

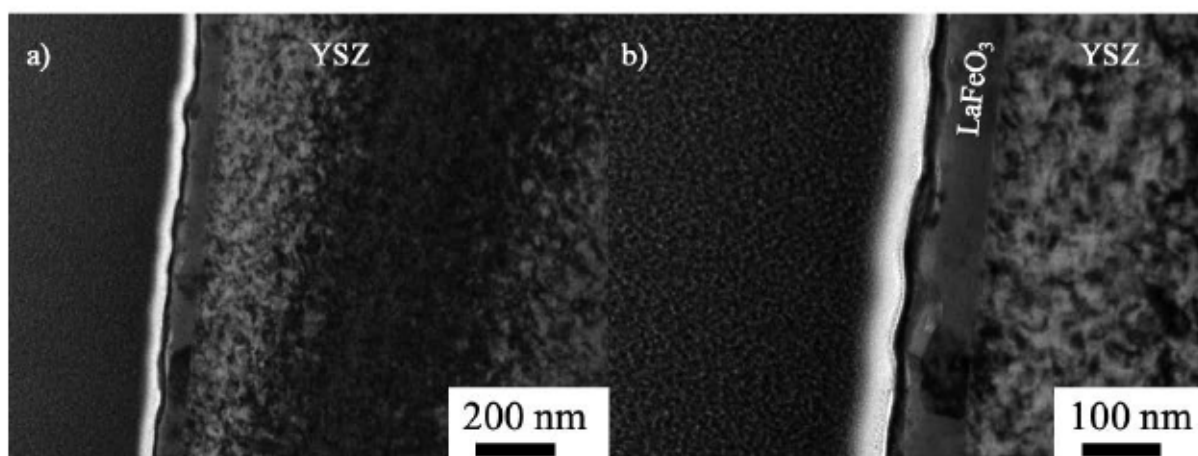


Figure 64. TEM image of LaFeO₃-750-YSZ95

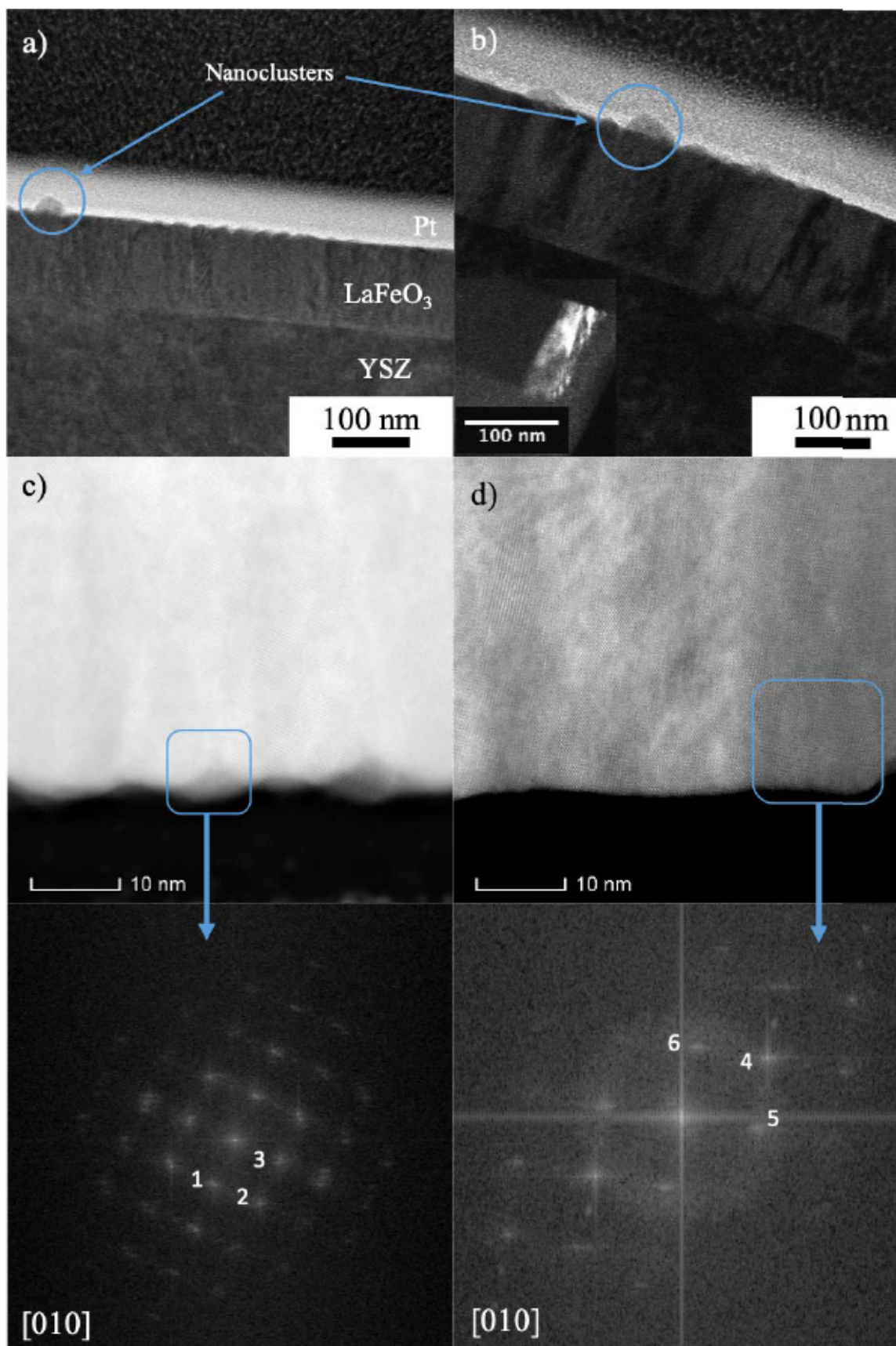


Figure 65. TEM images of LaFeO₃-850-YSZ95. a) evidence of flat and pointed grain termination b) columnar structure of the grain c) STEM-HAADF image of a "pointed" region along with FFT d) STEM HAADF image of a flat region along with FFT

Thin film deposited at 850°C on YSZ95 has thickness of 110 nm in region free from nanoclusters. Height of nanocluster is about 20 nm. Width of columns is 40 nm. The termination of columns is flat or pointed. According to the FFT analysis, the only phase present is LaFeO₃.

The FFT shown in Figure 65 indicates that (101)_o = (001)_c planes are parallel to the flat termination of the grain, and also built the side of the tipped grain, as for films grown on Si.

Table 31. FFT of LaFeO₃-850-YSZ95

Distance (nm)	Plane	Number	Fig.
0.39	(101)	1	81 c
0.29	(200)	2	
0.39	(10-1)	3	
0.28	(200)	4	81 f
0.39	(101)	5	
0.39	(10-1)	6	

As observed in XPS, thin film deposited at 1000°C has the thickest LaFeO₃ layer of all samples deposited on YSZ95. Thin film deposited at 1000°C have thicknesses up to 210 nm in rough zone and in flat zones the thickness is around 185 nm (see Figure 66a). Homogenous columns are growing directly from substrate up to the surface, no division of thin film is visible like in sample on Si. Hence, no reaction between YSZ and LaFeO₃ layer occurs, even at 1000°C deposition temperature. Columns have width up to 75 nm (see Figure 66b). Shape of columns termination can be observed in Figure 66b. All distances calculated from FFT came from LaFeO₃ (see Table 32). The indexation of the FFT indicate a growth direction of [200] and (101) or (10-1) planes exposed to gas (see Figure 66c). Again, the exposed planes are the ones of the {101} family, that is to say the {100} of the cubic perovskite cell.

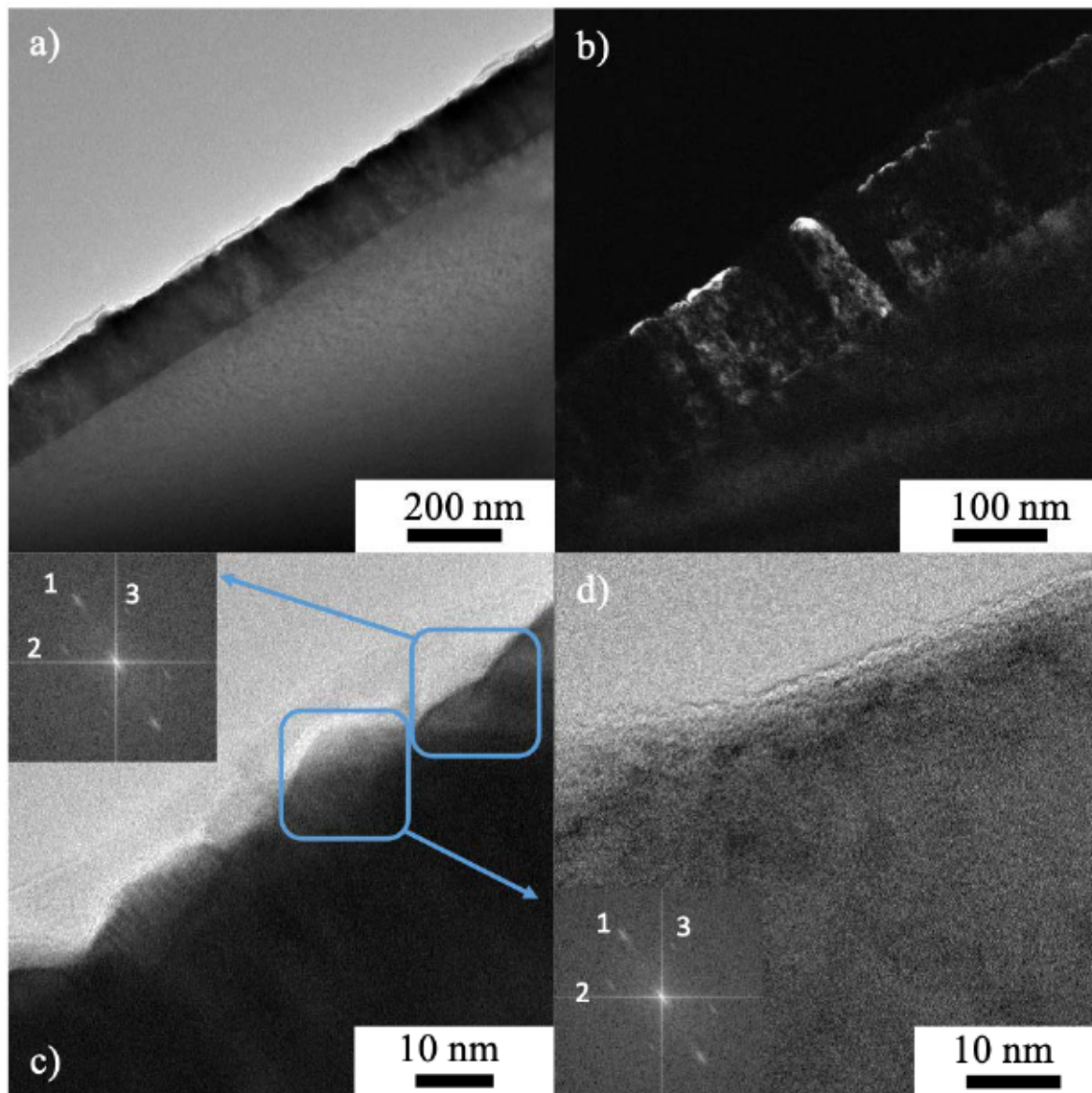


Figure 66. TEM images of LaFeO₃-1000-YSZ95. a) low magnification image showing the microstructure of the thin film. b) Dark field image showing the columnar structure of the layer. c) high magnification image showing pointed grain termination, with the corresponding FFT, d) high magnification image showing pointed grain termination, with the corresponding FFT

Table 32. FFT results of LaFeO₃-1000_YSZ95

Distance (nm)	Plane	Number
0.28	(200)	1
0.39	(101)	2
0.39	(10-1)	3

4.2.3 LaFeO₃ thin films on T-YSZ substrate

The T-YSZ substrate is polycrystalline with grains about 100 – 400 nm in size and is flexible, contrary to the two other substrates. On this surface was deposited thin films. The X-rays diffraction patterns of LaFeO₃ thin films on YSZ35, are shown in Figure 67. Diffractions patterns consist in peaks from the substrate and LaFeO₃. Substrate YSZ35 crystallize in a tetragonal crystal system but a monoclinic YSZ35 phase can be also observed. Penetration depth for LaFeO₃ with incident angle of $\alpha = 1^\circ$ is 89.5 nm. The fact that peaks from the substrate are observed indicates that thin films thickness is lower than penetration depth for both temperatures of deposition.

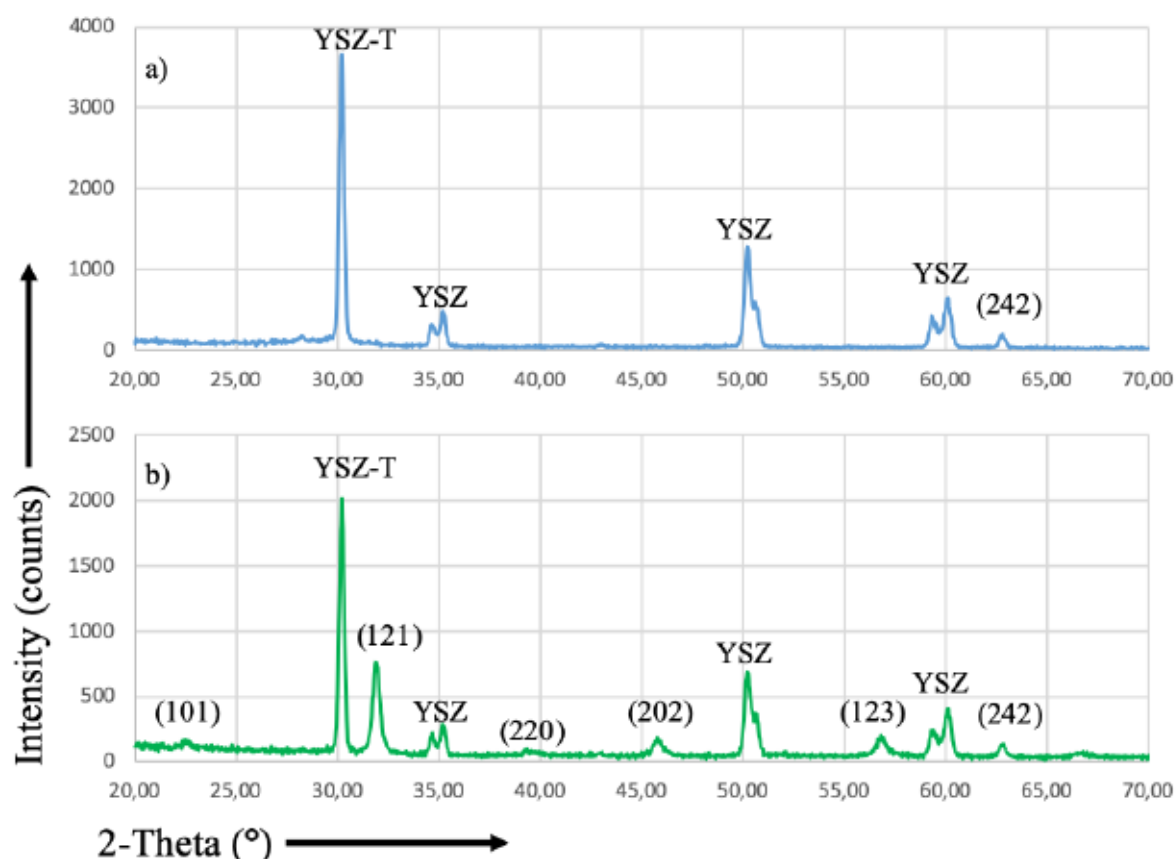


Figure 67. X-Ray Diffraction patterns of a) LaFeO₃-750-YSZ35 b) LaFeO₃-850-YSZ35

Intensity of LaFeO₃ peaks in thin film deposited at 850°C is much higher than in sample LaFeO₃-750-YSZ95. Based on those results, we can assume that with increase of temperature thin film thickness also increase. The XRD pattern of LaFeO₃-750-YSZ35 is mainly from the substrate and contains only two very low intensity (121) and (242) peaks of LaFeO₃ indicating

a very thin layer. Thin film deposited at 850°C has its most intense peak for the (121) reflection like it was the case in other thin films on Si and YSZ95.

On SEM micrographs (see Figure 70) we can observe similar topography to the one obtained for LaCoO₃-YSZ35, with large substrate grains covered by thin films at each temperature. Nanocluster are present at each temperature; they are frequent but smaller than those obtained on YSZ95 and Si.

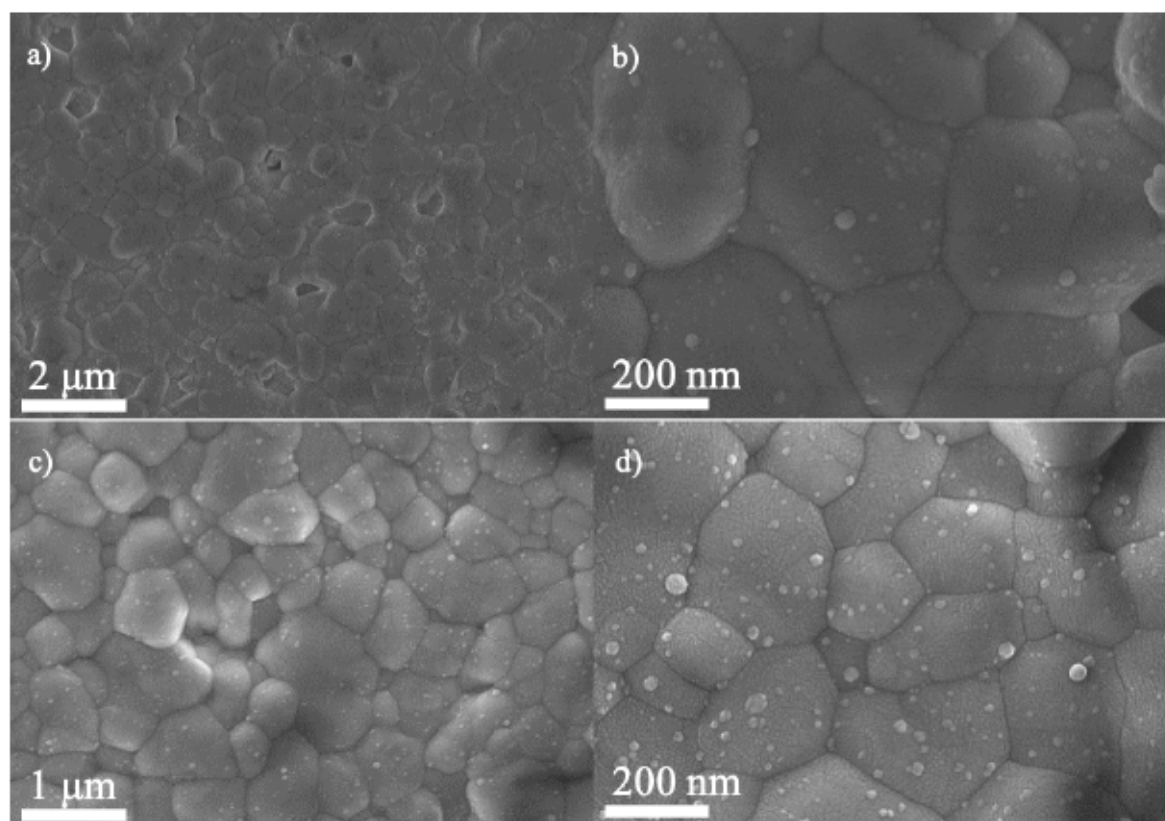


Figure 68. SEM micrographs of a) LaFeO₃-750-YSZ35 b) LaFeO₃-750-YSZ35 c) LaFeO₃-850-YSZ35 d) LaFeO₃-850-YSZ35

At higher magnification (see Figure 71) we can observe the shape of the small grains of LaFeO₃ thin films. Morphology can be divided in two regions “flat” and pointed as it was the case for LaFeO₃-850-Si (see Figure 51)

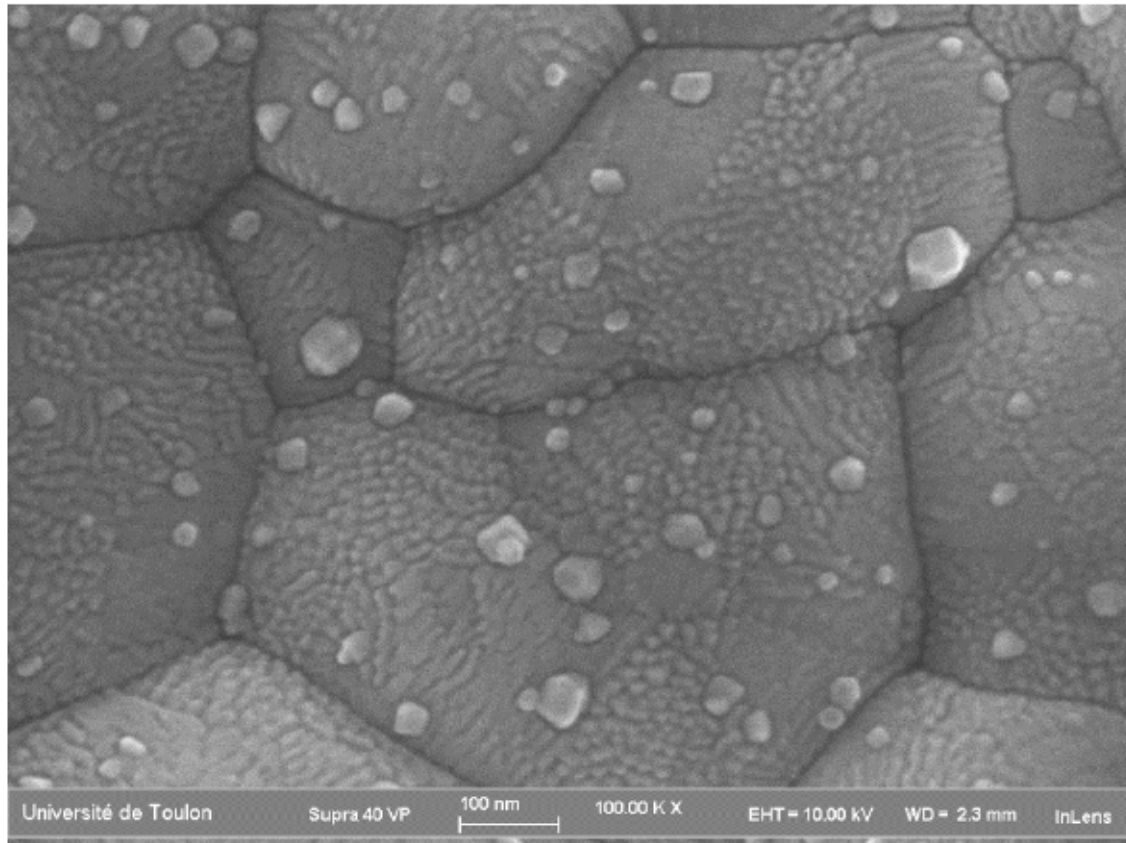


Figure 69. High magnification SEM micrograph of LaFeO₃-850-YSZ35

Each grain of YSZ35 is completely covered by nanometric grains of LaFeO₃ (see Figure 69), despite the bumpy surface of the substrate. Grain boundaries of YSZ are clearly visible.

To analyze roughness parameters, AFM technique was used (see Figure 70).

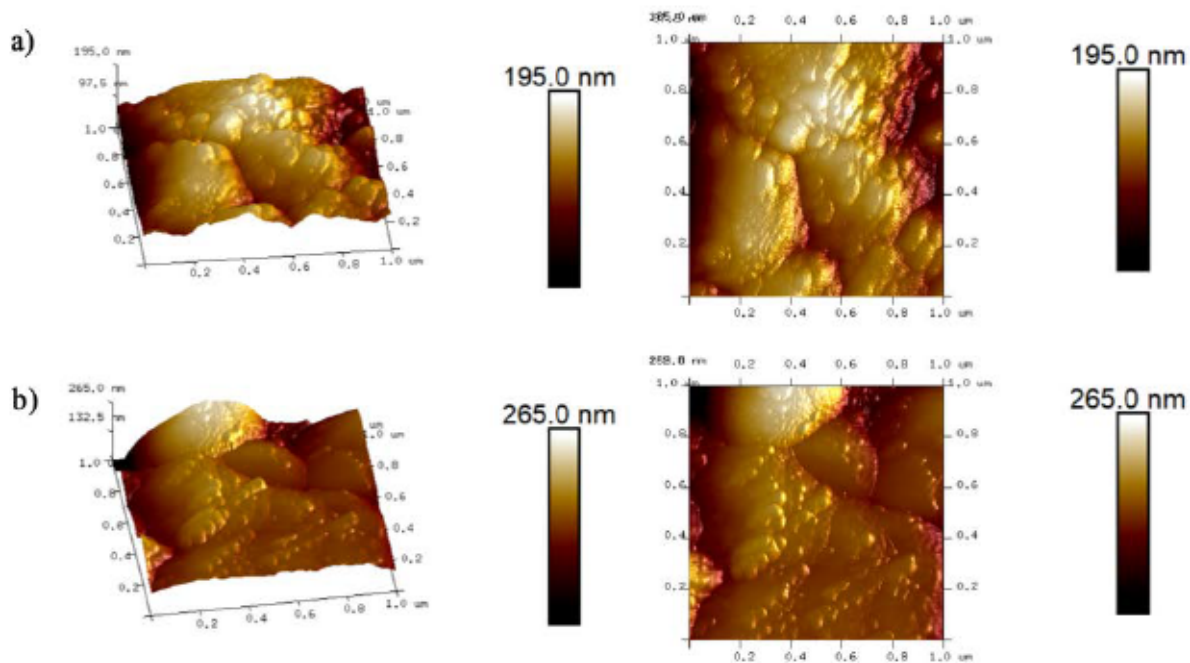


Figure 70. AFM of a) LaFeO₃-750-YSZ35 b) LaFeO₃-850-YSZ35

LaFeO₃ grains have similar shape in 750°C and in 850°C. Due to high roughness of substrate comparison of roughness parameters of LaFeO₃-YSZ35 thin films with thin films deposited on Si and YSZ95 is not possible. However, influence of process temperature is possible to determine. As observed in SEM, LaFeO₃-750-YSZ35 and LaFeO₃-850-YSZ35 surfaces exhibit small nanoclusters. We calculate the roughness parameters R_{max} , R_a and R_q , on regions without clusters. All results are presented in Table 33. R_a parameter is depended on temperature. With increase of process temperature R_a parameter also increases. This phenomenon was observed in all previous samples.

Table 33. Roughness parameters of LaFeO₃-YSZ35

Sample	R_a (nm)	R_{max} (nm)	R_q (nm)
LaFeO ₃ -750-YSZ35	37,3	412	50,4
LaFeO ₃ -850-YSZ35	46,2	324	56,4

Only LaFeO₃-850-YSZ35 was observed by TEM (see Figure 71), the other characterization technics having shown a too thin LaFeO₃ layer for LaFeO₃-750-YSZ35.

As we can observe in Figure 71a, the roughness of T-YSZ substrate is much higher than for Si or YSZ95, but the LaFeO₃ layer is homogeneously covering the substrate grain, with a nearly constant thickness of 105 nm. The LaFeO₃ grains present a columnar structure. Columns in this

samples have flat termination. FFT analysis (see Table 34) shows that the thin film contains only the LaFeO_3 phase

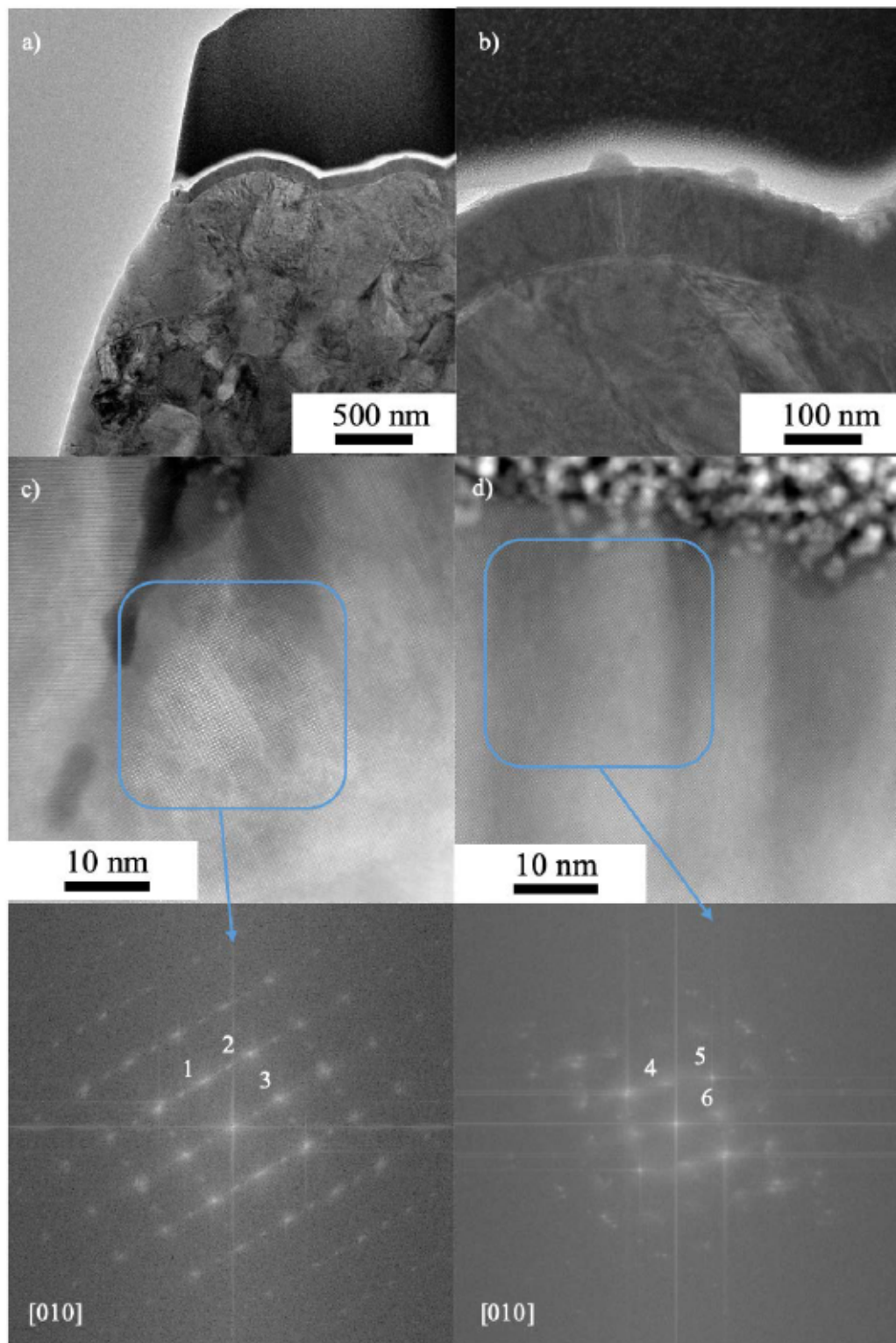


Figure 71. cross section TEM images of LaFeO_3 -850-YSZ35 a) low magnification image showing the homogeneous covering of the substrate b) droplets and columnar grains c) STEM-HAADF image of the layer at a grain boundary of the substrate along with FFT d) termination of LaFeO_3 grains along with FFT

. Concerning the orientation of LaFeO_3 grain, as for other substrates, one observes only (101) and (200) planes; however, to establish the growth direction and planes exposed to gas further investigations are needed. Micrographs obtained in TEM allows to measure thin film thickness which is 105 nm. As we can observe on Figure 71a surface of YSZ35 contains grains. Roughness of this substrate is much higher than Si or YSZ95. Grain are covered by thin film of LaFeO_3 with columnar structure. Columns in this samples have flat termination. FFT analysis show that thin film contains only LaFeO_3 phase (see Table 34).

Table 34. FFT of LaFeO_3 -850-YSZ35

Distance (nm)	Plane	Number
0.39	(10-1)	1
0.29	(120)	2
0.39	(101)	3
0.39	(10-1)	4
0.29	(120)	5
0.39	(101)	6

5 GAS MEASUREMENTS

From obtained results we can conclude that thin films with monocrystalline structure and highly developed surface are deposited at 850 °C and to a less extent at 750°C. After taking under consideration application of SE measurements were conducted only on thin films deposited at these temperatures on YSZ95 and YSZ35. First part determines described possibility of thin films application as SE in resistance gas sensor. Second part of this chapter is defining usefulness of proposed material as SE in electrochemical gas sensors. In both cases sensitivity towards NO₂ was tested.

4.3 RESISTANCE MEASUREMENTS

4.3.1 LaCoO₃

Deposited LaCoO₃-YSZ95 thin films were tested in the presence of NO₂ at a concentration from 2.5 ppm to 100 ppm in a temperature range: 25–550°C. The samples were placed in a cell. Before the first measurements the sample was heated to a temperature of 300°C with a continuous air flow for a period of 3 hours. The aim of this treatment was to clean the sample surface and the cell from contamination. In order to stabilize the measuring signal after reaching the assumed temperature, sample was held under voltage with air flow for the time needed to obtain a stable base line signal (R_{air}).

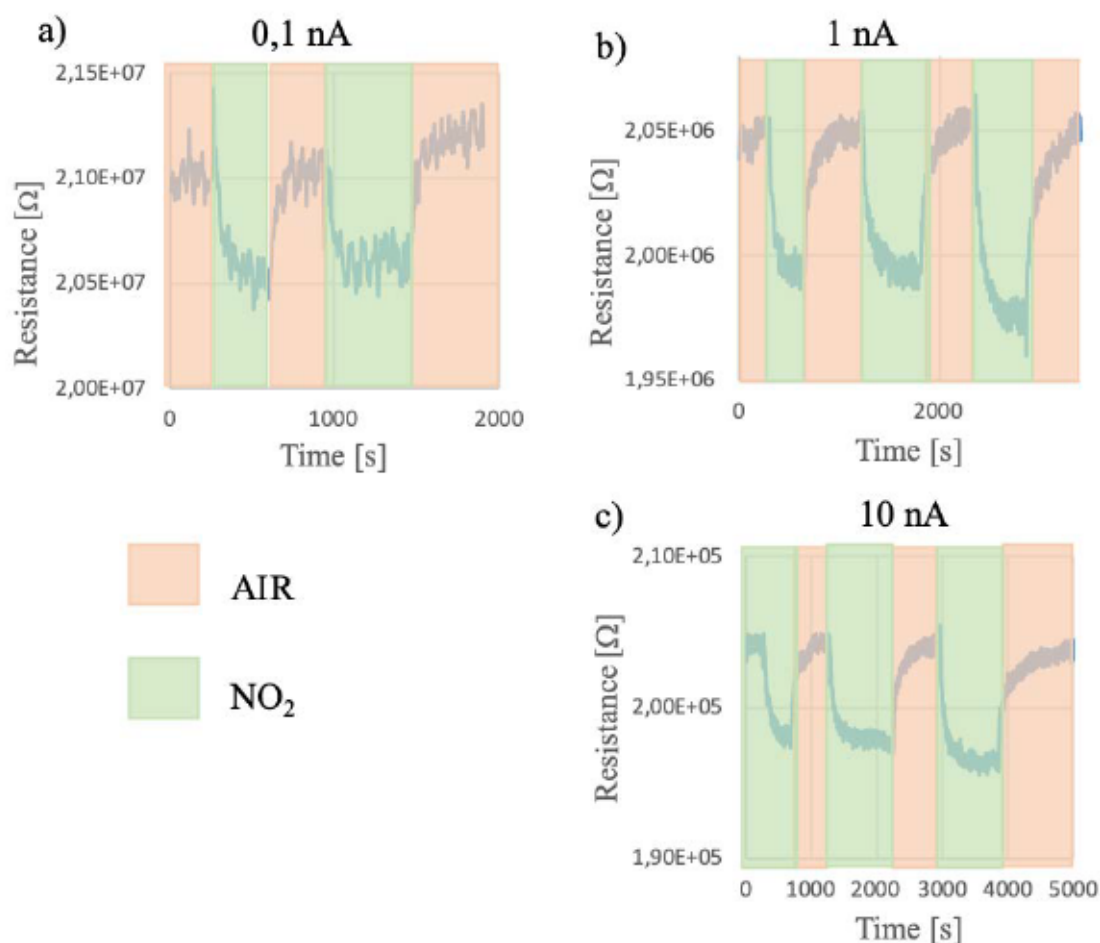


Figure 72. LaCoO₃-750-ysz95 response at 500°C exposed to 50 ppm of NO₂

To determine the effect of current on sensitivity, response under NO₂ at 500 °C was measured with different current: 0,1 nA (see Figure 72a), 1 nA (see Figure 72b), 10 nA (see Figure 72c) was investigated. Table 36 shows the sensitivity of the LaCoO₃-750-ysz95 layer in the presence of NO₂ using different currents.

Table 35. Sensitivity of LaCoO₃-750-YSZ95 for 50 ppm of NO₂ at 500°C

Current (nA)	Sensitivity (%)
0.1	4
1	4
10	4

Sensitivity did not change with change in current was observed only effect of current on the noise to signal ratio. With increase of current noise decrease. Further measurements were carried out using 1 nA.

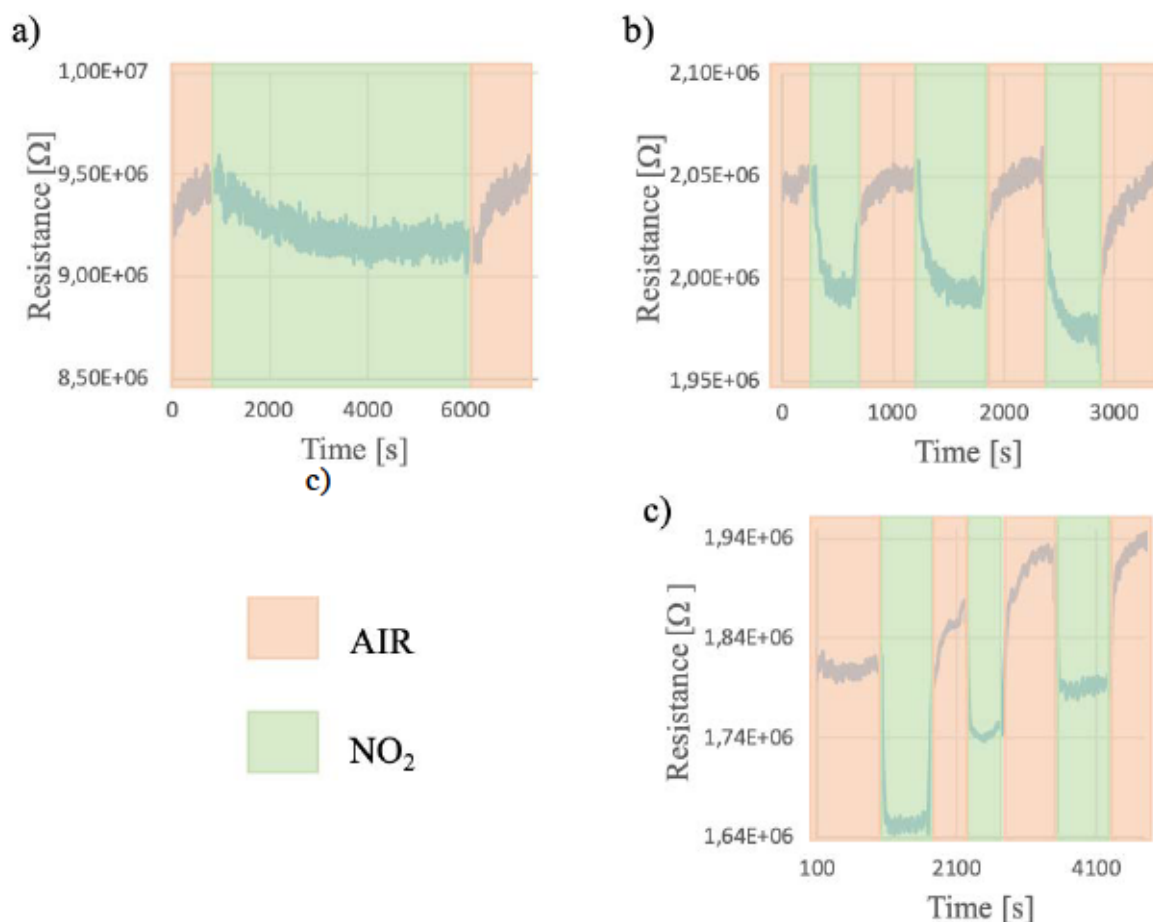


Figure 73. Response under NO₂ for LaCoO₃-750-YSZ95 at a) 450°C b) 500°C c) 550°C

Table 36. Sensitivity of LaCoO₃-750-YSZ95 under 50 ppm of NO₂

Temperature (°C)	Sensitivity (%)	Response Time (s)
450	5	1700
500	4	235
550	10	120

The LaCoO₃-750-YSZ95 thin film was tested in the temperature range from 25°C to 550°C. From 25°C- 400°C, the sensor under NO₂ did not react. The effect of working temperature on LaCoO₃-750-YSZ95 sensitivity is visible in Figure 73. The operation temperature affect sensitivity (see Table 36). No response is visible in T=450°C. As the temperature increases, the sensitivity increases, and response time is reduced. Change in the shape of the resistance curve in Figure 73b vs Figure 73c can be observed. At 550 °C, the resistance decreases rapidly (almost straight line) and fast reach minimum (stabilization). Decrease of temperature leads to change in response behavior, at 500 °C resistance decreases rapidly in the first phase, then the curve

slowly goes to stabilization (horizontal line). As a result of rising the temperature from 450°C to 550°C, the sensitivity of the sensor towards NO₂ increases, from 5% to 10% (see

Table 36). The difference in sensitivity at 450°C and 500°C is within the error of measurement, the signal at 450°C is characterized by the presence of noise (Figure 73a), which reduces the accuracy of the measurement. Response of LaCoO₃-750-YSZ95 with different NO₂ concentration at 550°C.

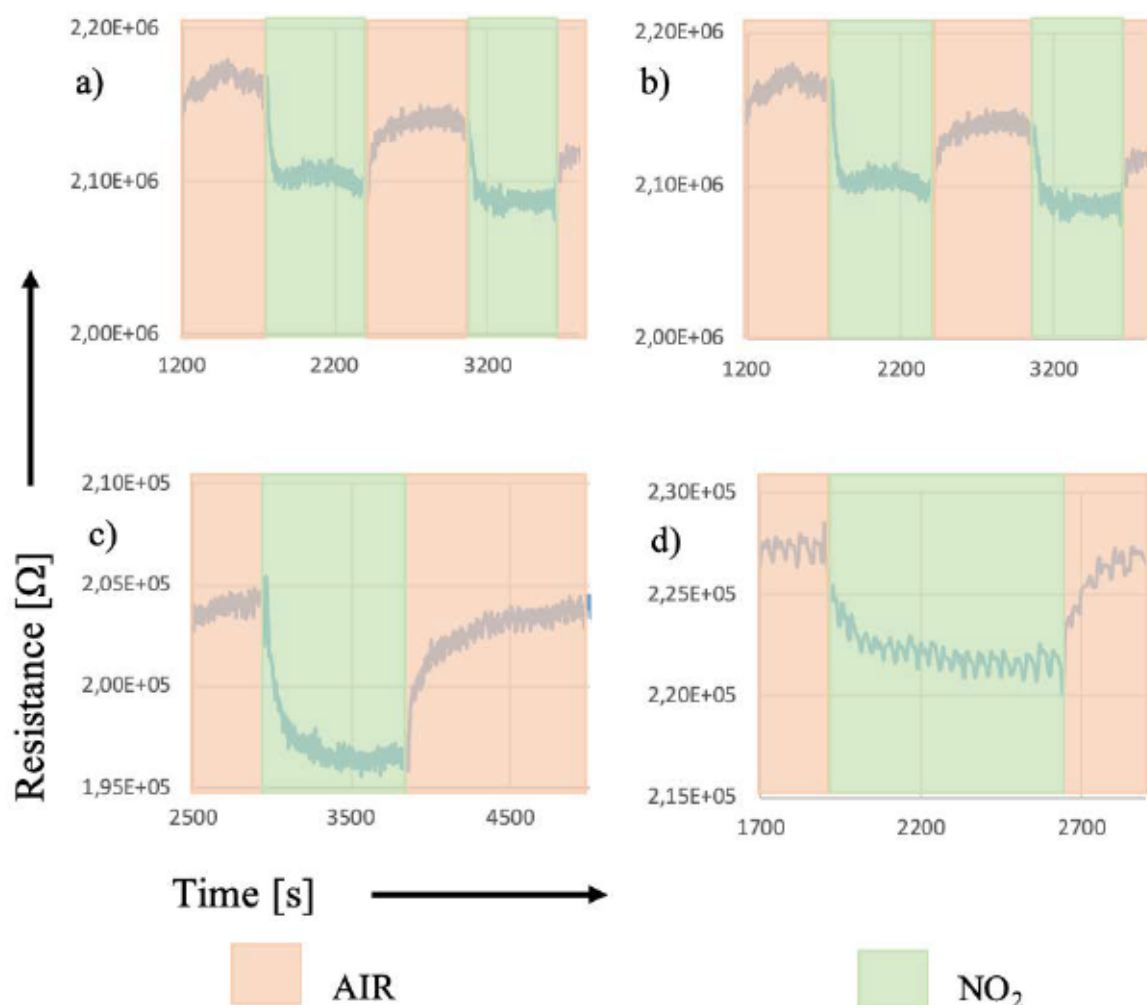


Figure 74 Response of LaCoO₃-750-YSZ95 at 550 °C a) 10 ppm, b) 20 ppm, c) 50 ppm d) 100 ppm.

Thin film of LaCoO₃-750-YSZ95 showed reactivity towards NO₂ in the temperature T= 500, 550°C and for different gas concentration (10-100 ppm).

Table 37. Sensitivity of LaCoO₃-750-YSZ95 at 550 °C for different concentration of NO₂

Temperature (°C)	Response Time (s)	Sensitivity (%)	NO ₂ Concentration
550	105	4	10 ppm
550	120	5	20 ppm

550	120	5	50 ppm
550	300	5	100 ppm

The layer showed reactivity from 450°C to 550°C and at concentrations from 10 ppm to 100 ppm. Thin films in NO₂ presence shows p-type response. This thin film show sensitivity from 10 to 100 ppm of NO₂ (see Table 37). Thin film deposited at 750°C reaches maximum sensitivity in 20 ppm.

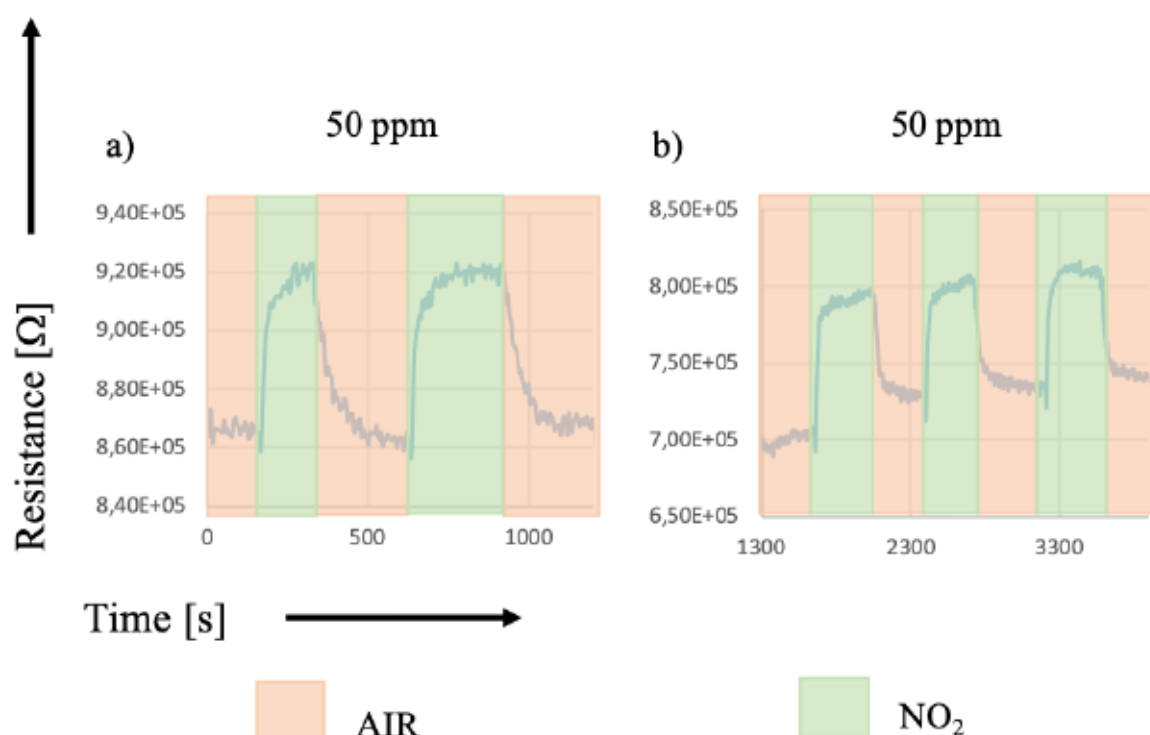


Figure 75. Response of LaCoO₃-850-ysz95 a) 500 °C b) 550 °C under 50 ppm of NO₂.

Thin film deposited at 850°C did not show reactivity towards NO₂ at 450°C. First response was recorded at 500°C under 50 ppm (see Figure 75a). Under 50 ppm sensitivity reach 8% which is 4% more than the sample produced in lower temperature. LaCoO₃-850-YSZ95 has a higher sensitivity (14%) than LaCoO₃-750-YSZ95 at 550°C (10%). The reactivity of LaCoO₃-850-YSZ95 starts at higher temperatures (500°C) than LaCoO₃-750-YSZ95 (450°C). Response type for both samples is different, due to the introduction of gas into the chamber, the resistance of the sensor for LaCoO₃-850-YSZ95 increased (n-type response). This means that the nature of the LaCoO₃-850-YSZ95 and LaCoO₃-750-YSZ95 responses is different.

Table 38. Influence of temperature on sensitivity of LaCoO₃-850-YSZ95

Temperature (°C)	Response Time (s)	Sensitivity (%)
450	0	0
500	30	8
550	25	14.5

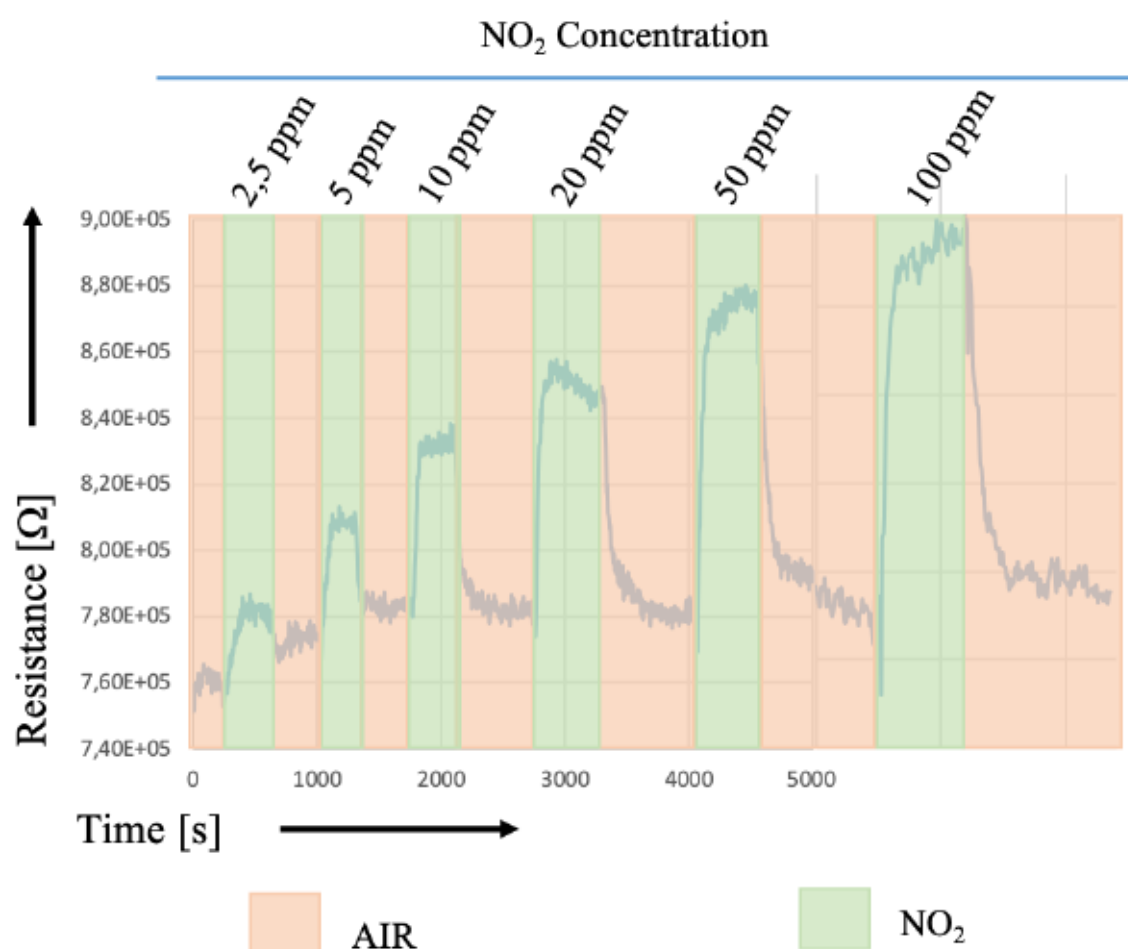


Figure 76. LaCoO₃-850-YSZ95 response under different NO₂ concentration.

Sensor gives response under wide range of NO₂ concentration, 2.5 ppm is the smallest value which was possible to obtained in our system. LaCoO₃-850-YSZ95 is showing sensitivity for lower values of NO₂ than LaCoO₃-750-YSZ95. Lowest NO₂ concentration which was possible to detect was 10 ppm. In Table 39, sensitivity under different concentration of NO₂ is presented.

Table 39. Sensor response in 550 °C under different gas concentration.

Temperature (°C)	Response Time (s)	Sensitivity (%)	NO ₂ Concentration
550	100	4	2,5 ppm
550	70	6	5 ppm
550	50	8	10 ppm
550	50	10	20 ppm
550	85	14.5	50 ppm
550	95	15	100 ppm

The LaCoO₃-850-YSZ95 thin film has not only a higher sensitivity towards NO₂ (see Table 39) than LaCoO₃-750-YSZ95 but also is reacting with smaller NO₂ concentration (2.5 ppm). In sample deposited at 850°C, noise was smaller and recovery time was lower. Due to high drift of base line and high noise signal ratio measurements was much more difficult in LaCoO₃-750-YSZ95.

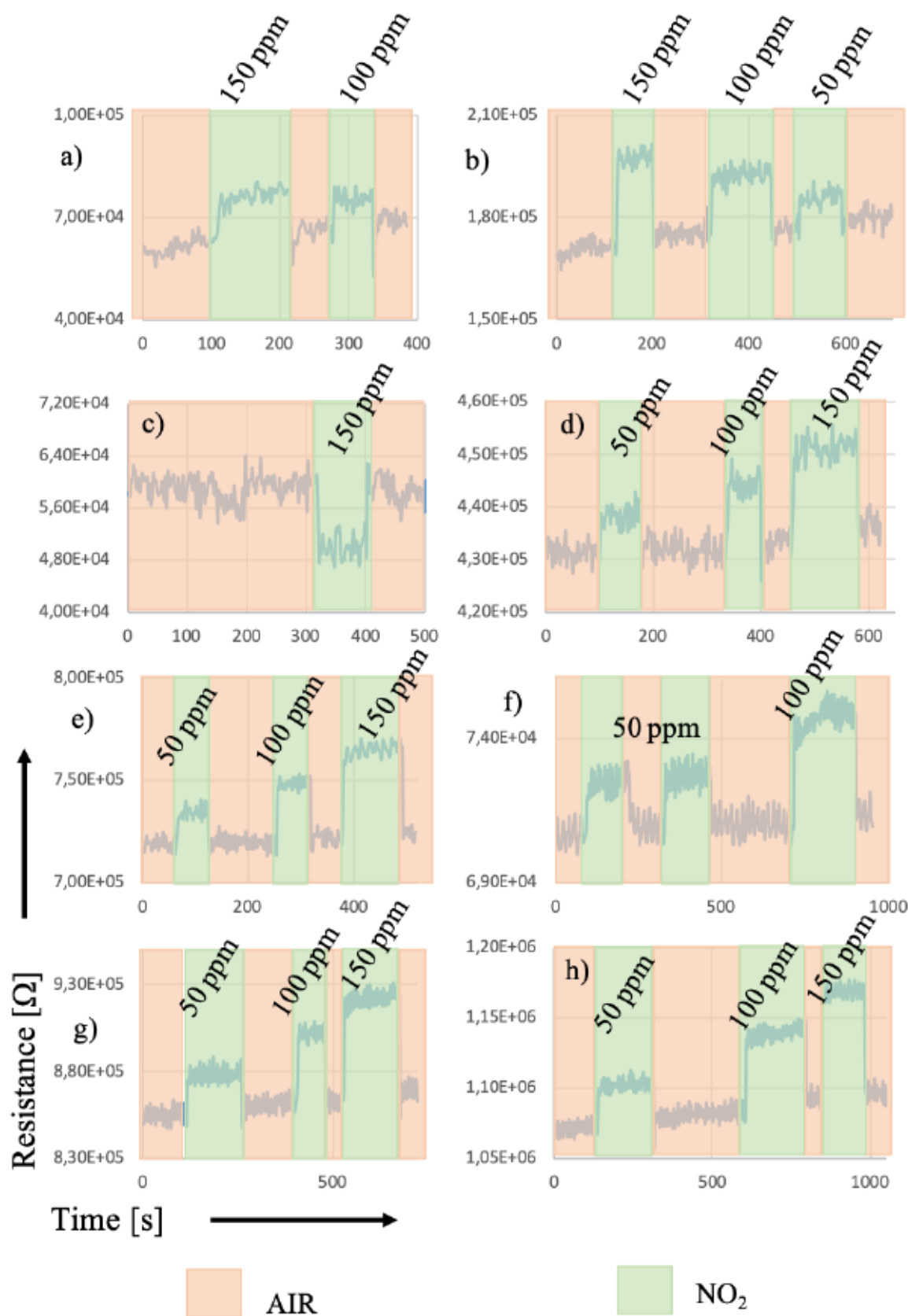


Figure 77. Reaction of $\text{LaCoO}_3_{850}\text{YSZ35}$ under NO_2 a) 50°C b) 100°C c) 150°C d) 200°C e) 250°C f) 300°C g) 350°C h) 400°C

Table 40. Sensitivity of LaCoO₃-850-YSZ35.

Temperature (°C)	Response Time (s)	Sensitivity (%)	NO ₂ Concentration (ppm)
50	12	26	100
50	20	45	150
100	4	16	50
100	4	20	100
100	4	22	150
150	2	26	150
200	20	4	50
200	20	5	100
200	14	7	150
250	3	4	50
250	4	6	100
250	8	8	150
300	4	5	50
300	9	8	100
350	6	5	50
350	10	7	100
350	16	10	150

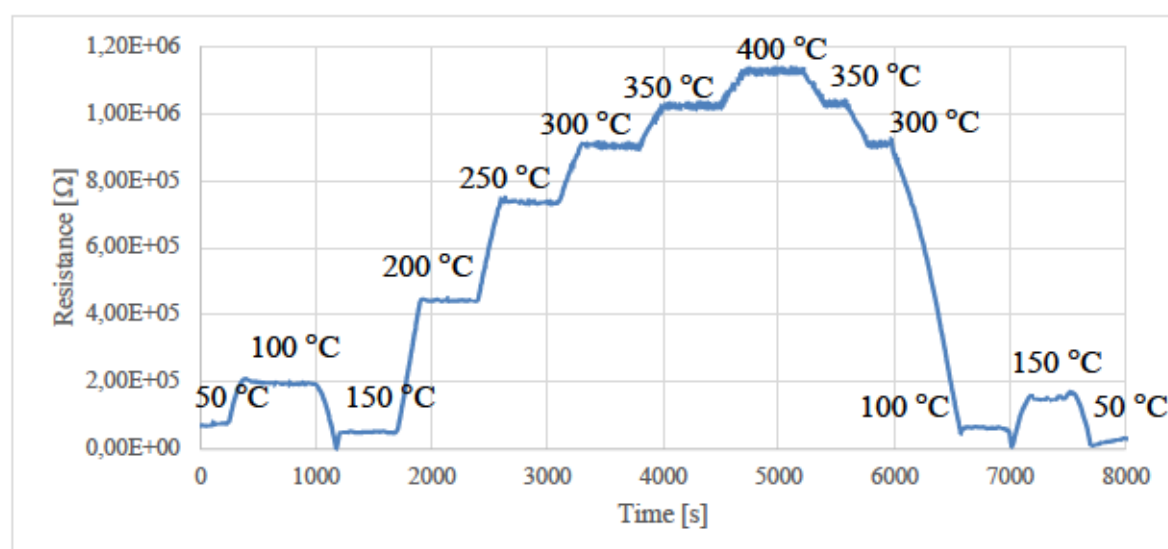


Figure 78. LaCoO₃-850-YSZ35 resistance in different temperatures.

LaCoO₃-850-YSZ35 is sensitive towards NO₂ in wide range of temperatures (50 to 400°C) (see Figure 77). Response time is proportional to NO₂ concentration above 150°C. Lowest response time was obtained at 150°C and 150 ppm of NO₂. N- type response was observed for all temperatures except 150°C where we can observe p-type response. Highest sensitivity was obtained at 50°C (45% for 150 ppm) (see Table 40). LaCoO₃-850-YSZ35 are characterized by

fast response time. Figure 78 presents the resistance at different temperatures. Sample was hold under continuous flux of air. Temperature was changed with 50°C step. We can observe nonlinear behavior of material.

4.3.2 LaFeO₃

Thin films LaFeO₃-T-YSZ95 were tested in the presence of gases at a concentration range from 2.5 ppm to 100 ppm (NO₂, NH₃, CO) in the temperature range from 25°C to 550°C. The samples were placed in a cell. Before first measurements sample was heated to a temperature of 300°C with a continuous air flow for a period of 3 hours. Aim if this treatment was to cleaning sample surface and cell from contamination. In order to stabilize the signals after reaching the assumed temperature, sample was held under voltage with air flow for the time needed to obtain a stable baseline (R_{air}). Figure 79 shows the results for LaFeO₃-750-YSZ95 sample in the presence of 50 ppm NO₂ at various temperatures.

LaFeO₃-750-YSZ95 sample was reactive towards NO₂ from 200°C. In lower temperatures sample did not show reactivity in gas presence. In 200 °C thin film is gives n-type response under gas (see Figure 79a). After heating to 250°C nature of response is changed to p-type. Sensitivity decreased significantly in range from 200 °C to 250°C (see Table 41). At 300°C thin films shows higher reactivity towards NO₂ than in other temperatures. Resistance curve runs rapidly to minimum and reach minimum. Therefore, after retracting NO₂ resistance is not reaching base line (R_{air}). Further temperature increase does not lead to sensitivity improvement. Shortest response time is obtained in 200°C (see Table 41).

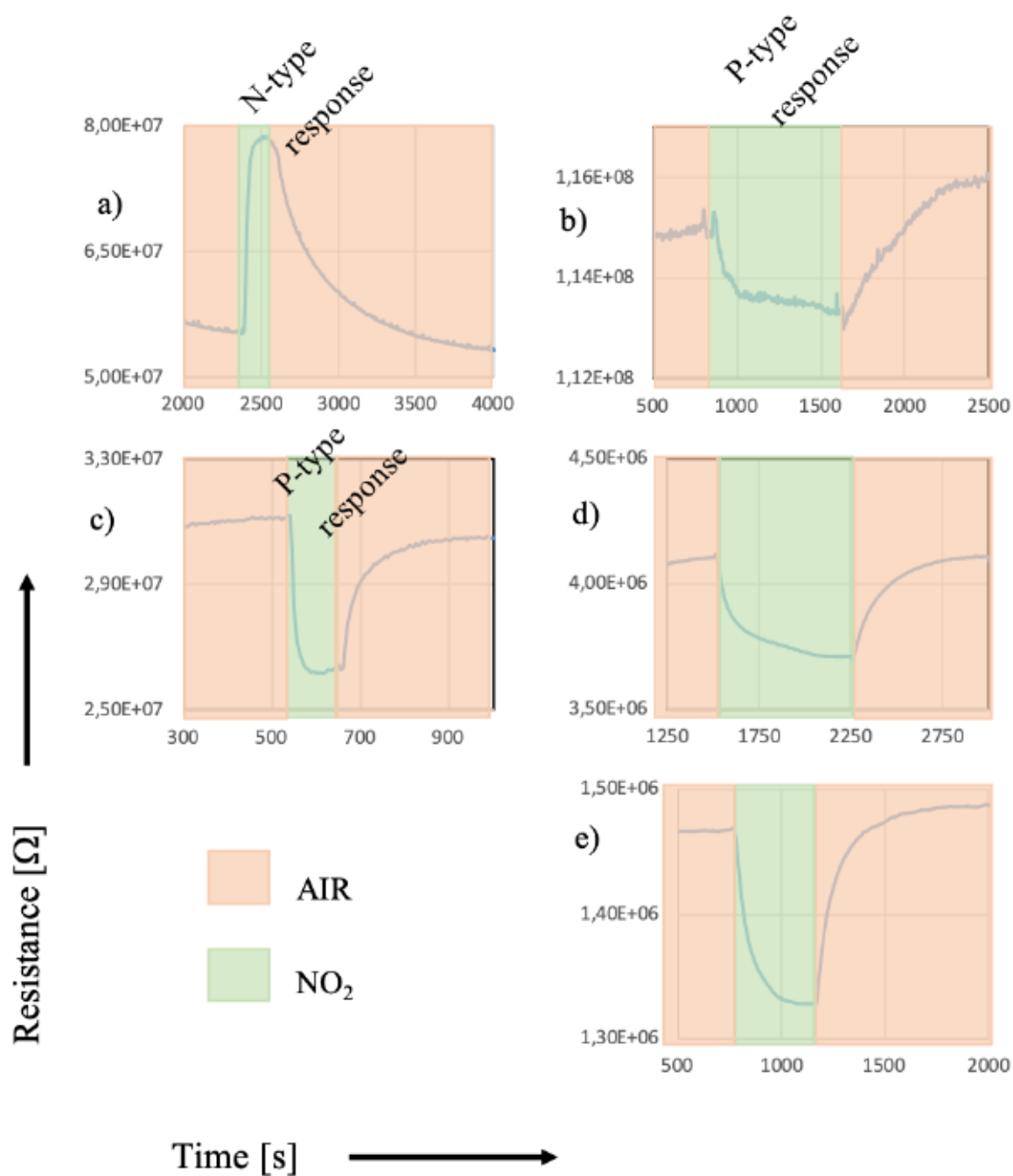


Figure 79. Response of LaFeO₃-750-YSZ95 in a) 200 °C b) 250 °C c) 300 °C d) 350 °C e) 400 °C under 50 ppm of NO₂

Table 41. Sensitivity and response time of LaFeO₃-750-YSZ 95.

Temperature (°C)	Sensitivity (%)	Response time (s)
200	49	40
250	-2	195
300	-16	85
350	-68	140
400	-11	195

After increasing the temperature up to 300°C response time also increase. Change of response from n-type to p-type can be caused temperature or gas concertation.

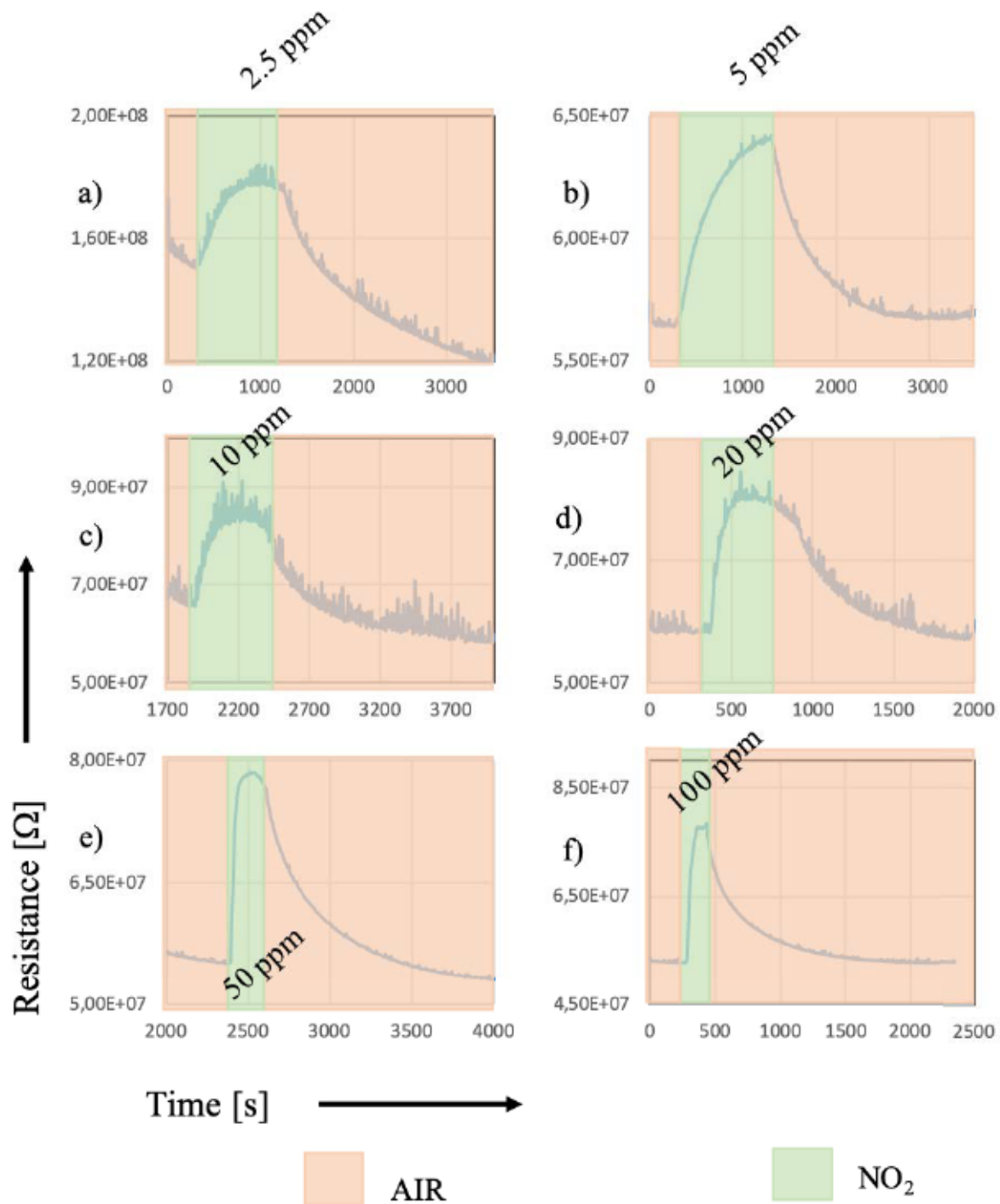


Figure 80. Response of LaFeO₃-750-YSZ95 a) 2,5 ppm at 200 °C b) a) 5 ppm in 200 °C c) 10 ppm in 200 °C d) 20 ppm in 200 °C e) 50 ppm f) 100 ppm

All obtained data at 200°C are characterized by high noise presence. Measurements was carried out with 100 nA to obtain best possible signal. At T=200 °C the sensitivity increases with NO₂

concentration up to 20 ppm (see Table 42). The response time decrease with increase of NO₂ concentration and the shortest time is in 50 ppm of NO₂.

Table 42. Sensitivity and response time of LaFeO₃-750-YSZ95 in 200 °C

Sensitivity (%)	NO ₂ Concentration (ppm)	Response time (s)
19	2.5	370
20	5	120
40	10	95
50	20	95
49	50	40
49	100	75

Thin film shows reactivity towards low NO₂ concentration (2.5 ppm). Sample reach saturation in 20 ppm of NO₂, further increase does not influence sensitivity (see Table 42).

The effect of change of conduction type is observed also in thin films LaFeO₃-850-YSZ95. LaFeO₃-850-YSZ95 sample was investigated towards reactivity to NO₂ in wide range of temperatures (25°C – 450°C) and concentrations (2.5 ppm –100 ppm) results are presented in Figure 81 and in Table 43. Up to 300°C sample present n type response. In 350°C both competitive conduction types are occurring in one time. From 400°C sample have p-type response. Time of n - type response decrease with increase of temperature. Shortest response time is observed after switch of response time (450°C).

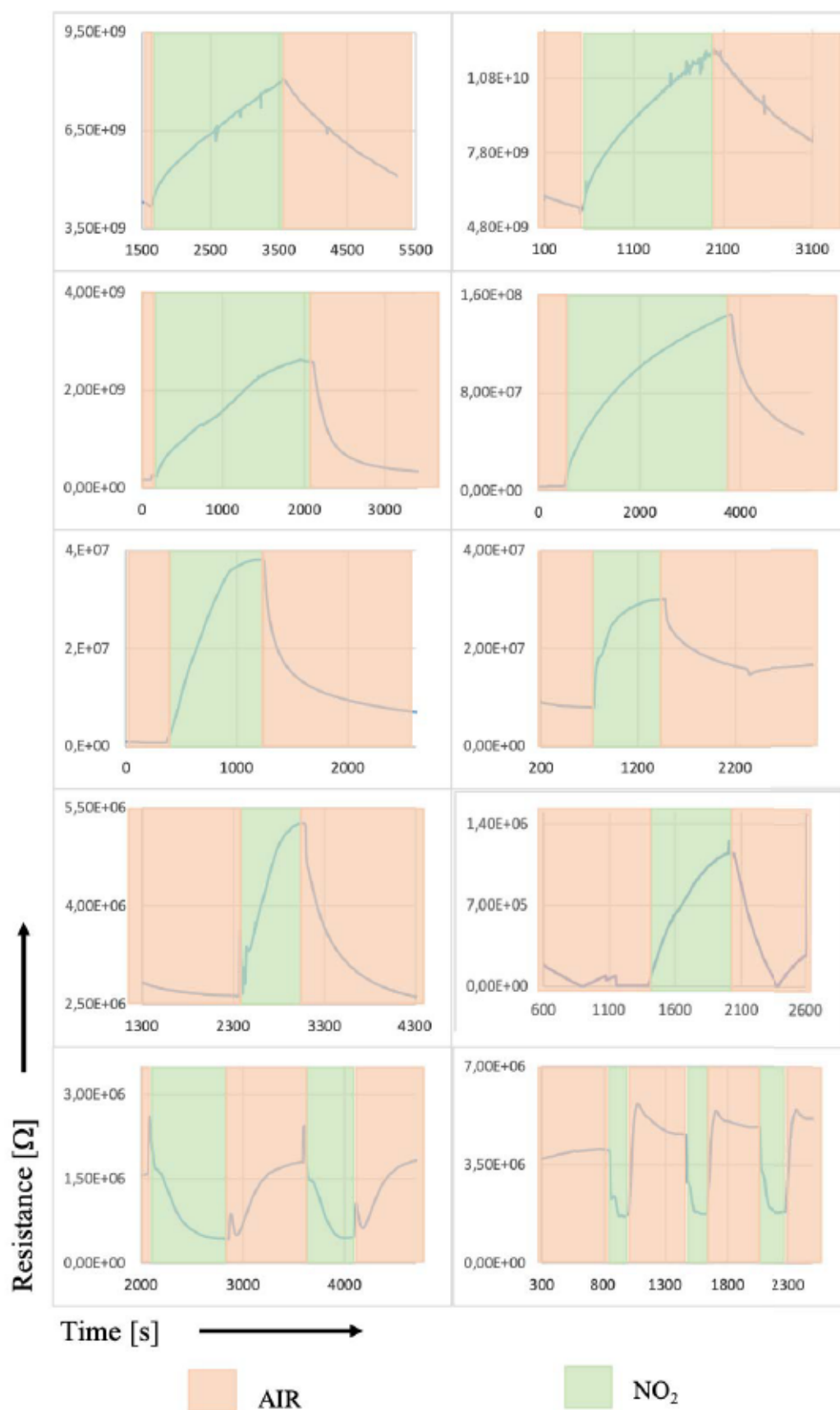


Figure 81. LaFeO_3 -850-YSZ95 a) 25°C, b) 50°C, c) 100°C, d) 150°C, e) 200°C, f) 250°C g) 300 C h) 350°C i) 400°C j) 450°C response under 50 ppm of NO_2

The LaFeO₃-850-YSZ95 thin film detect presence of NO₂ in a wide temperature range (from 25°C to 450°C). Interesting behavior of the material can be observed at 350° C, where the nature of response changes. At temperatures from 25°C to 300°C, after introducing NO₂ into the cell, thin film resistance increases. While at temperatures above 350°C in presence of NO₂, resistance decreases. At low temperatures, the sensor is characterized by an n-type response, in higher ones by a p-type. LaFeO₃-850-YSZ95 sensitivity reach 5800% (see Table 43). Compared to the results obtained for other samples, this sample is showing great sensitivity.

Table 43. LaFeO₃-850-YSZ95 Response under NO₂

Temperature (°C)	Sensitivity (%)
25	100
50	125
100	1500
150	4000
200	5800
250	280
300	170
350	285
400	-100
450	-95

Figure 83 is a graph of sensitivity as a function of temperature, the layer was exposed to 50 ppm NO₂ at temperatures from 25°C to 450°C to determine the optimum sensor operating temperature. Sensitivity in the n range is much higher than in the p range, the response time and the course of the resistance change significantly in the n and p ranges.

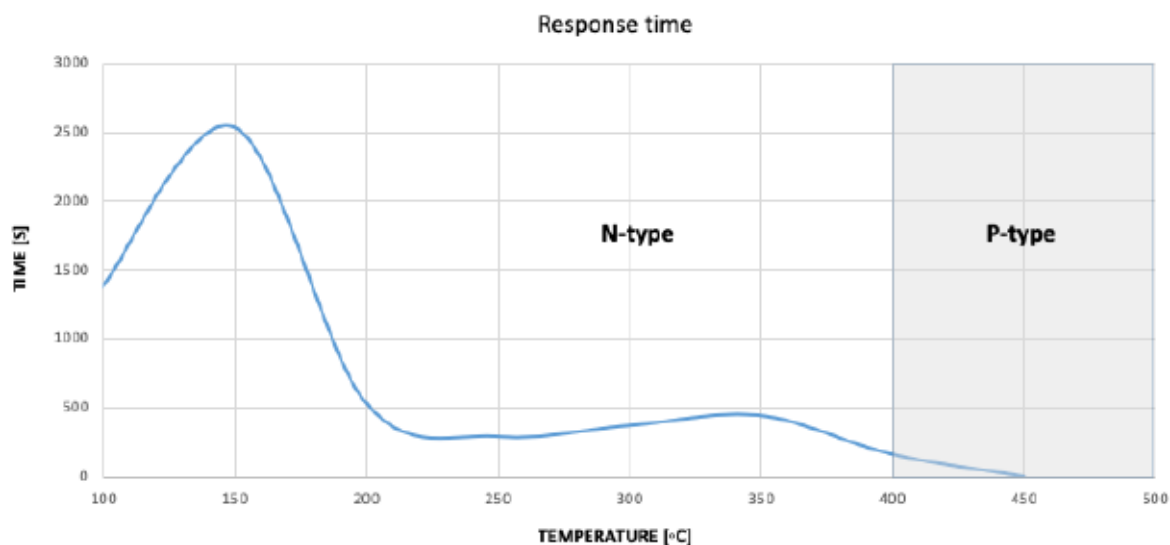


Figure 82. Response time in temperature LaFeO₃-850-YSZ95

The response time in the p-type range is much shorter than in the n-type range (see Figure 82). This is due to a different shape of the resistance curve. N- type response is characterized by slow approaching the maximum. At higher temperatures, the response is in the form of a vertical curve of resistance (see Figure 81j). To determine possible concentration range of NO₂, the sensor response was tested at temperature 200°C in concentration range from 2.5 ppm to 100 ppm (see Figure 83).

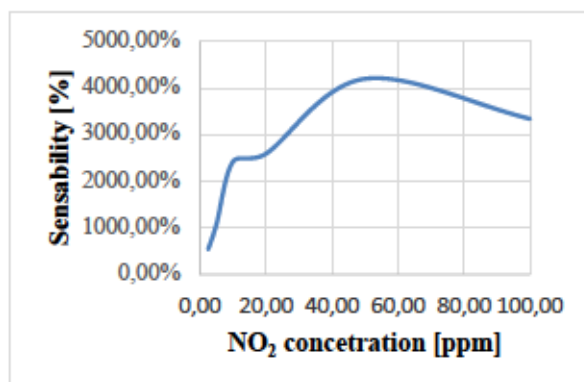


Figure 83. Sensitivity of LaFeO₃-850-YSZ in 200 °C in NO₂

LaFeO₃-850-YSZ95 is reactive towards wide range of NO₂ concentration. In our device 2.5 ppm is the lowest possible NO₂ concentration. High sensitivity towards 2.5 ppm of NO₂ (see Figure 84a) allows to assume that lower concentration would be detected too. After taking under consideration all obtained results for further test sample with the best performance was chosen (LaFeO₃-850-YSZ95). Not only sensitivity and response time is key parameter of gas sensor. Selectivity is also one of the most important abilities of sensor. To determine this parameter

LaFeO₃-850-YSZ95 was exposed on NH₃ and CO₂ gases. Obtained results allows to define selectivity of thin film deposited at 850 °C.

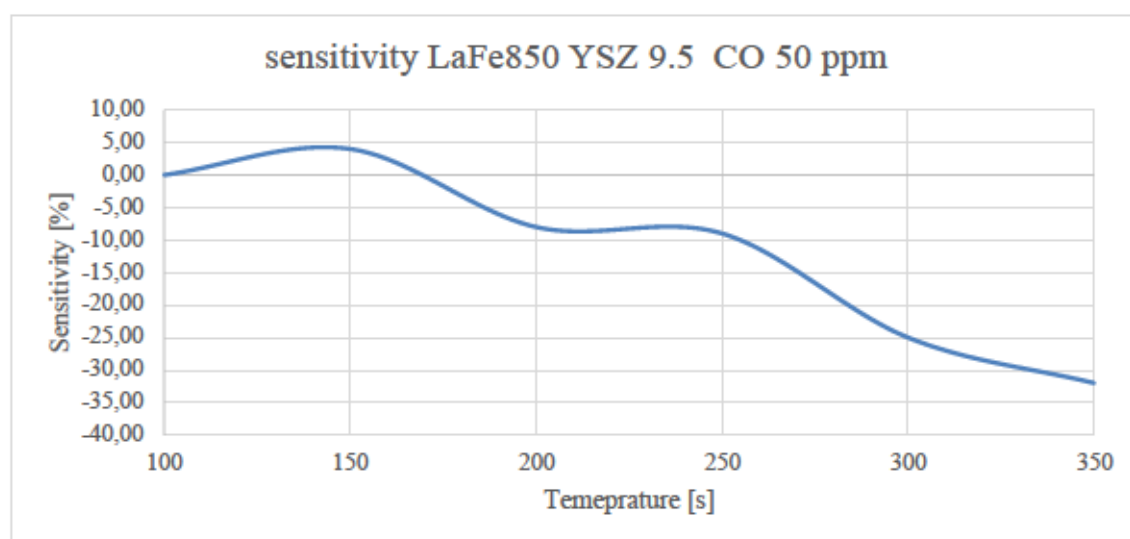


Figure 84. LaFeO₃-850-YSZ95 Response under 50 ppm of CO.

Response of thin film was tested under presence of CO in various temperatures. LaFeO₃-850-YSZ95 showed reactivity towards CO from 150°C. Sensitivity in this temperature was 4%. Resistance of thin film in CO presence increased after further increase of temperature to 200°C nature of response changed. After change of response (resistance decrease) sensitivity reach 8%. Maximum response of the sensor can be observed in 350°C (32%) (see Table 44). Obtained results allows us to conclude that thin film of LaFeO₃ deposited on YSZ95 is not selective. Reactivity towards CO and NO₂ was detected. However, sensitivity towards CO is much lower than for NO₂.

Table 44. LaFeO₃-850-YSZ95 Response under 50 ppm of CO.

Sample	Gas	Temperature (°C)	Sensitivity (%)
LaFeO ₃ -850-YSZ95	CO	150	4
		200	-8
		250	-9
		300	-25
		350	-32

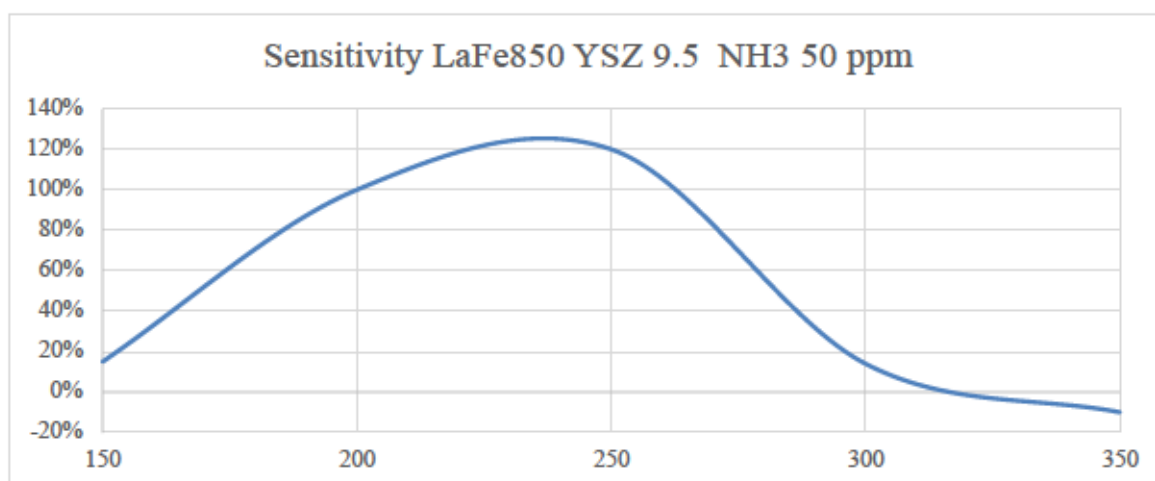


Figure 85. LaFeO₃-850-YSZ95 Response under 50 ppm of NH₃.

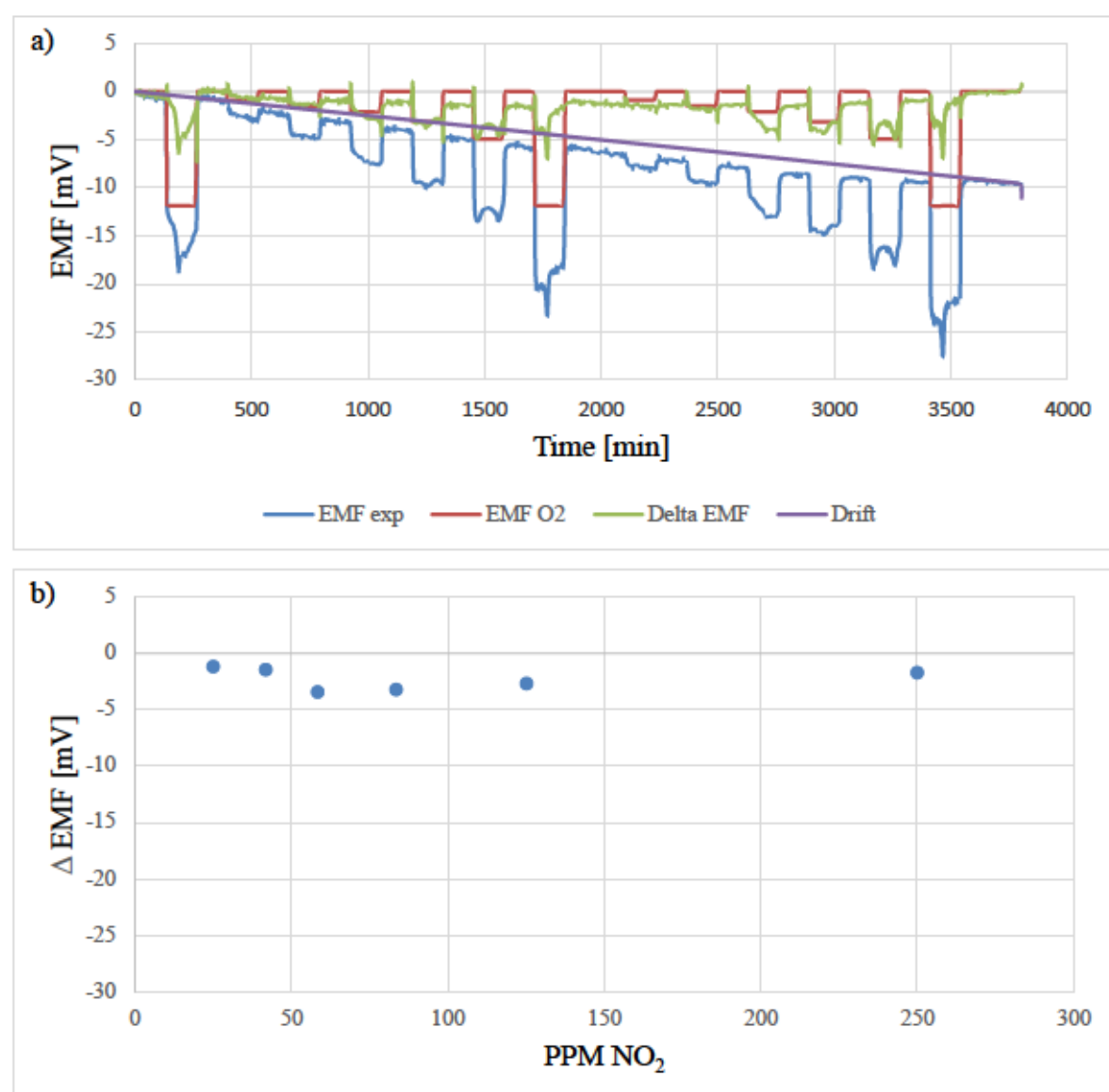
Further test was carried out in presence of NH₃. As was the case with CO working temperature starts at 150°C. In range from 150°C to 250°C response time is very long (see Table 45). Highest sensitivity sample reach at 250°C as it was observed for NO₂. In range from 150°C to 300°C after NH₃ injection resistance increase, in 350°C in gas presence thin film resistance decrease. Above 250°C response time is much shorter (45 s).

Table 45. LaFeO₃-850-YSZ95 Response under 50 ppm of NH₃.

Sample	Gas	Temperature (°C)	Response time (s)	Sensitivity (%)
LaFeO ₃ -850-YSZ95	NH ₃	150	1000	15
		200	2000	100
		250	1000	120
		300	45	14
		350	150	-10

4.4 ELECTROCHEMICAL MEASUREMENTS

Thin films were tested in the presence of NO_2 at a concentration from 17 ppm to 250 ppm in a temperature range: 500–700°C. Reference electrode was exposed on constant air pressure. SE was exposed at mixture of Air and NO_2 . Created EMF was measured. To calculate ΔEMF presented formula was used: $\Delta \text{EMF} = \text{EMF}_{(\text{experimental})} - \text{EMF}_{(\text{O}_2)}$. $\text{EMF}(\text{O}_2)$ is calculated value created due to change in partial pressure of oxygen due to change in NO_2 concentration.



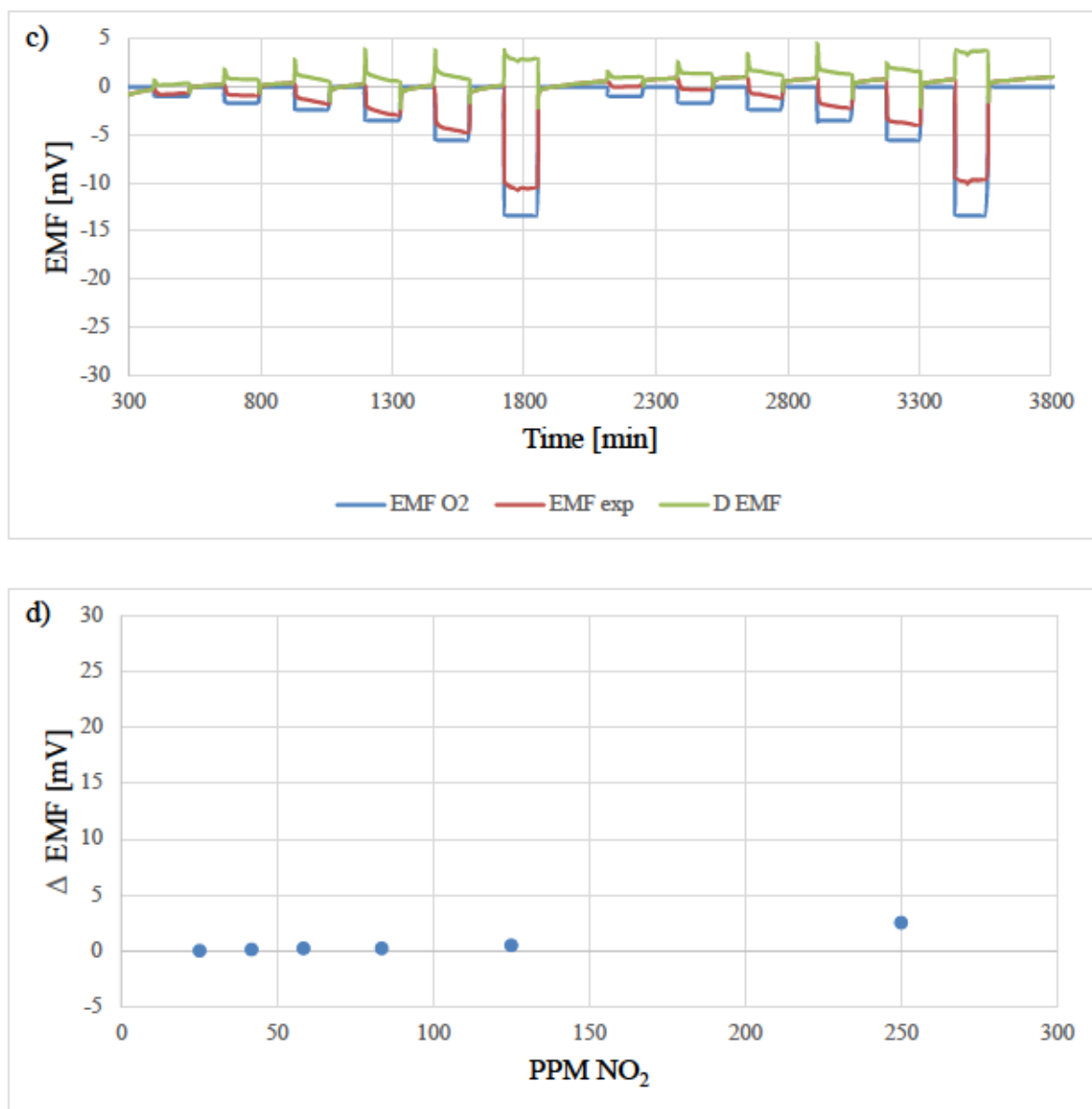


Figure 86. LaCoO₃-750-YSZ35 response under NO₂ in a) 500°C c) 600°C

In Figure 86b-d, we can observe change in Δ EMF under NO₂. Response of the sensor is range of measurement error this means that LaCoO₃-750-YSZ35 thin film is not sensitive towards NO₂ at 500°C and at 600°C. Drift of the signal is decreasing with temperature. At 500°C drift of the signal is strong (-11 mV in 3800 minutes). At 600°C drift is no longer present.

Due to high temperature (600°C) effect of NO₂ reduction to NO and O₂ is visible. Δ EMF have opposite values comparing to EMF O₂. This means gas behaves as reductive.

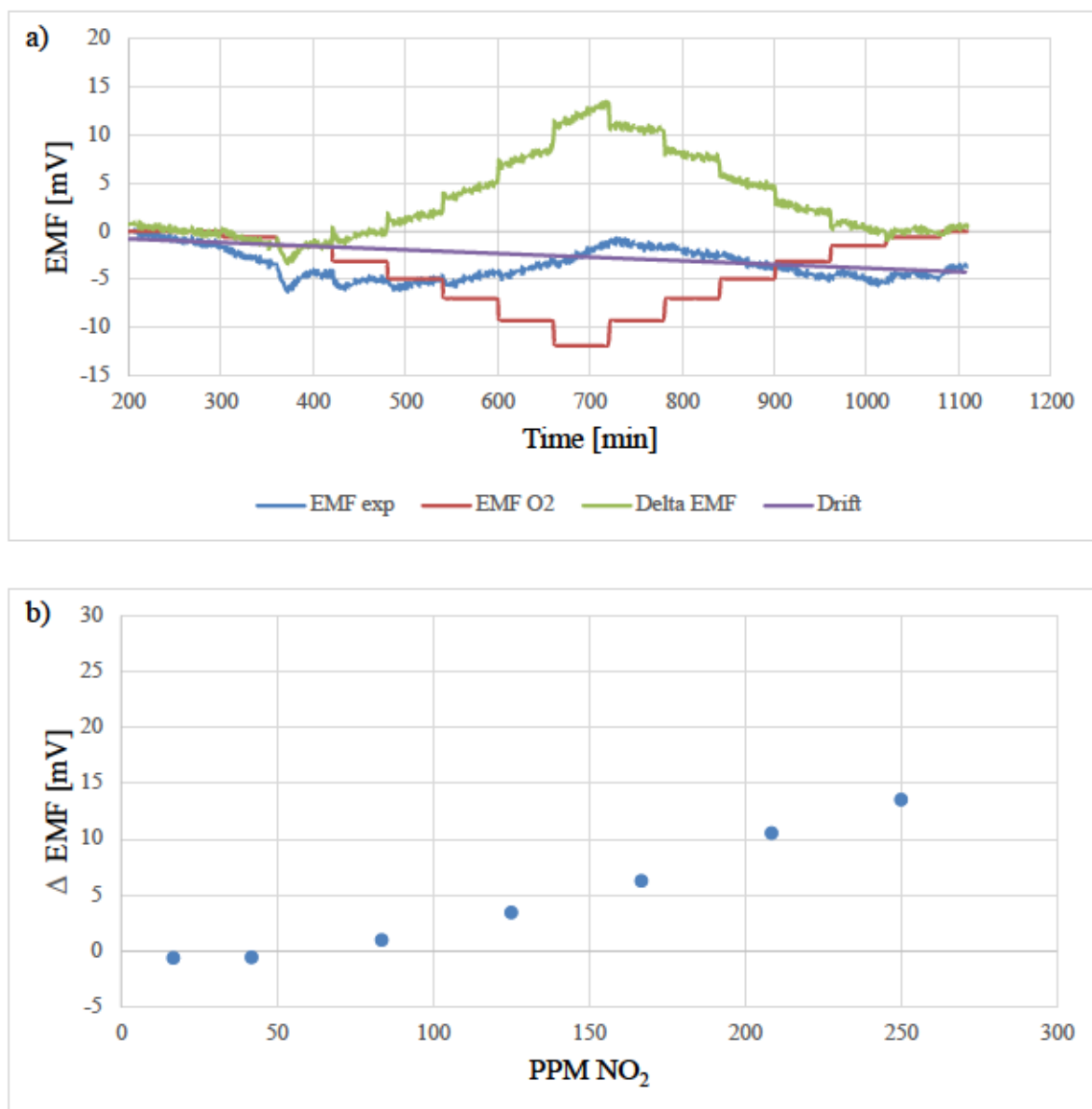


Figure 87. LaCoO₃-850-YSZ35 at 500°C.

In Figure 87 a response of LaCoO₃-850-YSZ35 under different NO₂ concentrations is presented. Signal drift is strong (-4,2 mV – 1000 min). Sensor is not sensitive towards NO₂. Δ EMF is created due to change of partial pressure of oxygen. On measuring side NO₂ is diluted with air. Increase of NO₂ concentration leads to decrease of oxygen concentration. On reference electrode oxygen pressure is constant that's why change in oxygen concentration in measuring side creates EMF. To extract signal created by NO₂ we need to calculate EMF generated by change in oxygen pressure. When sensor is not sensitive towards NO₂ then Δ EMF will have opposite values to EMF O₂.

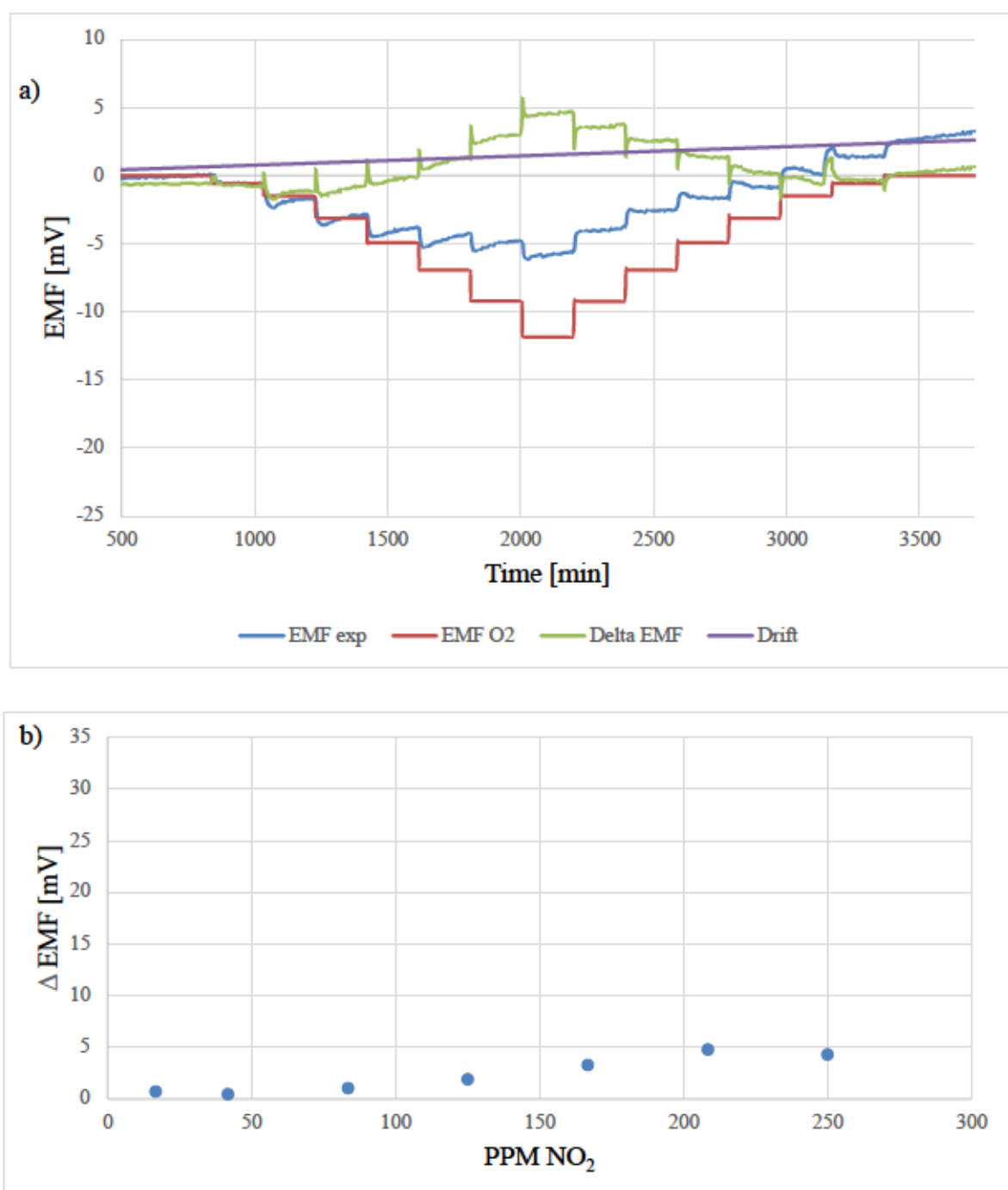
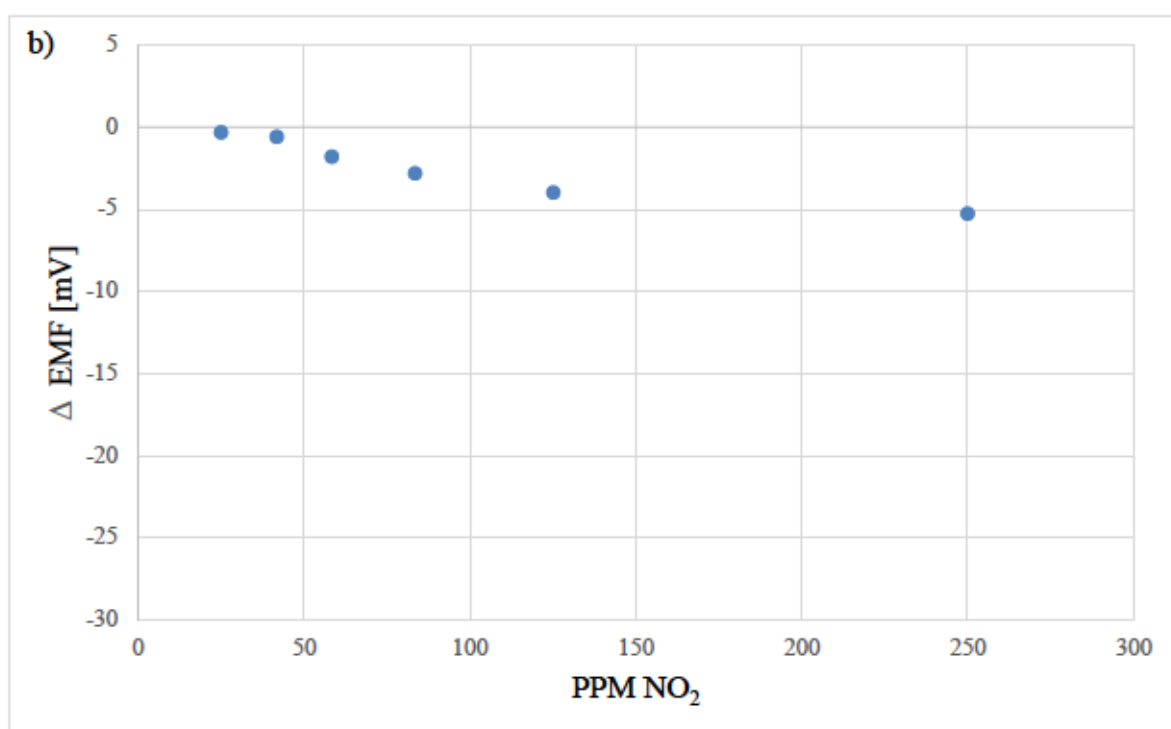
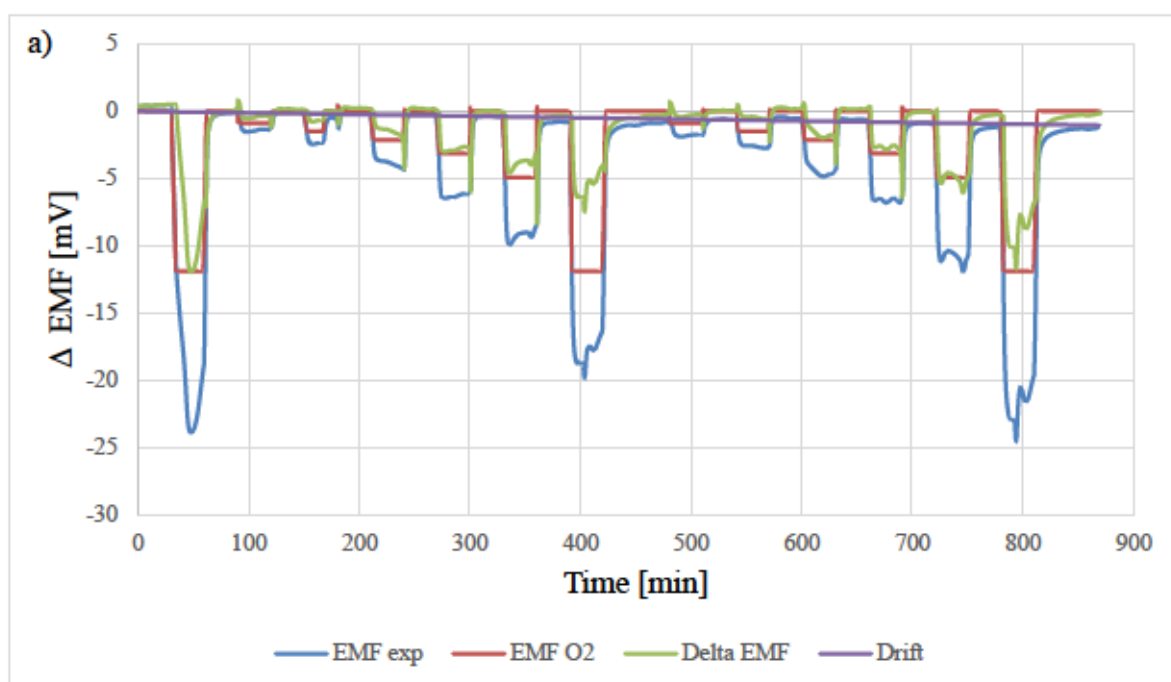


Figure 88. LaCoO₃-850-YSZ95 at 500°C.

Response of sample LaCoO₃-850-YSZ95 at 500 °C is presented in Figure 88a-b. Theoretical EMF for oxygen and experimental EMF for NO₂ is presented at Fig 91 a. Due to the signal drift (2.7 mV after 3800). As we can observe in Figure 88b change in EMF under different NO₂ concentration is low. Δ EMF obtained for 250 ppm of NO₂ is 4.3 mV. Sample LaCoO₃-850-YSZ95 is not sensitive toward NO₂ concentration.



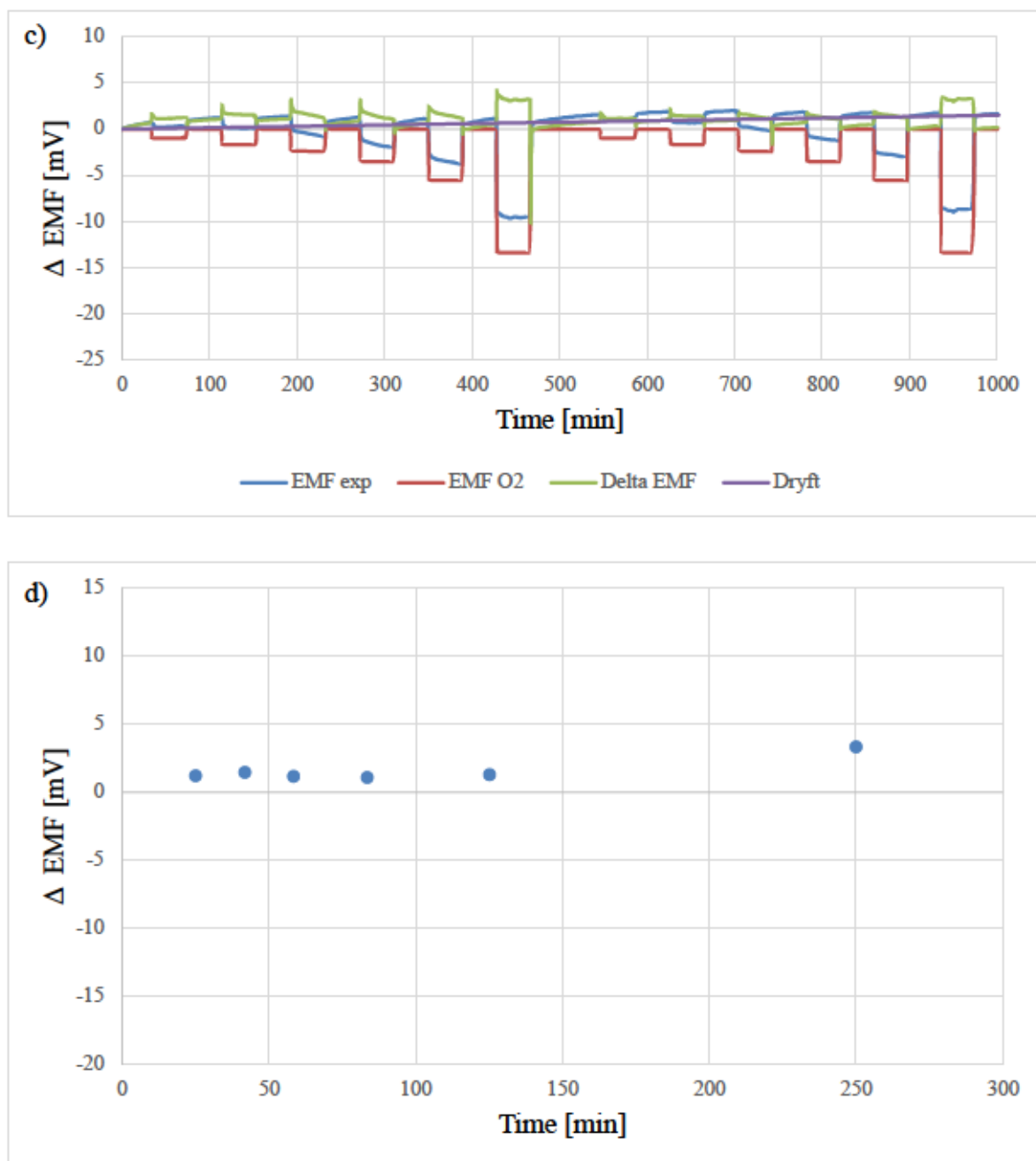


Figure 89. LaFeO₃-750-YSZ35 under NO₂ at a) 500°C b) 600°C

Response of sample LaFeO₃-750-YSZ35 at 500°C is presented in Figure 89 a-b. Theoretical EMF for oxygen and experimental EMF for NO₂ is presented in Figure 89a. Signal drift is low (-1mV after 1000 min). Δ EMF under different NO₂ concentration is low. Maximum Δ EMF is observed for 250 ppm of NO₂ (-5,3 mV). Sample LaFeO₃-850-YSZ35 show low sensitivity toward NO₂. LaFeO₃-750-YSZ35 at 600°C is not sensitive towards NO₂, signal drift is small (1.5 mV after 1000 min) this can be affected by presence of NO which is reductive gas. EMF created by NO and NO₂ have opposite signals that is why we are not observing the response.

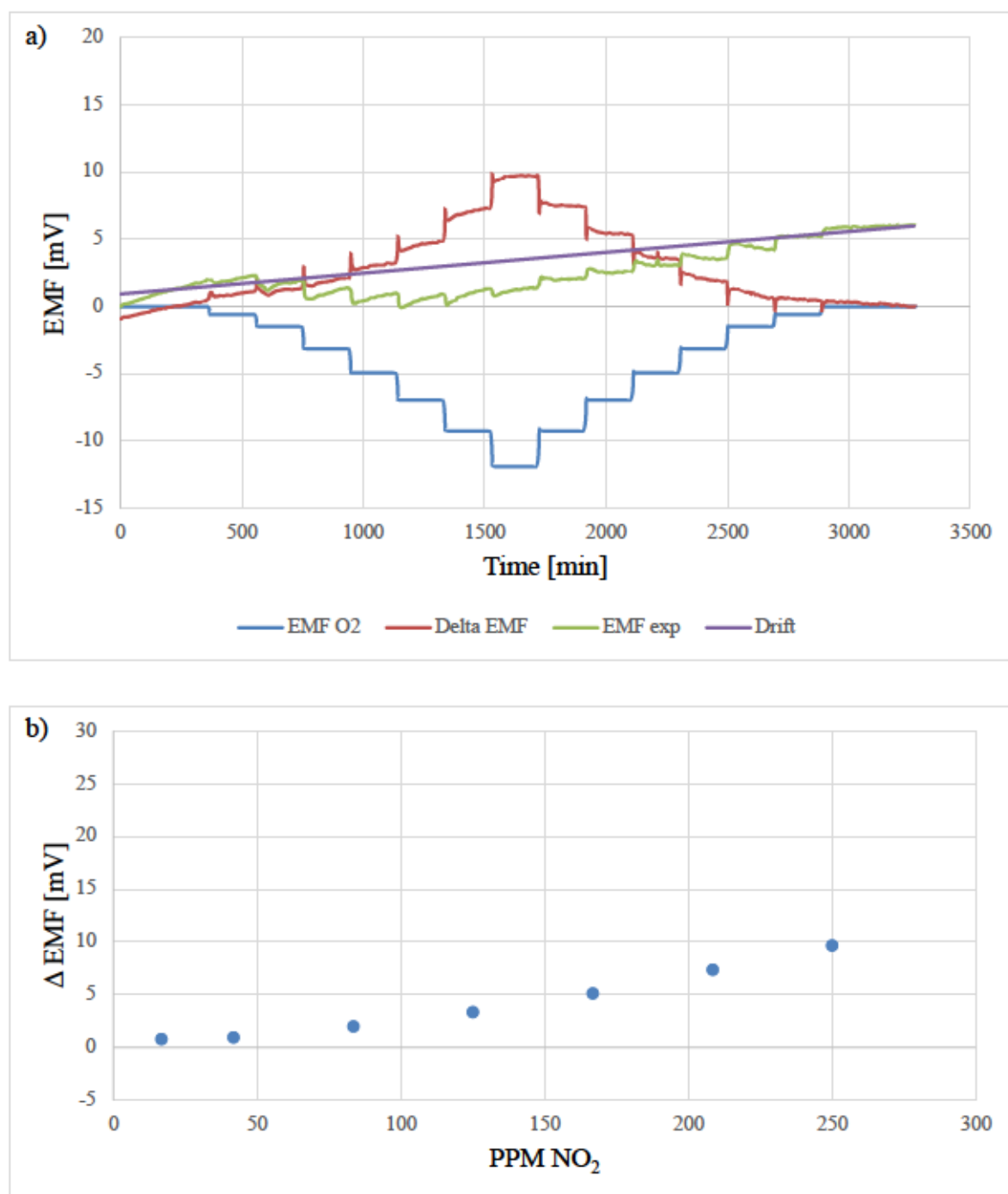


Figure 90. LaFeO_3 -850-YSZ35 at 500°C.

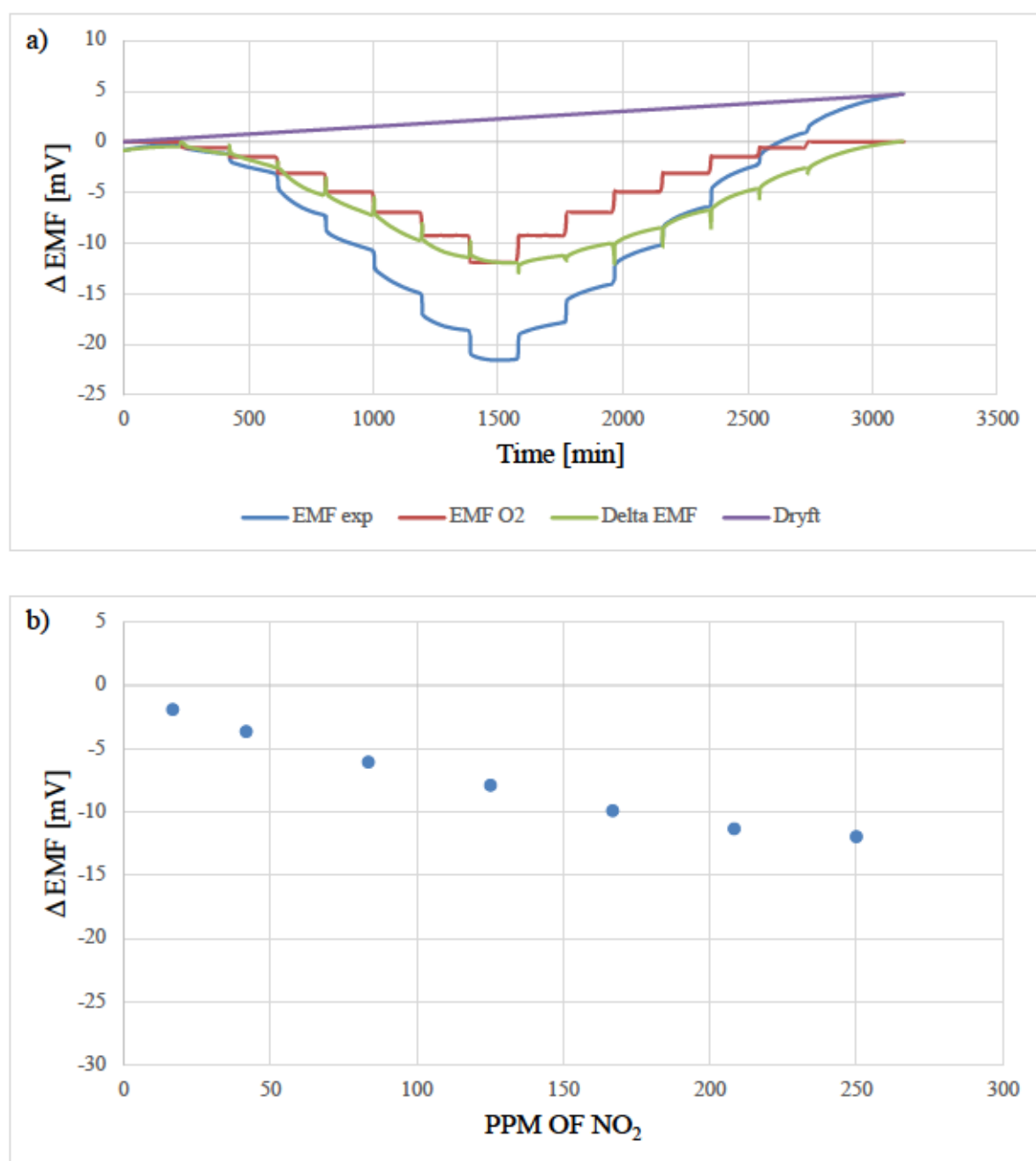


Figure 91. LaFeO₃-850-YSZ95 under NO₂ at 500°C.

Sample was exposed to NO₂ concentration: 17 ppm, 42 ppm, 83 ppm, 125 ppm, 166 ppm, 208 ppm, 250 ppm, 208 ppm, 166 ppm, 125 ppm, 83 ppm, 42 ppm, 17 ppm. After each change sample was hold. First and last measurement was carried out in Air presence. Change in EMF between first and last measurement can be explained by drift of the sample. This phenomenon can be observed in Figure 91a. Drift of the signal after 3100 is 4.7 mV. Δ EMF for 250 ppm of NO₂ is 11.93 mV. Ionic conductivity of YSZ95 at 500°C is low this can explain long response time. Low ionic conductivity of the substrate makes more difficult to establish local

equilibrium. Response time of LaFeO₃-850-YSZ95 is longer in comparison to LaFeO₃-850-YSZ35. Polycrystalline material shows higher ionic conductivity in lower temperatures due to grain boundaries.

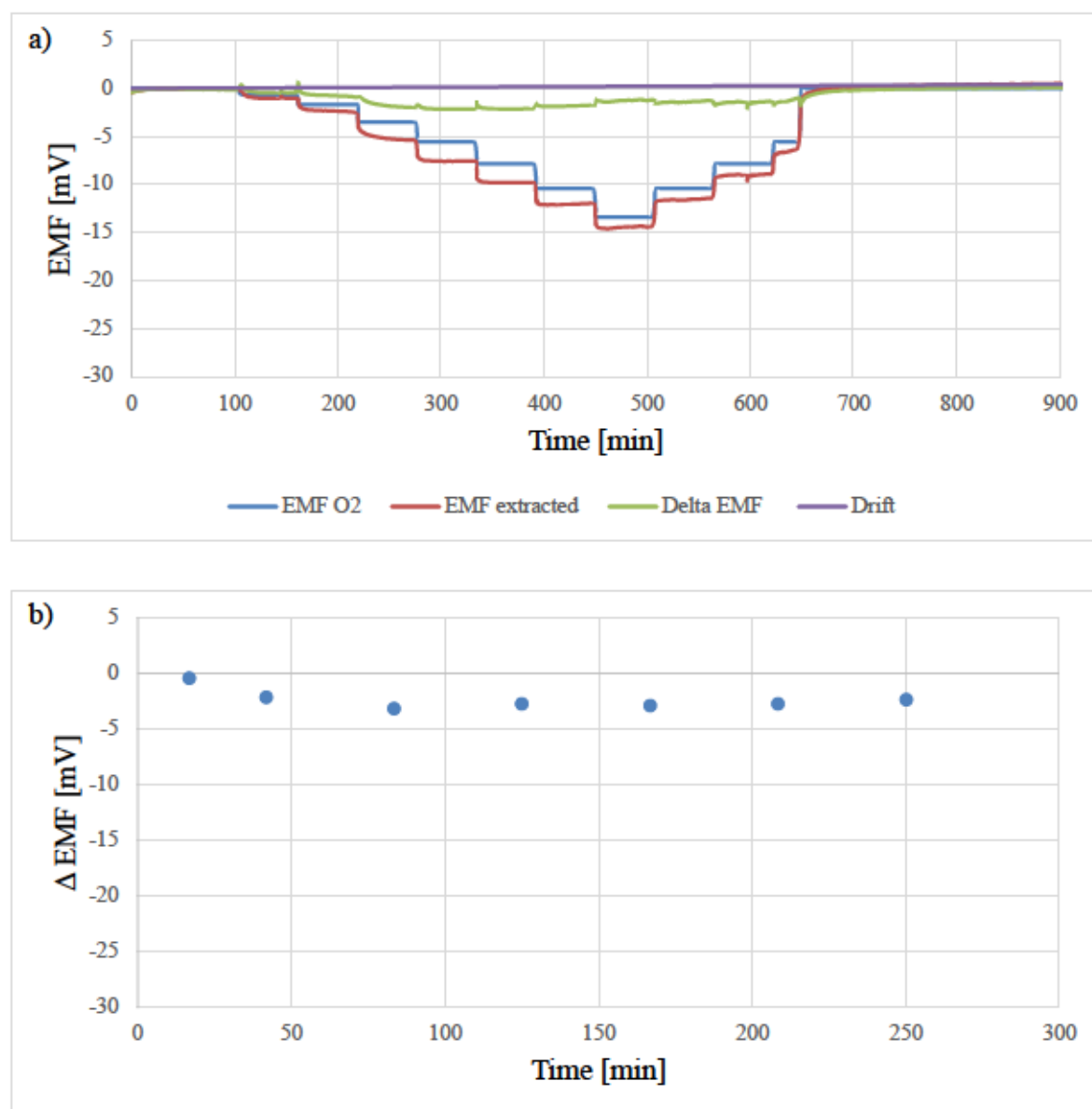


Figure 92. LaFeO₃-850-YSZ95 under NO₂ at 600°C.

After increasing of temperature up to 600°C drift is no longer present. Drift of base line is in range of measurements error (see Figure 92). Δ EMF under 250 ppm is -2,4 mV. Increased of temperature affect sensitivity of the sensor. In 500 °C sensor under 250 ppm sensor gives response of -11,93 mV. Sample LaFeO₃-850-YSZ95 show low sensitivity towards NO₂ at 600°C. Increase of temperature affect response time. In this temperature ion conductivity reach sufficient level to allow reach equilibrium under NO₂.

6 EXTENDED SUMMARY AND PERSPECTIVES

As part of this doctoral thesis, the microstructure and sensing properties towards NO_2 of thin layers of LaCoO_3 and LaFeO_3 were investigated. The thin films were deposited on three different substrates (Si, YSZ9,5, YSZ 3,5) using the PLD technique. The aim of this research was to produce nanocrystalline thin films sensitive towards NO_2 . The role of deposition parameters and substrate on the microstructure and chemical composition of the thin films was studied by XRD, SEM with EDS, TEM, XPS and AFM. The thin films were used as sensing electrode in resistance and potentiometric sensors, and sensitivity, detection times and electromotive force were measured at different temperatures and for different gas concentration (in the ppm range).

Thin films of LaCoO_3 and LaFeO_3 were deposited using the PLD technique at different temperatures $T = 750, 850, 1000^\circ\text{C}$. Other process parameters such as gas pressure in the chamber, energy density on the surface of the target, number of pulses were not varied in this study and selected based on literature and preliminary research. Deposition temperatures were chosen so that the deposited layers had a crystalline structure with nanometric grains. The structure and microstructure of all samples were characterized using XRD, SEM, EDS, TEM, AFM. Measurements in NO_2 were carried out on thin films deposited on YSZ substrate.

From the three deposition temperatures, 850°C is the one who led to single phased nanocrystalline thin films, with a low number of droplets on the surface, and without cracks. At a deposition temperature of 1000°C , there was a reaction between the Si substrate and the deposited layer, resulting in the formation of a La_2SiO_7 layer. In thin films deposited on YSZ9,5, at this temperature, an additional La_2O_3 phase was identified in the deposited layer. Thin films deposited at 750°C were subject to cracks, and many droplets (nanoclusters) at their surface. Because the deposited thin films did not meet the criteria set out in the thesis, they were not subjected to tests in gases.

Chemical analysis (EDS, XPS) showed that LaMO_3 ($M=\text{Co}, \text{Fe}$) thin films are non-stoichiometric, with 55 at.% La, 45 at.% M, and the formula should be written $\text{LaM}_{0.8}\text{O}_{3.5}$. This could be linked to the oxygen gas pressure in the deposition chamber. XPS revealed a small

amount of Fe^{4+} in the LaFeO_3 layers. Whatever the substrate, the grains had a columnar growth, with grain width in the nanometer range. The morphology of substrate (T-YSZ) strongly affected the morphology of the deposited thin films. Contrary to Si and C-YSZ, which are monocrystalline with a (100) orientation, T-YSZ substrate is polycrystalline with a granular structure and a highly developed bumpy surface. However, the thin films deposited on this substrate completely covered the substrate, up to the grain boundaries, maintaining the columnar structure typical of PLD.

Thin layers of LaCoO_3 deposited at $T = 750, 850^\circ\text{C}$ have the expected rhombohedral crystalline structure, with cell parameters lower than the bulk material. Changes in the size of the unit cell can be explained by the presence of Co vacancies that affect also the cobalt oxidation state, hence the ionic radius. The crystallite size determined by the W-H method and observation by SEM showed an increase in the size of crystallites and grains with the deposition temperature. The surface morphology is also affected by deposition temperature.

In the case of thin films of LaCoO_3 -850-Si, LaCoO_3 -850-YSZ95 the grains are faceted with triangular shape, while LaCoO_3 -750-Si, LaCoO_3 -750-YSZ95 the grains are smaller and do not appear faceted. Only the deposition temperature is different for these thin films, thus the ratio of substrate temperature to the melting point of LaCoO_3 . According to the Thornton model, at unchanged gas pressure, a T/T_m ratio from 0.4-0.45 corresponds to the border of zone 3 and zone 2, where a change of morphology is noticeable. TEM analysis showed that thin films deposited at $T = 750, 850^\circ\text{C}$ have columnar structure, with a grain width around 30 nm at 750°C and varying from 30 to 75 nm at 850°C . The thickness of the films varies from 60 nm (750°C YSZ) to 180 nm (850°C Si). Columnar grains have mainly a triangular section and flat termination, but some of the grains have rectangular section with a 4-facets tip termination. The determination of the crystallographic exposed facets by HREM indicates that for the two shapes, the same planes are exposed, corresponding to $\{100\}_c$ in case of Si substrate. Somewhat different results were obtained on C-YSZ substrate, with $\{110\}_c$ exposed facets, but further investigations on the C-YSZ samples are needed to confirm this result. The results of TEM analyzes are very important because it is the surface orientation that affects the properties (sensitivity) of gas-sensitive layers.

LaFeO₃ perovskite was the second material tested as potential SE layer in gas sensors application. Thin films were produced with the same parameters as thin layers of LaCoO₃.

Thin films of LaFeO₃ also have the expected orthorhombic crystalline structure with a mean 28 nm crystallite size for $T = 750\text{ }^{\circ}\text{C}$ and 40 nm for $T = 850\text{ }^{\circ}\text{C}$. LaFeO₃ similarly to LaCoO₃ present a decrease of the cell volume caused by the Fe deficiency and a change in the oxidation state. The morphology of the layer's surface deposited at $T = 750, 850\text{ }^{\circ}\text{C}$ does not change with the deposition temperature and is the same for thin films deposited on Si and YSZ95. On the surface there are two types of shape, elongated flat grains surrounded by bunched of smaller grains with tip termination. Nanoclusters with sizes of 50–100 nm are also observed. AFM analysis showed a decrease in R_{max} and R_q parameters as the temperature increase as a result of grain and crystallite growth. Research using TEM revealed columnar structure of thin films and the fact that the columns, similarly to LaCoO₃ thin films, have two types of termination, flat one and tip like, although the morphology of the surface if the layers looks different. High resolution transmission microscopy allowed to determine crystallographic planes of the exposed facets. For both shapes, the exposed facets are $\{101\}_O = \{001\}_C$. DFT calculations by X. Wang et al. [119] showed that in LaFeO₃ on surface created by $(010)_O$ planes high oxygen adsorption occurs. This leads to high reactivity towards oxygen. But no study about $\{101\}_O$ planes reactivity could be found in literature.

The sensing properties of the thin films were studied by resistance and electrochemical measurements in the presence of NO₂. These tests were carried out on the layers LaCoO₃-750-YSZ95, LaCoO₃-850-YSZ95, LaCoO₃-850-YSZ35, LaFeO₃-750-YSZ95, LaFeO₃-850-YSZ95, and LaFeO₃-850-YSZ35.

By analyzing the changes in resistance of LaCoO₃-YSZ95 thin films under NO₂ it was observed that the films weakly reacted to NO₂ from 2.5 ppm to 100 ppm in range of temperatures from 450 °C to 550 °C, with low sensitivity varying between 4 to 15% for layers on C-YSZ substrate. Thin film deposited at 850° C shows higher sensitivity towards NO₂ than thin film deposited at 750° C. As NO₂ concertation increased, sensitivity increased up to 100 ppm. Sensitivity also increased with the measurement temperature and the highest sensitivity was at $T = 550^{\circ}\text{C}$. Based on the results obtained, the reaction time was determined, which for $T = 550^{\circ}\text{C}$ is 25 s under 50 ppm of NO₂. Thin films of LaCoO₃-850-YSZ35 are characterized by fast response time and wide range of working temperatures from 50 °C to 450°C, and higher sensitivity than

thin film deposited on C-YSZ (up to 45%). The increase of sensitivity between LaCoO₃-850-YSZ95 and LaCoO₃-850-YSZ35 is induced by change of thin film morphology.

As for LaCoO₃, thin films of LaFeO₃ deposited at 750 °C on C-YSZ have lower sensitivity than those deposited at 850 °C. This could be linked to the occurrence of high density of nanoclusters on the surface of thin film deposited at 750 °C and thus, to a reduction of the active surface.

The LaFeO₃-850-YSZ95 thin film showed very high sensitivity, up to 4000% at 150°C for 50 ppm NO₂. LaFeO₃-850-YSZ95 showed response towards NO₂ even at ambient temperature. The analysis of resistance changes of LaFeO₃-YSZ95 as a function of temperature showed a change in the type of response for LaFeO₃-850-YSZ95 at T = 350°C from type n to type p. Change in response type was already observed in literature. At high temperature (400 °C), with a p-type response, the thin films are characterized by a short response time; t = 5 s for T = 450 °C. The response of LaFeO₃-850-YSZ95 towards reducing gas such as NH₃ and CO is very low compared to the sensitivity towards NO₂, indicating a selectivity of the thin film. LaFeO₃ thin films deposited on YSZ35 are characterized by no sensitivity toward NO₂.

Electrochemical sensors operating temperatures are in range of 400°C to 1000°C. Electrochemical test was done in range 400–600°C with different NO₂ and O₂ concentration. 400°C is not a high enough to start ion conductivity of the substrate. Temperatures higher than 600°C were not possible due to experimental setup. Because of the working principle of EGS sensors, substrate plays an important role in sensor performance. At 500°C, thin films deposited at 850°C on YSZ35 are characterized by faster response times than thin films deposited on YSZ95. This can be explained by the fact that, due to presence of grain boundaries, YSZ35 have higher ion conductivity in lower temperatures than YSZ95. LaCoO₃-750-YSZ35 is not sensitive towards NO₂. As for chemical sensing, electrochemical sensing with LaFeO₃-850-YSZ95 and LaFeO₃-850-YSZ35 are showing higher activity towards NO₂ than LaCoO₃ thin films.

LaCoO₃-850 -YSZ95 or -YSZ35 as well as LaFeO₃-850 -YSZ95 or -YSZ35 do not show sensitivity towards NO₂ at 600°C. Non sensitivity towards NO₂ at 600°C can be explained by decomposition of NO₂ at this temperature (NO₂ → NO + O₂).

Perspectives:

LaFeO₃ layers showed much better performances than LaCoO₃ layers. Created with the same protocol, these layers though differ chemically (M = Co, Fe), and in structure (orthorhombic, rhombohedral); however, both are deformed cubic perovskites. The morphology of the grains is also different resulting in the exposure of different facets to the gas of interest. In the future, further investigations are should be completed in order to link the exposed facets to the sensitivity of the layers, coupled with DFT calculations about the reactivity of these faces.

In addition, to check the influence of the non-stoichiometry of the layer in the sensing properties, stoichiometric thin films should be grown and their sensing properties compared to those of this work

Highlights :

1. PLD method allowed to deposit LaMO₃ (Co, Fe) thin films with columnar nanograins whatever the substrate (Si, C-YSZ, T-YSZ).
2. A deposition temperature of 850°C and an oxygen pressure of 40 mTorr led to single phased layers, slightly M deficient.
3. The exposed facets of the LaFeO₃ grains corresponds to {101}_O = {001}_C planes, building to types of shape termination.
4. Thin film LaFeO₃-850-YSZ95 showed very high sensitivity towards NO₂ as resistance gas sensor and works also as electrochemical gas sensor.
5. Thin films of LaCoO₃-T-S showed low sensitivity towards NO₂ as resistance gas sensor and as electrochemical one
6. The difference in sensitivity could be linked to different exposed facets in LaFeO₃ and LaCoO₃. The exposed facets of the LaCoO₃ grains correspond to {110}_C, but this has to be confirmed by further investigations
7. Use of YSZ35 as a substrate in electrochemical gas sensor allows to decrease working temperature and decrease response time. YSZ35 can replace standard Cubic-YSZ for electrochemical sensor as new flexible substrate.

7 FIGURE INDEX

Figure 1. SCR system in diesel engines developed to reduce NO _x emissions [2].	8
Figure 2. Gas sensor in the modern car exhaust system [3].	8
Figure 3. Illustration of a) the typical construction of a mixed-potential type YSZ-based sensor, including b) the electrochemical reactions that occur at the SE/YSZ interface and c) the equilibrium RE reaction of O ₂ at the interface of RE/YSZ, as well as d) the SE layer [20].	12
Figure 4. Schematic of current flow in a biased sensing element. O ²⁻ represents an oxygen ion in the YSZ substrate [3].	16
Figure 5. Influence of pore size and grain size on catalytic activity and NO ₂ decomposition on the SE surface [38].	17
Figure 6. Response vs. time for sensors Ia, IIa, and IIIa exposed to 500 ppm NO in 10% O ₂ at 550 °C. The sensing electrodes had initially the same thickness but different sintering temperatures of 1000, 1100 and 1200°C, respectively. The initial baseline at ~0mV represents the equilibrium response prior to introduction of the NO into the gas stream [41].	19
Figure 7. Resistance gas sensor equipped with membrane and heater [43].	20
Figure 8. Oxygen partial pressure as a function of temperature illustrating the desorption of oxygen from a semiconductor (ZnO) a) physical adsorption, b) chemisorption, c) surface defects, d) volume defects [25].	21
Figure 9. Configuration of a resistive gas sensor: (a) top view, (b) cross section view.	21
Figure 10. Sensitivity of perovskites in 60 ppm of NO ₂ [25].	22
Figure 11. a) N-type and b) P-type core-shell formation [59].	25
Figure 12. Gas sensing mechanism and equivalent circuit of n-type oxide semiconductors [60].	25
Figure 13. Sensing layer of p-type semiconductor [60].	26
Figure 14. Changes in electrical conductivity as a function of oxygen partial pressure for Mo ₂ -B ₂ O ₃ [61].	27
Figure 15. Example of cubic perovskite structure.	28
Figure 16. LaFeO ₃ structure, showing the tilting of the octahedra, in the Pnma setting.	29
Figure 17. LaCoO ₃ rhombohedral cell, showing the rotation of octahedra.	31
Figure 18. Co ³⁺ and Co ⁴⁺ spin states [74].	32
Figure 19. Phase diagram of Y ₂ O ₃ -ZrO ₂ [87].	35
Figure 21. PLD Aperture [94].	37
Figure 22. Scheme of a Nd:YAG laser [92].	38
Figure 23. Scheme of excimer laser [92].	39
Figure 24. Interaction of the laser on target.	40
Figure 25. Structure-zone diagram for thin films by Thornton [103].	41
Figure 26. Schematic three-zone model for the temperature dependence of the growth thin films. T _s /T _m represents the ratio of the substrate temperature to the melting point [104].	41
Figure 27. Impact of process parameters on thin films structure [63].	42

Figure 28. Scheme of conventional cross section sample preparation.....	50
Figure 29. Tripod method [110].	51
Figure 30. Schematic of the resistance gas experiment [112].	52
Figure 31. First stage of gas sensor preparation. Second stage of gas sensor preparation – SE deposition. Third stage of gas sensor preparation - Pt contact.	53
Figure 32. Prepared sample for resistance measurements a) Top view b) cross-section	54
Figure 33. Fully equipped electrochemical gas sensor.....	54
Figure 34. Schematic representation of cell.	55
Figure 35. X-Ray Diffraction pattern of a) LaCoO ₃ _750-Si, b) LaCoO ₃ _850-Si, c) LaCoO ₃ _1000-Si. The peaks are indexed in the hexagonal settings.	57
Figure 36. SEM micrographs of a) LaCoO ₃ -750-Si - 10x b) LaCoO ₃ -750-Si - 50x, c) LaCoO ₃ -850-Si - 10x, d) LaCoO ₃ -850-Si - 50x, e) LaCoO ₃ -1000-Si - 10x f) LaCoO ₃ -1000-Si - 50x.	59
Figure 37. AFM images of LaCoO ₃ -Si, a) LaCoO ₃ -750-Si, b) LaCoO ₃ -850-Si c) LaCoO ₃ -1000-Si.....	60
Figure 38. TEM images of LaCoO ₃ _750-Si a) columnar structure of the layer , and FFT of one grain b) low mag image of the layer, showing the shape of the grains termination, and the occurrence of nanocluster.....	61
Figure 39. TEM images of LaCoO ₃ _850-Si , along with one FFT from HREM image.	62
Figure 40. TEM images of LaCoO ₃ 1000C-Si a) grain termination, b) thin films division c) high magnification d) FFT	63
Figure 41. X-Ray Diffraction patterns of a) LaCoO ₃ -750-YSZ95, b) LaCoO ₃ -850-YSZ95, c) LaCoO ₃ - 1000-YSZ95. Indexation in the hexagonal settings.	65
Figure 43. SEM micrographs of LaCoO ₃ -YSZ95 a,b) LaCoO ₃ -750-YSZ95 c,d) LaCoO ₃ -850-YSZ95 e,f) LaCoO ₃ -1000-YSZ95.	67
Figure 44. Surface morphology of a) LaCoO ₃ -750-YSZ95 b) LaCoO ₃ -850-YSZ95 c) LaCoO ₃ -1000- YSZ95.	68
Figure 45. TEM Cross-section of LaCoO ₃ -750-YSZ95 a) low magnification b) details of the LaCoO ₃ grains.....	69
Figure 46. TEM Cross-section of LaCoO ₃ -850-YSZ95 a) low magnification image of the thin film b) evidence of columnar structure c) HREM image near the substrate along with FFT d) STEM- HAADF image of the top of one grain, along with FFT	70
Figure 47. TEM Cross-section of a) LaCoO ₃ -1000-YSZ95 b) columnar structure	71
Figure 48. XRD results of LaCoO ₃ -YSZ35 a) 750 °C b) 850 °C	72
Figure 49. SEM images of LaCoO ₃ -YSZ35 a) LaCoO ₃ -750-YSZ35 low mag. b) a) LaCoO ₃ -750 -YSZ35 thin film grains c) LaCoO ₃ -850-YSZ35 low magnification d) LaCoO ₃ -850-YSZ35 thin films grains.	73
Figure 50. AFM of LaCoO ₃ -YSZ35 a) LaCoO ₃ -750-YSZ35 b) LaCoO ₃ -850-YSZ35.....	74
Figure 51. TEM image of LaCoO ₃ -850-YSZ35.....	75
Figure 52. X-Ray Diffraction pattern of LaFeO ₃ -Si thin films indexed in the Pnma setting a) LaFeO ₃ - 750-Si, b) LaFeO ₃ -850-Si, c) LaFeO ₃ -1000-Si.....	77
Figure 53. SEM micrographs of a) Surface of LaFeO ₃ -750-Si with low mag. b) Morphology of LaFeO ₃ - 750-Si c) Surface of LaFeO ₃ -850-Si with low mag. d) Morphology of LaFeO ₃ -850-Si e) Surface of LaFeO ₃ -1000-Si with low mag. f) Morphology of LaFeO ₃ -1000-Si.	78
Figure 54. SEM micrographs of LaFeO ₃ -750- Si revealing surface microstructure in “flat” region.	79

Figure 55. Surface morphology of a) LaFeO_3 -750-Si b) LaFeO_3 -850-Si c) LaFeO_3 -1000-Si.....	80
Figure 56. TEM Cross-section of a) LaFeO_3 -750-Si b) LaFeO_3 -850-Si c) LaFeO_3 -1000-Si d) LaFeO_3 -1000-Si.....	82
Figure 57. Cross-section of LaFeO_3 -850-Si with FFT indexed in the Pnma setting a) flat termination, b) tip region, c) nanocluster d) surface morphology	83
Figure 58. TEM Cross-section of LaFeO_3 -1000-Si a) cross-section b) evidence of two phases in the thin film c) columns	84
Figure 59. X-Ray Diffraction patterns indexed in the Pnma setting of a) LaFeO_3 -750-YSZ95 b) LaFeO_3 -850-YSZ95 c) LaFeO_3 -1000-YSZ95	86
Figure 60. SEM micrographs of a) LaFeO_3 -750-YSZ95 b) LaFeO_3 -750-YSZ95 c) LaFeO_3 -850-YSZ95 d) LaFeO_3 -850-YSZ95 e) LaFeO_3 -1000-YSZ95 f) LaFeO_3 -1000-YSZ95.....	87
Figure 61. AFM of a) LaFeO_3 -750-YSZ95 b) LaFeO_3 -850-YSZ95 c) LaFeO_3 -1000-YSZ95.	88
Figure 62. XPS Spectra – a) Atomic concentration in LaFeO_3 -750-YSZ95 profile b) Atomic concentration in LaFeO_3 -850-YSZ95 c) Atomic concentration in - LaFeO_3 -1000-YSZ95..	90
Figure 63. XPS Analysis of a) C 1s LaFeO_3 -750-YSZ95 b) O 1s LaFeO_3 -750-YSZ95 c) LaFeO_3 -850-YSZ95 C 1s d) LaFeO_3 -850-YSZ95 O 1s e) LaFeO_3 -1000-YSZ95 C 1s e) LaFeO_3 -1000-YSZ95 O 1s.....	91
Figure 64. XPS Analysis of La 3d of thin films LaFeO_3 -750-YSZ95 a) 750 °C b) 850 °C c) 1000 °C	92
Figure 65. XPS results a) The Fe 2p spectrum obtained from the as received surface (before sputtering). b) LaFeO_3 _750_YSZ95 c) LaFeO_3 _850_YSZ95 d) LaFeO_3 _1000_YSZ95	93
Figure 66. TEM image of LaFeO_3 -750-YSZ95	94
Figure 67. TEM images of LaFeO_3 -850-YSZ95. a) evidence of flat and pointed grain termination b) columnar structure of the grain c) STEM-HAADF image of a “pointed” region along with FFT d) STEM HAADF image of a flat region along with FFT	95
Figure 68. TEM images of LaFeO_3 -1000-YSZ95. a) low magnification image showing the microstructure of the thin film. b) Dark field image showing the columnar structure of the layer. c) high magnification image showing pointed grain termination, with the corresponding FFT, d) high magnification image showing pointed grain termination, with the corresponding FFT	97
Figure 69. X-Ray Diffraction patterns of a) LaFeO_3 -750-YSZ35 b) LaFeO_3 -850-YSZ35.....	98
Figure 70. SEM micrographs of a) LaFeO_3 -750-YSZ35 b) LaFeO_3 -750-YSZ35 c) LaFeO_3 -850-YSZ35 d) LaFeO_3 -850-YSZ35.....	99
Figure 71. High magnification SEM micrograph of LaFeO_3 -850-YSZ35	100
Figure 72. AFM of a) LaFeO_3 -750-YSZ35 b) LaFeO_3 -850-YSZ35	101
Figure 73. cross section TEM images of LaFeO_3 -850-YSZ35 a) low magnification image showing the homogeneous covering of the substrate b) droplets and columnar grains c) STEM-HAADF image of the layer at a grain boundary of the substrate along with FFT d) termination of LaFeO_3 grains along with FFT	102
Figure 74. LaCoO_3 -750-ysz95 response at 500°C exposed to 50 ppm of NO_2	105
Figure 75. Response under NO_2 for LaCoO_3 -750-YSZ95 at a) 450°C b) 500°C c) 550°C	106
Figure 76 Response of LaCoO_3 -750-YSZ95 at 550 °C a) 10 ppm, b) 20 ppm, c) 50 ppm d) 100 ppm.	107
Figure 77. Response of LaCoO_3 -850-ysz95 a) 500 °C b) 550 °C under 50 ppm of NO_2	108
Figure 78. LaCoO_3 -850-YSZ95 response under different NO_2 concentration.....	109

Figure 79. Reaction of LaCoO_3 -850-YSZ35 under NO_2 a) 50°C b) 100°C c) 150°C d) 200°C e) 250°C f) 300°C g) 350°C h) 400°C	111
Figure 80. LaCoO_3 -850-YSZ35 resistance in different temperatures.	112
Figure 81. Response of LaFeO_3 -750-YSZ95 in a) 200 °C b) 250 °C c) 300 °C d) 350 °C e) 400 °C under 50 ppm of NO_2	114
Figure 82. Response of LaFeO_3 -750-YSZ95 a) 2,5 ppm at 200 °C b) a) 5 ppm in 200 °C c) 10 ppm in 200 °C d) 20 ppm in 200 °C e) 50 ppm f) 100 ppm	115
Figure 83. LaFeO_3 -850-YSZ95 a) 25°C, b) 50°C, c) 100°C, d) 150°C, e) 200°C, f) 250°C g) 300 C h) 350°C i) 400°C j) 450°C response under 50 ppm of NO_2	117
Figure 84. Response time in temperature LaFeO_3 -850-YSZ95	119
Figure 85. Sensitivity of LaFeO_3 -850-YSZ in 200 °C in NO_2	119
Figure 86. LaFeO_3 -850-YSZ95 Response under 50 ppm of CO	120
Figure 87. LaFeO_3 -850-YSZ95 Response under 50 ppm of NH_3	121
Figure 88. LaCoO_3 -750-YSZ35 response under NO_2 in a) 500°C c) 600°C	123
Figure 89. LaCoO_3 -850-YSZ35 at 500°C	124
Figure 90. LaCoO_3 -850-YSZ95 at 500°C	125
Figure 91. LaFeO_3 -750-YSZ35 under NO_2 at a) 500°C b) 600°C	127
Figure 92. LaFeO_3 -850-YSZ35 at 500°C	128
Figure 93. LaFeO_3 -850-YSZ95 under NO_2 at 500°C	129
Figure 94. LaFeO_3 -850-YSZ95 under NO_2 at 600°C	130

8 TABLE INDEX

Table 1. Examples of gas sensor application in various industries according to [1].....	7
Table 2. Electrical conductivity values of solid electrolytes at 600 °C [8] – [11]	13
Table 3. Electrode thickness and NO sensitivity for the sensors according to [41].....	19
Table 4. Crystal structure and properties of LaFeO ₃	30
Table 5. Structure and properties of LaCoO ₃	31
Table 6. Laser specification [91].....	37
Table 7. Excimer laser characteristic.....	39
Table 8 Parameters of mechanical alloying process.....	46
Table 9 Sample preparation for PLD process.....	46
Table 10. PLD parameters.....	47
Table 11. Sample list of LaFeO ₃	47
Table 12. Sample list of LaCoO ₃	47
Table 13. Parameters of PIPS process.....	50
Table 14. Parameters of Electrodes deposition	53
Table 15. Refinement parameters obtained in MAUD software.....	58
Table 16. EDS results of LaCoO ₃ -850-Si.....	59
Table 17 Roughness parameters of LaCoO ₃ -T-Si.....	61
Table 18. FFT results of LaCoO ₃ -750-Si from Figure 38.....	62
Table 19. FFT LaCoO ₃ -850-Si from Figure 39d.....	62
Table 20. FFT LaCoO ₃ -1000-Si from Figure 40d.....	63
Table 21. MAUD refinement results for LaCoO ₃ -YSZ95	65
Table 22. AFM results of LaCoO ₃ -YSZ95.....	68
Table 23. FFT results of LaCoO ₃ -850-YSZ95.....	71
Table 24. Roughness parameters of LaCoO ₃ -YSZ35.....	74
Table 25. MAUD results of LaFeO ₃ -Si, in the Pbnm space group.....	78
Table 26. Roughness parameters of LaFeO ₃ -Si thin films	81
Table 27. FFT from LaFeO ₃ -850-YSZ95.....	83
Table 28. FFT of LaFeO ₃ -1000-Si	85
Table 29. MAUD refinement results of LaFeO ₃ -YSZ95	86
Table 30. Roughness parameters of LaFeO ₃ -YSZ95	89
Table 31. FFT of LaFeO ₃ -850-YSZ95	96
Table 32. FFT results of LaFeO ₃ -1000_YSZ95	97
Table 33. Roughness parameters of LaFeO ₃ -YSZ35	101

Table 34. FFT of LaFeO ₃ -850-YSZ35	103
Table 35. Sensitivity of LaCoO ₃ -750-YSZ95 for 50 ppm of NO ₂ at 500°C	105
Table 36. Sensitivity of LaCoO ₃ -750-YSZ95 under 50 ppm of NO ₂	106
Table 37. Sensitivity of LaCoO ₃ -750-YSZ95 at 550 °C for different concentration of NO ₂	107
Table 38. Influence of temperature on sensitivity of LaCoO ₃ -850-YSZ95	109
Table 39. Sensor response in 550 °C under different gas concertation.....	110
Table 40. Sensitivity and response time of LaFeO ₃ -750-YSZ 95.....	114
Table 41. Sensitivity and response time of LaFeO ₃ -750-YSZ95 in 200 °C.....	116
Table 42. LaFeO ₃ -850-YSZ95 Response under NO ₂	118
Table 43. LaFeO ₃ -850-YSZ95 Response under 50 ppm of CO.....	120
Table 44. LaFeO ₃ -850-YSZ95 Response under 50 ppm of NH ₃	121

9 REFERENCES

- [1] J. R. Stetter and W. R. Penrose, "Sensors, Chemical Sensors, Electrochemical Sensors, and ECS," *J. Electrochem. Soc.*, vol. 150, no. 2, p. S11, 2003.
- [2] "Halon Lubricants - Midwest Oil Lubricant Distributor," [Online]. Available: <http://www.halon.com/products-and-services/def-products/>. [Accessed 16 10 2019].
- [3] D. L. West, F. C. Montgomery and T. R. Armstrong, "'NO-selective' NO_x sensing elements for combustion exhausts," *Sens. Actuators B-Chem.*, Vols. 111-112, pp. 84-90, Nov. 2005.
- [4] J.-C. Ding, H.-Y. Li and X. Guo, "CO sensing mechanism of LaCoO₃," *Solid State Ion.*, vol. 272, pp. 155-159, Apr. 2015.
- [5] J. Wu, "A Vehicle Exhaust NO_x Electrochemical Sensor Based on Au-Yttria Stabilized Zirconia Nanocomposite," *Int. J. Electrochem. Sci.*, vol. 12, pp. 1734-1741, Mar. 2017.
- [6] V. V. Plashnitsa, T. Ueda, P. Elumalai, T. Kawaguchi and N. Miura, "Zirconia-based planar NO₂ sensor using ultrathin NiO or laminated NiO-Au sensing electrode," *Ionics*, vol. 14, no. 1, pp. 15-25, 2008.
- [7] O. Alev, E. Şennik, N. Kılınç and Z. Z. Öztürk, "Gas Sensor Application of Hydrothermally Growth TiO₂ Nanorods," *Procedia Eng.*, vol. 120, pp. 1162-1165, 2015.
- [8] B. Timmer, W. Olthuis and A. van den Berg, "Ammonia sensors and their applications—a review," *Sens. Actuators B-Chem.*, vol. 107, no. 2, pp. 666-677, Jun. 2005.
- [9] J. W. Fergus, "A review of electrolyte and electrode materials for high temperature electrochemical CO₂ and SO₂ gas sensors," *Sens. Actuators B Chem.*, vol. 134, no. 2, pp. 1034-1041, 2008.

- [10] Y. Wang and J. T. W. Yeow, "A review of carb on nanotubes-based gas sensors," *J. Sens.*, vol. 2009, pp. 1-24, 2009.
- [11] C. S. Moon, H.-R. Kim, G. Auchterlonie, J. Drennan and J.-H. Lee, "Highly sensitive and fast responding CO sensor using SnO₂ nanosheets," *Sens. Actuators B-Chem.*, vol. 131, no. 2, pp. 556-564, May 2008.
- [12] R. M. Prasad, A. Gurlo, R. Riedel, M. Hübner, N. Barsan and U. Weimar, "Microporous ceramic coated SnO₂ sensors for hydrogen and carbon monoxide sensing in harsh reducing conditions," *Sens. Actuators B-Chem.*, vol. 149, no. 1, pp. 105-109, Aug. 2010.
- [13] M. Zhang, T. Xue, S. Xu, Z. Li, Y. Yan and Y. Huang, "Adverse effect of substrate surface impurities on O₂ sensing properties of TiO₂ gas sensor operating at high temperature," *Ceram. Int.*, vol. 43, no. 7, pp. 5842-5846, May 2017.
- [14] X. Deng, L. Zhang, J. Guo, Q. Chen and J. Ma, "ZnO enhanced NiO-based gas sensors towards ethanol," *Mater. Res. Bull.*, vol. 90, pp. 170-174, Jun. 2017.
- [15] B. Urasinska-Wojcik, T. A. Vincent, M. F. Chowdhury and J. W. Gardner, "Ultrasensitive WO₃ gas sensors for NO₂ detection in air and low oxygen environment," *Sens. Actuators B-Chem.*, vol. 239, pp. 1051-1059, Feb. 2017.
- [16] A. Dankeaw, G. Pongchan, M. Panapoy and B. Ksapabutr, "In-situ one-step method for fabricating three-dimensional grass-like carbon-doped ZrO₂ films for room temperature alcohol and acetone sensors," *Sens. Actuators B-Chem.*, vol. 242, pp. 202-214, Apr. 2017.
- [17] Y. Hu, O. K. Tan, J. S. Pan, H. Huang and W. Cao, "The effects of annealing temperature on the sensing properties of low temperature nano-sized SrTiO₃ oxygen gas sensor," *Sens. Actuators B-Chem.*, vol. 108, no. 1-2, pp. 244-249, Jul. 2005.
- [18] R. Sorita and T. Kawano, "A highly selective CO sensor using LaMnO₃ electrode-attached zirconia galvanic cell," *Sens. Actuators B-Chem.*, vol. 40, no. 1, pp. 29-32, May 1997.

- [19] S. Czekaj, F. Nolting, L. Heyderman, P. Willmott and G. van der Laan, "Sign dependence of the X-ray magnetic linear dichroism on the antiferromagnetic spin axis in LaFeO₃ thin films," *Phys. Rev. B*, vol. 73, pp. 1-4, Jan. 2006.
- [20] N. Miura, T. Sato, S. A. Anggraini, H. Ikeda and S. Zhuiykov, "A review of mixed-potential type zirconia-based gas sensors," *Ionics*, vol. 20, no. 7, pp. 901-925, Jul. 2014.
- [21] S. Capone, P. Siciliano, F. Quaranta, R. Rella, M. Epifani and L. Vasanelli, "Moisture influence and geometry effect of Au and Pt electrodes on CO sensing response of SnO₂ microsenors based on sol-gel thin film," *Sens. Actuator B-Chem.*, vol. 77, no. 1-2, pp. 503-511, Jun. 2001.
- [22] S. Saukko and V. Lantto, "Influence of electrode material on properties of SnO₂-based gas sensor," *Thin Solid Films*, vol. 436, no. 1, pp. 137-140, Jul. 2003.
- [23] H. Gourari, M. Lumbreras, R. Van Landschoot and J. Schoonman, "Electrode nature effects on stannic oxide type layers prepared by electrostatic spray deposition," *Sens. Actuators B Chem.*, vol. 58, no. 1-3, pp. 365-369, Sep. 1999.
- [24] X. Zhou, Y. Xu, Q. Cao and S. Niu, "Metal-semiconductor ohmic contact of SnO₂-based ceramic gas sensors," *Sens. Actuators B-Chem.*, vol. 41, no. 1-3, pp. 163-167, Jun. 1997.
- [25] T. Pisarkiewicz, "Mikrosensory gazów / gas microsenors," Uczelniane Wydaw. Nauk.-Dydakt. AGH im. S. Staszica, Kraków, 2007.
- [26] N. D. Tho and e. al., "High temperature calcination for analyzing influence of 3d transition metals on gas sensing performance of mixed potential sensor Pt/YSZ/LaMO₃ (M = Mn, Fe, Co, Ni)," *Electrochimica Acta*, vol. 190, pp. 215-220, Feb. 2006.
- [27] Z. Duan, Y. Zhang, Y. Tong, H. Zou, J. Peng and X. Zheng, "Mixed-Potential-Type Gas Sensors Based on Pt/YSZ Film/LaFeO₃ for Detecting NO₂," *J. Electron. Mater.*, vol. 46, no. 12, pp. 6895-6900, Dec. 2017.
- [28] F. Liu and e. al., "YSZ-based NO₂ sensor utilizing hierarchical In₂O₃ electrode," *Sens. Actuators B-Chem.*, vol. 222, pp. 698-706, Jan. 2016.

- [29] K. Cvejin, M. Šliwa, L. Manjakkal, J. Kulawik, G. Stojanović and D. Szwagierczak, "Impedancemetric NO sensor based on YSZ/perovskite neodymium cobaltite operating at high temperatures," *Sens. Actuators B-Chem.*, vol. 228, pp. 612-624, Jun. 2016.
- [30] A. Chamberland and M. Gauthier, "Solid-State Detectors for the Potentiometric Determination of Gaseous Oxides," *J. Electrochem. Soc.*, vol. 124, no. 10, pp. 1584-1587, 1977.
- [31] G. Hotzel and W. Weppner, "Application of fast ionic conductors in solid state galvanic cells for gas sensors," *Solid State Ion.*, Vols. 18-19, pp. 1223-1227, Jan. 1986.
- [32] N. Miura, S. Yao, Y. Shimizu and N. Yamazoe, "New auxiliary sensing materials for solid electrolyte NO₂ sensors," *Solid State Ion.*, Vols. 70-71, p. 572-577, May 1994.
- [33] P. Pasierb and M. Rekas, "Solid-state potentiometric gas sensors—current status and future trends," *J Solid State Electr.*, vol. 13, no. 1, pp. 3-25, 2009.
- [34] R. Ramamoorthy, P. K. Dutta and S. A. Akbar, "Oxygen sensors: Materials, methods, designs and applications," *J. Mat. Sc.*, vol. 38, no. 21, pp. 4271-4282, Nov. 2003.
- [35] A. Iio, H. Ikeda, S. A. Anggraini and N. Miura, "Sensing characteristics of YSZ-based oxygen sensors attached with BaxSr_{1-x}FeO₃ sensing-electrode," *Solid State Ion.*, vol. 285, pp. 234-238, Feb. 2016.
- [36] A. Cyza, Ł. Cieniek and A. Kopia, "Perovskite La_{1-x}Sr_xFeO₃ Thin Films Deposited by Laser Ablation Process," *Arch. Metall. Mater.*, vol. 61, no. 2, pp. 1063-1067, Jun. 2016.
- [37] A. Cyza, A. Kopia, Ł. Cieniek and J. Kusiński, "Structural Characterization of Sr Doped LaFeO₃ Thin Films Prepared By Pulsed Electron Deposition Method," *Mater. Today Proc.*, vol. 3, no. 8, pp. 2707-2712, 2016.
- [38] A. Kopia, Ł. Cieniek, K. Kowalski and J. Kusiński, "Influence of Sr-Doping on the Structure of LaCoO₃ Thin Films Prepared by Pulsed Laser Deposition," *Solid State Phenom.*, vol. 231, pp. 19-24, Jun. 2015.

- [39] T. Ueda, M. Sakai, K. Kamada, T. Hyodo and Y. Shimizu, "Effects of composition and structure of sensing electrode on NO₂ sensing properties of mixed potential-type YSZ-based gas sensors," *Sens. Actuators B-Chem.*, vol. 237, pp. 247-255, Dec. 2016.
- [40] P. Elumalai, J. Wang, S. Zhuiykov, D. Terada, M. Hasei and N. Miura, "Sensing Characteristics of YSZ-Based Mixed-Potential-Type Planar NO_x Sensors Using NiO Sensing Electrodes Sintered at Different Temperatures," *J. Electrochem. Soc.*, vol. 152, no. 7, pp. H95-H101, 2005.
- [41] P. Pasierb, "Potencjometryczne czujniki gazów / Potentiometric gas sensor," AGH, Krakow, 2010.
- [42] C. O. Park and N. Miura, "Absolute potential analysis of the mixed potential occurring at the oxide/YSZ electrode at high temperature in NO_x-containing air," *Sens. Actuators B-Chem.*, vol. 113, no. 1, pp. 316-319, Jan. 2006.
- [43] S. Zhuiykov and N. Miura, "Development of zirconia-based potentiometric NO_x sensors for automotive and energy industries in the early 21st century: What are the prospects for sensors?," *Sens. Actuators B-Chem.*, vol. 121, no. 2, p. 639-651, Feb. 2007.
- [44] L. Peter Martin, A. Quoc Pham and R. S. Glass, "Effect of Cr₂O₃ electrode morphology on the nitric oxide response of a stabilized zirconia sensor," *Sens. Actuators B-Chem.*, vol. 96, no. 1-2, p. 53-60, Nov. 2003.
- [45] N. Yamazoe, G. Sakai and K. Shimano, "Oxide Semiconductor Gas Sensors," *Catalysis Surveys from Asia*, vol. 7, no. 1, pp. 63-75, April 2003.
- [46] T. L. Hill, "Theory of Physical Adsorption," in *Advances in Catalysis*, vol. 4, V. K. E. R. W.G. Frankenburg, Ed., Academic Press, 1952, pp. 211-258.
- [47] F. Rouquerol, J. Rouquerol and K. Sing, "Introduction," in *Adsorption by Powders and Porous Solids: Principles, Methodology and Applications*, J. R. a. K. S. F. Rouquerol, Ed., Academic Press, 1999, pp. 1-26.

- [48] M. A. Peña and J. L. G. Fierro, "Chemical Structures and Performance of Perovskite Oxides," *Chem. Rev.*, vol. 101, no. 7, p. 1981–2018, July 2001.
- [49] T. Arima, Y. Tokura and J. B. Torrance, "Variation of optical gaps in perovskite-type 3d transition-metal oxides," *Phys. Rev. B*, vol. 48, no. 23, p. 17006–17009, December 1993.
- [50] Y. Tokura, "Metal-insulator phenomena in perovskites of transition metal oxide," *Phys. B Condens. Matter*, Vols. 237-238, pp. 1-5, July 1997.
- [51] P. Wu, J. H. Sun, Y. Y. Huang, G. F. Gu and D. G. Tong, "Solution plasma synthesized nickel oxide nanoflowers: An effective NO₂ sensor," *Mater. Lett.*, vol. 82, p. 191–194, September 2012.
- [52] N. G. Cho, I.-S. Hwang, H.-G. Kim, J.-H. Lee and I.-D. Kim, "Gas sensing properties of p-type hollow NiO hemispheres prepared by polymeric colloidal templating method," *Sens. Actuators B-Chem.*, vol. 155, no. 1, p. 366–371, July 2011.
- [53] N. G. Cho, H.-S. Woo, J.-H. Lee and I.-D. Kim, "Thin-walled NiO tubes functionalized with catalytic Pt for highly selective C₂H₅OH sensors using electrospun fibers as a sacrificial template," *Chem. Commun.*, vol. 47, no. 40, pp. 11300-11302, 2011.
- [54] B. Liu and e. al., "Synthesis and enhanced gas-sensing properties of ultralong NiO nanowires assembled with NiO nanocrystals," *Sens. Actuators B-Chem.*, vol. 156, no. 1, p. 251–262, August 2011.
- [55] X. Song, L. Gao and S. Mathur, "Synthesis, Characterization, and Gas Sensing Properties of Porous Nickel Oxide Nanotubes," *J. Phys. Chem. C*, vol. 115, no. 44, p. 21730–21735, November 2011.
- [56] D. Gopalakrishna, K. Vijayalakshmi and C. Ravidhas, "Effect of pyrolytic temperature on the properties of nano-structured CuO optimized for ethanol sensing applications," *J. Mater. Sci. Mater. Electron.*, vol. 24, no. 3, p. 1004–1011, March 2013.

- [57] M.-R. Yu, G. Suyambrakasam, R.-J. Wu and M. Chavali, "Performance evaluation of ZnO–CuO hetero junction solid state room temperature ethanol sensor," *Mater. Res. Bull.*, vol. 47, no. 7, p. 1713–1718, July 2012.
- [58] X. Liu, J. Zhang, Y. Kang, S. Wu and S. Wang, "Brochantite tabular microspindles and their conversion to wormlike CuO structures for gas sensing," *CrystEngComm*, vol. 158, no. 1, p. 299–303, November 2011.
- [59] Q. Wan and e. al., "Fabrication and ethanol sensing characteristics of ZnO nanowire gas sensors," *Appl. Phys. Lett.*, vol. 84, no. 18, p. 3654–3656, May 2004.
- [60] T. Siciliano, A. Tepore, G. Micocci, A. Serra, D. Manno and E. Filippo, "WO₃ gas sensors prepared by thermal oxidization of tungsten," *Sens. Actuator B-Chem.*, vol. 133, no. 1, p. 321–326, July 2008.
- [61] H.-J. Kim and J.-H. Lee, "Highly sensitive and selective gas sensors using p-type oxide semiconductors: Overview," *Sens. Actuators B-Chem.*, vol. 192, p. 607–627, March 2014.
- [62] N. Barsan, C. Simion, T. Heine, S. Pokhrel and U. Weimar, "Modeling of sensing and transduction for p-type semiconducting metal oxide based gas sensors," *J. Electroceramics*, vol. 25, no. 1, pp. 11–19, August 2010.
- [63] N. Q. Minh and T. Takahashi, *Science and Technology of Ceramic Fuel Cells*, Elsevier Science, 1995.
- [64] P. Lemmens and M. Johnsson, "Crystallography and Chemistry of Perovskites," in *Handbook of Magnetism and Advanced Magnetic Materials*, S. P. H. Kronmüller, Ed., Chichester, John Wiley & Sons, Ltd., 2007, p. hmm411.
- [65] H. N. Krogstad, "Deposition of Thin Film Electrolyte by Pulsed Laser Deposition (PLD) for micro-SOFC Development," Norwegian University of Science and Technology, Trondheim, 2012.

- [66] N. Afifah and R. Saleh, "Synthesis, Characterization and Catalytic Properties of Perovskite LaFeO₃ Nanoparticles," *J. Phys. Conf. Ser.*, vol. 710, p. 012030, April 2016.
- [67] J. W. Seo, E. E. Fullerton, F. Nolting, A. Scholl, J. Fompeyrine and J.-P. Locquet, "Antiferromagnetic LaFeO₃ thin films and their effect on exchange bias," *J. Phys. Condens. Matter*, vol. 20, no. 26, p. 264014, July 2008.
- [68] Z. Dai, C.-S. Lee, Y. Tian, I.-D. Kim and J.-H. Lee, "Highly reversible switching from P- to N-type NO₂ sensing in a monolayer Fe₂O₃ inverse opal film and the associated P–N transition phase diagram," *J. Mater. Chem. A*, vol. 3, no. 7, p. 3372–3381, February 2015.
- [69] S. B. Adler, "Factors Governing Oxygen Reduction in Solid Oxide Fuel Cell Cathodes," *Chem. Rev.*, vol. 104, no. 10, p. 4791–4844, October 2004.
- [70] J. B. Goodenough, "Localized versus Collective d Electrons and Néel Temperatures in Perovskite and Perovskite-Related Structures," *Phys. Rev.*, vol. 164, no. 2, p. 785–789, December 1967.
- [71] S. Sartipi, A. A. Khodadadi and Y. Mortazavi, "Pb-doped LaCoO₃ regenerative catalyst for automotive emissions control," *Appl. Catal. B Environ.*, vol. 83, no. 3–4, pp. 214–220, September 2008.
- [72] A. Mineshige and e. al., "Metal–Insulator Transition and Crystal Structure of La_{1–x}Sr_xCoO₃ as Functions of Sr-Content, Temperature, and Oxygen Partial Pressure," *Solid State Chem.*, vol. 142, no. 2, p. 374–381, February 1999.
- [73] V. V. Kharton and e. al., "Processing, microstructure and properties of LaCoO₃ ceramics," *J. Eur. Ceram. Soc.*, vol. 21, no. 13, pp. 2301–2309, November 2001.
- [74] N. Orlovskaya, Y. Gogotsi, M. Reece, B. Cheng and I. Gibson, "Ferroelasticity and hysteresis in LaCoO₃ based perovskites," *Acta Mater.*, vol. 50, no. 4, p. 715–723, February 2002.

- [75] S. T. Liu, Y. Wu and Y. Q. Jia, "Spin and valence state equilibria of cobalt and magnetic properties LaCoO_3 ," *J. Alloys Compd.*, vol. 200, no. 1-2, pp. 171-176, 8 October 1993.
- [76] I. P. W., *Monokryształy i nanocząstki wybranych manganitów i kobaltitów - wytwarzanie oraz właściwości magnetyczne*, Warszawa: PhD Thesis, 2014.
- [77] K. Asai and e. al., "Pressure Dependence of the 100 K Spin-State Transition in LaCoO_3 ," *J. Phys. Soc. Jpn.*, vol. 66, no. 4, pp. 967-970, April 1997.
- [78] C. H. Chen, H. Kruidhof, H. J. M. Bouwmeester and A. J. Burggraaf, "Ionic conductivity of perovskite LaCoO_3 measured by oxygen permeation technique," *J. Appl. Electrochem.*, vol. 27, no. 1, pp. 71-75, January 1997.
- [79] T. Ishigaki, S. Yamauchi, K. Kishio, J. Mizusaki and K. Fueki, "Diffusion of oxide ion vacancies in perovskite-type oxides," *J. Solid State Chem.*, vol. 73, no. 1, p. 179-187, March 1968.
- [80] H. Lu and e. al., "Ionic liquid-mediated synthesis of meso-scale porous lanthanum-transition-metal perovskites with high CO oxidation performance," *Chem. Commun.*, vol. 51, no. 27, p. 5910-5913, 2015.
- [81] C. A. Chagas, F. S. Toniolo, R. N. S. H. Magalhães and M. Schmal, "Alumina-supported LaCoO_3 perovskite for selective CO oxidation (SELOX)," *Int. J. Hydrog. Energy*, vol. 37, no. 6, p. 5022-5031, March 2012.
- [82] H. Taguchi, S. Yamasaki, A. Itadani, M. Yosinaga and K. Hirota, "CO oxidation on perovskite-type LaCoO_3 synthesized using ethylene glycol and citric acid," *Catal. Commun.*, vol. 9, no. 9, p. 1913-1915, May 2008.
- [83] P. M. Raccach and J. B. Goodenough, "First-Order Localized-Electron \rightleftharpoons Collective-Electron Transition in LaCoO_3 ," *Phys. Rev.*, vol. 155, no. 3, p. 932-943, March 1967.
- [84] A. M. Glazer, K. Roleder and J. Dec, "Structure and disorder in single-crystal lead zirconate, PbZrO_3 ," *Acta Crystallogr. B*, vol. 49, no. 5, p. 846-852, October 1993.

- [85] K. Huang, "Sr- and Ni-Doped LaCoO₃ and LaFeO₃ Perovskites," *J. Electrochem. Soc.*, vol. 145, no. 9, p. 3220, 1998.
- [86] K. Kobayashi, H. Kuwajima and T. Masaki, "Phase change and mechanical properties of ZrO₂-Y₂O₃ solid electrolyte after ageing," *Solid State Ion.*, Vols. 3-4, pp. 489-493, 1981.
- [87] T. K. Gupta, J. H. Bechtold, R. C. Kuznicki, L. H. Cadoff and B. R. Rossing, "Stabilization of tetragonal phase in polycrystalline zirconia," *J. Mater. Sci.*, vol. 12, no. 12, p. 2421-2426, December 1997.
- [88] T. K. Gupta, "Electrical Conductivity of Tetragonal Zirconia below the Transformation Temperature," *J. Electrochem. Soc.*, vol. 128, no. 4, p. 929, 1981.
- [89] W. Y. Yan, G. G. Reisner and F. D. Fischer, "Micromechanical study on the morphology of martensite in constrained zirconia," *Acta Mater.*, vol. 45, no. 5, p. 1969-1976, May 1997.
- [90] V. S. Stubican, R. C. Hink and S. P. Ray, "Phase Equilibria and Ordering in the System ZrO₂-Y₂O₃," *J. Am. Ceram. Soc.*, vol. 61, no. 1-2, pp. 17-21, January 1978.
- [91] R. C. Garvie, "The Occurrence of Metastable Tetragonal Zirconia as a Crystallite Size Effect," *J. Phys. Chem.*, vol. 69, no. 4, p. 1238-1243, April 1965.
- [92] K. Suzuki and K. Kijima, "Phase transformation of BaTiO₃ nanoparticles synthesized by RF-plasma CVD," *J. Alloys Compd.*, vol. 419, no. 1-2, p. 234-242, August 2006.
- [93] H.-U. Krebs and e. al., "Pulsed Laser Deposition (PLD) - A Versatile Thin Film Technique," in *Advances in Solid State Physics*, vol. 43, B. Kramer, Ed., Berlin, Springer, 2003, pp. 505-518.
- [94] J. kusinski, A. Kopia, L. Cieniek, S. Kac and A. Radziszewska, "Deposition of oxide and intermetallic thin films by pulsed laser (PLD) and electron beam (PED) methods," *Arch. Metall. Mater.*, vol. 60, no. 3, pp. 2173-2182, 2015.

- [95] H. Lee, C. H. J. Lim, M. J. Low, N. Tham, V. M. Murukeshan and Y.-J. Kim, "Lasers in additive manufacturing: A review," *Int. J. Precis. Eng. Manuf.-Green Technol.*, vol. 4, no. 3, p. 307–322, July 2017.
- [96] J. Berger and e. al., "Fiber-bundle coupled, diode end-pumped Nd:YAG laser," *Opt. Lett.*, vol. 13, no. 4, p. 306, April 1988.
- [97] B. Zhou, T. J. Kane, G. J. Dixon and R. L. Byer, "Efficient, frequency-stable laser-diode-pumped Nd:YAG laser," *Opt. Lett.*, vol. 10, no. 2, p. 62, February 1985.
- [98] R. Weber, B. Neuenschwander and H. P. Weber, "Thermal effects in solid-state laser materials," *Opt. Mater.*, vol. 11, no. 2-3, pp. 245-254, January 1999.
- [99] H. Hugel, "New solid-state lasers and their application potentials," *Opt. Lasers Eng.*, vol. 34, no. 4-6, pp. 213-229, October 2000.
- [100] J. P. Kruth, S. Kumar and J. Van Vaerenbergh, "Study of laser-sinterability of ferro-based powders," *Rapid Prototyp. J.*, vol. 11, no. 2, p. 287–292, December 2005.
- [101] K. Mumtaz and N. Hopkinson, "Selective laser melting of Inconel 625 using pulse shaping," *Rapid Prototyp. J.*, vol. 16, no. 4, p. 11, 2010.
- [102] H. Liao and J. Shie, "Optimization on selective laser sintering of metallic powder via design of experiments method," *Rapid Prototyp. J.*, vol. 13, no. 3, pp. 156-162, June 2007.
- [103] V. K. Balla, S. S. Bose and A. Bandyopadhyay, "Processing of Bulk Alumina Ceramics Using Laser Engineered Net Shaping," *Int. J. Appl. Ceram. Technol.*, vol. 5, no. 3, p. 234–242, May 2008.
- [104] D. Basting, K. D. Pippert and U. Stamm, "History and future prospects of excimer lasers," in *Second International Symposium on Laser Precision Micromachining*, Singapore, 2002.

- [105] X. Wang, J. Shao, H. Li, J. Nie and X. Fang, "Analysis of damage threshold of K9 glass irradiated by 248-nm KrF excimer laser," *Opt. Eng.*, vol. 55, no. 2, p. 027102, February 2016.
- [106] L. KyoungCheol and L. Cheon, "The Comparison of ITO Ablation Characteristics Using KrF Excimer and Nd:YAG Laser," in *Second International Symposium on Laser Precision Microfabrication*, Singapor, 2002.
- [107] J. A. Thornton, "Influence of apparatus geometry and deposition conditions on the structure and topography of thick sputtered coatings," *J. Vac. Sci. Technol.*, vol. 11, no. 4, p. 666–670, July 1974.
- [108] J. Jurusik and L. Żdanowicz, "Electron microscope investigations of the growth morphology of cadmium arsenide films vacuum deposited at various substrate temperatures," *Thin Solid Films*, vol. 67, no. 2, p. 285–292, April 1980.
- [109] J. Jurusik, "The columnar microstructure of amorphous cadmium arsenide thin films," *Thin Solid Films*, vol. 248, no. 2, p. 178–183, August 1994.
- [110] J. Marczak, Warsaw: Military University of Technology.
- [111] M. Phaneuf, "FIB for Materials Science Applications - a Review," in *Introduction to Focused Ion Beams*, Springer, Boston, MA, 2005, pp. 143-172.
- [112] A. Cyza, "Charakterystyka cienkich warstw LaCoO₃ i LaFeO₃ domieszkowanych Sr do zastosowań w detekcji gazów," Kraków, 2019.
- [113] A. Kopia, K. Kowalski, C. Leroux and J. R. Gavarrí, "Influence of the substrate on the structure stability LaLuO₃ thin films deposited by PLD method," *Vacuum*, vol. 134, p. 120–129, December 2016.
- [114] K. Kleveland, M.-A. Einarsrud and T. Grande, "Sintering of LaCoO₃ based ceramics," *J. Eur. Ceram. Soc.*, vol. 20, no. 2, p. 185–193, February 2000.

- [115] K. S. Ravichandran, S. An, R. E. Dutton and S. L. Semiatin, "Thermal Conductivity of Plasma-Sprayed Monolithic and Multilayer Coatings of Alumina and Yttria-Stabilized Zirconia," *J. Am. Ceram. Soc.*, vol. 82, no. 3, 2004.
- [116] E. C. Editors, "The thermal conductivity of silicon," May 1988. [Online]. Available: <https://www.electronics-cooling.com/1998/05/the-thermal-conductivity-of-silicon/>. [Accessed 02 11 2019].
- [117] M. Asheghi, M. N. Touzelbaev, K. E. Goodson, Y. K. Leug and S. S. Wong, "Temperature-Dependent Thermal Conductivity of Single-Crystal Silicon Layers in SOI Substrates," *J. Heat Transfer.*, vol. 120, no. 1, pp. 30-36, 1998.
- [118] O. Wiranwetchayan and e. al., "Characterization of perovskite LaFeO₃ synthesized by microwave plasma method for photocatalytic applications," *Ceram. Int.*, vol. 45, no. 4, p. 4802–4809, March 2019.
- [119] G. Beamson, A. Bunn and D. Briggs, "High-resolution monochromated XPS of poly(methyl methacrylate) thin films on a conducting substrate," *Surf. Interface Anal.*, vol. 17, no. 2, p. 105–115, February 1995.
- [120] M. M. Natile, A. Galenda and A. Glisenti, "From La₂O₃ To LaCoO₃ : XPS Analysis," *Surf. Sci. Spectra*, vol. 15, no. 1, p. 1–13, December 2008.
- [121] B. A. Hassel and A. J. Burggraaf, "Oxidation state of Fe and Ti ions implanted in yttria-stabilized zirconia studied by XPS," *Appl. Phys. Solids Surf.*, vol. 52, no. 6, p. 410–417, June 1991.
- [122] F. Zhang, A. Zhu, Y. Luo, Y. Tian, J. Yang and Y. Qin, "CuO Nanosheets for Sensitive and Selective Determination of H₂S with High Recovery Ability," *J. Phys. Chem. C*, vol. 114, no. 45, p. 19214–19219, November 2010.
- [123] Y. W. a. J. T. W. Yeow, "A Review of Carbon Nanotubes-Based Gas Sensors," *J. Sens.*, vol. 2009, pp. 1-24, 2009.

- [124] X. Wang, H. Qin, L. Sun and J. Hu, "CO₂ sensing properties and mechanism of nanocrystalline LaFeO₃ sensor," *Sens. Actuators B-Chem.*, vol. 188, p. 965–971, November 2013.
- [125] D. P. Volanti and e. al., "The Role of Hierarchical Morphologies in the Superior Gas Sensing Performance of CuO-Based Chemiresistors," *Adv. Funct. Mater.*, vol. 23, no. 14, p. 1759–1766, April 2013.
- [126] N. S. Ramgir and e. al., "Sub-ppm H₂S sensing at room temperature using CuO thin films," *Sens. Actuators B-Chem.*, vol. 151, no. 1, p. 90–96, November 2010.
- [127] Y. Qin and e. al., "Hierarchically Porous CuO Hollow Spheres Fabricated via a One-Pot Template-Free Method for High-Performance Gas Sensors," *J. Phys. Chem. C*, vol. 116, no. 22, p. 11994–12000, June 2012.
- [128] L. Ma and .. e. al., "Preparation of Co-doped LaFeO₃ nanofibers with enhanced acetic acid sensing properties," *Mater. Lett.*, vol. 200, p. 47–50, 2017.
- [129] I. S. Lyubutin, T. V. Dmitrieva and A. S. Stepin, "Dependence of exchange interactions on chemical bond angle in a structural series: Cubic perovskite-rhombic orthoferrite-rhombohedral hematite," *J. Exp. Theor. Phys.*, vol. 88, no. 3, p. 590–597, March 1999.
- [130] Y.-H. Choi, D.-H. Kim, S.-H. Hong and K. S. Hong, "H₂ and C₂H₅OH sensing characteristics of mesoporous p-type CuO films prepared via a novel precursor-based ink solution route," *Sens. Actuators B-Chem.*, vol. 178, p. 395–403, 2013.
- [131] S. M. Selbach, J. R. Tolchard, A. Fossdal and T. Grande, "Non-linear thermal evolution of the crystal structure and phase transitions of LaFeO₃ investigated by high temperature X-ray diffraction," *J. Solid State Chem.*, vol. 196, pp. 249–254, 2012.
- [132] H. L. e. al., "Laser in additive manufacturing: A review," *Int. J. Precis. Eng. Manuf. Green Technology*, pp. 307–322, Jul. 2017.

Mateusz JEDRUSIK

Institut de Matériaux Microélectronique et Nanosciences de
Provence, Université de Toulon,

Département d'Ingénierie des Surfaces et Caractérisation des
Matériaux Faculté des Sciences et technologies, AGH,
Cracovie

Microstructure et propriétés de détection de films minces de LaMO_3 ($M=\text{Co}, \text{Fe}$)

Des films minces de LaCoO_3 et LaFeO_3 ont été déposés sur des substrats de Si, YSZ cubique et YSZ quadratique, par PLD. Le but était d'obtenir des films minces nanocristallins sensible à NO_2 . Les films minces déposés sur YSZ ont été étudiés comme couches sensibles dans des capteurs résistifs et électrochimiques. Les films ont été caractérisés par DRX, MEB, AFM, XPS, MET-EDS. Une température de dépôt de 850°C permet d'obtenir des films minces monophasés et nanocristallins, avec un faible nombre de gouttes en surface, and sans fissures. Les films minces LaCoO_3 et LaFeO_3 ont respectivement des structures rhomboédrique et orthorhombique. Ils sont non-stoichiométriques, avec une formule chimique $\text{LaM}_{0.8}\text{O}_{3-\delta}$. Les facettes cristallographiques exposées aux gaz sont $\{101\}_\text{O} = \{001\}_\text{C}$ pour LaFeO_3 et $\{2-10\}_\text{H} = \{101\}_\text{C}$ pour LaCoO_3 , sur C-YSZ. Les films minces LaFeO_3 ont montré une très grande sensibilité à NO_2 , une bonne réponse même à température ambiante, ainsi qu'une sélectivité à NH_3 et CO . Les films LaCoO_3 ont faiblement réagi à NO_2 . En tant que capteur électrochimique, LaFeO_3 sur T-YSZ a montré de bonnes performances, ouvrant le champ de capteurs sur support flexible.

Mot clés : Films minces, pérovskites, capteurs de gaz

Microstructure and sensing properties of LaMO_3 ($M=(\text{Co},\text{Fe})$) thin films

Thin films of LaCoO_3 and LaFeO_3 were deposited on Si, YSZ cubic and YSZ tetragonal substrates, using Pulsed Laser Deposition. The aim was to produce nanocrystalline thin films sensitive towards NO_2 . The thin films deposited on YSZ were investigated as sensing electrode in chemical and electrochemical sensors. The thin films were characterized by XRD, SEM, AFM, XPS, TEM coupled with EDS. A deposition temperature of 850°C led to single phased nanocrystalline thin films, with a low number of droplets on the surface, and without cracks. The thin films LaCoO_3 and LaFeO_3 have respectively rhombohedral and orthorhombic structures. They are non-stoichiometric, with a chemical formula $\text{LaM}_{0.8}\text{O}_{3-\delta}$. The crystallographic facets exposed to the gas are $\{101\}_\text{O} = \{001\}_\text{C}$ for LaFeO_3 and $\{2-10\}_\text{H} = \{101\}_\text{C}$ for LaCoO_3 , on C-YSZ. The LaFeO_3 thin films showed very high sensitivity to NO_2 , good response even at ambient temperature as well as selectivity towards NH_3 and CO . LaCoO_3 thin films weakly reacted to NO_2 . In electrochemical sensors, LaFeO_3 on T-YSZ substrate had good performances, opening the field for new electrochemical sensors on flexible substrates.

Keywords: thin films, perovskites, gas sensors